

Carnegie Mellon University

CARNEGIE INSTITUTE OF TECHNOLOGY

THESIS

SUBMITTED IN PARTIAL FULFILLMENT OF THE REQUIREMENTS

FOR THE DEGREE OF Doctor of Philosophy

**TITLE Patient-Specific 3D Vascular Reconstruction and Computational
Assessment of Biomechanics – an Application to Abdominal
Aortic Aneurysm**

PRESENTED BY Samarth Shankar Raut

ACCEPTED BY THE DEPARTMENT OF

MECHANICAL ENGINEERING

ADVISOR, MAJOR PROFESSOR

DATE

DEPARTMENT HEAD

DATE

APPROVED BY THE COLLEGE COUNCIL

DEAN

DATE

Patient-Specific 3D Vascular Reconstruction and Computational Assessment of Biomechanics – an Application to Abdominal Aortic Aneurysm

Submitted in partial fulfillment of the requirements for

the degree of

Doctor of Philosophy

in

Department of Mechanical Engineering

Samarth S. Raut

M.S., Mechanical Engineering, Indian Institute of Technology, Bombay
B.S., Mechanical Engineering, Shivaji University, Kolhapur

Carnegie Mellon University
Pittsburgh, PA

August, 2012

Copyright Notice

© 2012, Samarth S. Raut

Acknowledgements

I express my sincere gratitude for my thesis advisor Prof. Ender Finol for providing me with all the necessary support and guidance, both in academic and non-academic matters. His flexible and nurturing attitude towards my research work and accessibility allowed me tremendous freedom to explore variety of aspects related to this multi-disciplinary research and thereby learn many skill sets. I am also thankful to my co-advisor Dr. Anirban Jana for his mentorship and frequent expert advices during the period of last four years. The extensive help for image segmentation received from Jesus Urrutia, Junjun Zhu, Dennis Ou, and Allen Chen cannot be separated from this research. I thankfully acknowledge contribution of Lourdes Rios and Dr. Vitaly Kheyfets for benchmarking of developed framework for mesh generation. Interesting technical, philosophical, and mostly random discussions with lab mate Abhay Ramachandra, especially while working in lab during late hours, deserve a special mention as it helped to keep up the momentum. Occasional help received from lab mates Dr. Santanu Chandra, Dr. Hong Zhang, Dr. Judy Shum, Kibaek Lee, Viji Manneth, and Peng Liu is appreciated. Friendly advices from lab mates Dr. Santanu Chandra and Dr. Vitaly Kheyfets during some important phases in last four years helped me to be on the right track.

Emotional strength and support I received from family and friends has also played important role. Confidence of Aai and Bapu (my parents), Dada (brother), and Didi (sister) in me kept me motivated. That warmth had its impact in spite of distance of thousands of miles! I am thankful to my friends for maintaining lively environment and wonderful group events that helped me rejuvenate intermittently. Thanks to my friends Mr. Anirban Roy, Puraskar Ingale, and Tanuka Biswas many logistical issues were ironed out before and after transition of my research to San Antonio. I appreciate help from my friend Dr. Manish Joglekar for proof reading the thesis manuscript.

I am thankful to the Department of Mechanical Engineering, Carnegie Mellon University (CMU) for providing me with this wonderful research opportunity. The enthusiastic help and flexibility I received from Mr. Chris Hertz has been very useful, especially in later part of my research after relocating to San Antonio. I am thankful to the Institute for Complex Engineered Systems (ICES-CMU) staff, especially, computer administrator Mr. Charlie Matous, Ms.

Rhonda Moyer, Ms. Christina Cowan, Ms. Alicia Angemeer, and Ms. Becca Gray who promptly offered help for my research every now and then. Infrastructure support from ICES, Pittsburgh Supercomputing Center, and the Department of Biomedical Engineering, University of Texas at San Antonio (UTSA), San Antonio is acknowledged. Anonymous helping hands through online forums such as www.linuxquestions.org and Wikipedia deserve a mention for their help towards solving various bottlenecks in this research. Also, use of open source codes [ISO2Mesh](#), [CGAL](#), [TetGen](#), [TetView](#), [Triangle](#), [MIPAV](#), and [MeshLab](#) is gratefully acknowledged.

I am very thankful to the members in my PhD thesis committee for their interest in my research as well as their valuable time, energy, and expert advice towards refinement of the research work. I would like to acknowledge research funding from Dean's Fellowship Carnegie Mellon University facilitated by the Department of Mechanical Engineering, John and Clair Bertucci fellowship facilitated through ICES, and NIH grants R21EB007651, R21EB008804, and R15HL087268 without which this work would not have been possible.

PhD Thesis Committee:

- 1) Prof. Ender A. Finol, PhD (Chair)
Carnegie Mellon University, Pittsburgh.
University of Texas at San Antonio, San Antonio.
- 2) Dr. Anirban Jana, PhD
Pittsburgh Supercomputing Center, Pittsburgh.
- 3) Dr. Satish Muluk, MD
Allegheny General Hospital, Pittsburgh.
- 4) Prof. Anne Robertson, PhD
University of Pittsburgh, Pittsburgh.
- 5) Prof. Kenji Shimada, PhD
Carnegie Mellon University, Pittsburgh.

Dedication

डोक्यावर हलकेच टपली मारत “जे काही पिकवायचं ते - इथेच” असं ज्यांनी सांगितलं
आणि ज्यांनी वैज्ञानिक दृष्टिकोन माझ्या अंगी रुजवला त्या आई आणि बापूंना अर्पण !

(Dedicated to Mom (“Aai”) and Dad (“Bapu”) who cultivated a scientific
approach within me and passed on their message while gently tapping on my
head -“harvest whatever you want - here” !)

Abstract

The current clinical management of abdominal aortic aneurysm (AAA) disease is based on measuring the aneurysm maximum diameter to decide when timely intervention can be recommended to a patient. However, other parameters may also play a role in causing or predisposing the AAA to either an early or delayed rupture relative to its size. Therefore, patient-specific assessment of rupture risk based on physical principles such as individualized biomechanics can be conducive to the development of a vascular tool with translational potential. To that end, the present doctoral research materialized into a framework for image based patient-specific vascular biomechanics assessment.

A robust generalized approach is described herein for image-based volume mesh generation of complex multidomain bifurcated vascular trees with the capability of incorporating regionally varying wall thickness. The developed framework is assessed for geometrical accuracy, mesh quality, and optimal computational performance. The relative influence of the shape and the constitutive wall material property on the AAA wall mechanics was explored. This study resulted in statistically insignificant differences in peak wall stress among 28 AAA geometries of similar maximum diameter (in the 50 – 55 mm range) when modeled with five different hyperelastic isotropic constitutive equations. Relative influence of regionally varying vs. uniform wall thickness distribution on the AAA wall mechanics was also assessed to find statistically significant differences in spatial maxima of wall stresses, strains, and strain energy densities among the same 28 AAA geometries modeled with patient-specific non-uniform wall thickness and two uniform wall thickness assumptions. Finally, the feasibility of estimating in vivo wall strains from individual clinical images was evaluated. Such study resulted in a

framework for in vivo 3D strain distributions based on ECG gated, unenhanced, dynamic magnetic resonance images acquired for 20 phases in the cardiac cycle. Future efforts should be focused on further development of the framework for in vivo estimation of regionally varying hyperelastic, anisotropic constitutive material models with active mechanics components and the integration of such framework with an open source finite element solver with the goal of increasing the translational potential of these tools for individualized prediction of AAA rupture risk in the clinic.

Keywords: Patient-specific biomodeling, anatomical mesh fairing, uncertainties in biomodeling, in vivo material characterization, in vivo strain, variable wall thickness, computed tomography, magnetic resonance imaging, abdominal aortic aneurysm, AAA, vascular biomechanics.

Table of Contents

Acknowledgements	vii
Dedication	ix
Abstract.....	xi
List of Tables	xix
List of Figures.....	xxi
Chapter 1. Biological, Geometric, and Biomechanical Factors Influencing Abdominal Aortic Aneurysm Rupture Risk: a Comprehensive Review	27
1.1 INTRODUCTION.....	29
1.2 BIOLOGICAL FACTORS	31
1.2.1 Matrix-metallo-proteinases (MMPs)	33
1.2.2 Tissue inhibitors of metalloproteinases (TIMP)	35
1.2.3 Macrophage and lymphocyte presence	36
1.2.4 Autoimmune response	37
1.2.5 Reactive Oxygen Species (ROS)	38
1.2.6 C-Reactive Protein (CRP).....	40
1.2.7 Dyslipidemia	40
1.2.8 Mycotic aneurysms	41
1.2.9 Genetic aspects.....	41
1.2.10 Miscellaneous factors.....	42
1.2.11 Summary of etiology.....	43
1.3 GEOMETRIC FACTORS	45
1.3.1 Baseline diameter and propensity of AAA development	45
1.3.2 Importance of shape for wall mechanics	46
1.3.3 ILT as a geometric feature	47
1.3.4 Wall thickness as geometric feature	47
1.3.5 Correlation of geometric features with peak wall stress	48
1.3.6 Geometry quantification	49
1.4 BIOMECHANICAL FACTORS: FEA, CFD, AND FSI ANALYSES	52
1.4.1 Initial studies with idealized model	57

1.4.2	Patient-specific modeling of AAA geometry	57
1.4.3	Metrics for material failure criteria.....	58
1.4.4	AAA material behavior and constitutive models.....	58
1.4.5	Influence of ILT on peak wall stress.....	59
1.4.6	Influence of calcification	60
1.4.7	Influence of initial AAA configuration.....	61
1.4.8	Effect of blood flow	63
1.4.9	Comments regarding simulation framework	66
1.5	SPECIFIC AIMS.....	68
1.6	SUMMARY	70
Chapter 2. A Framework for Multi-Domain Volume Meshing of Blood Vessels for Finite Element Modeling: Application to Abdominal Aortic Aneurysms		73
2.1	INTRODUCTION.....	75
2.2	BACKGROUND.....	77
2.2.1	Relevant computational geometry concepts	77
2.2.2	Surface reconstruction in biomodeling	80
2.2.3	Volume mesh generation for biomodeling	81
2.2.4	Multi-domain mesh generation	82
2.3	METHODOLOGY	84
2.3.1	Overview	84
2.3.2	Volumetric data creation.....	85
2.3.3	Surface mesh extraction.....	88
2.3.4	Surface mesh refinement.....	89
2.3.5	Wall extrusion.....	92
2.3.6	Multi-domain mesh generation sequence	95
2.3.7	Mesh quality assessment.....	97
2.3.8	Export module.....	101
2.3.9	Validation protocol	102
2.4	RESULTS.....	105
2.4.1	Phantom based studies	107
2.4.2	Patient-specific studies.....	119
2.5	DISCUSSION	126
2.5.1	Contribution	126

2.5.2	Salient features.....	127
2.5.3	Distance field interpolation.....	133
2.5.4	Effect of smoothing iterations.....	136
2.5.5	Comparisons with other relevant frameworks	144
2.5.6	Limitations	148
Chapter 3. Evaluation of the Effects of Aneurysm Geometry and Vascular Wall Material Properties on the AAA Wall Mechanics		149
3.1	INTRODUCTION.....	151
3.2	METHODS.....	154
3.2.1	The AAA subject population	154
3.2.2	Finite element discretization	156
3.2.3	Constitutive material models	157
3.2.4	Finite element analysis.....	158
3.2.5	Convergence study.....	160
3.2.6	Statistical analysis	161
3.3	RESULTS.....	162
3.3.1	Normalized variations	162
3.3.2	Analysis of variance.....	167
3.4	DISCUSSION	168
3.4.1	Relevance to prior work.....	169
3.4.2	Study outcomes.....	172
3.4.3	Limitations	174
3.5	CONCLUSION	176
Chapter 4. Assessment of the Effect of Regional Variations in Wall Thickness on the AAA Wall Mechanics		177
4.1	INTRODUCTION.....	179
4.2	METHODS.....	182
4.2.1	The AAA subject population	182
4.2.2	Image segmentation	182
4.2.3	Finite element discretization	183
4.2.4	Patient-specific non-uniform wall thickness (PSNUT)	185
4.2.5	Material model	187
4.2.6	Finite element analysis.....	187

4.2.7	Convergence study.....	187
4.2.8	Statistical analysis.....	188
4.3	RESULTS.....	189
4.4	DISCUSSION	197
4.4.1	The need for modeling non-uniform wall thickness.....	197
4.4.2	Wall extrusion vs. mask dilation approach.....	199
4.4.3	Comments on convergence study	201
4.4.4	Limitations	202
4.5	CONCLUSION	203
Chapter 5. Development of a Framework for the Estimation of In Vivo Patient-Specific Strain of the Diseased Abdominal Aorta.....		205
5.1	INTRODUCTION.....	207
5.2	METHODS.....	209
5.2.1	Image acquisition and segmentation.....	209
5.2.2	3D Surface reconstruction.....	210
5.2.3	Intraluminal pressure estimation.....	211
5.2.4	In vivo strain estimation.....	212
5.3	RESULTS.....	215
5.4	DISCUSSION	219
Chapter 6. Conclusions and Future Work.....		225
6.1	CONCLUSIONS.....	227
6.2	FUTURE WORK.....	228
References.....		231
APPENDICES.....		247
APPENDIX A: Analytical calculations of phantom.....		247
A)	Volume calculation for phantom	247
B)	Analytical area calculation for phantom	248
C)	Wall domain-specific volume	248
APPENDIX B: Metric definitions for mesh characterization.....		251
A)	r-R ratio formula	251
B)	relAreaErr	251
C)	relVolErr	252
D)	distErr	252

E)	<i>distErr_max</i>	252
F)	<i>distErr_avg</i>	252
G)	<i>distErr_std</i>	252
APPENDIX C: CT image acquisition parameters and AAA maximum diameter for shortlisted cohort.....		253
APPENDIX D: Exploration of computational performance of FE solver for optimized settings towards effective computational resource utilization		255
a)	Problem statement.....	255
b)	Computational Resource:.....	255
c)	Methods.....	255
d)	FE Details.....	255
e)	Material Models	255
f)	Observations and results	255
g)	Conclusion	256
APPENDIX E: Scripts for pre-processing and automated execution of FEA simulations		257
a)	Bash Script.....	257
b)	Adina preprocessing commands	260
APPENDIX F: Results of the mesh sensitivity study for patient-specific model U032		265
APPENDIX G: Mesh convergence study to assess effect of number of wall layers..		269
APPENDIX H: Demonstration of calculation of intra- and inter-patient variability		273
APPENDIX I: Qualitative observations on the location of the AAA maximum first principal stresses		276
APPENDIX J: Estimated statistics of wall thickness in AAA sac		281
APPENDIX K: 3D Interactive model (enabled only when using PDF viewer)		283

List of Tables

Table 1: Abbreviations used in subsequent literature review summary tables.....	53
Table 2: Literature review summary - solid mechanics simulations of AAA –Part 1	54
Table 3: Literature review summary - solid mechanics simulations of AAA –Part 2	55
Table 4: Literature review summary – Fluid-Structure-Interaction simulations of AAA	56
Table 5: Voxelization error - effect of image resolution.....	107
Table 6: Voxelization error - effect of symmetry.	108
Table 7: Voxelization error - effect of radius variation.	108
Table 8: Effect of different distance field creation approaches.....	108
Table 9: Effect of mask resolution on phantom reconstruction using finalized meshing parameters....	118
Table 10: Mesh quality obtained for phantom using finalized meshing parameters.....	119
Table 11: Effect of distance field creation on geometrical aspect of patient-specific model.	119
Table 12: Benchmarking with commercial code (values in bold font highlight sliver-free status; if slivers are present, range for worst 50 elements is reported).....	121
Table 13: Summary of DICOM image data for shortlisted cohort (units: millimeter).	155
Table 14: Summary of material models explored.	158
Table 15: Mean and standard deviations of the four maximum biomechanical parameters for each material model.	162
Table 16: Mean and standard deviations of the four average biomechanical parameters for each material model.	163
Table 17: Average variation in the normalized absolute maximum biomechanical parameters in intra- patient and inter-patient data analysis.	164
Table 18: Average variation in the normalized absolute average biomechanical parameters in intra- patient and inter-patient data analysis.	164
Table 19: p-values obtained by ANOVA for maximum and average biomechanical parameters.....	167
Table 20: Brief summary of previously reported experimental measurements on wall thickness (eAAA – electively repaired AAA; rAAA – ruptured AAA).....	180
Table 21: Statistical summary of maximum biomechanical parameters for the wall thickness modeling strategies.	191
Table 22: Statistical summary of spatially averaged biomechanical parameters for the wall thickness modeling strategies.	191
Table 23: Signed and unsigned average of percentage errors in 28 datasets considering the maximum biomechanical parameters in the AAA sac. Consistent underestimation is seen as there is little difference in signed and unsigned averages of the %error in biomechanical parameters for UT and PSUT approach (using results from the PSNUT strategy as the reference standard). S – Signed, US – Unsigned.....	191
Table 24: Signed and unsigned average of percentage errors in 28 datasets considering average values of the biomechanical parameters in the AAA sac. No consistent underestimation or overestimation is seen as there is appreciable difference in signed and unsigned averages of the %error in	

biomechanical parameters for UT and PSUT approach (using results from the PSNUT strategy as the reference standard). S – Signed, US – Unsigned.....	192
Table 25: p-values obtained by ANOVA analysis for maximum biomechanical parameters corresponding to three approaches for wall thickness modeling.....	192
Table 26: p-values obtained by ANOVA analysis for average biological parameters corresponding to three approaches for wall thickness modeling.....	192
Table 27: Pressure-strain modulus calculation.	217
Table 28: AAA maximum diameter and image parameters in the shortlisted population cohort.	253
Table 29: Explored configurations for simulation execution and corresponding execution time	256

List of Figures

Figure 1 : Abdominal Aortic Aneurysm	29
Figure 2: Succession of biological events related to AAA rupture. Reproduced in modified form from [16] with permission.	31
Figure 3: Localized stresses, fragmented medial proteins, and genetic predisposition likely attract inflammatory cells into the aortic wall. Released chemokines, cytokines, and reactive oxygen species by these inflammatory cells result in further influx of leukocytes, and further medial degradation. IEL – internal elastic lamina; EEL- external elastic lamina; Reproduced from [39] with permission.	36
Figure 4: Estimated wall thickness distribution (in mm) in a point cloud resulting from a segmented CT dataset [2].	48
Figure 5: (a) 1-D size indices: maximum diameter (Dmax), proximal neck diameter (Dneck,p), distal neck diameter (Dneck,d), sac height (Hsac), neck height (Hneck), sac length (Lsac), neck length (Lneck), bulge height (Hb); (b) 1-D size index: centroid distance at the maximum diameter (dc). Reproduced from Shum [2].....	50
Figure 6: Schematic of 2D shape indices providing an approximate measure to construct the global AAA shape: diameter to height ratio (DHR), diameter to diameter ratio (DDR), height ratio (Hr), bulge location (BL), asymmetry (β), and tortuosity (T). Reproduced from Martufi et al [101].	51
Figure 7: Displacement and stress distribution in three patient-specific geometries for both the CT image based analysis and the zero pressure configuration. Analysis based on the zero pressure configuration yielded a larger peak wall stress (reproduced from unpublished data).....	62
Figure 8: Maximum and average principal stress and strain waveforms for a patient-specific AAA obtained using direct FSI, uncouple FSI and transient FEA. The stress and strain follow the inlet velocity waveform rather than the pressure waveform boundary condition (reproduced from unpublished data).....	65
Figure 9: Important factors affecting computational wall mechanics evaluation (ignoring image segmentation errors) and scope of presented research highlighted by ovals with thickened borders.	70
Figure 10: Meshing using subdivision of image segmentation splines.	81
Figure 11: Limitations of commercial codes. eVoMaC approach (Simpleware®) (a), b), c), and d)) reported in Young [6]. Voids (a) and (b) and typical voxelized pattern/coordinate frame dependency (c) and d). Wall in d) in red is obtained by outward extrusion while ILT in green is obtained by eVoMaC method. Example reconstruction using Mimics® (e, f, g, h); e) attempted without mask dilation/erosion; f) and g) show typical coordinate frame dependent pattern dominated by vertical and horizontal grid lines; h) shows irregular mesh pattern across thickness.	83
Figure 12: Block diagram illustrating the proposed framework (AAAMesh).	85
Figure 13: Input mask and continuous distance field (a) 4-domain mask; 0, 1, 2, and 3 represent the domains of interest in the mask e.g. 0 - abdominal cavity, 1 - vascular wall, 2 - intraluminal	

thrombus, and 3 - lumen, respectively; b) 2D slice in z-plane of the extracted distance field for perfectly circular cross section.....	86
Figure 14: Surface mesh quality metric (minimum r-R ratio) as a function of sliver removal iterations using the edge collapse technique.	89
Figure 15: Schematic of surface meshing operations.....	91
Figure 16: Flowchart for wall extrusion code Wall-E (dotted line - optional, continuous line – default). ..	93
Figure 17: A unit depicting scheme for inner wall surface interface.	97
Figure 18: Hexahedral element node numbering scheme in natural coordinates.	99
Figure 19: Phantom of idealized model (to be reconstructed) for validation and one exemplary mask.	103
Figure 20: Sphere marching approach for calculating the exact perpendicular distance of a point from an analytical surface for validation of the meshing strategy.....	104
Figure 21: Coordinate frame convention (+x from patient's right to left; +y from anterior to posterior; +z from leg to head) and an asymmetric phantom for validating directionality.....	105
Figure 22: Isocontours of distance field resulting from different interpolation strategies. Center figure shows representative color plot of distance field for vertical mid slice using phantom model and strategy d). Rectangle marks area zoomed in a), b), c) and d). a) No interpolation b) 2D interpolation c) 3D grid distance d) 3D Euclidean distance.....	109
Figure 23: Qualitative comparison of influence of different distance field creation approaches on surface roughness and <i>distErr</i> : (a) no distance field interpolation (0D), (b) interpolation in the plane of the image (2D), and (c) 3D interpolation. Color legend refers to <i>distErr</i> metric.....	111
Figure 24: Comparison of Laplace and Taubin smoothing algorithms on geometric accuracy of phantom using <i>distErr</i> (cm) as a metric. x-axis shows number of smoothing iterations applied and legend denotes different element sizes. a) Laplace smoothing, y-axis: <i>distErr</i> (cm); b) Taubin smoothing, y-axis: <i>distErr</i> (cm); c) Laplace smoothing, y-axis: standard deviation in <i>distErr</i> (cm); d) Taubin smoothing, y-axis: standard deviation in <i>distErr</i> (cm).	113
Figure 25: Comparison of Laplace and Taubin smoothing algorithms on geometric accuracy of phantom using relative error in area and volume as a metric. x-axis shows number of smoothing iterations applied and legend denotes different element sizes. a) Laplace smoothing, y-axis: relative area error; b) Taubin smoothing, y-axis: relative area error; c) Laplace smoothing, y-axis: relative volume error; d) Taubin smoothing, y-axis: relative volume error.	115
Figure 26: Effect of Laplace and Taubin smoothing on surface mesh quality of the phantom. x-axis shows number of smoothing iterations applied and legend denotes different element sizes; y-axis: r-R ratio average (ideal value 1); a) Laplace smoothing; b) Taubin smoothing.....	117
Figure 27: Comparison of smoothing action of Laplace and Taubin smoothing algorithms. Effect of 6 Laplace iterations shown in views on left; effect of 20 Taubin iterations shown in views on right. Laplace action is concentrated at high curvature and Taubin action more or less distributed however more inclined to pushing back outward.	118
Figure 28: Effect of distance field creation strategy on the extracted surface of a patient-specific model. a) 0D interpolation; b) 2D interpolation; c) 3D interpolation (Euclidean).	120
Figure 29: Comparison of Laplace and Taubin smoothing algorithms on geometric accuracy of patient-specific model using relative error in area and volume as a metric. x-axis shows number of smoothing iterations applied and legend denotes different element sizes. a) Laplace smoothing, y-	

axis: relative area error; b) Taubin smoothing, y-axis: relative area error; c) Laplace smoothing, y-axis: relative volume error; d) Taubin smoothing, y-axis: relative volume error.	123
Figure 30: Effect of Laplace and Taubin smoothing on surface mesh quality of the patient-specific geometry; x-axis shows number of smoothing iterations applied and legend denotes different element sizes; y-axis: r-R ratio average (ideal value 1); a) Laplace smoothing; b) Taubin smoothing.	124
Figure 31: AAAMesh generated multi-domain mesh of aneurysm. Wall is formed by hexahedral elements and ILT by tetrahedral elements. It highlights complex ILT configuration having some part of it exposed at the outlet cross section. Ends are forced to be flat.....	125
Figure 32: AAAMesh ability to handle acute bifurcations and robustness for handling practical scenarios; (a) case 1, (b) case 1 zoomed at bifurcation, (c) case 2 with free form ends, (d) case 2 zoomed at bifurcation.	125
Figure 33: Multi-domain meshing challenges.	129
Figure 34: Different approaches to model ILT adhesion to wall.....	131
Figure 35: Schematic explaining why voxel based volume estimation closely approximates actual volume.....	132
Figure 36: Schematic illustrating 2D distance field creation strategy and anisotropy in grid spacing. Filled circle is inside while unfilled is outside object and arrow length represents distance field magnitude using 2D interpolation with sign change near boundary. Green stars approximately locate zero and dashed black line shows corresponding reconstructed erroneous surface. Green circle locates one location where error would be more if 2D interpolation is used instead of 3D - a) depiction of 2D approach with actual anisotropic grid spacing b) depiction of ideal uniform grid spacing.....	134
Figure 37: Rationale behind volume accuracy and overestimation of surface area.	136
Figure 38: Volume as a shape distortion metric – regional changes may counteract each other.	136
Figure 39: Optimal smoothing iterations different for different mesh density (size); iliac distortion with number of Laplace smoothing iterations (nLaplace) (a) size 14, nLaplace=14, (b) size 32, nLaplace = 1, (c) size 32, nLaplace 14.	142
Figure 40: Schematic comparing Laplace and Taubin smoothing action.	142
Figure 41: Schematic showing variability in the maximum diameter measurement and its dependence on the orientation of the reference plane.....	151
Figure 42: AAAMesh GUI snapshot.....	156
Figure 43: The range of material parameter variation in the c_1 - c_2 space for the hyperelastic isotropic constitutive model.....	157
Figure 44: Distribution of the maximum biomechanical parameters in AAA models with the highest and lowest norm of variability in intra-patient and inter-patient data analysis.	165
Figure 45: Intra-patient and inter-patient absolute normalized percentage variations in the maximum and average biomechanical parameters.	166
Figure 46: Typical maximum and average stresses obtained in this work superimposed on previously reported uniaxial tensile data reproduced from Raghavan and Vorp [3].	175
Figure 47: Framework for image segmentation with capability of variable wall thickness estimation [2].	184
Figure 48: Schematic of cosine correction for mesh extrusion.....	185

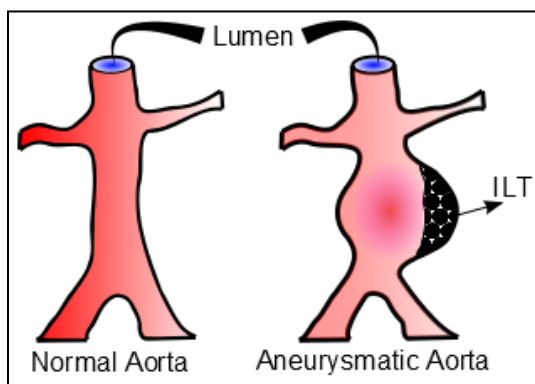
Figure 49: Intermediate steps in wall thickness implementation and qualitative assessment with final mesh, a) superimposition of splines and surface mesh, b) interpolated wall thickness, c) qualitative assessment of thickness modeling by comparing interpolated thickness distribution and final FE volume mesh.	187
Figure 50: Convergence study showing incremental percentage differences (y-axis) in biomechanical parameters along with an increase in the factor (x-axis) governing average edge length of the surface mesh elements used for wall extrusion (proportional relationship). An increase in the number of elements will have a quadratic relationship with this factor. Convergence study pertaining to: a) systolic blood pressure (120 mmHg); b) diastolic blood pressure (80 mmHg); c) amplitude of pressure wave (40 mmHg)	190
Figure 51: Box-and-whisker plots highlighting differences in results for three wall thickness modeling strategies, a) Maximum first principle stress (N/cm^2); b) Average first principle stress (N/cm^2); c) Maximum first principal strain; d) Average first principal strain; e) Maximum strain energy density ($105erg/cm^3$); f) Average strain energy density ($105erg/cm^3$); g) Maximum displacement (cm); h) Average displacement (cm).	194
Figure 52: Comparison of regional distribution of the biomechanical parameters for AAA model U037 obtained with UT – uniform thickness ($=0.15\text{ cm}$), PSUT – patient-specific uniform thickness ($=0.2044\text{ cm}$), PSNUT – patient-specific non-uniform thickness ($=0.2044 \pm 0.0487$, minimum 0.07615 , max $= 0.3991$, unit: cm). PS1 – maximum principal stress, PE1 – minimum principal strain, SED – strain energy density, Disp – Displacement magnitude.	195
Figure 53: Zoomed view of the comparison of regional distribution of the biomechanical parameters for AAA model U37 obtained with UT – uniform thickness ($=0.15\text{ cm}$), PSUT – patient-specific uniform thickness ($=0.2044\text{ cm}$), PSNUT – patient-specific non-uniform thickness ($=0.2044 \pm 0.0487$, minimum 0.07615 , max $= 0.3991$, unit: cm). PS1 – maximum principal stress, PE1 – minimum principal strain, SED – strain energy density, Disp – Displacement.	196
Figure 54: Limitations of mask dilation approach for wall thickness modeling: a) errors due to inherent differences in rectangular image grid and circular shape of the anatomy; b) effective thickness along the local normal direction is a function of the slope in the plane normal to the image for the same dilation ‘t’ in the image plane (L denotes the direction of image stacking); c) Schematic with 1 px dilation showing non-uniform dilation around the periphery (Px – pixel resolution).....	202
Figure 55: Schematic of the imaged AAA in the coronal plane, from the renal arteries to the aorto-iliac bifurcation; AAA sac slices in a transverse plane were used for this study.....	209
Figure 56: Exemplary reconstructed AAA outer surfaces for phase #1, #3, and #19 and superimposition of phase #3 and phase #19 with phase #1.....	211
Figure 57: Scaled pressure waveform for patient #1 obtained by combining patient-specific brachial cuff measurements with data reported earlier by Veer et al [1].	212
Figure 58: 2D schematic of deformation; reference configuration (Ω_0), deformed configuration (Ω'), displacement vector field (u), and position vectors X and x	213
Figure 59: Unrealistic first principal strain near distal end and neck region (likely due to lack of image contrast and resolution related distortions).	216
Figure 60: Depiction of zones #1 and #2 considered for analysis.	216
Figure 61: Strain distribution at zone #1 evaluated at near systole.	216
Figure 62: Variation of the maximum first principal strain over one cardiac cycle.	218

Figure 63: Variation of the area weighted spatial mean of the maximum first principal strain.....	218
Figure 64: Histogram endorsing the assumption of wall displacement along local normals.	221
Figure 65: Visual representation of computational performance.	256
Figure 66: Mesh convergence study - biomechanical parameter absolute values.....	266
Figure 67: Mesh convergence study - incremental change in biomechanical parameter.	268
Figure 68: Schematic illustrating rationale behind high stresses in saddle shaped surface region	276
Figure 69: Close correlation in saddle point and high stress region in 28 patient-specific geometries under identical material model parameters and pressure loads.	280

Chapter 1. Biological, Geometric, and Biomechanical Factors Influencing Abdominal Aortic Aneurysm Rupture Risk: a Comprehensive Review

1.1 INTRODUCTION

An abdominal aortic aneurysm (AAA) is a focal abnormal widening of the aorta larger than 1.5 times its normal healthy diameter. It is associated with degradation of connective tissue in the arterial wall and is most often found with a deposition from inside, called intra-luminal-thrombus (ILT), consisting of fibrinous blood clots and cell debris (see schematic in Figure 1). The hollow cavity through which blood flows is called the lumen.



The underlying cause for the formation of an aneurysm can be either inherited (i.e., Marfan syndrome or Ehlers Danlos syndrome) or acquired, with risk factors including hypertension, atherosclerosis, and smoking among others. Maximum aortic diameter and

Figure 1 : Abdominal Aortic Aneurysm

expansion rate are the strongest clinical

predictors of aneurysm rupture [4]. AAAs are potentially life-threatening medical conditions often requiring surgical intervention. The reported incidence of AAA is a 4.9%-9.9% in the United Kingdom, accounting for more than 8000 deaths in the United Kingdom [5, 6] and 15000 deaths in the US every year [7]. AAA surgical interventions continue to pose a serious risk on patients with a mortality rate of about 5% on patients with stable AAA in the US, and about 1-5% in the best centers in the UK [6]. More than 50% of patients die before reaching the hospital after AAA rupture, with emergency repair having about 40–50% mortality [6]. To reduce aneurysm related mortality, several countries have implemented population screening programs among the

population with risk factors. Currently, clinical practice is to repair an AAA exceeding 5.5 cm in men, whereas in women a maximum diameter of 5.0 cm is considered as threshold since women with aneurysm have an increased risk of rupture [8, 9]. However, it has been reported that only 25% of AAAs rupture in a patient's lifetime [10], and therefore clinicians need start to compare the risk of rupture with the risk of repair, particularly because of the increased operative mortality in the elder patients [11].

Recent research has pointed the unsuitability of deciding a surgical repair based solely on the maximum diameter criterion [10, 12-15]. It is known that small AAAs can rupture and large AAAs can remain stable. Therefore, other rupture risk parameters are needed as an alternative to the customary AAA size and expansion rate. A biomechanics based approach may be a viable option. Recent work by Gasser et al [16] found that biomechanical parameters such as Peak Wall Stress (PWS) and Peak Wall Rupture Risk (PWRR) were 1.17 and 1.43 times higher in ruptured AAAs compared to those in diameter-matched unruptured aneurysms. McGloughlin and Doyle [17] make a concise review on recent biomechanics-based rupture risk biomarkers for AAA examining their potentiality as clinical decision-making tools.

This chapter reviews factors involved in AAA development and rupture risk, considering i) biological factors involved in the genesis, development, and rupture of AAA; ii) geometric features that discriminate AAA population subsets; and iii) biomechanical factors implicated in the evaluation of rupture risk based on the AAA patient-specific geometry, wall structure, and mechanical response.

1.2 BIOLOGICAL FACTORS

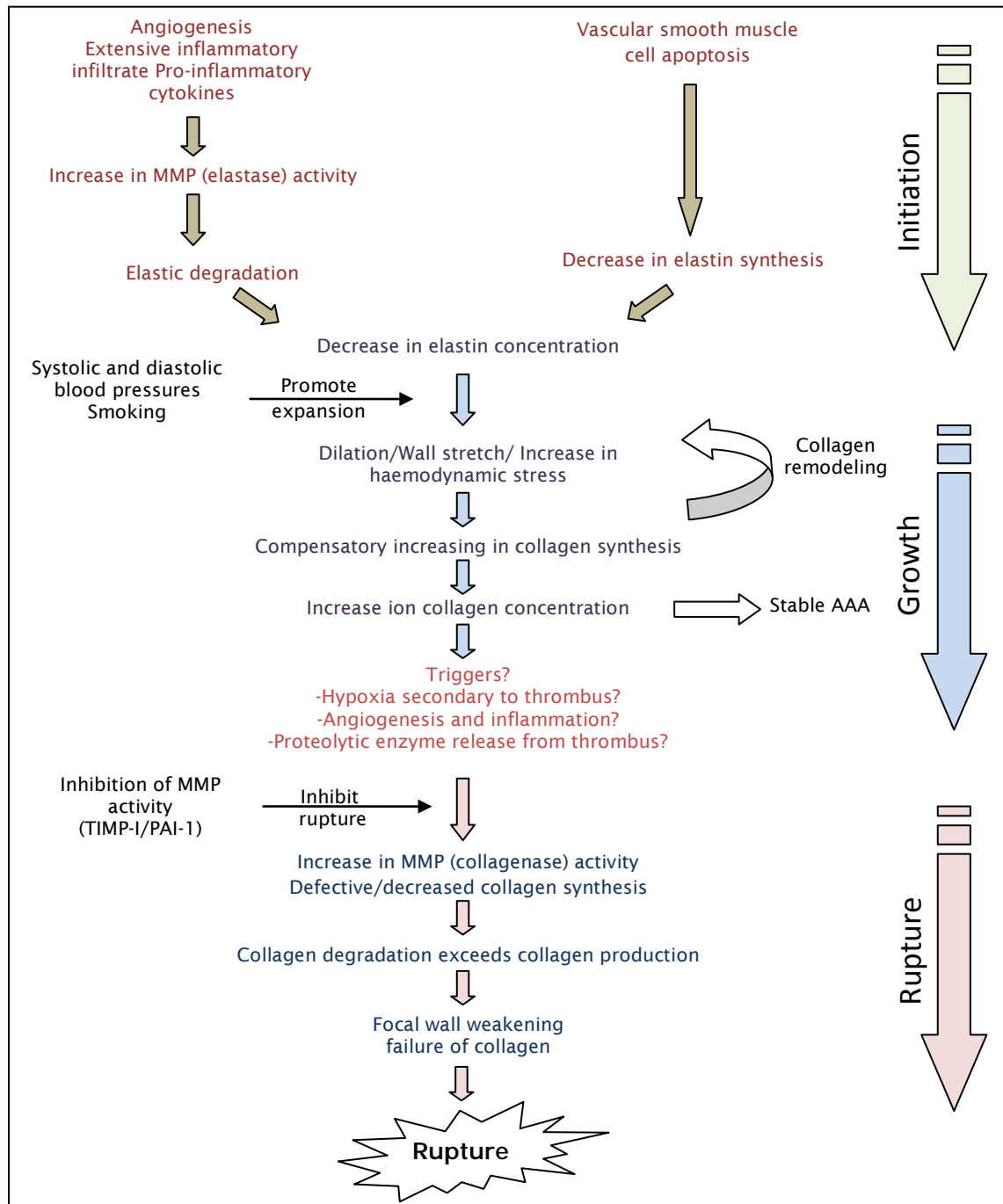


Figure 2: Succession of biological events related to AAA rupture. Reproduced in modified form from [16] with permission.

The pathogenesis of AAAs is still relatively unknown. Presence of immune reaction factors such as macrophage and lymphocytes, SMC (smooth muscle cell) apoptosis, degraded extracellular matrix (ECM), neovascularization, and increased concentration levels of certain types of matrix-metallo-proteinases (MMP) are commonly observed in the aneurysmal aorta (see Figure 2).

Degradation of protein content of aortic wall is mainly caused by proteases. Proteases are typically named by adding suffix “-ase” to the name of major target substrate that they hydrolyse e.g. elastase hydrolyses elastin, lactase hydrolyses lactose, collagenase hydrolyse collagen and so on [18]. Thus, proteases are a subset of enzymes responsible for hydrolysis action on a protein component (proteolysis). They can be further classified into four categories based on the mechanism of action – serine proteases, cystein proteases, aspartic proteases, metalloproteases [19]. Out of these, matrix-metallo-proteinases (MMPs) have been widely implicated in AAA pathogenesis and hence are described in detail in subsequent section.

Even though MMPs predominantly are involved in fibrinolysis, enzymes other than MMPs such as cystein proteases have been also implicated in the fibrinolysis process [20]. Abisi et al [21] compared the cystein protease activity in the AAA wall with that in the Atherosclerotic Occlusive Disease (AOD) wall using a bio-immunosorbent assay and observed that members of cathepsin family are overexpressed in the aneurysmatic wall and their inhibitor cystatin C is downregulated. Activity of MMP-9 was found to correlate positively with cathepsin L and negatively with cystatin C. This could have implications for a pharmacological pathway to control wall degradation by upregulating cystatin C artificially.

1.2.1 Matrix-metallo-proteinases (MMPs)

MMPs are zinc and calcium dependent endopeptidases of the metzincin superfamily of proteinases that degrade elastin and collagen. MMP-2, 9, and 12 have all been postulated to have a significant role in aneurysm formation. MMP in its non-activated form is called proMMP and is activated by an outside agent. MMP-1 and 8 are metalloproteinases associated with the degradation of collagen in aortic tissue. Higashikata et al [22] showed elevated levels of these MMPs in aneurysmal tissue when compared to normal aortic tissue. Most frequently implicated MMPs are discussed below.

1.2.1.1 MMP-2

Many investigators have also examined the role that MMP-2 (Gelatinase A or 72 kDa type IV collagenase) plays in the developing aneurysm. MMP-2 is expressed by vascular smooth muscle cells and may facilitate the degradation of both elastin and collagen in the aortic wall. Investigators have found elevated levels of both MMP-2 mRNA and protein levels in aneurysmal tissue when compared with normal tissue and atherosclerotic tissue. It is suggested that MMP-2 is responsible for the initial formation of small aneurysms, while MMP-9 is responsible for the growth in moderate sized aneurysms (5 to 7 cm diameter) [23, 24]. Higher MMP-9 expression in the AAA wall relative to AOD samples has been reported elsewhere [21]. It supports the view that AOD and AAA have different pathologies.

1.2.1.2 MMP-9

MMP-9, also known as Gelatinase B or 92kD type IV collagenase, is predominantly produced by macrophages and constitutes the major elastase in human AAAs, while minimal amounts are found in normal aortic tissue. Biopsies of aneurysm walls in patients undergoing open AAA repair have revealed that the patients with medium sized aneurysms (5-6.9 cm) had a significantly higher level of MMP-9 activity than did either

patients with small aneurysms (< 5 cm) or patients with large aneurysms (> 7 cm) [25]. Experimentation with MMP-9 knockout (MMP-9 KO) mice has shown that MMP-9 is necessary for the initiation of aneurysm formation [26]. MMP-9 knockout and wild-type mice were subjected to intra-abdominal CaCl_2 which instigates inflammatory response resulting in an aortic aneurysm formation in wild-type mice, but no significant dilation in the MMP-9 KO mice aortas. Comparison of MMP concentrations in ruptured aneurysms at the site of rupture with those on the anterior aorta showed that concentrations of MMP-8 and MMP-9 were significantly elevated at the site of rupture when compared to a site on the anterior aortic wall [27, 28]. Another study [29] has shown that serum MMP-9 levels first increase after a week and then drop after a month when measured pre- and post-operatively in a patient that underwent open AAA repair. Peterson et al [30] examined MMP-2 and MMP-9 and their relationship with size and aneurysm rupture. They found that the MMP-9 levels were significantly higher in ruptured aneurysms when compared to both large aortic aneurysms and medium sized aneurysms. They also found that the MMP-9 activity was inversely associated with diameter in large aneurysms.

Fontaine et al [31] proposed that intraluminal thrombus absorbs blood components and stores, releases, and participates in the activation of proteases involved in aneurysmal evolution. Spontaneous clotting of the blood was found to induce the release of pro-MMP-9 into serum that is 4 folds higher than the paired control plasma and that fibrinolysis progressively releases more MMP-9 in a time dependent manner. They also report that leukocytes are the main source of MMP-9 during clot formation. This is in agreement with the clinically observed fact that patients with previously stable

AAAs had a seemingly high rate of early rupture after undergoing an unrelated operation [32].

1.2.1.3 MMP-12

MMP-12's role in aneurysm formation is much less defined. Some studies have shown increased MMP-12 protein expression in AAA, but without MMP-12 mRNA expression. Pyo et al [33] performed a study on MMP-12 knockout mice that puts into question its role in the aneurysm formation. They studied MMP-12 knockout mice, MMP-9 knockout mice, and MMP-12/MMP-9 knockout mice together and found that MMP-9 knockout mice were protected from artificial aneurysm formation, while MMP-12 knockout mice developed aneurysm dilation. Longo et al [34] found after artificially inducing aneurysm in a MMP-12 knockout and wild type mouse that the increase in aorta diameter was about 26 ± 14 % in MMP-12 knockout mouse against the 63 ± 5 % increase in the normal wild type mouse. They suggest that the macrophage recruitment was reduced due to absence of MMP-12 resulting in smaller dilation.

1.2.2 Tissue inhibitors of metalloproteinases (TIMP)

TIMP are predominant inhibitors of MMP activity. In the normal human aorta, a balance in the tissue levels of MMP and TIMP helps to create equilibrium in the ECM between synthesis and degradation. TIMP-1 is a specific inhibitor of MMP-9. Eskandari et al [35] subjected both TIMP-1 knockout mice and wild-type mice to intra-aortic infusion of elastase to stimulate aneurysm growth. The TIMP-1 knockout mice demonstrated a significant increase aortic diameter when compared to the wild-type variety. It is also reported that TIMP-1 deficiency contributes to a reduction in atherosclerotic plaque size but promotes aneurysm [36]. It should be noted that it is the imbalance between degradation and repair activities of the vascular wall that results in an aneurysm formation and not the degradation activity alone.

1.2.3 Macrophage and lymphocyte presence

Histologically, it has been observed that macrophages and lymphocytes are present in the aneurysmal wall. What triggers the penetration of these immune system cells into the wall is still unknown. Elastin degradation products are proposed to be chemo-attractant proteins for the macrophages [37]. Kazi et al [38] have observed the chemotaxis and have verified the presence chemo-attractant proteins within the wall covered by intraluminal thrombus. The observed deposition of immunoglobulin (IG) in the aneurysmatic aortic wall also substantiates the fact that the pathogenesis of AAA may have origin in the autoimmune response. Macrophages and lymphocytes secrete a cascade of cytokines that results in activation of many proteases (see Figure 3).

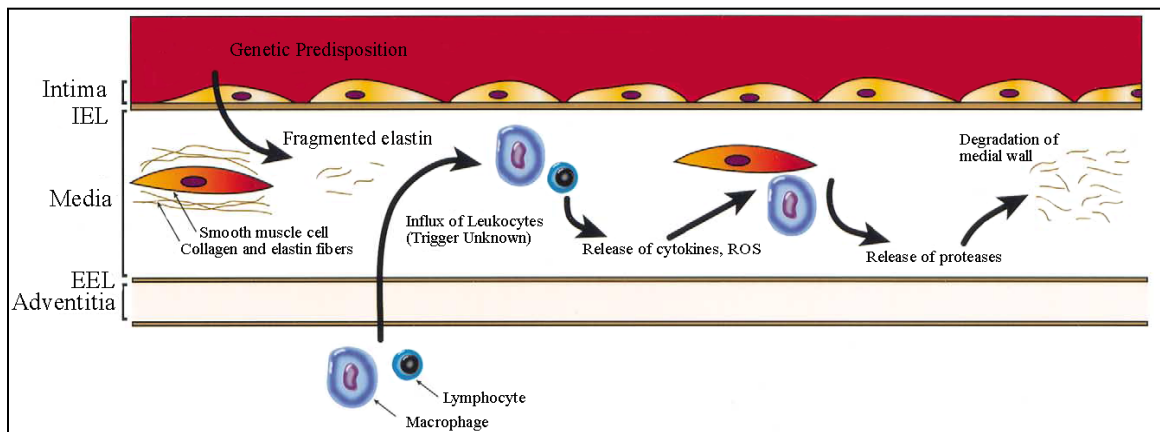


Figure 3: Localized stresses, fragmented medial proteins, and genetic predisposition likely attract inflammatory cells into the aortic wall. Released chemokines, cytokines, and reactive oxygen species by these inflammatory cells result in further influx of leukocytes, and further medial degradation. IEL – internal elastic lamina; EEL- external elastic lamina; Reproduced from [39] with permission.

Also, 55% of the aneurysmatic population has been found infected with chlamydiae pneumonia [39]. A recently applied Positron Emission Tomography (PET) imaging method for detecting metabolic activity in aneurysm is based on the fact that macrophages are engaged in significant glycolysis activity on their surface. The positron emitting chemical marker called fluorodeoxyglucose (F18 FDG) was used to trace glycolysis activity on aneurysm surface [40-42].

Mast cells (MC), which are an integral part of the immune system, are also implicated in AAA pathogenesis [43]. This fact is supported by previously reported findings that MC deficient rats and mice are protected from AAA. Structurally and functionally MCs are very close to basophils in that they carry histamine and heparin in form of granules and are born in bone marrow. However, unlike basophils that leave bone marrow only at maturity, mast cells enter blood flow and mature at the tissue site where they get planted. Mayranpaa et al [44] reported association of mast cells and neovascularization with AAA. High densities of neovessels and MCs were observed in the media layer of the artery wall and also in thrombus-covered AAA samples. MCs were found in close apposition to neovessels making it a possibility that mast cells participate in the neovascularization process. MCs are also involved in proteolysis of the extra-cellular-matrix.

1.2.4 Autoimmune response

T-cells are suggested to have an influence on the production of MMP by macrophage activation. The type-1 T helper cells (Th-1) tend to release proinflammatory cytokines. This was proven due to elevated levels of the cytokines associated with the Th-1 cell immune response in the blood and aortic tissue of AAA patients [45]. An advanced stage of AAA growth also reveals type-2 T helper cells (Th-2) associated with cytokines IL-4

and IL-10. However, experimental findings suggest that these cytokines restrain aneurysmal degradation [45]. Conversely, Schonbeck et al [46] suggest that Th-1 cytokines govern atheroma while Th-2 govern AAA expansion. Hence, it is argued that the Th-2 activity directs the atheroma to AAA formation.

Xiong et al [47] reported that mice lacking IL-10 developed larger aneurysms than wild-type controls. They also reported that the larger aneurysms occur in CD4 deficient and IL-4 deficient mice. Since Th-1 cytokines are IFN- γ , IL-2, IL-12, IL-15, and IL-18 whereas Th-2 cytokines are IL-4, IL-5, and IL-10, the aforementioned experimental observations substantiate the proinflammatory action of Th-1 and the inhibitory action of Th-2 cells. Experimentally, it was found that the mouse with absent CD4⁺ T-cells exhibited aneurysm formation. IL-6 and IL-8 were found to have an inflammatory action whereas IL-10 is anti-inflammatory [48]. A correlation between AAA surface area and mean plasma IL-6 levels was reported by Dawson et al [49], suggesting prominent IL-6 generation in the aneurysmal aorta. An investigation into the genetic basis of interleukins concluded that an allele of genotype IL-10-1082 is more common in AAA patients compared to the control group [50]. However, independent association of IL-10 with AAA could not be established when other risk factors such as smoking, gender, etc., were considered. This fact supports the possibility that the IL-10-1082 genotype may have an association with various AAA risk factors and not to AAA formation directly.

1.2.5 Reactive Oxygen Species (ROS)

In-vitro studies suggest that ROS activate MMP [51], thereby having an important role in AAA pathogenesis. ROS are also found to cause apoptosis of the vascular smooth muscle cells, contributing to wall weakening. High levels of DNA fragmentation are found in

aneurysmal medial smooth muscle cells; they are a marker for SMC apoptosis. The wall, though under degradation because of protease action, is simultaneously being synthesized because of protein generation by SMCs. ROS accelerate the wall degradation by promoting MMP action as well as decreasing protein synthesis by SMC apoptosis and damage to the structural integrity of the wall. It is hypothesized that ROS activate the pro-MMPs by covalently modifying the sulfur group of the cysteine switch [52].

Miller et al [53] observed $[O_2^-]$ levels in AAA wall by lucigenin-enhanced chemoluminescence and confirmed that those are 2.5 times higher than the neighboring non-aneurysmal region of the same aorta, i.e. ROS in the AAA wall are locally elevated. They state that the ROS levels are enhanced in aneurysmal tissue compared to an atherosclerotic one and that increased $[O_2^-]$ levels are predominantly produced by SMC, though both SMC and phagocytes generate $[O_2^-]$. This outcome was based on three observations: i) the $[O_2^-]$ levels were diffusely increased throughout the medial layer and not restricted to areas of macrophages or monocytes; ii) the phagocyte form of the oxidase predominantly used reduced form of Nicotinamide Adenine Dinucleotide Phosphate (NADPH), whereas the vascular oxidase used both reduced form of Nicotinamide Adenine Dinucleotide (NADH) and NADPH as substrates. NADH-stimulated $[O_2^-]$ levels were increased in the AAA; iii) NADPH subunits in the AAA were not confined to the region of leukocytes.

Alternative studies have focused on molecules such as inducible Nitric Oxide Synthase (iNOS) and endothelial Nitric Oxide Synthase (eNOS), and their role in inflammation and the pathogenesis of AAA. iNOS promotes formation and activity of peroxynitrite resulting in an oxidative action [54]. Conversely, eNOS, also known as

NOS₃, helps in the vasodilation and has a role in atherosclerosis [48]. eNOS and iNOS are responsible for the synthesis of nitric oxide; iNOS is Ca²⁺ insensitive whereas eNOS is not. At high levels, nitric oxide can become toxic and helps to degrade elastin in the wall. Johanning et al [55] infused rat aorta with elastase, which produced elevated levels of iNOS. They then selectively inhibited iNOS, which significantly reduced aneurysm size. A study with human subjects found that iNOS expression was present in the AAA wall whereas virtually no iNOS expression was found in the normal aorta [54].

1.2.6 C-Reactive Protein (CRP)

CRP, produced mainly by hepatocytes in the liver, has been established as an important factor in the atherosclerosis pathology [48]. Increased high-sensitive-C-Reactive Protein (hsCRP) has been observed in AAA patients [56]. This observation was supported by Wiernicki et al [57] as they found a correlation between haptoglobin polymorphism and AAA, and elevated CRP levels in the AAA patients. However, growth rate was found not to have a significant association with CRP levels in a multivariate analysis.

1.2.7 Dyslipidemia

Dyslipidemia is abnormal amount of lipids in blood. The association of lipids found in abnormal concentrations in the blood with AAA is highly debated. Baumgartner et al [58] in their study involving total of studied 68,236 human subjects in 44 countries and reported no association between hypercholesterolemia and AAA; this outcome is supported by Schlosser et al [59]. However, surprisingly it has been reported that patients taking lipid lowering drugs have about 1.2 mm per year lower growth rate of AAA compared to that of the non-users of lipid lowering drugs [59]. It is reported by Golledge et al [60] that the AAA has no association with low-density-lipoproteins (LDL), however, AAA is associated with high-density-lipoproteins (HDL). The discrepancy in

these findings can be attributed to the fact that there is no clear definition of dyslipidemia and the fact that on-going lipid modifying treatments may have confounding influence on the findings. Also, it is important to interpret significance of the lipid factor relative to other predominant AAA risk factors in future work pertaining to the subject. Total cholesterol level is reported to have decreased overall amongst population from 1980's to end of 1990's by Wanhainen et al [56].

1.2.8 Mycotic aneurysms

Aneurysms originating from microorganism infections are known as mycotic aneurysms. Most of such cases are predominantly reported from East Asian countries and the majority of these patients had diabetes [61]. Three predominantly involved microorganisms in AAA are *salmonella* (15%), *staphylococcus* (28%), and *streptococcus* (10%) [62]. There has been a case reported by Morrow et al [63] where the infection is said to have migrated from appendicitis to infrarenal segment non-contagiously.

1.2.9 Genetic aspects

Genome wide association studies have consistently reported associations between a region on chromosome 9p21.3 and a broad range of vascular diseases, such as coronary artery disease (CAD), aortic and intracranial aneurysms and type-2 diabetes (T2D) [64]. Ethnic association of AAA disease and frequently observed familial history has established genetic link of AAA by now [8, 48, 65-67]. Familial history is found in 15% of AAA patients [48]. This emphasizes the need to explore genetic aspects involved in AAA. Marfan syndrome (MFS) and Thoracic Aortic Aneurysm and Dissection (TAAD) have been well characterized for their genetic links compared to AAA [48]. However, genome wide studies have made advances in recent year to finger point the location on chromosomes related to AAA disease. Shibamura et al [67] reported loci of the AAA to be

19q13 (AAA1) and 4q31 (AAA2). Recently, Elmore et al [68] reported the AAA loci to be 3p12.3. Genetic link relating some of the individual risk factors has also been explored. Functional MMP-9 polymorphism (C-1562T) was found common in AAA patients [69]. Interleukin genotype IL-10-1082A allele was found to be frequent amongst AAA patients. A recent genome-wide study involving 1292 individuals with AAA and 30,503 controls found that A allele of rs7025486 on 9q33 was found to associate with AAA, with an odds ratio (OR) of 1.21 and p-value 4.6×10^{-10} [70].

1.2.10 Miscellaneous factors

1.2.10.1 Gender dependence

Gender dependence of the AAA and association with smoking was highlighted in the UK Small Aneurysm Trial that based its finding on 1090 patients (UKSAT) [8]. The trial found that female patients have less occurrence of AAA, however, chances of rupture of AAA were found higher in female patients. Biomechanical aspects were explored from gender perspective by Larsson et al [71], however, differences found were not statistically significant. Their relatively smaller pool of patients could be the culprit. Also, chances of occurrence of AAA in the family of female patients were found higher than that in case of the male patients. Association of smoking has been debated since many of the studies that include the smoking as a variable in patient trial have not taken into account the COPD as a separate fact [72].

1.2.10.2 Diabetic influence

Influence of diabetes on AAA is debated. Baumgartner et al [65] report inverse association. Diabetic patients with Haptoglobin polymorphisms Hp 2-1 and Hp 2-2 phenotype are reported to have lower elasticity compared to those with Hp 1-1 phenotype. However, in most of the mycotic aneurysms *diabetes mellitus* is found to be common [61]. Wanhainen et al [56] found no correlation in diabetes and AAA.

1.2.10.3 Platelet activation inhibition

Inhibition of platelet activation is reported to have reduced aneurysm diameter, thrombus development, platelet CD41 expression, leukocyte infiltration, and elastic degradation of the aortic wall in experiment with rat model [73]. Platelet activating factor is phospholipids activator produced by neutrophils, basophils, platelets, and epithelial cells. It plays a role in leukocyte functioning and platelet aggregation. It promotes MMP activity and migration of macrophages and leukocytes into the vessel wall thereby promoting aneurysmal deterioration. Species such as plasmin, plasminogen, and tissue plasminogen inhibitor (tPA) which are involved in fibrinolysis have also been implicated in AAA etiology. Plasminogen is inactive form of an enzyme plasmin which actively breaks down blood clot. In presence of tissue plasminogen activator (tPA) plasminogen produces plasmin for fibrolysis. Plasminogen Activator Inhibitors (PAI) regulate plasminogen activator action. tPA is reported to be present in increased mass concentration in AAA patients compared to that in control subjects. However, concentration of tPA/PAI-1 complex in blood plasma samples were similar [74]. Angiogenesis Converting Enzyme inhibitors (ACE inhibitor) were associated with aneurysm growth rate by Sweeting et al [75]. However, previously it has been reported that use of ACE inhibitors reduces aneurysm rupture risk [76, 77]. These two observations leave us with an interesting possibility that though ACE inhibitors increase growth rate they also increase material strength or reduce inhomogeneity in aortic wall or reduce hypertension thereby reducing risk of rupture.

1.2.11 Summary of etiology

According to the aforementioned discussion, AAA etiology can be summarized as follows:

- (1) Some unknown event attracts the attention of leukocytes to the infrarenal segment of aorta;
- (2) Penetration of the leukocytes into the wall of aorta;
- (3) Macrophages start secreting chemokines, ROS, pro-MMPs in extracellular fluid;
- (4) pro-MMP gets activated;
- (5) TIMP presence may attempt to neutralize the MMP activity;
- (6) MMP activity dominates the TIMP resistance. Thus, net result is degradation of structural matrix proteins;
- (7) Over a period the activity continues. The loss of elastin reduces the stiffness of the wall. Therefore, the aorta begins to bulge out in form of an aneurysm;
- (8) Collagen degradation weakens the wall;
- (9) Smooth muscle cells undergo apoptosis. This hampers the rebuilding activity of wall structural proteins;
- (10) Interstitial collagen distribution becomes disorganized;
- (11) Aneurysm increasingly expresses T cells, B cells, and plasma cells. This highlights the momentum of the autoimmune system;
- (12) Th-1 cells are encouraging the inflammatory action and thereby aneurysm whereas Th-2 cells try to suppress the same.

1.3 GEOMETRIC FACTORS

Currently, the clinical management of AAAs is based on maximum diameter and expansion rate of an aneurysm [4, 5]. However, reports show that these two metrics are not a reliable measure of individual rupture risk. This is evident by the small aneurysms (diameters less than 5.0 cm) that do rupture and the larger aneurysms that have exceeded the threshold size for elective intervention that do not rupture. In an autopsy study of four hundred and seventy-three non-resected aneurysms [78], 13% of the aneurysms with a maximum diameter less than 5.0 cm ruptured and 60% with diameters greater than 5.0 cm remained intact. Other studies report similar findings of small aneurysms rupturing, indicating that the current use of the maximum diameter or expansion rate may be insufficient in that it underscores the variable behavior of individual aneurysms.

1.3.1 Baseline diameter and propensity of AAA development

In an interesting study by Solberg et al [79], where 4265 subjects with a normal sized aorta resulted in 116 AAAs diagnosed after 7 years, a statistical analysis revealed that the baseline diameter was a highly significant ($p < 0.001$), strong (95% CI: 7–76 times higher risk) and gender-independent risk factor for developing AAA. They also found that median diameter increases less with age compared to mean diameter, indicating that there was less increase in diameter for people with smaller aorta in the beginning. Another interesting finding of the study was that when adjusted for age and aortic diameter, male sex was not significantly associated with AAA. It implies that geometry matters more than gender and hence biological differences. These findings are in agreement with previously reported fact that growth rate of larger non-aneurysmatic aorta was higher than the smaller non-aneurysmatic aorta [80]. These findings

emphasize the role of size as a geometric factor involved in the aneurysmatic condition of the aorta and progression of disease.

1.3.2 Importance of shape for wall mechanics

The mechanics of the AAA wall and the resulting distribution of wall stress are primarily determined by the individual shape, not size, of the aneurysmal aorta. While precise soft tissue characterizations of the wall and thrombus, as well as patient-specific blood flow velocity measurements, are important to achieve accurate computational predictions of the flow-induced wall stresses, the native AAA geometry is the most important feature to consider in evaluating the wall mechanics. Limiting the characterization of geometry to the measurement of maximum diameter or expansion rate from medical images is not the best strategy to address the at-risk status of aneurysms on an individual basis. AAA shape is complex; most aneurysms are generally tortuous, asymmetric, and with amorphous multi-layered ILT [10]. Moreover, the implementation of patient-specific non-uniform thickness of the arterial wall in the analysis is a complex task, due primarily to limitations in the current technology to measure this parameter non-invasively.

Early studies report on the power of shape measures to distinguish between normal and abnormal brain surface shapes and to establish a relationship between the shape of the human brain surface and the function of the underlying tissue [81]. Preliminary work in aneurysm biomechanics suggested that the curvature is more important than diameter [82, 83]. Recent studies describe the derivation of a set of global indices for the size and shape of cerebral aneurysms for assessment of their rupture potential and choosing the appropriate clinical treatment modality [84]. Ruptured AAAs seem to be less tortuous and have a larger cross-sectional diameter asymmetry [84]. Ruptured AAAs seem to be less tortuous and have a larger cross-sectional diameter

asymmetry [85] , which is consistent with FEA studies showing that the highest wall stress is obtained in AAAs with an asymmetric geometry [13]. Moreover, the location of maximum stress is at the aorta-aneurysm inflection point where the aneurysm curvature changes from concave to convex [13] which was also observed in symmetric models earlier [86]. Idealized fusiform and saccular models have also shown that wall stress increases with bulge diameter and asymmetry [87, 88]. Idealized fusiform and saccular models have also shown that the wall stress increases with bulge diameter and asymmetry [87, 88].

1.3.3 ILT as a geometric feature

A common feature in most AAAs is the presence of an ILT. ILT is known to alter the stress distribution in the aneurysmal wall [73, 80, 81] and directly affect AAA growth and rupture [8, 28, 73, 79, 83, 89] making it important in AAA biomechanics. Statistical models for non-invasive wall strength estimations have used local ILT thickness as a parameter [90].

1.3.4 Wall thickness as geometric feature

A factor of significant importance in AAA rupture risk prediction is the non-uniformity of the wall thickness. Figure 4 shows an estimation of AAA wall thickness distribution obtained from an AAA CT scan [91]. Di Martino et al [92], using a laser micrometer, measured the thickness of AAA wall specimens, obtained fresh from the operating room from patients undergoing surgical repair. A significant difference was found in wall thickness between ruptured (3.6 ± 0.3 mm) and electively repaired (2.5 ± 0.1 mm) aneurysms as well as an inverse correlation between wall thickness and local tissue strength was noted.

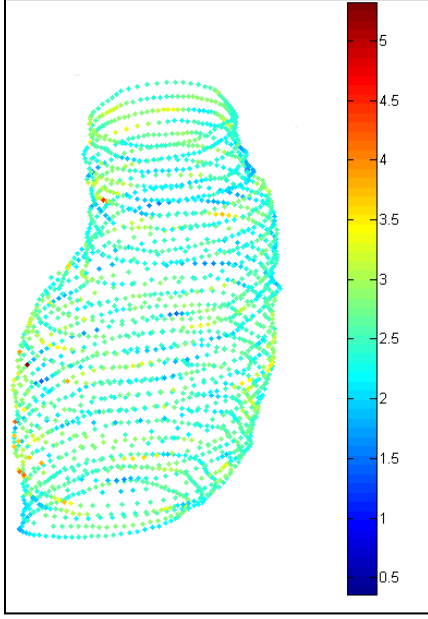


Figure 4: Estimated wall thickness distribution (in mm) in a point cloud resulting from a segmented CT dataset [2].

The tensile strength of ruptured AAA tissue was found to be lower than that for electively repaired tissue (54 N/cm^2 vs. 82 N/cm^2). In the same study, it was found that AAA rupture is associated with aortic wall weakening, but not with wall stiffening.

Since AAA wall strength in large aneurysms did not correlate positively with the maximum transverse diameter, wall thickness would be a better predictor of rupture for large AAAs. In an autopsy study, Raghavan et al [93] analyzed the tissue properties of three un-ruptured and one ruptured AAA revealing that all aneurysms had

considerable regional variation in wall thickness and there was a significant reduction in wall thickness near the rupture site. Similarly, Mower et al [94] demonstrated that the wall thickness represents a major parameter influencing wall stress distribution, rather than aneurysm maximum diameter alone.

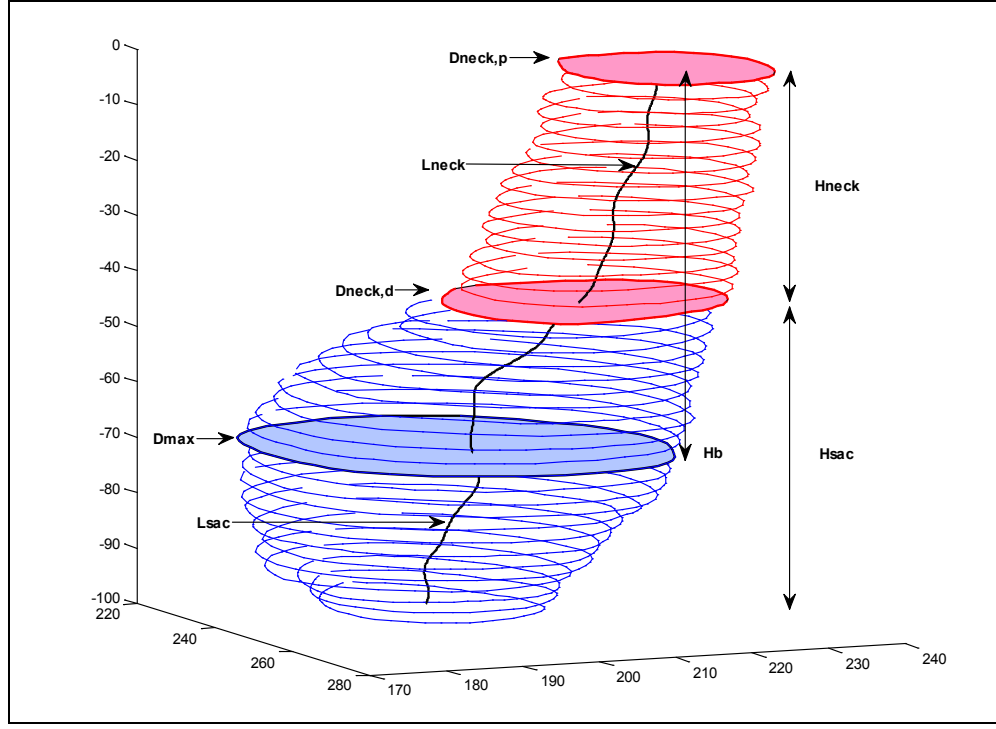
1.3.5 Correlation of geometric features with peak wall stress

Geometric features have been shown to be significant predictors of peak wall stress (PWS) and subsequent risk of rupture or tendency [12, 13, 95]. Multiple regression analysis was performed on 39 patients and 17 features to assess the influence of the features on the peak wall stress [96]. Among the geometrical parameters, PWS was correlated with the mean centerline curvature, the maximum centerline curvature, and the maximum centerline torsion of the AAAs, with mean centerline curvature as the only significant predictor of PWS and subsequent rupture risk resulting from the multiple

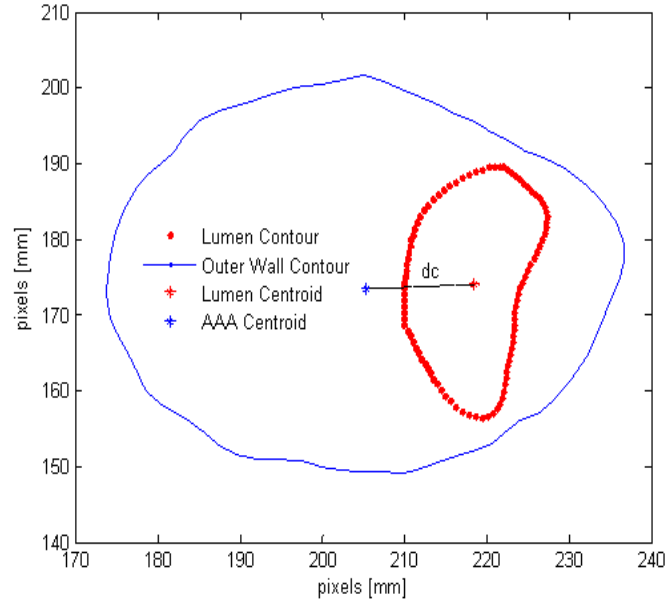
regression analysis. A multivariate analysis of 40 variables of 259 aneurysms revealed that ruptured aneurysms tend to be less tortuous and have a greater cross-sectional diameter asymmetry (Fillinger et al [97]). Current research had been concerned with identifying features in aneurysm morphology that are correlated with peak wall stress, and therefore rupture. Georgakarakos [98] developed a linear model to associate PWS and geometric parameters. They report that the optimal predictive model can be formulated as follows: $PWS = 8.791 + 2.3953 * MaxDiameter + 25.2923 * IntTortuosity$ [98] where *MaxDiameter* is maximum in-plane diameter and *IntTortuosity* is internal tortuosity.

1.3.6 Geometry quantification

In a previous study, Somkantha et al trained a Naïve Bayes classifier using three features (area, perimeter, and compactness) derived from image segmentation to discriminate between healthy and diseased arteries [91, 99]. Using 30 images for training and 20 images for testing, they obtained accuracy levels of 95%. However, as the aneurismal aorta is larger than a healthy aorta, it is unsurprising that these size features can accurately discriminate between healthy and diseased aortas. Shum et al [91, 100] developed a quantitative pipeline consisting of images segmentation and geometry quantification to compute 64 features that describe the size, shape, wall thickness, and curvature for a subset of ruptured and unruptured aneurysms (see Figure 5). Utilizing these features, a decision tree model (see Figure 6) was trained on 76 AAAs and a prediction accuracy of 87% for sac length, surface area, tortuosity, and the ratio of ILT to AAA volume was obtained (Shum et al [2, 100]).



a)



b)

Figure 5: (a) 1-D size indices: maximum diameter (D_{max}), proximal neck diameter ($D_{neck,p}$), distal neck diameter ($D_{neck,d}$), sac height (H_{sac}), neck height (H_{neck}), sac length (L_{sac}), neck length (L_{neck}), bulge height (H_b); (b) 1-D size index: centroid distance at the maximum diameter (dc). Reproduced from Shum [2].

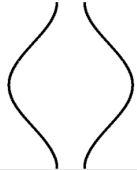
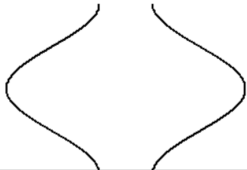
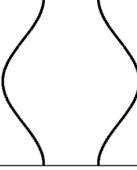
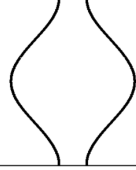
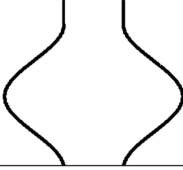
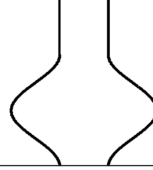
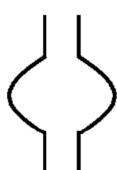
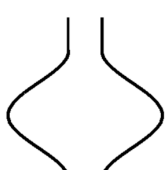
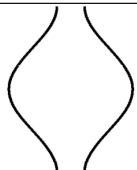

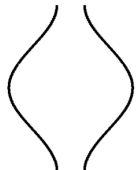

2D Shape Index	Low	High
<i>DHr</i>		
<i>DDr</i>		
<i>Hr</i>		
<i>BL</i>		
β		
<i>T</i>		

Figure 6: Schematic of 2D shape indices providing an approximate measure to construct the global AAA shape: diameter to height ratio (DHr), diameter to diameter ratio (DDr), height ratio (Hr), bulge location (BL), asymmetry (β), and tortuosity (T). Reproduced from Martufi et al [101].

In addition to linking geometric features to rupture potential, five “*geometric biomechanical factors*” (deformation rate, asymmetry, saccular index, relative wall

thickness, and growth rate) were recently combined to obtain a *rupture risk qualitative indicator* (Vilalta et al [102]). This index was defined to monitor the evolution of patients with aneurysms by integrating geometric information obtained from periodic checkups in an effort to improve the accuracy of rupture risk assessment. Validation studies were only performed on one clinical case and three cases obtained from the literature, and a broader study enrolling more patients is currently in progress. Results show that the deformation rate and growth rate are more influential on the rupture potential of aneurysms than the maximum diameter, and that a rupture risk qualitative indicator greater than 0.64 (nondimensional, based on the weighted averages of the five geometric biomechanical factors) indicates elective repair should be considered.

1.4 BIOMECHANICAL FACTORS: FEA, CFD, AND FSI ANALYSES

As per the popular approach, from a purely biomechanical viewpoint, an aneurysm rupture is a phenomenon that occurs when the mechanical stress acting on the dilating inner wall exceeds failure strength of the wall. Therefore, a criterion for repair based on quantifying AAA wall stress and strength could facilitate a better method to determine at-risk AAAs. Unfortunately, obtaining in vivo patient-specific measurements of tissue stresses or strength non-invasively is currently not feasible. However, mathematical and computational models that accurately compute the aneurysmal wall stress can be utilized to evaluate the AAA biomechanical environment at the organ scale. In addition, recent research has pointed the unsuitability of deciding a surgical repair based solely on the maximum diameter criterion [10, 12-15]. Therefore, alternative rupture risk parameters need to be proposed as an alternative to the classical AAA size and expansion rate [17].

A biomechanics based approach has been extensively researched as a solution for rupture risk assessment. An extensive literature review was performed and Table 1, Table

2, Table 3, and Table 4 summarize some of the relevant and highly cited work in the field of solid mechanics and fluid-structure-interaction analysis of AAA. We note that the isotropic hyperelastic material model proposed by Raghavan and Vorp [3] has been used widely.

Table 1: Abbreviations used in subsequent literature review summary tables

Abbreviation	Meaning
3DAO	3D Active Object
ALE	Arbitrary Lagrangian Eulerian coupling
Asym	Asymmetry
AxiSym	Axisymmetric
Avg Sys	Average of systolic pressure measured for each patient
Bifur	Bifurcation
BIM	Backward integral method
Ca	Calcification
E	Linear
GC-circle	Gauss curve for anterior and posterior with circular c/s fitted in between
HE	Hyperelastic isotropic
HEaniso	Hyperelastic anisotropic
I	Idealized
Implicit	Modeled by varying material properties of select elements in mesh
N	No
PC	Point cloud
PHE	Porohyperelastic
PS	Patient specific
PWS	Peak wall stress
Quad-04	4 noded quadrilateral element
S	Shell
S3	3 noded shell element
S4	4 noded shell element
S8	8 noded shell element
SS	Surface smoothing
Tri-3	3 noded triangle
Y	Yes

Table 2: Literature review summary - solid mechanics simulations of AAA –Part 1

(Please refer to Table 1 for abbreviations used.)

First Author (year)	Focus	PS/I	Cases	Reconstruction Strategy	Bifur	ILT	Ca	FEA Solver	Pressure	Residual Stress	Element Type	Material Model
Fillinger (2003)	Rupture risk vs Max Dia	PS	103	PC, Decimation, SS	Y	N	N	ABAQUS	PS	N	S(3 ?)	HE [3]
Raghavan (2000)	Patient specific AAA analysis	PS	7	PC, Decimation, SS	N	N	N	ANSYS	PS	N	S4	HE [3]
Fillinger (2002)	Wall stress and rupture risk	PS	48	PC, Decimation, SS	Y	N	N	ABAQUS	PS	N	S(3 ?)	HE [3]
Vorp (1998)	Geometry effect	I	10	GC-circle	N	N	N	ANSYS	120 mmHg	N	S4	E-5 MPa
Wang (2002)	ILT effect	PS	4	PC, decimation, SS, 3D Solid (Pro-E), Wall by extrusion const thk, PATRAN for meshing	N	Y	N	ABAQUS	PS	N	Tet-10	HE [3]
Venkatasubramanian (2004)	rupture Vs non-rupture using PWS	PS	27	PC, Rhino Surface	N	N	N	ANSYS	120 mmHg	N	S6	HE [3]
Inzoli (1993)	PWS and ILT	I	1	Axisym 2D	N	Y	N	BRAVO3	120 mmHg	N	Quad-04	E-2 Mpa
Di Martino (1998)	ILT effect on AAA biomechanics (Expt+Sim)	I	1	2D, plane stress	N	Y	N	Patran	120 mmHg	N	Quad-04	E, HE
Elger (1996)	Shape and PWS	I	1	2D axisym	N	N	N	Analytical membrane theory	parameter	N	No FEM	E

Table 3: Literature review summary - solid mechanics simulations of AAA –Part 2

(Please refer to Table 1 for abbreviations used.)

First Author (year)	Focus	PS/I	Cases	Reconstruction Strategy	Bifur	ILT	Ca	FEA Solver	Pressure	Residual Stress	Element Type	Material Model
Stringfellow (1987)	PWS and geometry	I	2	Cyl and Sphere	N	N	N	Nastran	100 mmHg	N	Hex-08	E-3 Mpa
Di Martino (2003)	Effect of ILT mat. prop. variation	I	1	Bell Curve Shaped	N	Y	N	ABAQUS	?	N	Hex-08	HE
Speelman (2007)	Ca effect on AAA biomechanics	PS	6	?	N	Y	Y	ABAQUS	16 kPa	N	Quad-04	HE - [3]
Truijers (2007)	PWS	PS	30	PC, decimation, SS	N	N	N	ABAQUS	PS	N	S(3 ?)	HE - ([3]
Rodriguez (2008)	Diameter, asym. and mat. Prop.	I	1	Gaussian variation in Diameter and location of center	N	N	N	ABAQUS	16 KPa	N	Hex-08	HE , HEaniso
Doyle (2007)	Comparison of Modeling techniques	I	3	Marching Cube (Mimics)	N	Y	N	ABAQUS	120 mmHg	N	S3	E-4.66 Mpa, HE [3]
Li (2008)	ILT and Ca effect on AAA biomechanics	PS	20	Marching Cube (Simpleware)	Y	Y	Y	ABAQUS	AvgSys	N	Tet-(4?)	HE - [3]
Doyle (2009)	Vessel asym. as diagnostic tool	PS	15	Marching Cube (Mimics)	N	N	N	ABAQUS	120 mmHg	N	S(3?)	HE - [3]
Heng(2008)	PWS in rAAA and eAAA	PS	70	PC, Rhino Surface	N	N	N	ANSYS	PS	N	S8	HE - [3]

Table 4: Literature review summary – Fluid-Structure-Interaction simulations of AAA

(Please refer to Table 1 for abbreviations used.)

Year	First Author	Coupling	Wall Material	ILT Material	Fluid	InletBC	OutletBC
2001	Di Martino	ALE	E-2.7 Mpa	E=0.11 Mpa	Newtonian	5xDia extension with Flat Velocity profile	time varying pressure
2005	Scotti	Iteratively Coupled	E-2.7 Mpa	-	Newtonian	parabolic profile	time varying pressure
2005	Wolters	ALE, iterative coupling	E	-	Carreau–Yasuda model (Shear thinning)	plug profile	Zero-traction
2006	Leung	ALE, Fully Coupled	HE – [3]	-	Newtonian	plug profile	time varying pressure
2007	Papah-rilaou	decoupled	HE – [3]	E=0.11 Mpa	Newtonian	PS Womersley	Flow split (?)
2007	Scotti	ALE, Fully Coupled	HE – [3]	HE	Newtonian	plug profile	time varying pressure
2006	Frauen-felder	Fully Coupled	?	-	Newtonian	plug profile	Zero-traction
2009	Rissland	Fully Coupled	HEaniso	E=0.11 Mpa	Newtonian	plug profile	time varying pressure
2006	Li	Fully Coupled	E-4.66 Mpa		non-Newtonian	parabolic profile	time varying pressure
2009	Bluestein	Decoupled	HE	E=0.11 Mpa	Newtonian	steady plug flow	Zero-traction (?)

1.4.1 Initial studies with idealized model

Early studies used Laplace's law to correlate AAA diameter and rupture [103]. However, this approach ignores the complex geometry and boundary conditions as well as the presence of the ILT. In this regard, calculation of the peak wall stress by using finite element analysis was first applied to a two dimensional simple geometric shape of AAA by Stringfellow et al [89]. Their work showed that AAA models with the same diameter but different geometry had different wall stress pointing to the importance of AAA shape and the non adequacy of Laplace's law even for an idealized approximation of complex geometries. This work was later corroborated by other researchers [86, 104].

1.4.2 Patient-specific modeling of AAA geometry

Fillinger et al [12, 13] showed the feasibility of using finite element analysis (FEA) for patient-specific wall stress calculations and reported statistically significant differences in peak stress for ruptured/symptomatic AAAs (46.8 N/cm²) in comparison with those electively repaired (38.1 N/cm²). They also demonstrated that maximum wall stress correlated more closely with the risk of rupture than maximum diameter [13]. In their study, wall stress was calculated by using FEA applied to a population of 103 patients, from which wall stress at a threshold of 44 N/cm² had 94% sensitivity and 85% accuracy in predicting rupture, compared to 81% sensitivity and 73% accuracy with the maximum diameter at a threshold of 5.5 cm. A similar study was undertaken by Venkatasubramaniam et al [95] with 27 patients, from which 15 AAAs ruptured. They found that ruptured AAAs had significantly higher peak wall stress than non-ruptured AAAs (77 N/cm² vs. 55 N/cm²). Both studies [13, 95] found a strong correlation between areas of high stress and the rupture site, based on quasi-static computational solid stress calculations applying a uniform intraluminal pressure directly on the wall. However,

these findings were challenged by Georgakarakos et al [105]. They found the location of peak wall stress not may not necessarily coincide with the site of rupture. It was reasoned that the wall strength is important to be considered as well.

1.4.3 Metrics for material failure criteria

Next logical step toward rupture risk assessment is to evaluate stress against strength. Geest et al [106] proposed a statistical model involving local ILT thickness, normalized transverse diameter, gender and family history to non-invasively estimate wall strength. In their work, Rupture Potential Index (RPI) was proposed as a metric to quantify risk due to stress considering ratio of wall stress and wall strength. Recent work by Maier et al [107] compared the efficacy of diameter, stress and RPI to estimate rupture. Maximum wall stress and maximum RPI were found to be increased in symptomatic and ruptured cases compared to unruptured cases. Apart from stress-strength approach, proven approach in the field of hyperelasticity of using strain energy density as a failure criterion has been emphasized by Volokh [108].

1.4.4 AAA material behavior and constitutive models

An accurate and reliable stress analysis of AAA requires not only a precise three-dimensional description of the aneurysm but also an appropriate constitutive law for the material. Most of the earlier studies on AAA have relied on isotropic models [3, 12, 13, 86, 89, 92, 95, 109, 110] assuming an incompressible behavior for the arterial wall. Such models have limited accuracy for AAA stress analysis since ex vivo biaxial experiments on human AAA tissue conducted by Vande Geest et al [111] demonstrated that the aneurysmal degeneration of the aorta leads to an increase in mechanical anisotropy, with the circumferential direction being the preferential stiffening direction. A number of anisotropic constitutive models have been proposed for AAA tissue [88, 112-114]. In

general, using anisotropic constitutive model results in significantly higher peak wall stress in both idealized and patient-specific geometries [88, 115, 116]. In this regard, anisotropic model results are more sensitive to changes in geometric parameters such as symmetry and aneurysm length. A recent study conducted by Gasser et al [117] indicates that ILT has a major impact on AAA biomechanics and rupture risk, and hence, needs to be considered in meaningful FE simulations. In addition, they also claim that inter-patient variability might reduce the importance of considering anisotropic behavior, whereas the geometry is the most critical property to be considered on a structural analysis.

1.4.5 Influence of ILT on peak wall stress

The role of intraluminal thrombus (ILT) on AAA is quite significant and some authors have suggested that ILT growth and volume may be related to AAA risk of rupture [118]. An ILT is found in most AAAs of clinically relevant size. Recently there was interesting finding that larger ILT means larger growth rate but also reduced wall stress [119]. Some studies have suggested that hypoxia in the AAA wall covered by ILT causes degradation of the extracellular matrix and subsequent wall weakening, being one of the precursors for AAA bulging [120, 121]. Georgakarakos et al [122] have found reduction in the peak wall stress in patient-specific geometries including the ILT modeled using linear material properties (Young modulus $E = 0.11$ MPa and Poisson ratio 0.45) and wall modeled by using hyperelastic material proposed by Raghavan and Vorp [3]. These observations have also been corroborated by other studies [112, 121, 123]. In addition, the study by Thubrikar et al [124] indicates a considerable transmural variation of the maximum principal stress, for which 3D continuum models or advanced shell models are required. A diameter matched approach was used by Gasser et al [117] to emphasize inclusion of

ILT in analysis for better ability to distinguish ruptured and non-ruptured aneurysms. However, there is still some concern regarding the protective role of the ILT. Despite ILT's impact on aneurysm disease, from a biomechanics perspective, thrombus development and its relation to aneurysm rupture is still not clearly understood. Whether it increases or decreases the risk of aneurysm rupture, i.e., reinforces proteolytic activity [84] thereby weakening the wall [85], or ILT internal fissures cause stress concentrations on wall [125] or buffers against wall stress [87] and provides support by padding and thereby reducing stress, is still subject to debate.

From a mechanical point of view, ILT is usually considered as a homogeneous incompressible hyperelastic solid [121, 126, 127]. However, recent developments prefer describing ILT constitutive behavior using nonlinear viscoelasticity [127], an observation also supported by the recent work by Gasser et al. [117]. In this work they also found ILT to be vulnerable against cycling loads with the ILT material showing significant decreasing strength with respect to the number of load cycles increasing the likelihood of ILT failure and the consequent overstress of the AAA wall as found in [125]. Researchers have used local ILT wall thickness to model reduction in wall strength [106].

1.4.6 Influence of calcification

Most of the aneurysms are associated with localized calcifications. Researchers have taken those into considerations for simulation of AAA biomechanics. However, it has not been extensively researched yet. There are conflicting reports whether presence of calcification increases [107, 128] or decreases [129] wall stress. There are challenges such as distinguishing calcification boundary from lumen during segmentation and high sensitivity toward 3D reconstruction approach. e.g. initial work by Speelman et al [107] modeled calcification implicitly by modifying material property of the neighborhood wall

elements whereas image mask operations are reported in other literature - Maier et al [129] modeled multidomain geometry with calcification embedded in ILT region beneath wall and Li et al [128] modeled calcification to be embedded within wall domain. Owing to smaller thickness of wall, such subtle differences are likely to cause huge differences in stress results. Also, material property information is scarce for calcification [128].

1.4.7 Influence of initial AAA configuration

Most computational geometries used for AAA finite element analysis, i.e. the arterial wall and lumen, are typically generated from multiple CT images acquired at one instant (gated) or multiple instants within the cardiac cycle, hence these geometries do not correspond to the geometry in the unloaded state or corresponding to zero internal pressure. Thus, the application of a physiological pressure boundary condition to these pre-deformed geometries may have a significant effect on the wall stress distribution results. Ideally, the physiological pressure conditions should be applied to the unloaded geometry or zero pressure geometry to get physiological stress results.

A number of numerical techniques have been developed and applied to recover approximately the zero pressure configurations from an aneurysm reconstructed from gated CT images [130, 131]. Some of the results from these studies are contradictory. The works by de Putter [132] and Speelman [133] conclude that not accounting for the zero pressure configuration may lead to an overestimation of the maximum peak wall stress, whereas Raghavan et al [130] and Lu et al [134] arrive at different conclusions. It is worth mentioning that in all previous works pertaining to retrieval of zero pressure configurations, the presence of the ILT has been neglected in the calculations and the AAA wall has been modeled as an isotropic material.

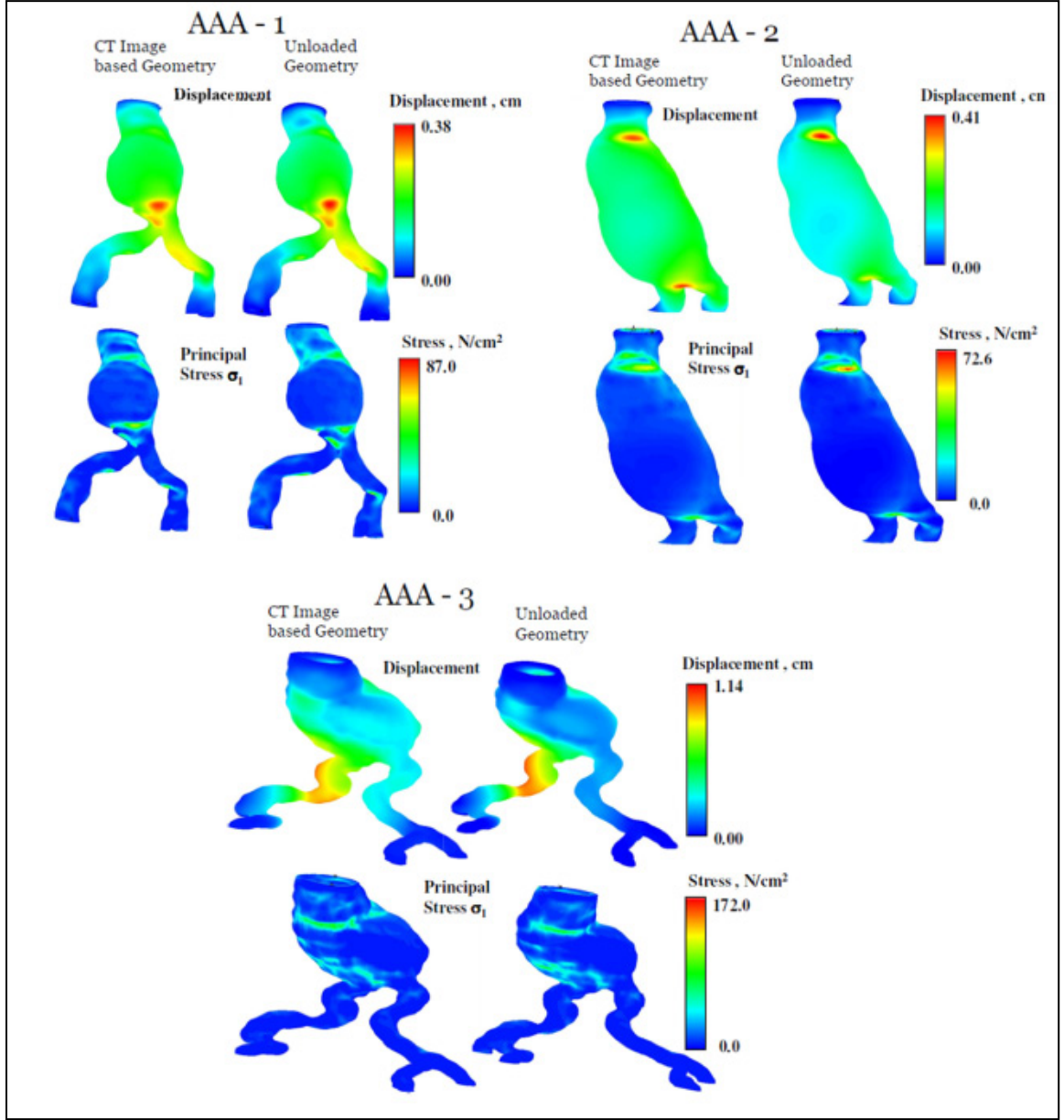


Figure 7: Displacement and stress distribution in three patient-specific geometries for both the CT image based analysis and the zero pressure configuration. Analysis based on the zero pressure configuration yielded a larger peak wall stress (reproduced from unpublished data).

Hsu et al [135] also proposed an iterative procedure for obtaining a prestress model for vascular fluid-structure interaction simulation, where they modified the solid

modeling procedure of the FSI formulation to account for the tissue prestress by employing an additive decomposition of second Piola-Kirchoff stress tensor. Their results suggest that the model without prestress tends to over inflate resulting in a significant difference in the wall shear stress and wall tension.

In our laboratory, a new algorithm has been developed and applied to patient-specific models of AAA including the ILT and the wall thickness [136]. Preliminary results obtained assuming a nonlinear isotropic behavior for both the AAA wall and the ILT for 3 patient-specific AAA models (AAA-1, AAA-2 and AAA-3) show that not accounting for the unloaded configuration may overestimate the maximum displacement of the AAA, and underestimate the peak wall stress by as much a 20% (see Figure 7).

1.4.8 Effect of blood flow

Most of the wall stress distribution on AAA has been obtained from structural analysis of AAA models by applying a uniform pressure on the inner surface of aneurysm sac. The limitation of this approach is that the hemodynamics of the blood flow through the aneurysm and the compliant nature of the AAA wall are not accounted for. One of the pioneering works that account for the effect of blood flow on the peak wall stress of AAA was conducted by Di Martino et al [110]. Their fluid-structure interaction (FSI) analysis of a realistic aneurysm aorta model showed that the complicated hemodynamics would considerably affect the stress distribution, but also reported the cushioning effect of ILT on the AAA wall. However, in their work, the wall and ILT were considered linear elastic and isotropic in behavior. The nonlinear behavior of the wall and ILT as well as more complex flow conditions has been considered in a series of works conducted by Scotti et al [137-139].

These studies have demonstrated the importance of considering the nonlinear elastic behavior of the structure. Also the comparative study between FSI (coupled and decoupled) and Computational Solid Mechanics (CSM) analysis of patient-specific AAA performed by Scotti et al [139] show that the non uniform pressure distribution in the inner surface of the AAA due to the flow yielded a maximum peak wall stress up to 20% higher compared to that obtained with static wall stress analysis when a uniform systolic pressure of 117 mmHg is applied. In these studies it is concluded that FSI analysis has the potential to capture the fluid dynamics inside a complex AAA structure accurately and hence is a better approach for calculating the wall stress and studying rupture risk. Leung et al [140] also compared the stress results obtained from fluid-structural interaction (FSI) model and computational static structural (CSS) model and reported that the addition of fluid flow and compliant wall can change the local stresses slightly but has negligible effect on the peak wall stress. However, they did not consider the presence of ILT in their analysis. One of the main conclusions that can be extracted from these studies is that using a non-uniform pressure distribution on the AAA sac can substantially improve structural analysis avoiding computationally extensive FSI analysis for determining AAA rupture risk. Results from Scotti et al [137, 138], as well as the importance of considering ILT in FSI analysis were corroborated by subsequent authors [141-143].

A recent study by Chandra et al [144] demonstrated the effect of MRI derived inlet flow boundary conditions on the fluid-structure-interaction modeling of a patient-specific AAA model with ILT. Comparison of results obtained from fully coupled FSI simulations, decoupled FSI simulations and transient FEA simulations revealed that the stress-strain variations follow the inlet velocity boundary condition rather than the

pressure outlet boundary condition and further emphasizes on the fact that peak systolic pressure does not provide the phase for peak stress and strain (see Figure 8).

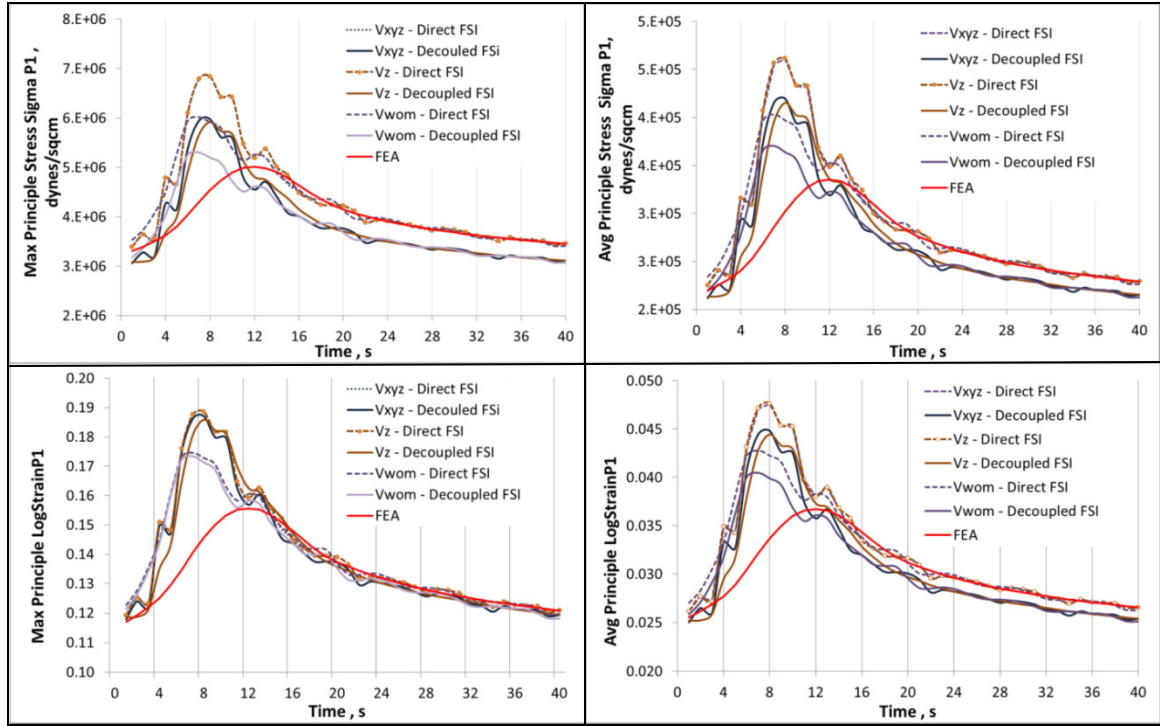


Figure 8: Maximum and average principal stress and strain waveforms for a patient-specific AAA obtained using direct FSI, uncouple FSI and transient FEA. The stress and strain follow the inlet velocity waveform rather than the pressure waveform boundary condition (reproduced from unpublished data).

The influence of material anisotropy in FSI simulations have been investigated by Rissland et al [145] and Xenos et al [146]. In their work, Rissland and colleagues introduced a new anisotropic material model of AAA wall to perform FSI simulations of patient-specific AAA geometries in order to develop more reliable predictor for risk of rupture. The ILT was still modeled as a linearly elastic compressible material. The results clearly indicate that the isotropic material properties have less stress values than anisotropic model resulting in underestimation of the risk of rupture.

1.4.9 Comments regarding simulation framework

Field of computational biomechanical analysis is very interesting and has tremendous implications over clinical management of AAA, however, it is very important to understand responsible use of this tool. There are two aspects of it – understanding of basics and communication of results. With the simplicity of the computational tools, both in terms of availability of software as well as hardware capabilities, plethora of results without substantial thought to setup of the simulation may dilute the importance of this technique. Especially with respect to third party commercial software it is important to understand both advantages and disadvantages of the available options. Also, use of multiple software tools and data transition increases probability of mistakes sneaking in. As a remedy one can think of few standard known cases as reference cases and verify the simulation set up using that before actually applying it to actual patient cases. Understanding of basic concepts in relevant fields such as imaging, mesh generation, Finite Element Method or Finite Volume method could help to avoid misleading results. Even if one performs simulation correctly, inherent complexities of this multidisciplinary field are difficult to cover to each minute detail while communicating findings of the research. Some conventions and codes may be established for biomechanical simulation similar to ASTM international standards. This aspect is covered in more depth by Erdemir et al [147].

Convergence analysis also poses another challenge especially in case of patient-specific analysis. There is no unique guideline that indicates the need to evaluate stress or displacement or wall shear stress, etc., for convergence. Ideally, refined mesh for convergence should be embedded within coarser mesh [148], which is hard to achieve in patient-specific analysis especially due to limitations imposed due to computer memory.

Another problem of importance is consideration to spatial location of the quantity under investigation while probing for convergence. In case of patient-specific geometries like aneurysms with bifurcation, it is not easy to define certain location or set of location consistently for different mesh resolutions due to lack of mathematical equations that can define tessellated geometry precisely. It would be ideal if mesh independency is verified for each simulation, however, at least one reference mesh independence study for given model set up is needed.

Different sources of variables confound the simulation studies. The modeling strategy also differs from group to group (see Table 2, Table 3, and Table 4). The field of mesh quality inspection has not received the due attention in literature to emphasize its role. Adequate attention is needed for segmentation as field is not yet evolved to automate image segmentation completely, especially for small features which have dominating impact on results e.g. wall region. There are user dependent controls during 3D reconstruction such as image filters and morphological operation sequence, mesh smoothing etc. where there is no exact definition to decide the course of action e.g. which domain should be given priority over other near the common interface in multi-domain meshing or how smooth a geometry is smooth enough. Attempts to address interoperator and intraoperator variability studies such as [91, 149] could improve reliability. Few complications in AAA biomechanics such as use of shell vs. tetrahedral mesh and inclusion of ILT were assessed in [150], however, more rigorous work by including additional complications like bifurcation, material properties, smoothness, etc., would add more knowledge for the community. On the other hand with improving hardware capabilities, some of the difficulties and previous assumptions can be done away with e. g. increased resolution of images, increased mesh density, use of 3D

elements instead of shell elements, complicated material models and boundary conditions are possible to be implemented. Investigations such as [151] that verify computational techniques against reality using experimental set-up or peer-to-peer comparison of results for common test problem closely imitating given scenario should be encouraged as it would bring more reliability to computational biomechanics among medical community. Non-invasive in vivo assessment of pressure measurement is another area that poses great challenge leading to the use of simplified assumptions. Similarly field of extracting in vivo material properties is still in its infancy. For patient specific clinical management, it could be possible to investigate alternative indices for risk assessment and correlated them with simulations results and use them as a handy tool that can be used by surgeons without any need to have detailed knowledge of complicated simulation framework.

1.5 SPECIFIC AIMS

The present work is targeted at in vivo patient-specific evaluation of vascular biomechanics toward rupture risk analysis. The following hypotheses were tested:

#1) In an unruptured, asymptomatic AAA, the wall mechanics (displacements, stresses, and strains) is the outcome of primarily the patient specific aneurysm shape and to a lesser extent, the constitutive material property model used to characterize the vascular wall.

#2) Regional variations in the vascular wall thickness yield significantly different wall mechanics estimations when compared to an arbitrarily assumed uniform wall thickness.

To this end, the following specific aims were completed in this work:

Specific Aim 1: Evaluate the effects of aneurysm shape and vascular wall material property variation on AAA wall mechanics.

Specific Aim 2: Assess the effect of regional variations in wall thickness on the AAA wall mechanics.

Specific aim 3: Develop a framework for the estimation of in vivo patient-specific heterogeneous strain and material property distribution in the diseased abdominal aorta.

Substantial efforts in this research were devoted towards development of following components: i) Framework capable of incorporating image based information pertaining to geometry and variable wall thickness into 3D patient-specific FE mesh generation for FSI, CFD and CSM studies; ii) Framework for in-vivo evaluation of heterogeneous material properties.

1.6 SUMMARY

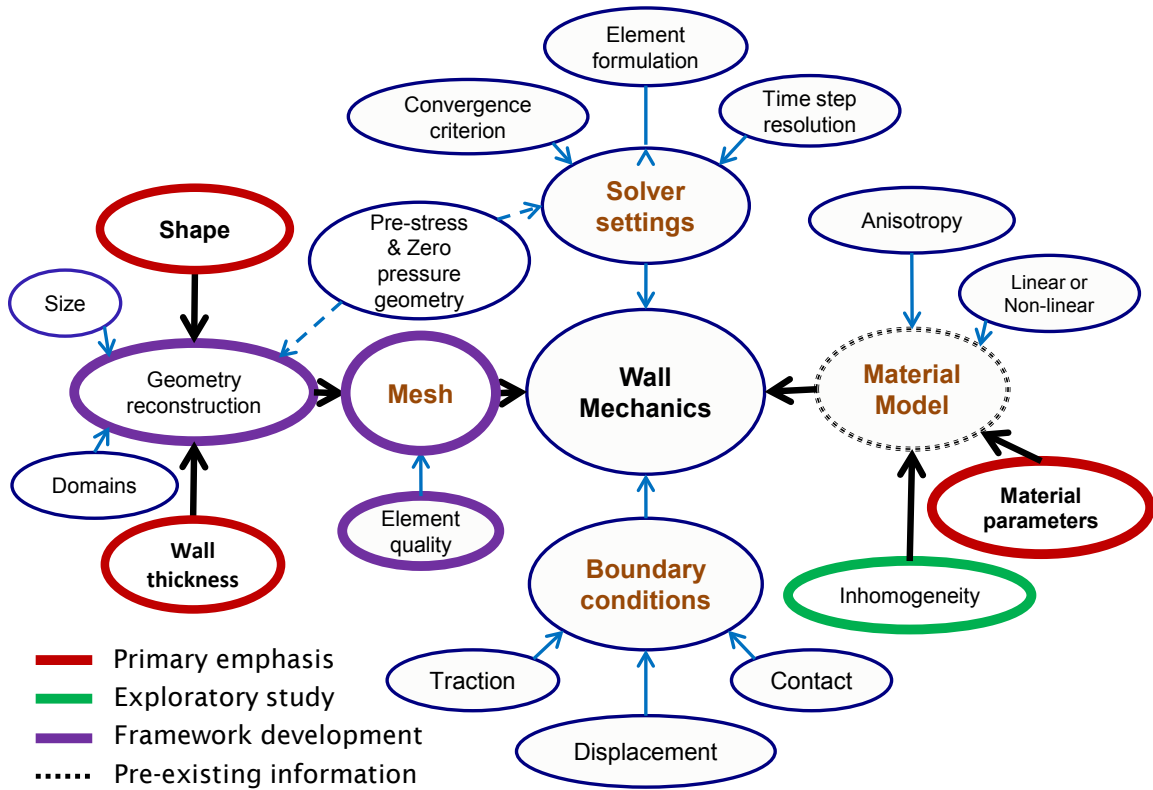


Figure 9: Important factors affecting computational wall mechanics evaluation (ignoring image segmentation errors) and scope of presented research highlighted by ovals with thickened borders.

Figure 1 shows important factors affecting computational evaluations of blood vessel wall biomechanics with strategy and scope of this research highlighted. Important and relevant findings from this research are presented in five chapters. Chapter 1 presented a summarized information regarding background and state-of-the-art AAA modeling techniques. First, it reviewed biological aspects implicated in AAA initiation, growth, and rupture. Then, previous work toward morphological assessment of AAA by geometry quantification to estimate risk of rupture was presented briefly. Finally, biomechanics based approach is elaborated with important previously reported results in computational and experimental assessment of AAA biomechanics, especially focusing

on CSM and FSI studies. Important limitations along with subtle aspects of computational evaluation technique are briefly discussed paving way for Chapter 2 that focuses on accurate implementations toward FSI, CFD and CSM simulations.

Chapter 2 describes the novel, robust, and integrated approach, called as AAAMesh, used for obtaining finite element discretization (FE mesh) for multi-domain vasculatures with unknown number of bifurcations, complex shapes, and random occurrences of ILT. It has distinct capability of modeling regional variations in wall thickness. It also presents a verification of this framework using various metrics, most prominent of which is *distErr*. Dedicated test framework evaluates dimensional accuracy using a phantom geometry for reference and highly precise error estimators. Effect of Laplace and Taubin surface tessellation smoothing algorithms on geometry are detailed. All directional, dimensional, and mesh quality aspects were studied using numerous combinations of settings used for AAAMesh to determine optimum settings for mesh generation for phantom as well as representative patient-specific geometry. Important observations pertaining to optimum smoothing of tessellations are documented. AAAMesh was implemented for the execution of Specific Aims 1, 2, and 3, and presented in Chapters 3, 4, and 5, respectively.

Chapter 3 discusses effect of patient-specific shape variability vs. possible material variations based on previous experimental findings and cohort of diameter-matched AAA patients and thus addresses specific aim 1. This study focuses on assessing effect of variation rather than evaluating absolute values of stress in vivo accounting for all sorts of complications. Precisely uniform wall thickness and generalized power law neo-Hookean (hyperelastic) material model dependent on only the first invariant of the Cauchy deformation tensor were employed. Five-different materials properties and 28

patient-specific cases were simulated and qualitative, quantitative, and statistical analysis of simulation results is presented.

Chapter 4 presents work pertaining to specific aim2 where effect of variable wall thickness is studied. Using 28 diameter-matched cohort of patient-specific geometries and 3 different approaches of wall thickness modeling in each case, 84 FE simulations were performed. Results of those simulations are qualitatively, quantitatively, and statistically analyzed.

Chapter 5 presents a novel framework for patient-specific heterogeneous material property estimations using ECG gated steady-state-free-precession (SSFP) MR imaging technique applied to capture 20 different deformed shapes of AAA. Novel use of post-processing tools for analyzing data not originating from FE simulations and dedicated native scripting for materializing continuum mechanics theory is presented for extracting in vivo heterogeneous strain information which is later translated into material property information. In this exploratory study, a linear material model is assumed and characterized by a pressure-strain modulus.

Finally, chapter 6 summarizes outcomes of this research work and provides suggestions for future directions.

Chapter 2. A Framework for Multi-Domain Volume Meshing of Blood Vessels for Finite Element Modeling: Application to Abdominal Aortic Aneurysms

2.1 INTRODUCTION

Most of the clinical decisions today are based on historical statistical data and hence lack patient-specific management of the disease; however, with the advances in technology, more importance is nowadays being placed on patient specificity. In the future, integration of high resolution medical imaging, computational methods, and engineering knowledge into clinical management of diseases is expected to play an important role in this drive toward individualized treatment options. Improvements in hardware capabilities are augmenting this process. For example, problems involving 200 to 2000 degrees of freedom were solved on MIT's analog computers in 1930s and 1940s [152], whereas now the capability to solve problems with a few million degrees of freedom is common. Leveraging such infrastructure toward translational research is leading to a better understanding of healthcare and disease progression as well as cost reduction. Healthcare of cardiovascular disease, in particular, has been reported to cost €192 billion in 2006 and 48% of all deaths in EU are linked to cardiovascular disease [153].

Current protocols for image-based biomodeling have serious shortcomings, especially with respect to hollow geometries where feature sizes can be small compared to the overall dimensions of the geometry e.g. blood vessel walls in which the wall thickness is small compared to the cross sectional diameter. Estimating and modeling the vessel wall thickness accurately is important because the wall is the main load bearing component. One of the root causes for loss of accuracy while modeling small features is that most medical imaging modalities yield images on a rectangular pixelated grid in Cartesian coordinates whereas blood vessels have quasi-circular cross-sections. This discrepancy results in “stair-case” patterns in the 3D-reconstructed geometry as

well as distortions introduced with direction dependent changes made during image morphological operations such as image dilation or image erosion.

It is important to achieve high accuracy in the geometric reconstruction and subsequent geometry quantification operations for modeling applications such as biomechanics, growth and remodeling, and biotransport assessment. Particularly, if mechanical stresses and strains are the objectives of the study, it is essential to accurately identify local features such as wall thickness and curvature, while filtering out spurious abnormalities resembling spikes and voids. In addition, the proper design of customized medical devices such as stents, heart valves, and hearing aids, will benefit from precise geometric reconstructions. Considering the translational possibilities of integrating engineering techniques in individualized healthcare, this field needs a thoroughly verified and validated framework for performing patient-specific modeling. Specifically for cardiovascular modeling, it would be valuable to have a framework that ensures geometric accuracy of thin walled objects with the implementation of spatial variation of individualized wall thickness estimations with multi-domain modeling capabilities so that features such as lumen, wall, thrombus, plaques, and calcifications can be modeled.

In this chapter, we present an integrated framework that can model complex vascular geometries having multiple branches or bifurcations, multiple domains, and thin walled geometries for clinical image based reconstruction of the aneurysmatic aorta, for the intended application of computational biomechanics of abdominal aortic aneurysm (AAA). Starting from 4-domain 2D segmented binary masks, the framework tomographically reconstructs the vasculature, outputting a multi-domain finite element (FE) discretization. The spatial distribution of arbitrary or individualized wall thickness can also be incorporated in the FE model. Verification of the proposed framework is

provided with a validation based on digital phantoms of known dimensions. Such rigorous, systematic characterization of image based reconstruction is considered a first step towards establishing a future protocol for the comparison of different strategies for topology derivation and volume mesh generation of vascular structures. The modeling framework presented herein has been developed for applications of vascular biomechanics, but can be extended for others such as biomolecular reactivity and osmosis.

2.2 BACKGROUND

Most of the initial mesh generation algorithms were targeted at industrial applications that involve parametric geometries of fairly regular shape, typically consisting of mathematically well-defined edges and faces. Automated mesh generation strategies improve efficiency by reducing user intervention, user bias, and the need for technical expertise. Automated mesh generation is challenging even in such well-defined geometries, and it becomes all the more challenging in the case of complex geometries such as anatomical shapes (e.g., blood vessels and organs). As it is difficult to express them in parametric form, these complex shapes are represented by a collection of linear patches called Piecewise-Linear-Complexes (PLC), which define their boundaries. Such a representation by means of collecting non-overlapping, small simple elements with no gaps is called a tessellation.

2.2.1 Relevant computational geometry concepts

2.2.1.1 Object representation

A surface can be represented in explicit form as $\vec{p} = f(u, v)$, or in implicit form as $f(\vec{p}) = 0$, where \vec{p} denotes position vectors corresponding to set of points on surface for specified values of parameters u and v . In the explicit form it is easier to obtain geodesic

points that belong to an object [154], e.g. given a parametric equation of a sphere ($x = r \cos \theta \sin \phi$; $y = r \sin \theta \sin \phi$; $z = r \cos \phi$), with r being prescribed radius and θ and ϕ being parameters, one can enumerate points on the intersection with the z -plane by keeping ϕ constant. However, given a point in space, it is not always straightforward to decide if it belongs to an object, e.g. given a point with a position vector $\vec{p}(x, y, z)$, it is not clear if it is on a circle using the parametric form. On the other hand, the implicit representation is convenient if any point in space is to be queried, but it is difficult to enumerate geodesic points when using this representation [154] e.g. given an equation $x^2 + y^2 + z^2 - r^2 = 0$ and prescribed radius r for a spherical surface, it is trivial to verify whether a point with a position vector $\vec{p}(x, y, z)$, is on the surface but it is difficult to enlist points, arranged in spatial order, say for intersection with specified z -plane. Volume representation implicitly depicts the object, not through equations but through the collection of grid points, e.g. isosurfaces defined in some space provided the scalar values are assigned to all grid points. It stores values of the variables of interest for all grid points within a bounding box that encloses the entire object. Thus, it is a robust approach to represent arbitrarily shaped objects. Hence, the following discussion focuses on mesh generation from volume representation. This review is on image-based anatomical reconstructions where typically a tessellated representation is used because of the robustness it offers. Another advantage of volume representation is that it is amenable for Boolean operations [154].

2.2.1.2 Generalized surface mesh extraction

The methods for extraction of surface meshes from volumetric data can be either grid-based or grid-less [154]. Methods such as Marching Cubes [155] and Extended Marching Cubes [154] are grid-based methods. The use of octree data structures is accepted for

grid-based methods. Octree techniques facilitate subdividing cubic cells until a prescribed high resolution is achieved to capture the local feature appropriately [156]. However, the output of grid-based methods is coordinate-frame dependent. Examples of grid-less method are those that use improvement of existing deformable surface tessellation templates, advancing front techniques, or those that use ray tracing followed by Delaunay tessellation. Grid-less methods are typically suitable if the surface is smooth [154].

Several algorithms have been developed for the extraction of surfaces from volumetric data. The Marching Cubes algorithm [155] was the first major step toward extraction of isosurfaces from volumetric data. Based on true-false values at eight corners of a cube and exploiting symmetry, 15 templates were proposed for surface reconstruction. It is a robust algorithm that results in continuous triangular faces that are guaranteed to be closed and manifold [157]. Because nodes can be located only on edges, small angles and sharp features can disappear as well as badly shaped triangles may form when using Marching Cubes. In addition, the uniformity of the grid is another limitation of this algorithm. It was improved in the Extended Marching Cube method [154] by using a “directed distance” field instead of a distance field alone, and by detecting the presence of sharp features inside a cube by examining normals associated with the intersection points on the edges of the cube. The need for explicitly checking for feature presence was eliminated in the Dual Marching method [158].

2.2.1.3 Surface mesh smoothing (mesh fairing)

Surface meshes reconstructed from real world data can reflect undesired noise, reduction of which is achieved by surface mesh smoothing. Laplacian mesh smoothing is the simplest form of smoothing algorithm where nodes are moved toward the barycenter

of surrounding node positions [159]. However, shrinkage is well-known problem associated with it. Taubin [160] proposed a modification in the Laplace smoothing algorithm to make it a low pass filter that mitigates shrinkage problem. Both Laplace and Taubin algorithms have the advantage of being linear in number of nodes, i.e. lesser computational load. However, the smoothing action is uniform along the entire surface. Multi-resolution action using constrained minimization of discrete energy functionals [161] and basic signal processing operations of upsampling, downsampling, and filtering [162] has been reported. Implicit mesh smoothing using diffusion and curvature flow was proposed by Desbrune et al [163]. Recently, Li et al [159] proposed a feature preserving mesh smoothing based on principal curvature, weighted bi-quadratic Bezier surface, and least square fit. Yamada et al [164] proposed an iteration-based algorithm with discrete spring model where the spring length was set proportional to the local curvature and the energy of system was minimized to obtain node movement necessary for surface fairing.

2.2.2 Surface reconstruction in biomodeling

A simple contour based approach was reported in the reconstruction of a right ventricular valve [165], for which a biquadratic surface patch was used for smoothing. The biquadratic surface patch was also used to study the curvature of aneurismal surfaces [166]. A similar approach for patient-specific aneurysm surface geometry reconstruction (excluding the iliac bifurcation) was reported by Raghavan et al [3]. The earliest report on AAA reconstruction including the aorto-iliac bifurcation was that of Fillinger et al [12]. Similarly, a template geometry and extended-free-form-deformation approach was implemented in [167]. Overall, the contour based approach was limited for well-behaved geometries and is not amenable for those with high tortuosity and strong

changes in surface curvature. There was also dependency of the meshing pattern on the coordinate frame orientation. Surface mesh quality improvement using mass-spring model for cerebral aneurysm has been reported [168].

2.2.3 Volume mesh generation for biomodeling

Methods for volume mesh generation from tomographic image data provide the basis for developing patient-specific computational models. Tomographic reconstruction of anatomical objects was popularized with studies of the femur. Keyak et al [169] modeled the femur by cube shaped voxels corresponding to image pixels. The Marching Cube algorithm was extended for volume meshing by using tetrahedron templates instead of triangular surface facets in the VOMAC approach [170]. Tetrahedral and hexahedral mesh generation from volumetric data with adaptive sizing was reported by Zhang et al [171] using dual contour and octree methods. Antiga et al [172] describe a framework for image based lumen segmentation and tetrahedral volume meshing for CFD simulations. Recently, single-domain hexahedral mesh generation for the vascular lumen was proposed in [173],[174] with branching templates for bifurcations.

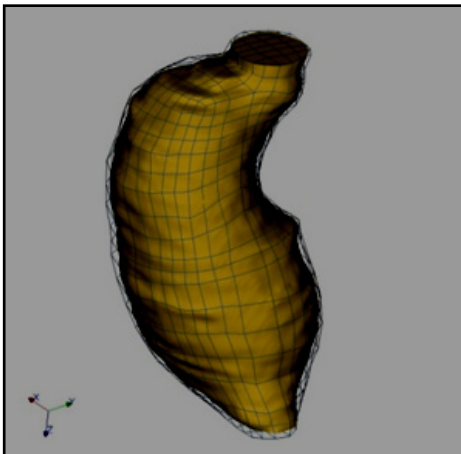


Figure 10: Meshing using subdivision of image segmentation splines.

Automatic hexahedral mesh generation remains a challenge for patient specific vascular structures due to their random shapes and arbitrary presence of multi-domain entities (e.g., blood clots, calcifications, plaque, thrombi, coartaction, and intravascular implants). A simple approach of subdividing image segmentation splines and connecting them to form surface meshes has been extensively as a

strategy to generate hexahedral meshes. However, as seen in Figure 10, this approach yields uneven element sizes with larger elements present near the maximum vessel diameter and a relatively fine mesh present at smaller cross-sections due to the requirement of having the same number of subdivisions across a circumference. Alternatively, a building block based approach has also been implemented, which creates a scaffold around the geometry and uses it as a template for projecting mesh points on the actual object surface. It also faces difficulties similar to the spline based reconstruction in that there is limited control over element size and an ensuing scaffold dependent pattern in the mesh. In addition, the generation of proper building blocks requires significant manual effort for complex geometries.

2.2.4 Multi-domain mesh generation

Multi-domain meshing for cardiovascular applications poses a challenge for realistic physics based modeling due to the number of domains involved and the complex shapes of the interfaces between them. Multi-domain mesh generation techniques were reported recently by (Zhang et al [175], Young et al [157], Fang et al [176], and Peng [177]). Fang et al [176] describe image based tetrahedral meshing focusing on anatomical shapes. An approach for AAA multi-domain meshing was reported [177], but limited to tetrahedral elements for each domain. Young and colleagues [157] expanded upon the VOMAC algorithm [170] for meshing multiple domains, an approach used for the development of the Simpleware® meshing tools (Simpleware Ltd., Exeter, UK). As seen in Figure 11 a) approach of using tetrahedral elements to fill volume defined by boundary surfaces, described in [157], [170], [176], and [177] fails leading to gaps and artifacts while modeling thin walled objects. Typical coordinate frame pattern and dependency can also be seen in Figure 11 c) and d); reconstruction using another commercial

software Mimics® is shown in Figure 11 e) to h). Similar to Simpleware®, reconstruction of wall directly using masks was unsuccessful. Modified masks, under assumption of uniform wall thickness, can give better results however typical rectangular grid pattern with skinny elements (Figure 11 f) and g)) and irregularity across wall thickness (Figure 11 h)) is often observed. Another off-the-shelf application reported by Auer et al [123], A4research® (Vascops, Stockholm, Sweden) can generate hexahedral-dominated meshes of the vascular wall and intraluminal thrombus for the clinical management of AAAs.

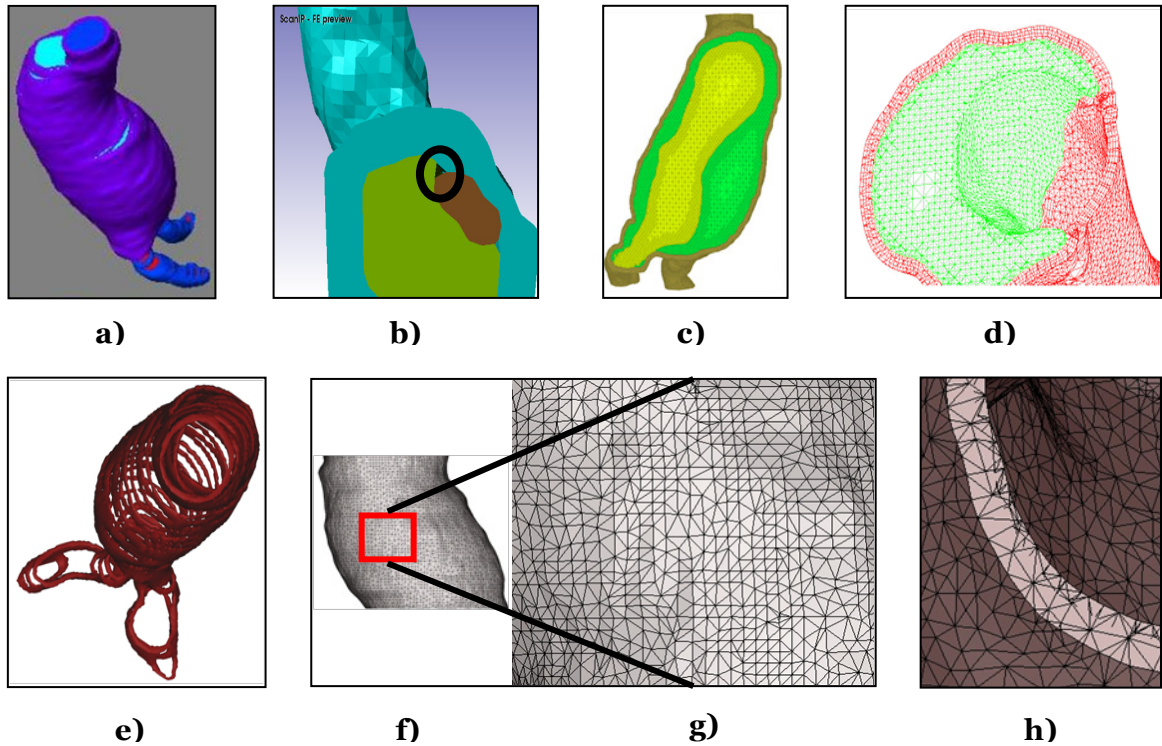


Figure 11: Limitations of commercial codes. eVoMaC approach (Simpleware®) (a), b), c), and d)) reported in Young [6]. Voids (a) and (b) and typical voxelized pattern/coordinate frame dependency (c) and d). Wall in d) in red is obtained by outward extrusion while ILT in green is obtained by eVoMaC method. Example reconstruction using Mimics® (e, f, g, h); e) attempted without mask dilation/erosion; f) and g) show typical coordinate frame dependent pattern dominated by vertical and horizontal grid lines; h) shows irregular mesh pattern across thickness.

The use of high quality tetrahedral elements for generating meshes of thin walled structures, such as blood vessels, remains a challenge as the individual element size needs to be small enough to adequately resolve the wall thickness. However, this yields a large number of degrees of freedom leading to high computational costs for the subsequent physics simulation. For rupture risk assessment of aneurysms, the wall geometry is of utmost importance, as wall mechanics parameters are likely affected by the thickness of the vasculature. Rupture being spatially local event, spatial accuracy in modeling regional variations in wall is important. The use of a uniform mesh density in the model is not practical since the arterial cross-section is typically large compared to the load-bearing wall thickness. In this work, we demonstrate the use of hexahedral and wedge shaped elements for efficient aneurysm wall meshing within the context of reducing the degrees of freedom for such thin walled geometries.

2.3 METHODOLOGY

2.3.1 Overview

A framework was developed for the multi-domain meshing of vascular structures that imports binary masks resulting from segmented clinical images (typically, CT or MRI) and outputs volume meshes suitable for finite element modeling, geometry quantification operations [2] and mesh quality metrics. Figure 12 shows a schematic of this framework (named “AAAMesh”) in which the main modules or building blocks are: i) volumetric data creation (from the binary masks) ; ii) surface mesh extraction; iii) wall extrusion; iv) multi-domain meshing; v) quality inspection; vi) geometry quantification; and vii) file export utility. Some of the algorithms used in the surface mesh generation and multi-domain meshing modules are inspired by previous work by Fang et al [176],

which is reported in the open source code iso2mesh (<http://iso2mesh.sourceforge.net>) and Liu [177].

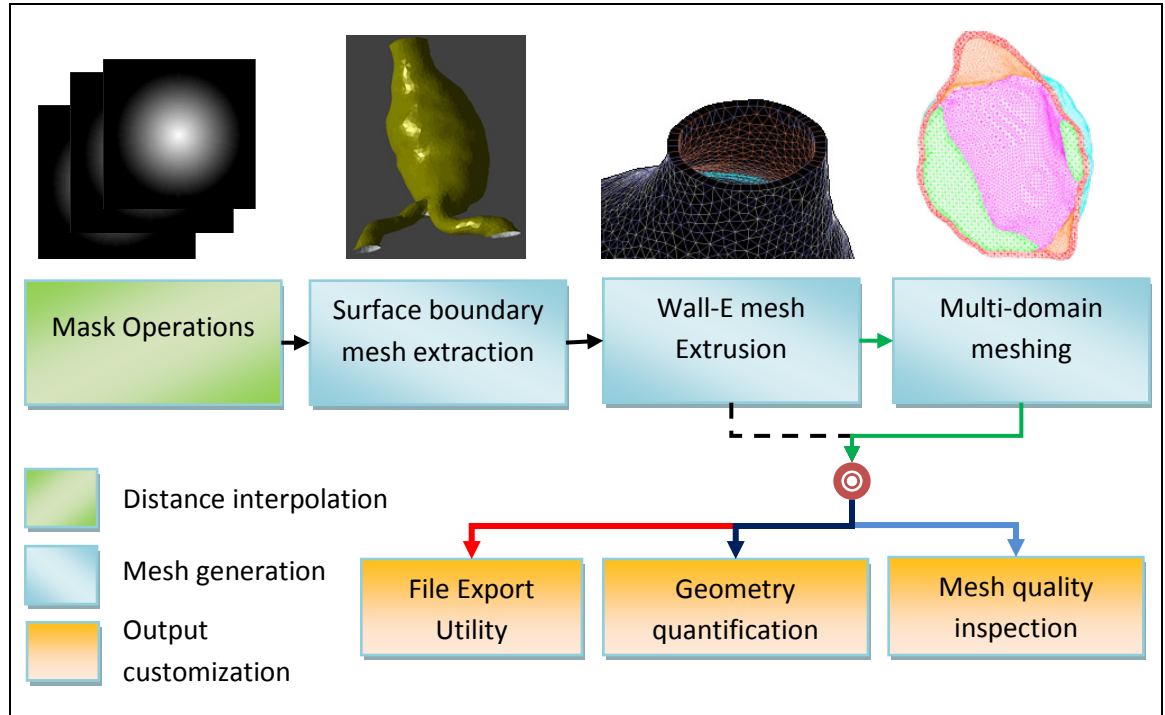


Figure 12: Block diagram illustrating the proposed framework (AAAMesh).

2.3.2 Volumetric data creation

Binary masks are obtained via segmentation of MRI or CT images (contrast-enhanced or unenhanced) and are the input for the operations in this framework. These are 2D slices extracted from the 3D object along a coordinate frame plane (usually labeled the z-plane) that encloses the region of interest. The framework imports the stack of 4-domain 2D masks obtained after image segmentation (Figure 13 a) along with additional DICOM header information, such as pixel size and slice spacing. The four domains are lumen, intraluminal thrombus (ILT), wall, and background (abdominal cavity), in the case of an AAA image dataset.

The following steps describe the mask operations:

1. The masks are stacked to form a regular 3D grid of voxels. A few additional slices are appended at the proximal and distal ends (padding) by duplicating the existing first and last masks to facilitate a cutting operation that is performed after surface extraction in Section 2.3.3. These 4-domain masks are converted to four single binary domain (BD) masks that represent the boundaries of the lumen, inner wall and outer wall surfaces, and an additional cloud surface which is the surface of a dummy mask obtained by dilating the outer wall boundary outward for verifying the normal direction.

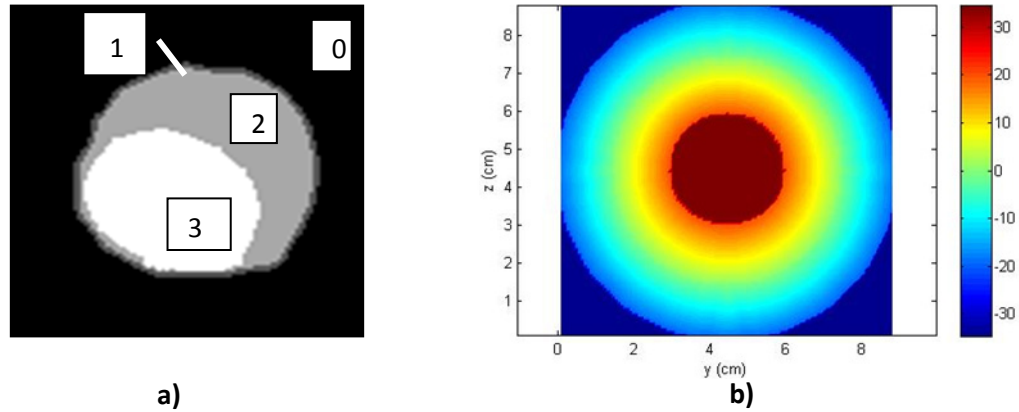


Figure 13: Input mask and continuous distance field (a) 4-domain mask; 0, 1, 2, and 3 represent the domains of interest in the mask e.g. 0 - abdominal cavity, 1 - vascular wall, 2 - intraluminal thrombus, and 3 - lumen, respectively; b) 2D slice in z-plane of the extracted distance field for perfectly circular cross section

2. For verification purposes, a script was written to provide estimated volumes of individual domains based on voxel counts in each mask.
3. Internal point computation: the surface mesh extraction strategy used in this framework is based on the loose ε -sampling method [178]. It requires a point internal to the AAA sac to compute surface points by ray-tracing to form ε -

samples [179] prior to the extraction of the surface. The location of an internal point specific to each BD volumetric data is not necessary, as for vascular geometries a point internal to the lumen will always be internal to the other BDs. Since the masks are binary, they are converted into a distance field, represented by $d(i, j, k)$, where (i, j, k) are grid indices, that is varying smoothly in the 3D space for robust handling and realistic reconstruction of 3D surfaces (Figure 13b). If the voxel belongs to the inside of the BD of interest, Ω_{in} , it is assigned a value equal to the scalar distance from the closest voxel belonging to the outside region, Ω_{out} . Every voxel that is inside the domain is given a positive value and those outside are given a negative value. Thus, a value corresponding to the zero isosurface represents the surface boundary of the domain Ω_{in} . Four different approaches for obtaining distance field were explored:

a) The distance field being same as stacked images having constant positive value for voxels inside and constant negative for voxels outside;

b) 2D grid distances; $d(i, j, k) = \sqrt{(i - I_m)^2 + (j - J_m)^2}$ where m 'th voxel is under consideration and (I_m, J_m, k) are grid indices of closest voxel belonging to other domain in same plane;

c) 3D grid distances; $d(i, j, k) = \sqrt{(i - I_m)^2 + (j - J_m)^2 + (k - K_m)^2}$ where (i, j, k) are grid indices of m 'th voxel under consideration and (I_m, J_m, K_m) are grid indices of closest voxel belonging to other domain;

d) 3D Euclidean distances accounting for anisotropic grid spacing normalized with minimum grid spacing;

$d(i, j, k) = \sqrt{(\Delta_x(i - I_m))^2 + (\Delta_y(j - J_m))^2 + (\Delta_z(k - K_m))^2}$ where (i, j, k) are grid indices of m 'th voxel under consideration and (I_m, J_m, K_m) are grid indices of closest voxel belonging to other domain and Δ_x, Δ_y , and Δ_z are grid spacings in Euclidean frame.

4. For computational ease I_m, J_m, K_m were considered only within a sufficiently large sphere around voxel radius of which happens to be the ceiling limit imposed on $d(i, j, k)$ if no neighbor voxel from other domain is found within this sphere. Method d) is selected (For more details refer Section 2.4.2.1.1, Figure 22, and Section 2.5.3).

2.3.3 Surface mesh extraction

The framework makes use of the open-source code Computational Geometry Algorithms Library (CGAL 3.6) [180] to extract a surface mesh from the volume data generated with the protocol described in Section 2.3.2. The strategy for surface mesh extraction is to start with the volume data for the BD and given an internal point, create sample points on the surface using ray tracing in random directions originating from the point. Using the previously validated approach of ϵ -sampling [179], the ϵ -sample of a surface \mathbf{S} is a point set \mathbf{E} that is sufficiently dense with respect to the medial axis of the surface [178]. Boissonnat and Oudot [178] reported on the concept of loose ϵ -sampling in which an algorithm proposed for surface reconstruction was derived from the surface meshing algorithm described by Chew et al [181]. The triangulated surface resulting from this method is close to the ideal surface \mathbf{S} (i.e., a small/minimum Hausdorff distance) and capable of providing good approximations for normals, areas, and curves. The end result is the tessellation of each BD in the vasculature, consisting of three-noded triangles.

2.3.4 Surface mesh refinement

The aforementioned algorithm assumes \mathbf{S} to be \mathcal{C}^2 continuous and without boundary (edge), and thus CGAL yields unrealistically rounded proximal and distal edges in the vascular surface mesh. Hence, the CGAL output mesh is clipped at the proximal and distal ends by horizontal cutting planes. As this operation introduces sliver-like elements, it is followed by a sliver removal operation by means of edge collapse (Figure 14, taking r-R ratio as a criterion for mesh quality) and subsequent smoothing. For both operations, the % change in surface area and volume of the convex hull was monitored and is ensured to be within user controlled prescribed limits.

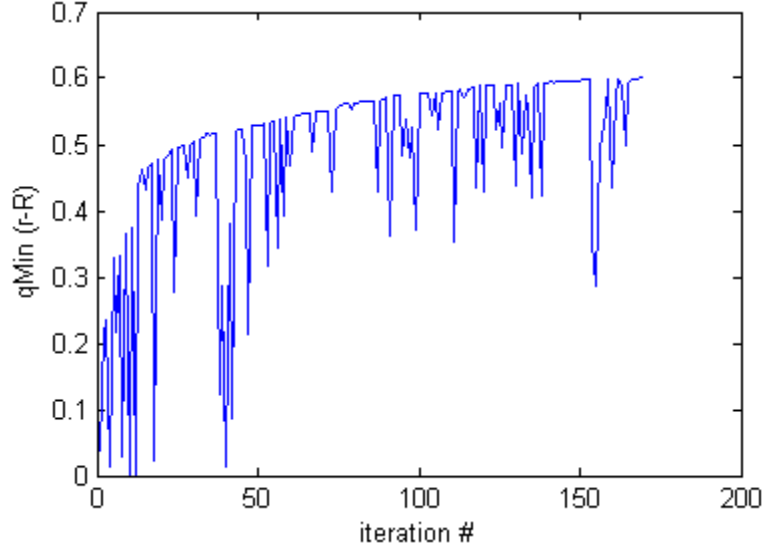


Figure 14: Surface mesh quality metric (minimum r-R ratio) as a function of sliver removal iterations using the edge collapse technique.

Surface mesh smoothing is accomplished by performing Laplacian and Taubin smoothing iterations [182, 183] using a script that can be applied to any polyhedral mesh made of nodes located only on the element vertices. A first-order neighborhood approach was followed for both smoothing strategies. The smoothing algorithms were implemented for a given tessellation T by expressing it as a graph, $T = (V, E)$, composed

of a set of n_V vertices $V = \{v_i : 1 \leq i \leq n_V\} : v_i \in \mathcal{R}^3$ and a set of n_E edges $E = \{e_k : 1 \leq k \leq n_E\}$, with each edge defined by two vertices, i.e. $e_k = (\tilde{v}_1^k, \tilde{v}_2^k) : \{\tilde{v}_1^k, \tilde{v}_2^k\} \in V$ with $\tilde{v}_1^k, \tilde{v}_2^k$ not identical. This representation in terms of edges rather than facets offers many computational advantages for edge detection, neighborhood and connectivity exploration, and smoothing operations that reflect in the efficiency of the code. For the sake of brevity, the following equations use v_k and the position vector \vec{v}_k interchangeably.

For each iteration of Laplacian smoothing, the position vector \vec{v}_k is updated by,

$$v'_k = \alpha v_k + (1 - \alpha) \Delta v_k \quad \dots \text{Eqn. 2-1}$$

In this work the default value for parameter α was set to 0.66.

Each iteration of Taubin smoothing comprises the following two operations applied subsequently [182]:

$$v'_k = v_k + \lambda * \Delta v_k \quad \dots \text{Eqn. 2-2}$$

and

$$v''_k = v'_k + \mu * \Delta v'_k \quad \dots \text{Eqn. 2-3}$$

with $\mu < 0 < \lambda$, where $N_{neigh_1}^k$ is the number of elements in the first-order neighborhood of the k 'th node:

$$\Delta v_k = \frac{1}{N_{neigh_1}^k} \sum_{j=1}^{j=N_{neigh_1}^k} (v_j - v_k) \quad \dots \text{Eqn. 2-4}$$

and

$$\mu = \left(k_{PB} - \frac{1}{\lambda}\right)^{-1} \quad \dots \text{Eqn. 2-5}$$

The parameters k_{PB} and λ were set to 0.1 and 0.5, respectively. The application of the two operations in sequence effectively results in a low-pass filter.

Volume and surface mesh changes were monitored during the smoothing operations after every iteration. In the framework, the end user can provide a number of iterations for each type of smoothing (either Laplacian or Taubin). The framework's GUI also provides an additional 'smart smoothing' option which smooths the vascular geometry until a percentage change in volume is achieved within a specified tolerance, i.e. the number of smoothing iterations are implicitly set (see Figure 15).

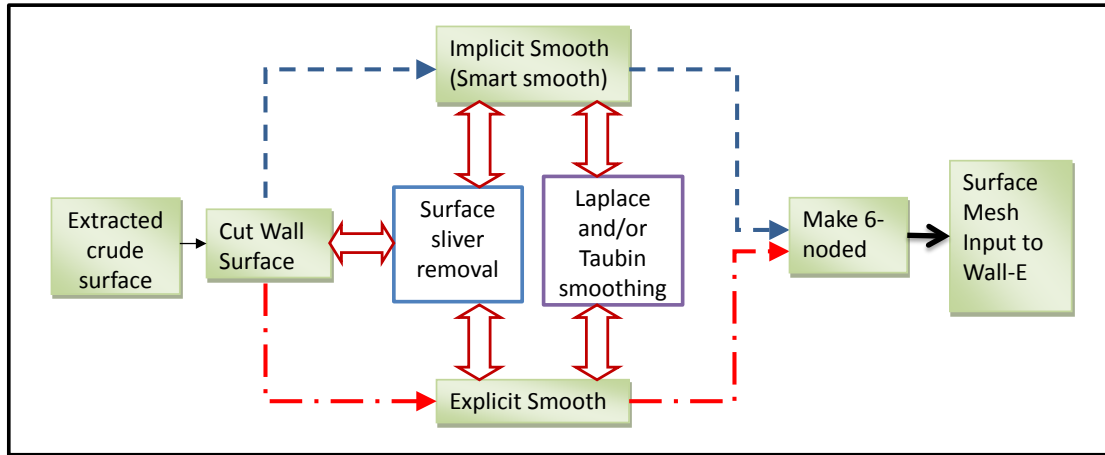


Figure 15: Schematic of surface meshing operations.

The edge nodes at proximal and distal ends are restricted to in-plane movement to avoid unnatural spikes and sharpness of the surface at these ends. Finally, the 3-noded triangular surface mesh is converted to a 6-noded triangular surface mesh by introducing additional nodes at the midpoint of each triangle edge. While the surface mesh will still have a linear order of accuracy, the additional nodes will benefit the

subsequent finite element modeling by allowing higher order interpolation functions, which would otherwise need a highly dense 3-noded linear mesh to resolve regions of high stress gradients.

2.3.5 Wall extrusion

A wall mesh extrusion algorithm was implemented in the AAAMesh framework to model the vasculature with either a uniform wall thickness or regional variations of wall thickness. The wall extrusion code (Wall-E, shown schematically in Figure 16) functions as a stand-alone module that creates a layered volume mesh by acting on the 6-noded surface mesh given as input. It calculates local nodal normal directions from facet normal directions in its neighborhood; for facet normal direction verification, it uses reference nodes from an auxiliary reference surface mesh positioned radially either on the inner side or on the outer side of the 6-noded surface mesh. The simplest way to generate the auxiliary mesh is to create auxiliary masks by dilating an actual mask by an arbitrary but reasonable number of pixels. For each triangle on the surface mesh, a nearest neighbor node is calculated from the auxiliary mesh nodes and the corresponding vector is used for deciding the outward direction for each triangle.

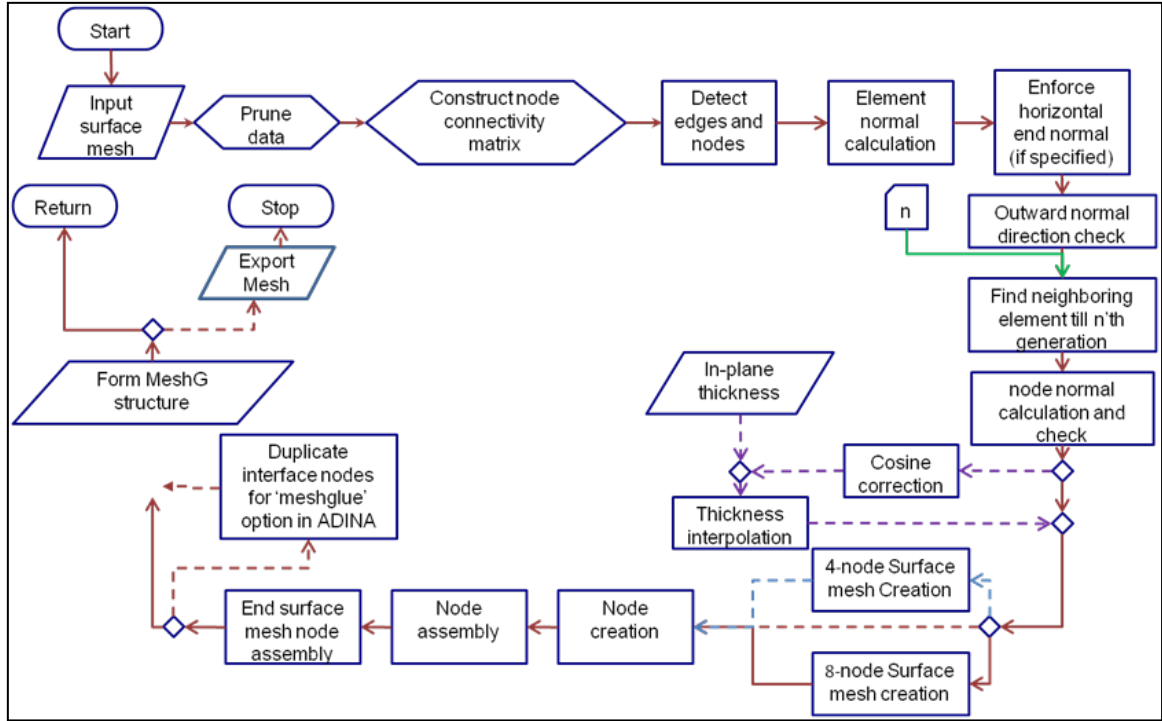


Figure 16: Flowchart for wall extrusion code Wall-E (dotted line - optional, continuous line – default).

This algorithm is efficiently implemented by using a binning technique (simplified k-d tree approach) where the entire reference point cloud is divided into smaller bins depending upon the Z-coordinate prior to evaluating the nearest neighbor. Based on the triangles that define the input surface and outward normal directions of a triangular facet, this extrusion code evaluates elemental normal directions, finds facets lying in the n 'th order nodal neighborhood, and finds nodal normals by determining the average of the elemental normal direction cosines corresponding to those facets. The input tessellation is a PLC defined by a set of faces, as for wall extrusion the elemental normal and a minimum of 3 nodes in the correct sequence are needed for each triangular facet. If required, Wall-E code can perform a check for node sequence, where it evaluates the normal direction of each neighboring element and its consistency with respect to the normal of the element under consideration, and corrects its normal based on the

majority of the directions of the neighbors. In most cases this approach converges after a couple of iterations. However, convergence is not always guaranteed as sequential improvements may result in the same normal directions recursively. As an alternative, an option is provided in the AAAMesh GUI to estimate the outward normal direction by meshing the interior volume of the vasculature (lumen and intraluminal thrombus in the case of an AAA) with the open source software TetGen (<http://tetgen.berlios.de/>) to obtain face normal directions by taking into account node numbering in the tetrahedra. However, this alternate approach is possible only if the geometry can be completely enclosed as is the case of a blood vessel.

Mathematically, the tessellation T is expressed as a graph $T = (V, F)$, composed of a set of n_V vertices $= \{v_i : 1 \leq i \leq n_V\} : v_i \in \mathcal{R}^3$ and a set of n_F facets $F = \{f_k : 1 \leq k \leq n_F\}$ with each facet defined by p vertices, i.e. $f_k = (\tilde{v}_1^k, \tilde{v}_2^k, \dots, \tilde{v}_p^k)$. Currently we use $p = 6$. Even though three mid-nodes for each triangle amongst $p = 6$ may appear redundant, this makes the module versatile by not modifying nodes on the input mesh by the parent calling function. Thus, it can be coupled with other input sources and approaches, e.g. it can be used for creating boundary layers for computational fluid dynamics meshes. Using a source surface mesh in this manner is possible only in the case of wedge elements resulting from triangle extrusion, since for hexahedrons additional nodes have to be inserted while converting the triangular mesh to a quadrangle mesh prior to extrusion. The unique capability of Wall-E is to have node-to-node control on the wall thickness during the extrusion process. Measurement of in-plane thickness from image segmentation software can be used by considering the vector component of in-plane thickness along the local nodal normal direction (additional

details in Section 4.2.4). For each surface node on the inner wall surface mesh, the unit normal direction vector is given by,

$$\vec{n}_j = \frac{\sum_{i=1}^{N_e} \vec{e}_i}{\left\| \sum_{i=1}^{N_e} \vec{e}_i \right\|} \quad \dots \text{ Eqn. 2-6}$$

where, \vec{n}_j is the unit nodal normal for the node under consideration (node j), N_e is the number of elements that fall within the q 'th order neighborhood $G_{neigh_q}^j$ around node j , and \vec{e}_i is the unit normal for the i 'th element. Here, ' q ' is calculated automatically in Wall-E by determining the approximate multiple of surface facet segment lengths that can be fitted within a specified radius from each node. This approach is used since it makes the process of estimating the correct neighborhood level independent of the mesh size. In-plane thickness values from 3D point cloud obtained by stacking segmented splines in sac region are corrected for equivalent local normal directions and then interpolated onto surface mesh nodes. Wall-E also identifies relevant facesets such as inner wall, outer wall, and end faces for boundary condition application. It is capable of handling multiple inlets and outlets.

2.3.6 Multi-domain mesh generation sequence

For multi-domain mesh generation, the main challenge is to ensure a good quality mesh that maintains a proper interface with all neighboring domains and that the interfaces associated with each domain are identified correctly. In addition, for the case of AAA meshing, there is uncertainty regarding the number of individual domains due to the unpredictable number of patient-specific intraluminal thrombi and their locations within the AAA sac. They may lie completely enclosed by the wall or may have some surface exposed if they are located near the inlet or outlet cross sections.

In the proposed framework, the outer wall surface mesh is extruded inward following the protocol described in Section 2.3.5. The resulting inner wall surface mesh obtained from these operations does not define a completely enclosed space since the inlet and outlet cross-sections remain open. The corresponding edges are extracted, which define the boundary of the 2D region required to close these cross-sections. This is performed with a triangular mesh patch created using the Triangle code developed at Carnegie Mellon University (<http://www.cs.cmu.edu/~quake/triangle.html>) [184, 185]. This yields a surface triangle mesh at the proximal and distal ends of the vascular model that represent the combined lumen and ILT ends (should ILT exist at the ends). The interior volume of the AAA sac (lumen and ILT combined element set, E_{combo}) is meshed with TetGen, which is based on boundary constrained Delaunay tetrahedralization [186]. The surface mesh obtained a priori for the lumen, surface S_{L1} , using the methods described in Sections 2.3.3 and 2.3.4, is used to seed nodes prior to tetrahedralization as well as with Wall-E to offset the luminal surface inward by a marginal distance δ_{offset} to obtain S_{L2} . Using S_{L2} as the reference, all nodes corresponding to the element set E_{combo} are identified as either inside or outside the surface using a ray tracing algorithm. Now amongst the ILT-lumen collective mesh elements, all elements that have all their nodes outside are registered as ILT elements and the rest are registered as lumen elements. A nodal connectivity search within the ILT volume is carried out using a marching front approach to find an open surface set and the spatially disconnected ILT regions. These are distinguished by repeating the search on the subset of elements that remains after subtracting elements belonging to an identified ILT region from the set of still unidentified elements. Facets need to be identified for applying various boundary conditions to simulate the proper physics. A typical interface unit is shown in Figure 17.

AAAMesh is built on a data organization scheme that can handle arbitrary multi-domain structures and store the interfaces in a systematic manner. Up to 99 domains and their

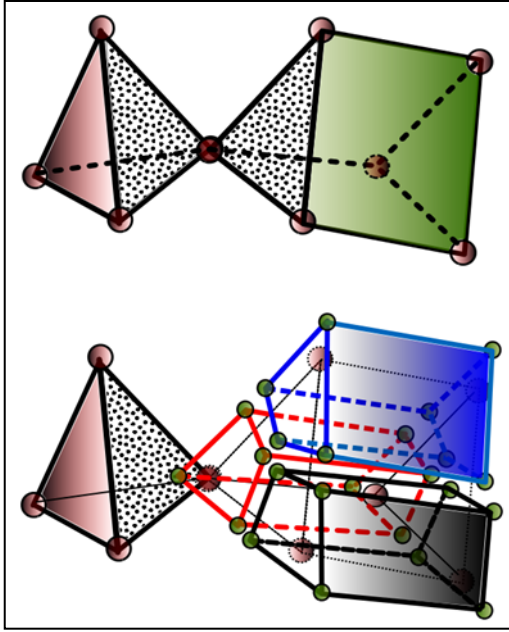


Figure 17: A unit depicting scheme for inner wall surface interface.

interfaces can be stored compactly with the restriction that the first domain must be the outermost region meshed with hexahedral or wedge elements and the rest of the domains are meshed with tetrahedral elements. A systematic numbering convention enables to identify multiple facesets that require the application of a single boundary condition, e.g. consider an AAA with three distinct ILT regions interfacing with the lumen and the wall. Thus, for a finite element analysis simulation it would be required to select the

interfaces ILT1-to-lumen, ILT2-to-lumen, ILT3-to-lumen, and wall-to-lumen (the latter can be in itself a collection of discontinuous facesets) to apply a pressure boundary condition.

2.3.7 Mesh quality assessment

For each vascular geometry, AAAMesh can assess its volume and surface area by summation of the volumes and surface areas of the individual elements of the volume mesh. The mesh quality module also provides statistics on the following three quality metrics – i) Jacobian; ii) Condition number; and iii) Oddy metric.

2.3.7.1 Mesh quality metrics

The aforementioned metrics are based on the Jacobian matrix \mathbf{J} that relates derivatives in natural coordinate system to those in local coordinate systems of an element. Earlier it has been defined based on element edge vectors as reported by [187] and [188]. However, we use the following definition of the Jacobian matrix, which is more relevant for FEM applications, as reported by [148, 175]:

$$J_{ij} = \frac{\partial}{\partial \xi^j} (\phi_k x_k^i) \quad \dots \text{Eqn. 2-7}$$

where, ξ^j are the element natural coordinates ($j = 1, 2, 3$), x_k^i are the local coordinates for the k 'th node of the element in question ($i = 1, 2, 3$), and ϕ_k are the N weight functions defined in natural coordinates and corresponding to the N nodes of the element ($k=1, \dots, N$). The Jacobian matrix can be expanded in matrix form as

$$\mathbf{J} = \begin{bmatrix} x_1 & x_2 & x_3 & \dots & x_{N-1} & x_N \\ y_1 & y_2 & y_3 & \dots & y_{N-1} & y_N \\ z_1 & z_2 & z_3 & \dots & z_{N-1} & z_N \end{bmatrix} \begin{bmatrix} \frac{\partial \phi_1}{\partial \xi} & \frac{\partial \phi_1}{\partial \eta} & \frac{\partial \phi_1}{\partial \zeta} \\ \frac{\partial \phi_2}{\partial \xi} & \frac{\partial \phi_2}{\partial \eta} & \frac{\partial \phi_2}{\partial \zeta} \\ \frac{\partial \phi_3}{\partial \xi} & \frac{\partial \phi_3}{\partial \eta} & \frac{\partial \phi_3}{\partial \zeta} \\ \vdots & \vdots & \vdots \\ \frac{\partial \phi_N}{\partial \xi} & \frac{\partial \phi_N}{\partial \eta} & \frac{\partial \phi_N}{\partial \zeta} \end{bmatrix} \quad \dots \text{Eqn. 2-8}$$

2.3.7.2 Mesh quality assessment for hexahedral elements

Functions ϕ_k are characteristic of every element type. For hexahedral elements, depicted in Figure 18, the following relations are used:

$$\phi_1 = (1 - \xi) * (1 - \eta) * (1 - \zeta)$$

$$\phi_2 = (\xi) * (1 - \eta) * (1 - \zeta)$$

$$\phi_3 = (\xi) * (\eta) * (1 - \zeta)$$

$$\phi_4 = (1 - \xi) * (\eta) * (1 - \zeta)$$

$$\phi_5 = (1 - \xi) * (1 - \eta) * (\zeta)$$

$$\phi_6 = (\xi) * (1 - \eta) * (\zeta)$$

$$\phi_7 = (\xi) * (\eta) * (\zeta)$$

$$\phi_8 = (1 - \xi) * (\eta) * (\zeta)$$

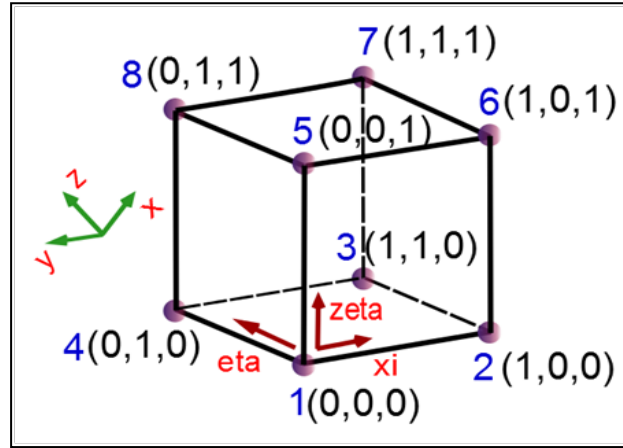


Figure 18: Hexahedral element node numbering scheme in natural coordinates.

It should be noted that the change in node numbering scheme and the location of the origin will change the interpolation functions defined above and hence there will be a difference in the Jacobian definition when compared to work published by others. Based on these functions, three columns for the derivative matrix J are:

$$\frac{\partial \phi_k}{\partial \xi} = \begin{Bmatrix} -(1-\eta) * (1-\zeta) \\ (1-\eta) * (1-\zeta) \\ \eta * (1-\zeta) \\ -\eta * (1-\zeta) \\ -(1-\eta) * \zeta \\ (1-\eta) * \zeta \\ \eta * \zeta \\ -\eta * \zeta \end{Bmatrix}; \quad \frac{\partial \phi_k}{\partial \eta} = \begin{Bmatrix} -(1-\xi) * (1-\zeta) \\ -\xi * (1-\zeta) \\ \xi * (1-\zeta) \\ (1-\xi) * (1-\zeta) \\ -(1-\xi) * \zeta \\ -\xi * \zeta \\ \xi * \zeta \\ -(1-\xi) * \zeta \end{Bmatrix}; \quad \frac{\partial \phi_k}{\partial \zeta} = \begin{Bmatrix} -(1-\xi) * (1-\eta) \\ -\xi * (1-\eta) \\ -\xi * (\eta) \\ -(1-\xi) * \eta \\ (1-\xi) * (1-\eta) \\ \xi * (1-\eta) \\ \xi * \eta \\ (1-\xi) * \eta \end{Bmatrix}$$

... Eqn. 2-9

The following relations were implemented as reported in [175]:

- 1) Determinant of the Jacobian matrix J
- 2) Condition number, defined as

$$Condition\ Number = \frac{1}{3} * |J^{-1}| * |J| = \frac{1}{3} * \left(\frac{|J|}{\det(J)} \right) * |J|$$

... Eqn. 2-10

- 3) Oddy metric, defined as

$$Odddy = \frac{(|J^T J|^2 - \frac{1}{3} * |J|^4)}{(\det(J))^{4/3}}$$

... Eqn. 2-11

For 2) and 3) we use the Frobenius norm $|J|$, which is analogous to the L2-norm in vectors:

$$|J| = \sqrt{(\text{trace}(J^T J))}$$

... Eqn. 2-12

These operations are performed at each corner node of the mesh. From a finite element formulation point of view, the calculations should be performed at the integration points within each element. However, we evaluate the quality metrics at the corner nodes, which are more prone to become singular compared to the integration points located near the center of an element. For each domain in the mesh, minimum, maximum, mean, and standard deviations are reported for the three metrics of quality.

2.3.7.3 Mesh quality assessment for tetrahedral elements

For tetrahedral elements, the mesh quality is assessed by calculating the ratio of the radius of an inscribed sphere to the radius of the circumscribing sphere for each element [177]:

$$rR = \frac{216 \times V^2}{A \times \sqrt{(p_1 + p_2 + p_3)(p_1 + p_2 - p_3)(p_1 - p_2 + p_3)(-p_1 + p_2 + p_3)}} \quad \dots \text{Eqn. 2-13}$$

where A is the sum of the areas of all four triangular faces, V is the volume of the tetrahedron, and p_k is the product of the length of two non-intersecting edges, e.g. if \vec{a}_{ij} is an edge joining the i th and j th node of the tetrahedron, $p_1 = |\vec{a}_{14}| \cdot |\vec{a}_{23}|$ and the volume is defined as $V = \frac{1}{6}(\vec{a}_{14} \cdot (\vec{a}_{12} \times \vec{a}_{13}))$. Alternatively, the volume of a tetrahedron can also be calculated as

$$V = \frac{1}{6} \det \begin{pmatrix} x_1 & y_1 & z_1 & 1 \\ x_2 & y_2 & z_2 & 1 \\ x_3 & y_3 & z_3 & 1 \\ x_4 & y_4 & z_4 & 1 \end{pmatrix} \quad \dots \text{Eqn. 2-14}$$

Another quality metric relevant to tetrahedral elements is the maximum and minimum element volume. The AAAMesh quality module reports values of maximum, minimum, mean, and standard deviation of the tetrahedral mesh volume.

One other metric used is the Joe-Liu parameter evaluated as reported by [175]:

$$JLP = \frac{2^{\frac{4}{3}} \times 3 \times V^{\frac{2}{3}}}{\sum_{i=1}^{i=3} \left[\sum_{j=i+1}^{j=4} |\vec{a}_{ij}|^2 \right]} \quad \dots \text{Eqn. 2-15}$$

where, the denominator is the sum of the squares of all edge lengths.

2.3.8 Export module

The mesh type needed for a finite element simulation will depend on the intended physics modeling, e.g. in simulations involving only the wall domain, the user do not need to export the lumen and ILT domain meshes. The export module in AAAMesh can output a wall volume mesh or a surface mesh in the form of shell elements. For a CFD simulation, only the lumen domain may be needed. In addition, the various domains

involved can be exported with either quadratic or linear elements. The module also exports the mesh file in a variety of formats: (i) NASTRAN file format with hyperleastic structural material properties and boundary conditions typical of AAA physics modeling; (ii) STL file format for rapid prototyping; a universal mesh format for visualization purposes; and (iii) MATLAB native format with extension *.mat for processing in other modules external to AAAMesh such as for detailed geometry quantification. This section of file formats is written in a modular manner so that it can retrieve and process any previously generated mesh data instead of needing to execute the meshing algorithms again. It also has a geometry evaluation feature that can analyze the mesh and quantify volume and surface area.

2.3.9 Validation protocol

The proposed framework was evaluated for its accuracy and mesh quality metrics with respect to a digital aneurysm phantom template, shown in Figure 19. A MATLAB code was written in parametric form to create 4-domain masks of this template. This dummy input was provided to AAAMesh and tessellated surface mesh was generated that approximates the ideal mathematical surface. Precise quantification of the discrepancy between the AAAMesh generated surface mesh and the ideal mathematical reference surface is provided to explore effect of various mesh generation settings such as surface mesh density, smoothing algorithm, and the number of corresponding smoothing iterations.

The aneurysm in this phantom is of size $R_{\min} = 1$ cm, $R_{\max} = 3$ cm, $L = 9$ cm, and was created using a sinusoidal variation of the radius and the center of the cross-sections. The annular ILT thickness was set to 0.5 cm and it spans to 50% of total axial

length such that it is positioned symmetrically. The radius was prescribed as a function of the z (axial) coordinate following the relation:

$$r(z) = R_{min} + \frac{1}{2}(R_{max} - R_{min}) \left(1 - \cos(2\pi z/L)\right)$$

... Eqn. 2-16

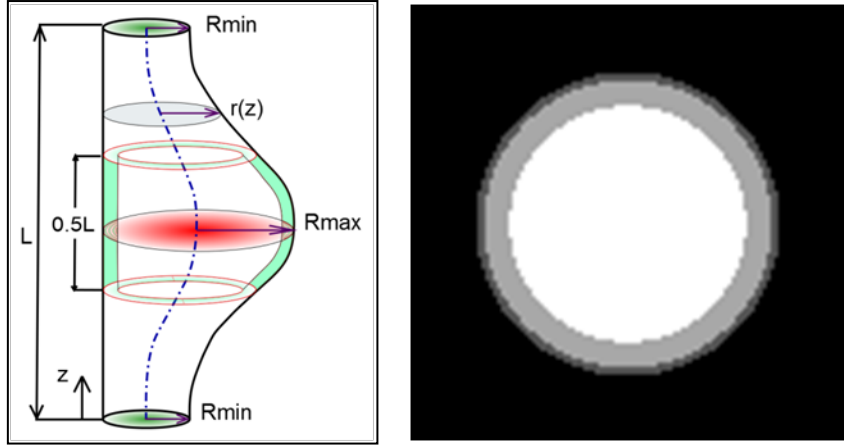


Figure 19: Phantom of idealized model (to be reconstructed) for validation and one exemplary mask.

A set of masks of size 512 x 512 pixels was created with a pixel spacing of 0.075 cm and slice spacing of 0.3 cm with the aforementioned radius variation along the axial length of the aneurysm. Centerline asymmetry was confined to the YZ plane. The outer wall surface of this phantom can be analytically described as the isosurface $\Phi = 0$ for $0 \leq z \leq L$:

$$\Phi = (x - X_c)^2 + (y - Y_c(z))^2 - (r(z))^2,$$

... Eqn. 2-17

where $Y_c(z) = Y_c + (r(z) - R_{min})$ and X_c and Y_c represent the coordinates of the centroid in the first and last slices. The surface mesh obtained using the generated masks was then compared with the analytical surface to establish error bounds.

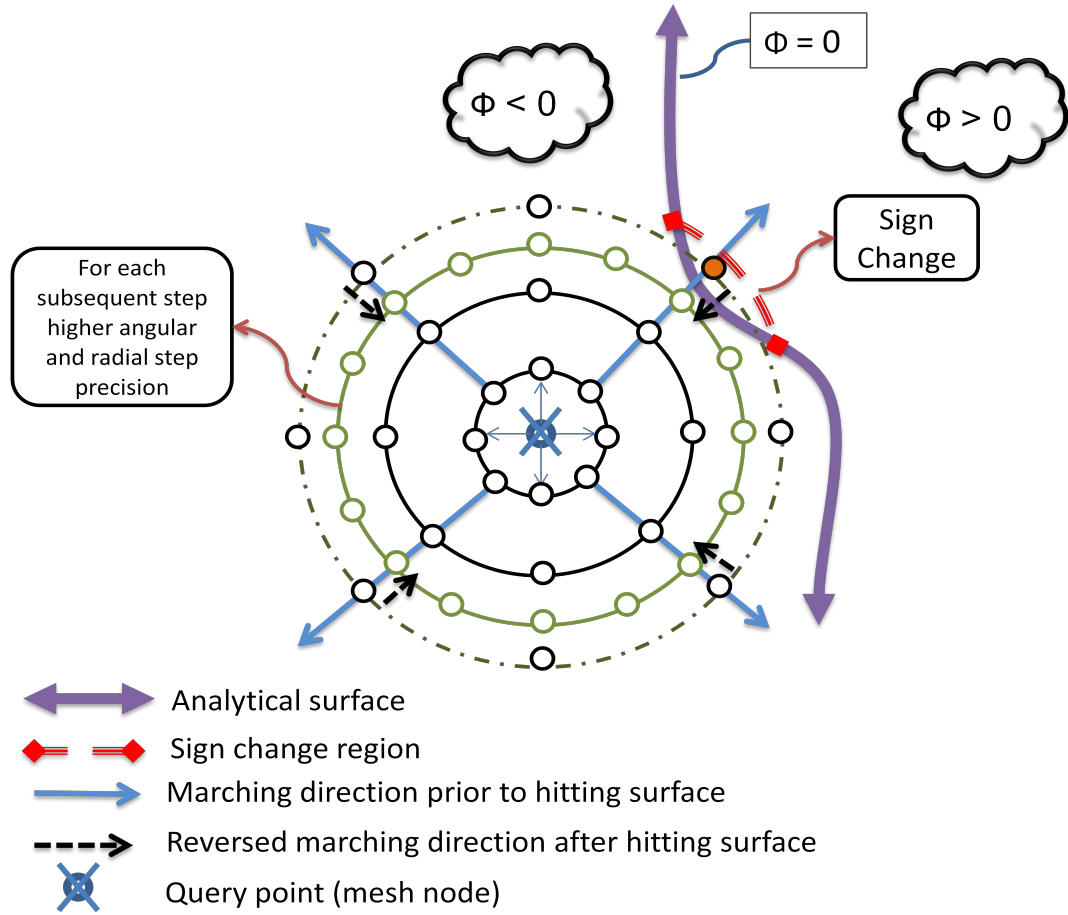


Figure 20: Sphere marching approach for calculating the exact perpendicular distance of a point from an analytical surface for validation of the meshing strategy.

The signed perpendicular distance of each surface mesh node from the analytical surface was obtained using a sphere front marching approach, illustrated in Figure 20. Outward and inward marches alternate each other. The direction reversal is triggered by a change in sign amongst marching points on the spherical front. Each reversal has an increased angular resolution for grid point spacing as well as an increased radial resolution of marching steps. This method ensures that we are measuring the perpendicular distance from the analytical surface in 3D. The estimated error in this approach is $distErr = \max(R_{step}, R(1 - \cos(\theta/2)))$, where R_{step} is the radial resolution, R is the measured distance corresponding to the ongoing marching iteration, and

θ represents the angle subtended by two neighboring marching points at the query node (mesh node). Unless $R \gg R_{step}$ or the angular resolution is coarse, this error is usually equal to R_{step} . Given an initial marching step size δX_0 and final desired smallest step Δ after the $(p - 1)$ 'th reversal, we can arrange all intermediate steps in a geometric series for better performance. If r denotes the ratio of the geometric series, $r = \left(\frac{\delta X_0}{\Delta}\right)^{\frac{1}{(p-1)}}$, then in stepsize δX_{n-1} the n 'th step will be $\delta X_{n-1} = \delta X_0 \times r^{n-1}$.

A second asymmetric phantom with a bifurcation, shown in Figure 21, was used for verification of the directionality of the output mesh.

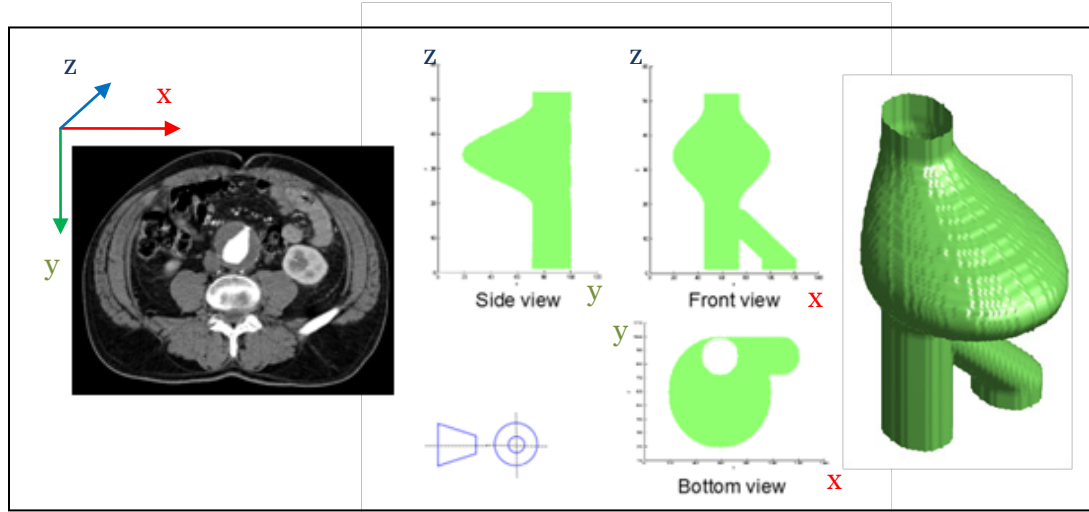


Figure 21: Coordinate frame convention (+x from patient's right to left; +y from anterior to posterior; +z from leg to head) and an asymmetric phantom for validating directionality.

2.4 RESULTS

The framework is characterized by considering two sample cases – the idealized phantom and a patient-specific geometry. The idealized phantom is targeted mainly to evaluate the accuracy of the image based reconstruction of the surface whereas the patient specific geometry demonstrates the implementation of the meshing algorithms

while exploring if any suitable surrogate index can be developed for deciding the optimum number of smoothing iterations. Results from 952 different combinations of settings (14 mesh sizes \times 17 different iterations \times 2 smoothing algorithms \times 2 geometries) are summarized below.

For idealized/phantom geometries, the assessment of the output mesh is based on geometrical accuracy and mesh quality. Geometrical error comprises errors in variables such as surface area, volume, and distance whereas the mesh quality involves the surface mesh quality metric ratio of incircle radius to circumcircle radius (r-R ratio). The following results present these errors in two categories – first, a cumulative geometric error measured for input masks of typical pixel resolution of 0.075 cm in the image plane and a 0.3 cm slice thickness and second, a comprehensive error measured for a sensitivity study of input mask resolution and meshing parameters. The distance error (*distErr*) obtained by the spherical marching front is obtained by using a radial resolution of 2×10^{-5} cm, i.e. 1×10^{-5} when normalized with $R_{avg} = 2$ cm, and an angular resolution of $\frac{\pi}{72}$ radians between the marching points in the spherical coordinate system. It should be noted that the geometrical errors reported here are cumulative errors since they include errors in pixelation of the ideally smooth phantom geometry's masks in addition to the surface approximation error for the object. Thus, the reported errors are expected to be greater than the actual reconstruction error of the framework.

For the patient-specific geometry, to evaluate the geometrical errors the corresponding ideal reference value is not available except for the voxel derived estimation of the volume. Therefore, we provide sample meshes for different patient-specific aneurysm geometries for qualitative evaluation of the resulting volume meshes

and a comparison with commercial software Mimics® is provided using an exemplary patient-specific case.

2.4.1 Phantom based studies

2.4.1.1 Error estimation - Voxalization error during phantom creation

An asymmetric aneurysm phantom (Asym13n) was generated with the phantom template described in Section 2.3.9 with $R_{min} = 1 \text{ cm}$, $R_{max} = 3 \text{ cm}$, and $L = 9 \text{ cm}$. Hence, the analytically calculated volume is 127.2324 cm^3 (refer to Appendix A for details). Table 5 represents a comparison of volumes obtained by the sum of voxel volumes belonging to object, here on referred to as VoxVolume. This validates the mask creation module; considering the objective of this validation, instead of domain-specific volumes only the total volume of aneurysm is considered where the outer wall represents the boundary of the phantom with ends closed by flat surfaces. The effect of symmetry in the phantom model is observed in Table 6 where the volume error of the asymmetric aneurysm is identical to that obtained with a symmetric aneurysm (Sym13n) of the same dimensions. Table 7 describes the effect of radius variation of the aneurysm phantom template by comparing the volume error of a cylindrical phantom (Cyl0100n, representing a normal, healthy vessel) with that of three asymmetric aneurysms of various sizes given by their maximum radius.

Table 5: Voxelization error - effect of image resolution

Pixel spacing (cm)	Slice spacing (cm)	# Voxels	VoxVolume (cm3)	% error
0.075	0.3	75959	128.1808	0.7454
0.025	0.3	683719	128.1973	0.7583
0.075	0.1	226733	127.5542	0.2529
0.025	0.1	2040875	127.5547	0.2533

Table 6: Voxelization error - effect of symmetry.

Phantom	Pixel spacing (cm)	Slice spacing (cm)	# Voxels	VoxVolume (cm ³)	%error
Asym13n	0.075	0.3	75959	128.18	0.7454
Sym13n	0.075	0.3	75959	128.18	0.7454

Table 7: Voxelization error - effect of radius variation.

Phantom	L (cm)	R _{min} (cm)	R _{max} (cm)	Voxels	VoxVolume (cm)	% error
Cyl0100n	9	1	1	17143	28.93	2.3148
Asym12n	9	1	2	40407	68.19	1.5417
Asym13n	9	1	3	75959	128.18	0.7454
Asym14n	9	1	4	124119	209.45	0.4448

2.4.1.2 Effect of distance field interpolation strategy

Results of four different strategies for distance interpolation are shown in Figure 22.

Color plot at center describes representative distance field extracted from phantom model described in Section 2.3.9 for mid-slice parallel to image stacking direction such that it contains centerline. For comparison, rectangular area marked by red rectangle was qualitatively explored and contour lines are shown corresponding to different strategies. Results for image interpolation based smoothing are shown in Table 8, Figure 22, and Figure 23, based on three different approaches- 0D, 2D, and 3D, explained below.

Table 8: Effect of different distance field creation approaches.

Approach	distErr_max (cm)	distErr_avg (cm)	distErr_std (cm)	InOutRatio	Area (cm ²)	Volume (cm ³)
Ideal	0	0	0	1	113.097	127.232
0D	0.1280	-0.000063	0.03599	0.9562	138.734	126.977
2D	0.0918	0.032711	0.01645	0.0178	133.612	131.300
3D	0.0613	-0.000964	0.01790	1.1387	131.693	126.861

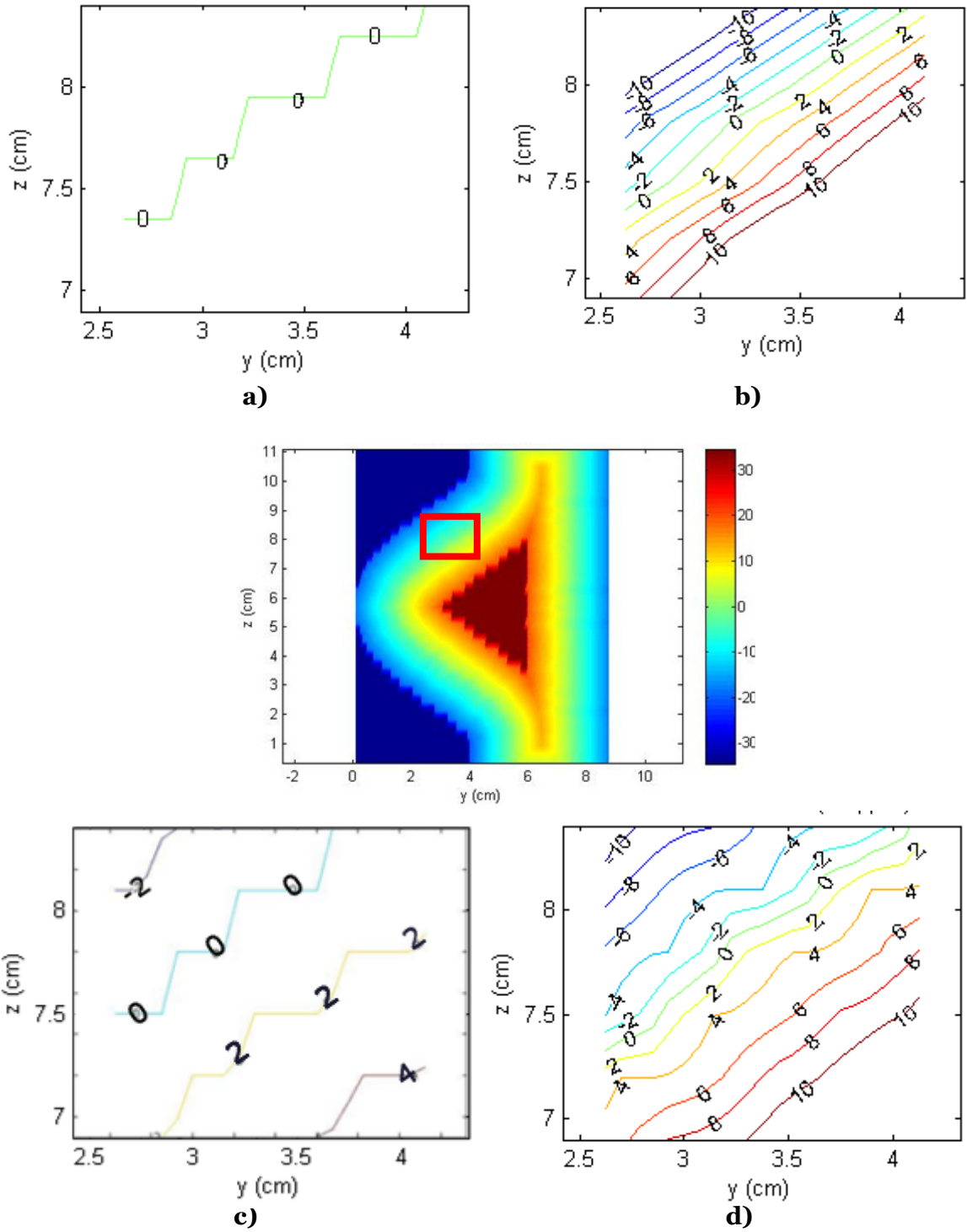


Figure 22: Isocontours of distance field resulting from different interpolation strategies. Center figure shows representative color plot of distance field for vertical mid slice using phantom model and strategy d). Rectangle marks area zoomed in a), b), c) and d). a) No interpolation b) 2D interpolation c) 3D grid distance d) 3D Euclidean distance

The isosurface is extracted from this distance field and hence carries its characteristics. Figure 23 illustrates, from left to right, the isosurface for a) no distance field interpolation (oD), i.e. data at grid points in binary form, b) interpolation in the plane of the image (2D), and c) 3D interpolation. ‘3Dgrid’ approach in Figure 22 c) was discarded and instead more accurate 3D Euclidean approach in Figure 22 d) retained for creating a distance field from the segmented image volumetric data. These surfaces are presented without any subsequent Laplacian or Taubin smoothing iterations in order to preserve their original characteristics. If *distErr* denotes list of nodal signed distances from ideal surface calculated as per procedure described in Section 2.3.9, Table 8 indicates that 3D interpolation is the best approach for creating a distance field from segmented images based on a quantitative comparison of the following parameters: i) *distErr_max* – maximum of $|distErr|$, ii) *distErr_avg* – global mean of *distErr*, iii) *distErr_std* – standard deviation of *distErr*, iv) *InOutRatio* - ratio of number of nodes positioned inside or on ideal surface (non-positive *distErr*) to number of nodes positioned outside (positive *distErr*) of ideal surface, iv) surface area – sum of individual area of triangular facets, and v) volume - sum of individual volume of triangular facets.

2.4.1.3 Sensitivity analysis

Mesh smoothing affects reconstructed surface. This effect can be desired as well as undesired. Following sub-sections summarize detailed analysis of total 476 different combinations of settings (14 mesh sizes \times 17 different numbers of iterations \times 2 smoothing algorithms) and corresponding AAAMesh executions to study effect smoothing on geometrical accuracy and mesh quality of phantom Asym13n.

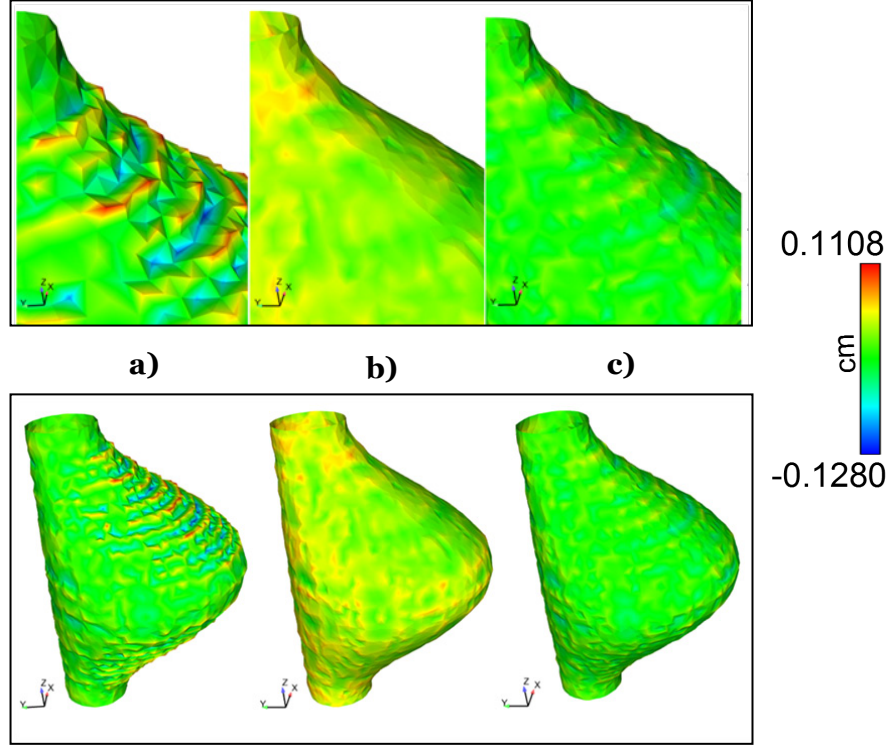
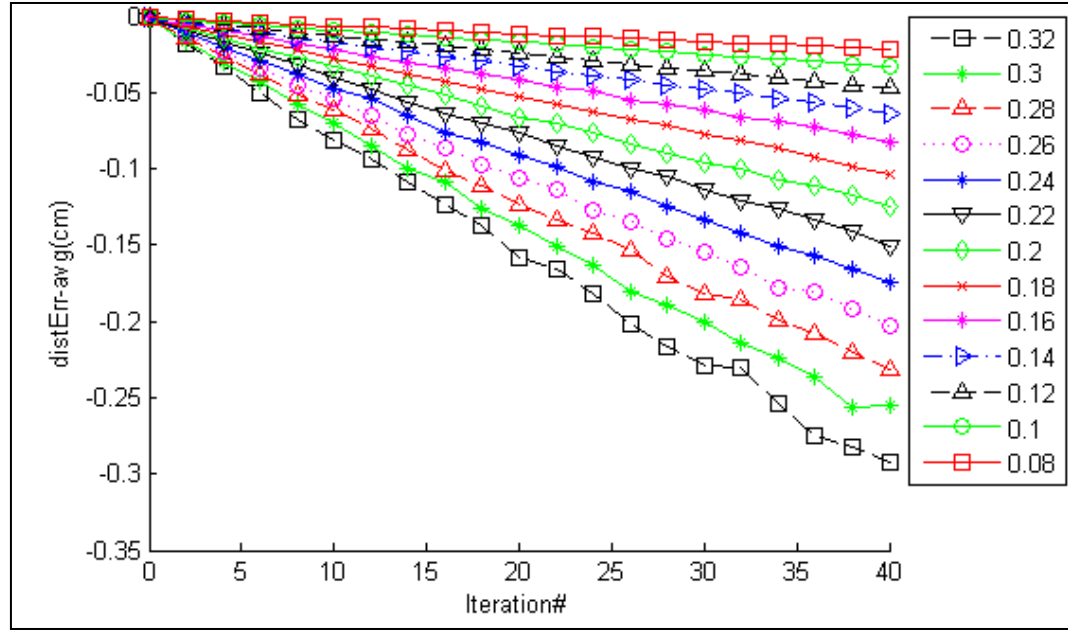


Figure 23: Qualitative comparison of influence of different distance field creation approaches on surface roughness and *distErr*: (a) no distance field interpolation (oD), (b) interpolation in the plane of the image (2D), and (c) 3D interpolation. Color legend refers to *distErr* metric.

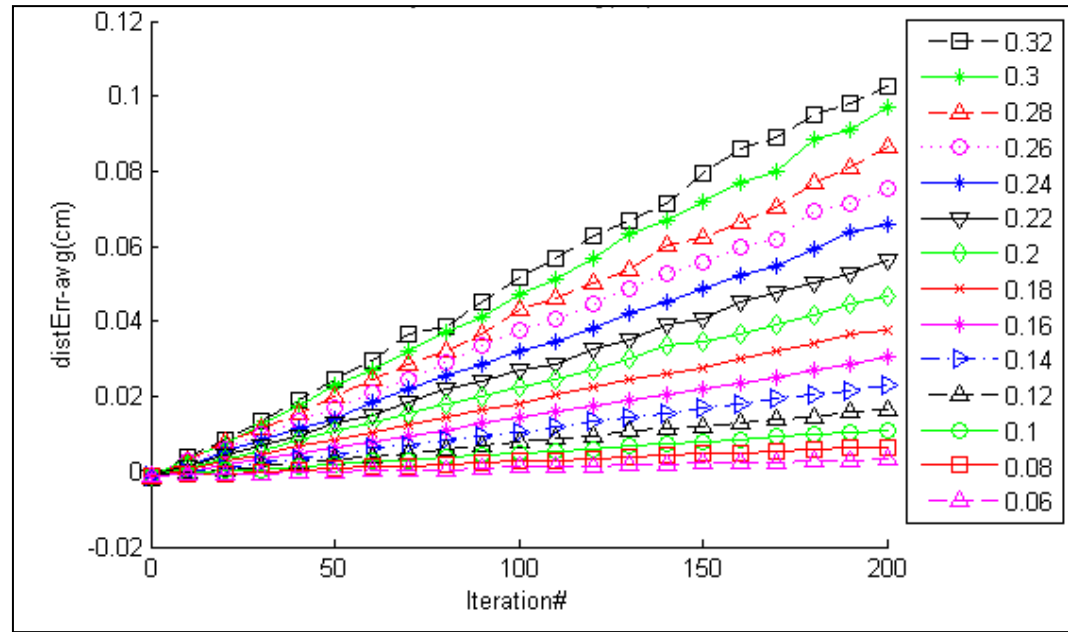
2.4.1.3.1 Geometrical accuracy

This section elaborates on effect of mesh smoothing on geometrical accuracy. The response of the 3-noded triangular surface to different number of smoothing iterations and mesh sizes (mesh densities) was critically examined. Figure 24 and Figure 25 illustrate the behavior of the following geometric variables: *distErr_avg*, *distErr_std*, *relAreaErr* and *relVolErr* when subjected to Laplacian or Taubin smoothing iterations independently. Relative area error, denoted as ‘*relAreaErr*’ is the error in surface area normalized by the analytical area; similarly, ‘*relVolErr*’ is the error in volume normalized by the analytical volume (see Appendix B for details on these calculations). The

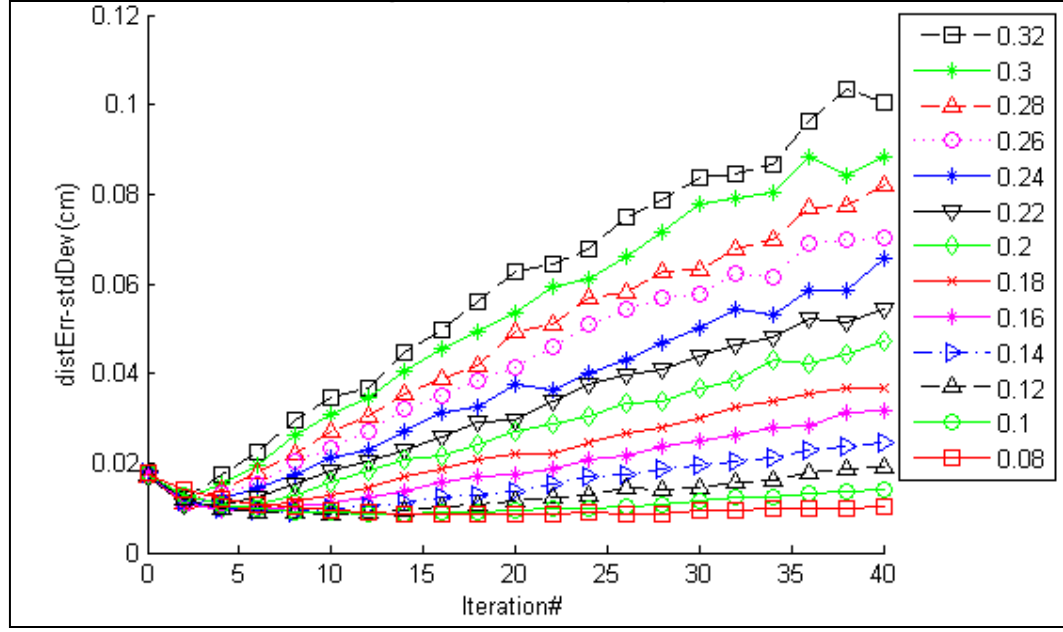
minimum distance of every node on the surface mesh to the analytical surface was calculated as explained in Section 2.3.9.



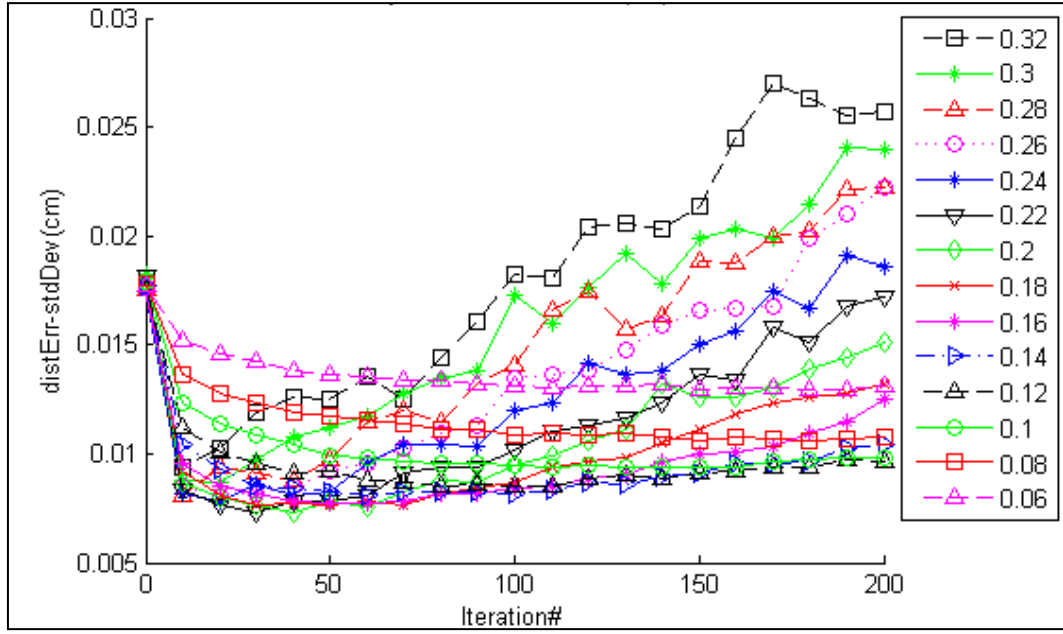
a)



b)

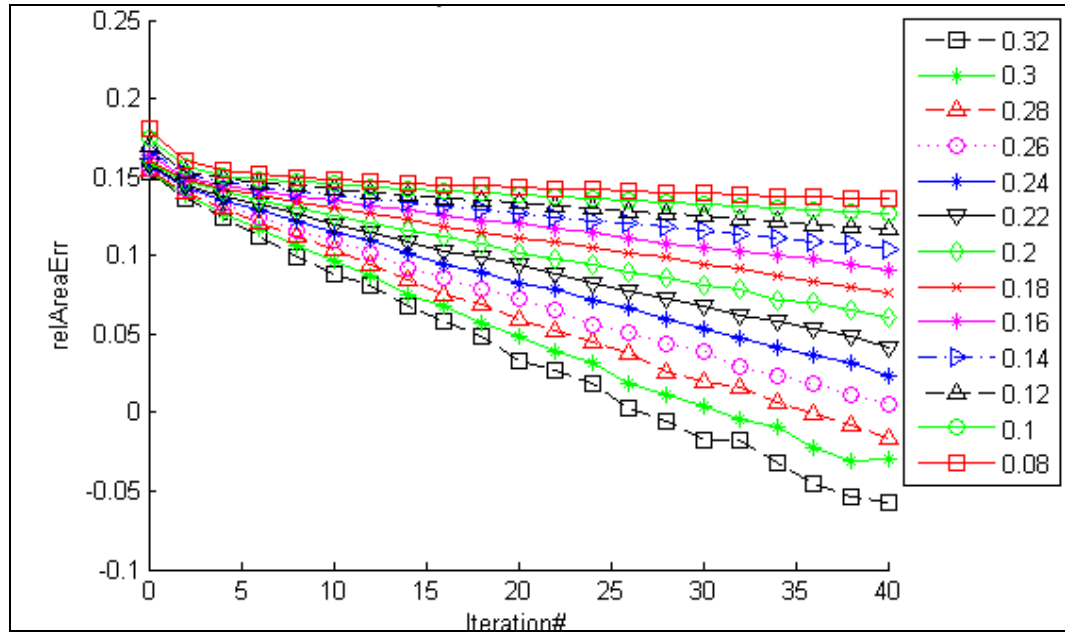


c)

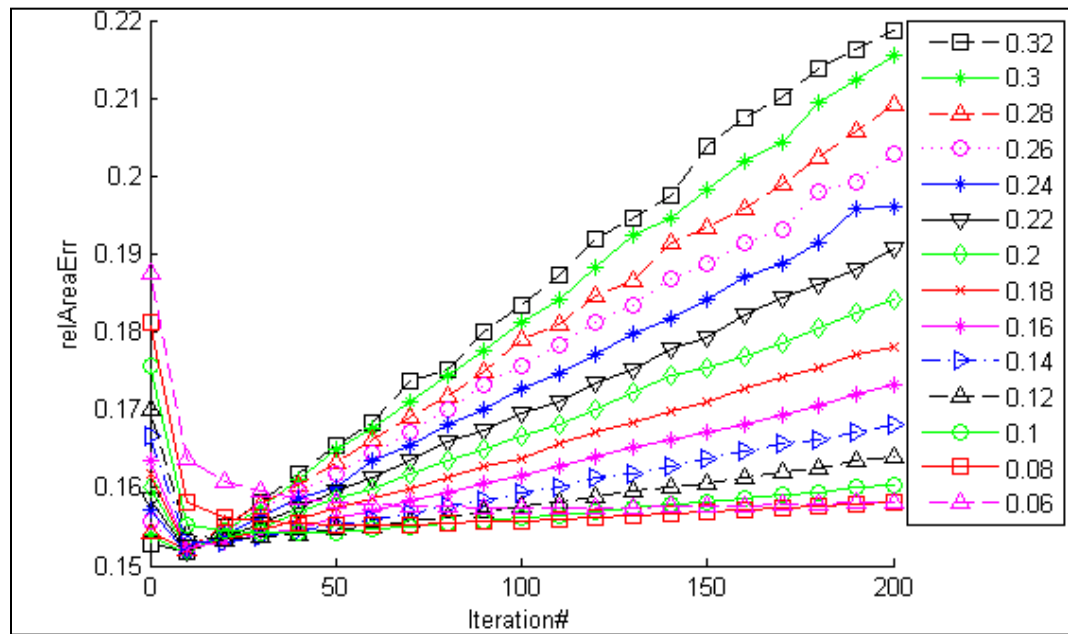


d)

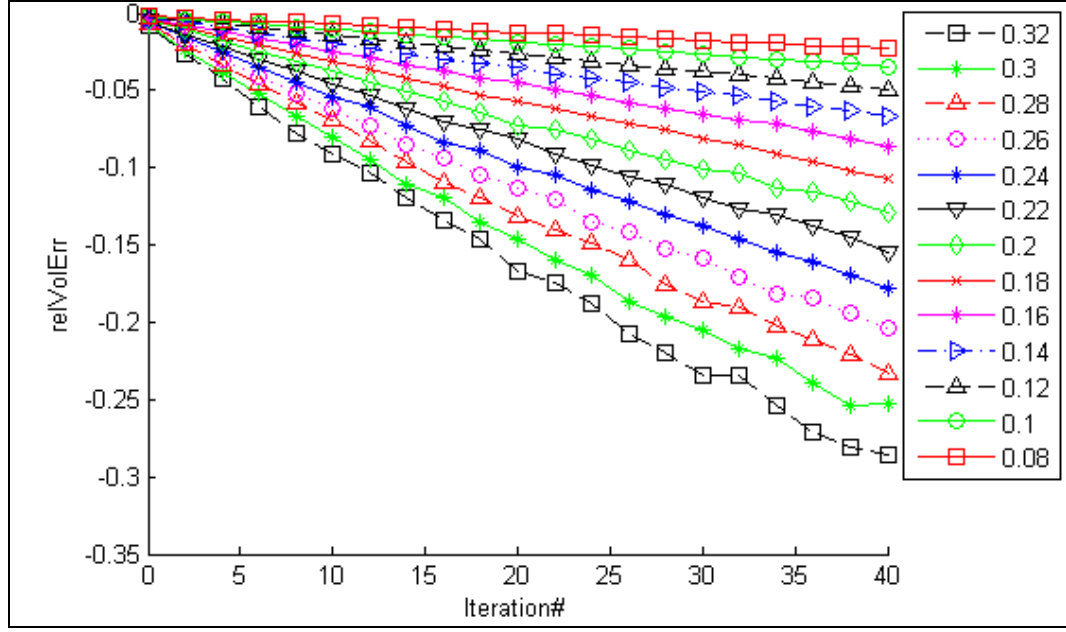
Figure 24: Comparison of Laplace and Taubin smoothing algorithms on geometric accuracy of phantom using distErr (cm) as a metric. x-axis shows number of smoothing iterations applied and legend denotes different element sizes. a) Laplace smoothing, y-axis: distErr (cm); b) Taubin smoothing, y-axis: distErr (cm); c) Laplace smoothing, y-axis: standard deviation in distErr (cm); d) Taubin smoothing, y-axis: standard deviation in distErr (cm).



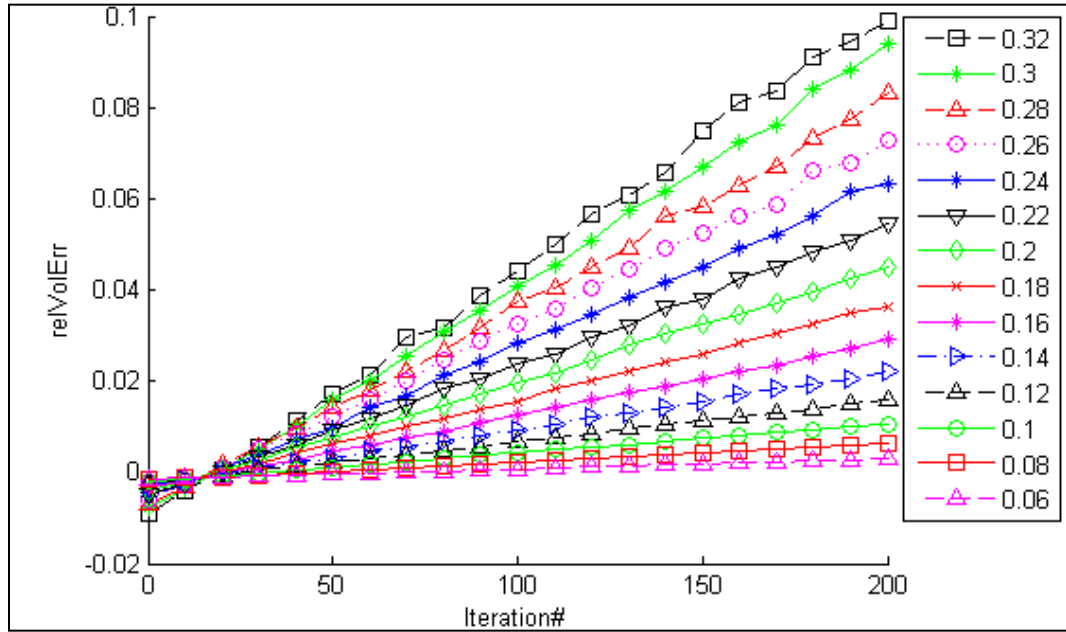
a)



b)



c)



d)

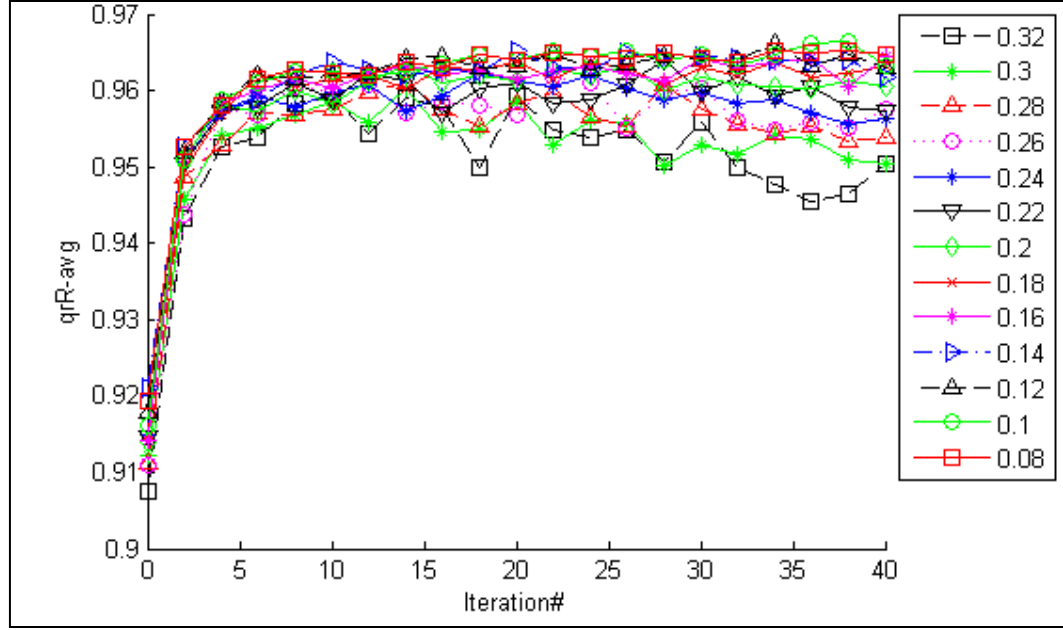
Figure 25: Comparison of Laplace and Taubin smoothing algorithms on geometric accuracy of phantom using relative error in area and volume as a metric. x-axis shows number of smoothing iterations applied and legend denotes different element sizes. a) Laplace smoothing, y-axis: relative area error; b) Taubin smoothing, y-axis: relative area error; c) Laplace smoothing, y-axis: relative volume error; d) Taubin smoothing, y-axis: relative volume error.

2.4.1.3.2 Surface mesh quality

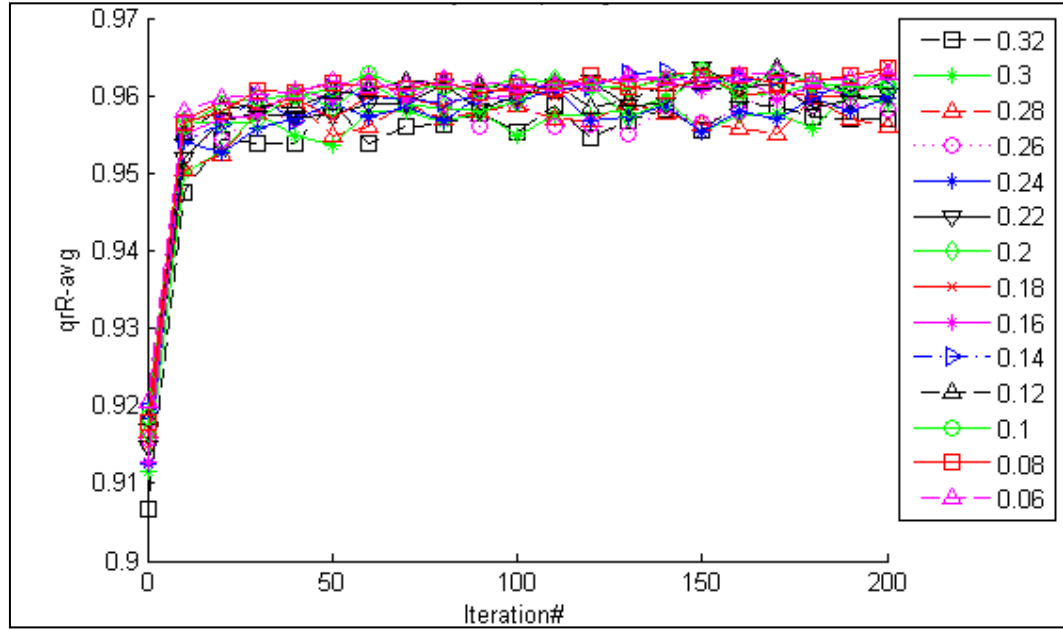
The r-R quality metric was computed after applying smoothing iterations to evaluate the effect of smoothing on surface mesh quality of the phantom geometries. As it was seen in Section 2.4.1.3.1, Laplacian and Taubin smoothing affect the geometrical accuracy of phantom surface. While most of the geometry metrics except maximum distance error (plot not included) degrade due to smoothing, the surface mesh quality mostly benefits by smoothing until it reaches a saturation value. Three different metrics for the quality of the surface mesh were evaluated: r-R, e-E, and R-e. r-R ratio is the ratio of 2 times the radius of the incircle to the radius of the circumcircle; e-E is the ratio of the shortest to the longest edge of the triangle; and R-e is the ratio of the circumcircle to the smallest edge. It was found that for most mesh sizes, these metrics follow a similar trend. However, we found r-R ratio to be the most sensitive to the presence of slivers, since the incircle radius decreases concomitantly with the increase in circumcircle radius. Hence, for the sake of brevity only r-R ratio plots are included (Figure 26).

2.4.1.4 Finalized settings and exemplary results for phantom

Based on the previous findings we consider 4-6 Laplace iterations to be optimum and 15-25 Taubin iterations to be optimum. Asym13 phantom with element size 16, 6 Laplace iterations, no Taubin iterations on left and Asym13 phantom with element size 16, no Laplace iterations, 20 Taubin iterations on right are shown in Figure 27. Voxel volume is calculated considering voxels at top and bottom slice to contribute only half the voxel volume each due to partial volume effect. Partial volume effect is not considered to be applicable on the side surfaces due to the fact that roughly the partial volume of boundary voxels missed while considered as outside will be equal to the excess partial volume coming from boundary voxels counted as inside the boundary.



a)



b)

Figure 26: Effect of Laplace and Taubin smoothing on surface mesh quality of the phantom. x-axis shows number of smoothing iterations applied and legend denotes different element sizes; y-axis: r-R ratio average (ideal value 1); a) Laplace smoothing; b) Taubin smoothing.

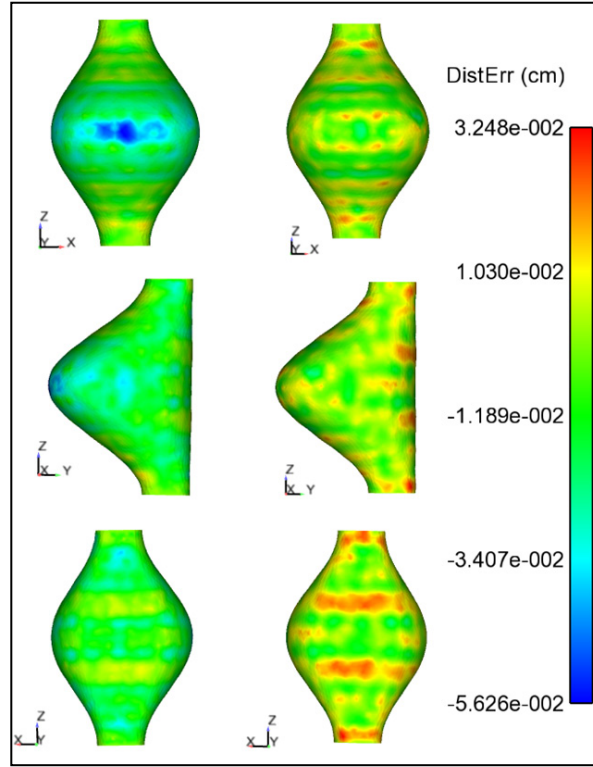


Figure 27: Comparison of smoothing action of Laplace and Taubin smoothing algorithms. Effect of 6 Laplace iterations shown in views on left; effect of 20 Taubin iterations shown in views on right. Laplace action is concentrated at high curvature and Taubin action more or less distributed however more inclined to pushing back outward.

Table 9: Effect of mask resolution on phantom reconstruction using finalized meshing parameters.

Quantity	Analytical	Asym13n			
		Measured Value		% Error	
		NormalMsk **	FineMsk †	NormalMsk **	FineMsk †
Area (cm^2)	113.097	128.9564	129.0009	14.022	14.0621
Volume (cm^3)	127.2324	125.0381	125.1116	-1.72	-1.6669
VoxVolume (cm^3)	127.2324	127.2476	127.5547	0.0119	0.2533
Dist error (cm)	--	0.0522	0.0532	--	--
Wall domain volume (cm^3)	20.2514*	18.4662	18.4736	-8.8151	-8.7786

* approximation; ** pixel spacing 0.075 cm, slice spacing 0.3 cm; † pixel spacing 0.75 cm, slice spacing 0.1 cm

Table 10: Mesh quality obtained for phantom using finalized meshing parameters.

Metric	Asym13			
	Min	Max	Average	Standard deviation
Det_J	6.8e-5	0.001571	0.000438	0.000199
Oddy metric	0.001202	11.0936	1.1224	0.7824
Condition #	10.5820	44.0315	16.0341	3.0659

2.4.2 Patient-specific studies

Analysis of different mesh configuration settings was done using a randomly selected patient-specific mask image set as an input to AAAMesh framework. Following sections elaborate these results.

2.4.2.1 Surface meshing

2.4.2.1.1 Effect of interpolation

The effect of the interpolation strategy for creating the distance field can be seen qualitatively in Figure 28. Further based on non-zero pixel count, voxVolume was found to be 158.4553 cm³ for this patient-specific geometry. Table 11 comparatively demonstrates area and volume evaluation. Interesting rationale behind overestimation of area by OD interpolation and overestimation of volume in case of 2D interpolation is presented in Section 2.5.3.4. Inability to capture surface correctly when it is almost parallel to 2D interpolation plane (image plane) can be noticed for 2D interpolation. In spite of being computationally expensive, 3D interpolation is seen to be more reliable method.

Table 11: Effect of distance field creation on geometrical aspect of patient-specific model.

Method	Area (cm ²)	Volume (cm ³)
Voxel derived	--	158.4553
0D	207.0673	157.7514
2D	199.7807	163.1807
3D	197.4413	157.3216

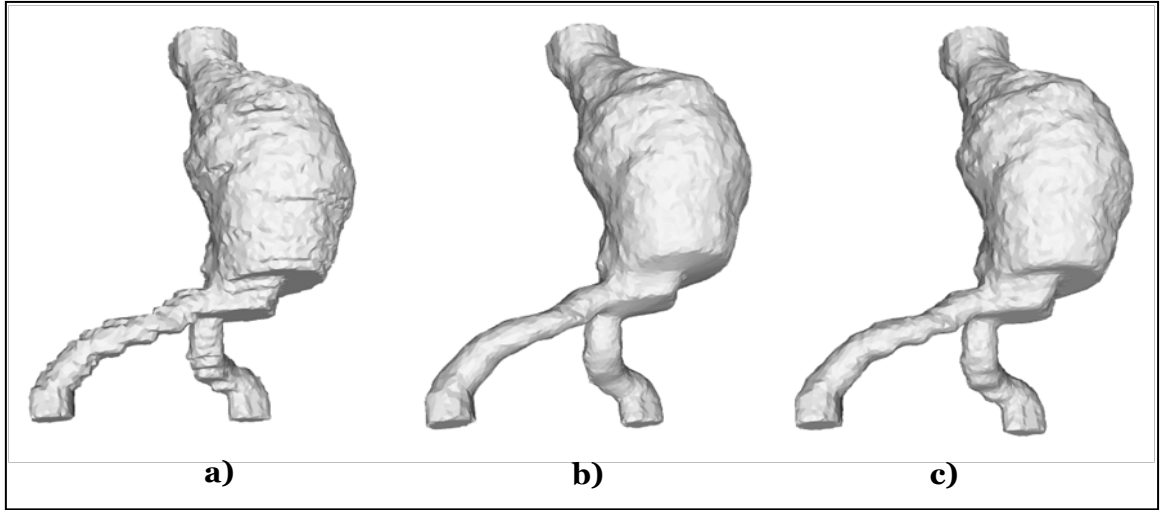


Figure 28: Effect of distance field creation strategy on the extracted surface of a patient-specific model. a) 0D interpolation; b) 2D interpolation; c) 3D interpolation (Euclidean).

2.4.2.1.2 Effect of smoothing on geometry

In case of patient-specific models we do not know the reference ideal surface for calculation of distance error (*distErr*) using the strategy implemented for idealized phantom used previously in section 2.4.1. Hence, exploration about smoothing effects on geometrical aspects are only limited to area and volume of the model. Figure 29 presents the changes in relative area and volume metrics with Laplace and Taubin smoothing iterations.

2.4.2.1.3 Effect smoothing on mesh quality metrics

Similar to phantom model average r-R ratio quality metric is again explored for comparative behavior when subjected to Laplace and Taubin smoothing iterations independently. Results are presented in Figure 30.

2.4.2.2 Qualitative evaluation of mesh quality

Mesh quality can be appreciated from Figure 31 and Figure 32. Complicated configurations involving exposed ILT faces at inlet outlet sections, ability to handle acute

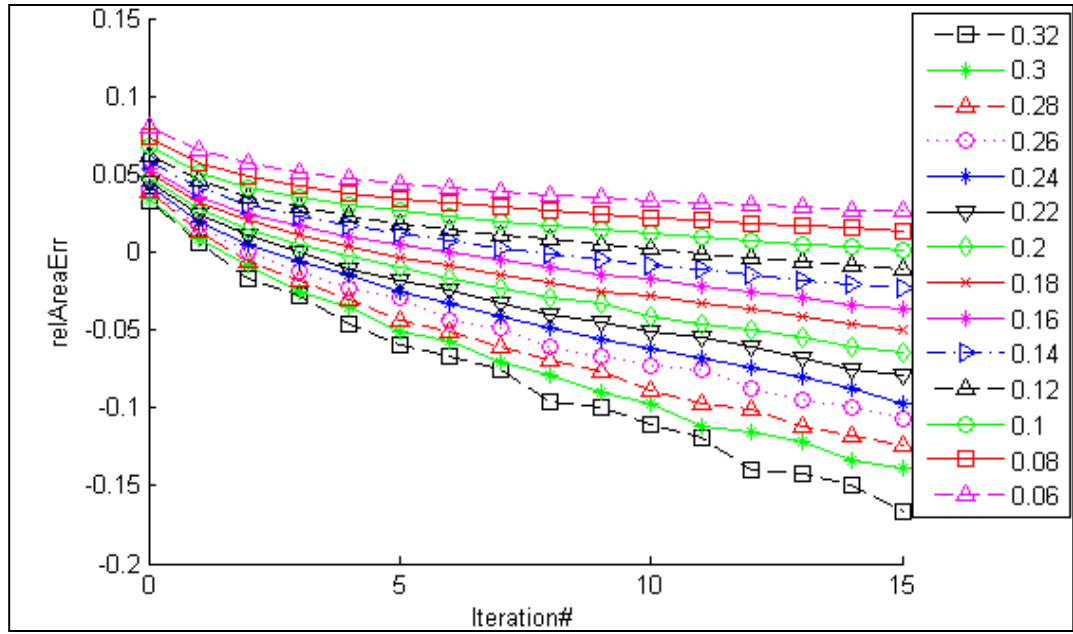
bifurcations without resulting in sharp corner, grid independent mesh, uniform distribution of elements, and controlled number of layer within wall can be seen.

2.4.2.3 Comparison with commercial code

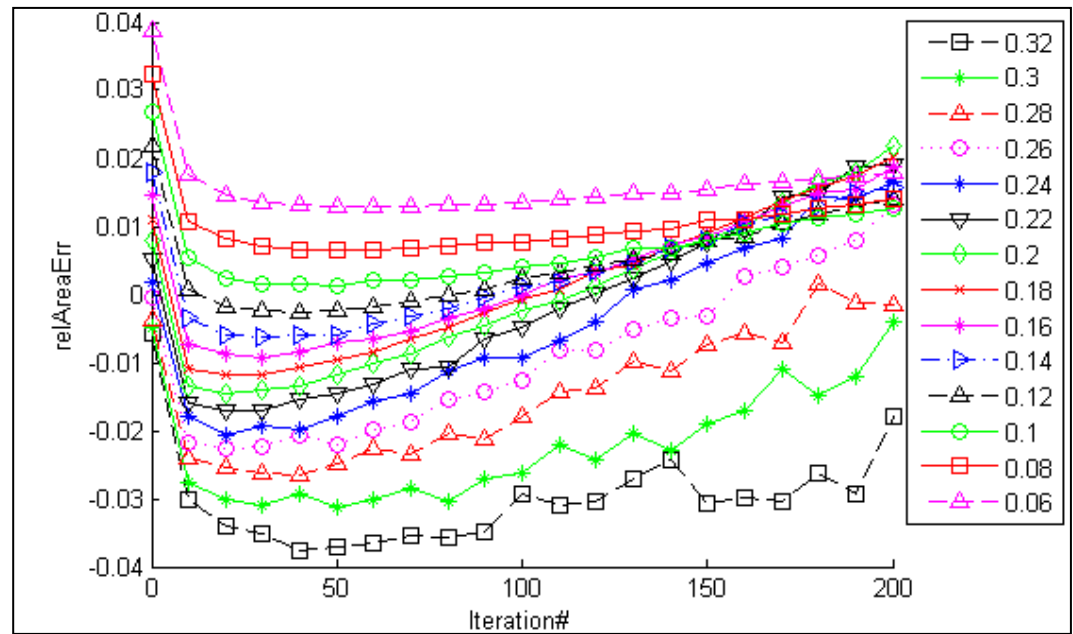
For a geometry selected from pool of ~100 segmented patient-specific masks, the following results were obtained using Mimics (see Table 12). Expert users of AAAMesh and Mimics were given task of obtaining mesh for given patient-specific mask image set with uniform and variable wall thickness with limitations of maximum 0.1 million total number of elements and objective of best quality mesh with minimum number of elements for wall domain and an average edge length approximately 0.125 cm. Mimics could not mesh the mask data directly for modeling variable wall thickness. Different quality metric were evaluated using Sandia National Laboratory's geometry and mesh generation toolkit Cubit® (version 13.2).

Table 12: Benchmarking with commercial code (values in bold font highlight sliver-free status; if slivers are present, range for worst 50 elements is reported)

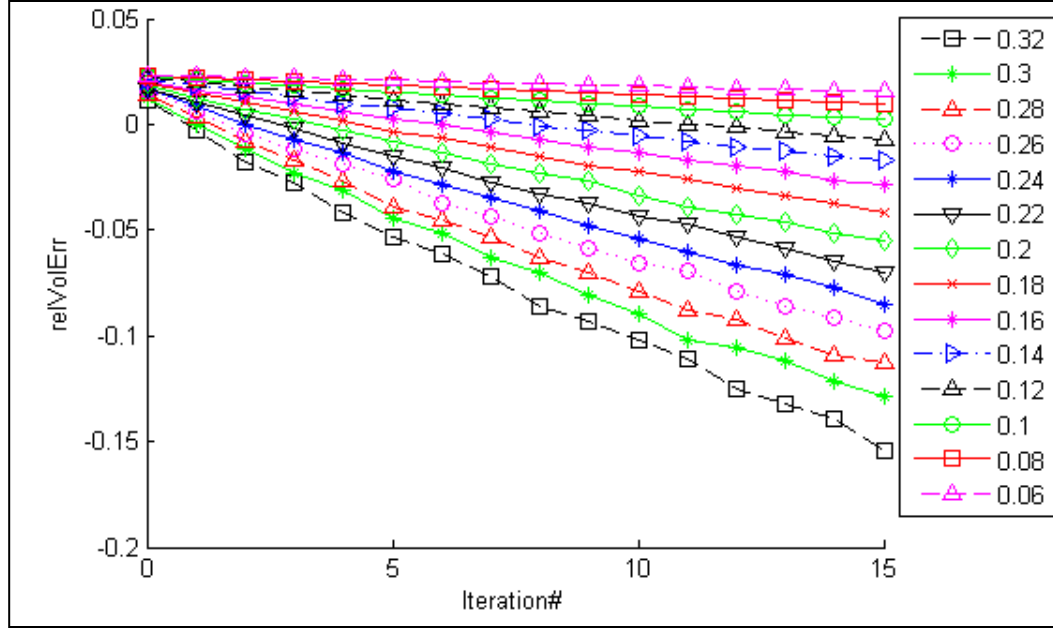
Metric	Type	Possible range	Acceptable range	Ideal	Uniform*		Non-Uniform*	
					AAAMesh	Mimics	AAAMesh	Mimics
Distortion	Hex	[0,1]	[0.6,1]	1	0.3250-0.4067	--	0.2951-0.4008	FAILED
	Tet	[-1,1]	[0.6,1]	0	--	> 0.6	--	
Scaled Jacobian	Hex	[-1,1]	[0.5,1]	1	0.2330-0.3835	--	0.2150-0.3920	
	Tet	[-1,1]	[0.2,1]	1	--	0.0199-0.0461	--	
Shape	Hex	[0,1]	[0.3,1]	1	>0.3	--	>0.3	
	Tet	[0,1]	[0.2,1]	1	--	0.1088-0.1342	--	
Condition	Hex	[1,inf]	[1,8]	1	<8	--	<8	
	Tet	[1,inf]	[1,3]	1	--	14.061-8.286	--	
Elements					64,470	109,419	64,710	



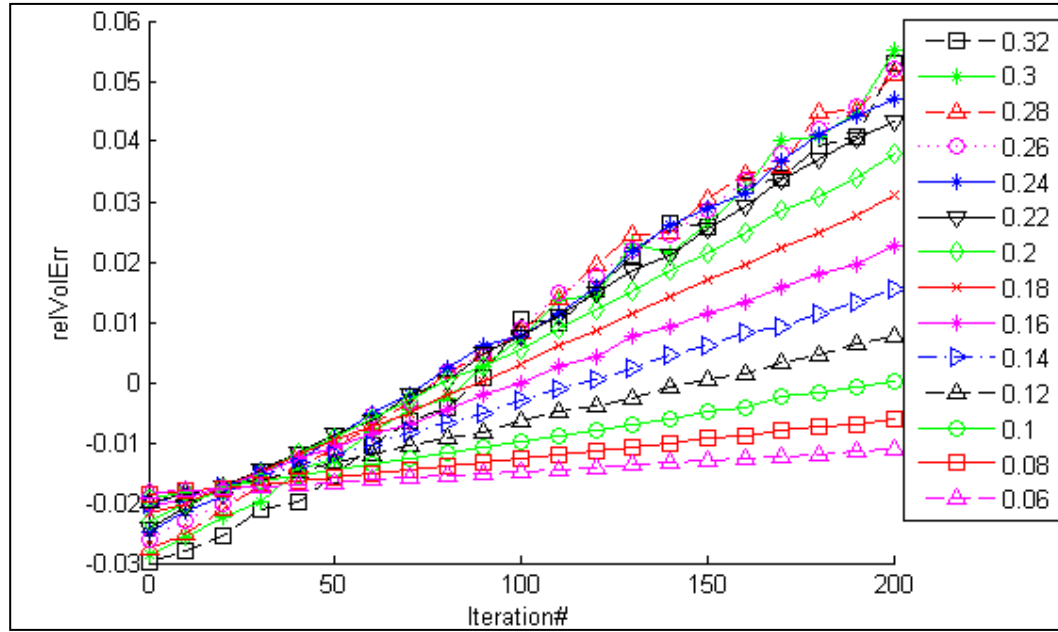
a)



b)

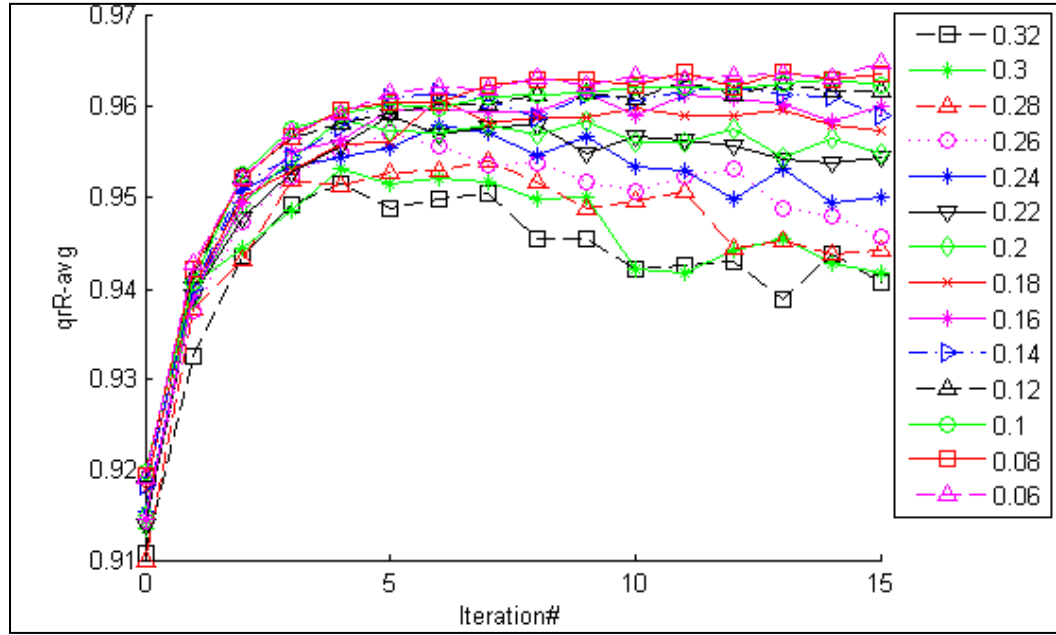


c)

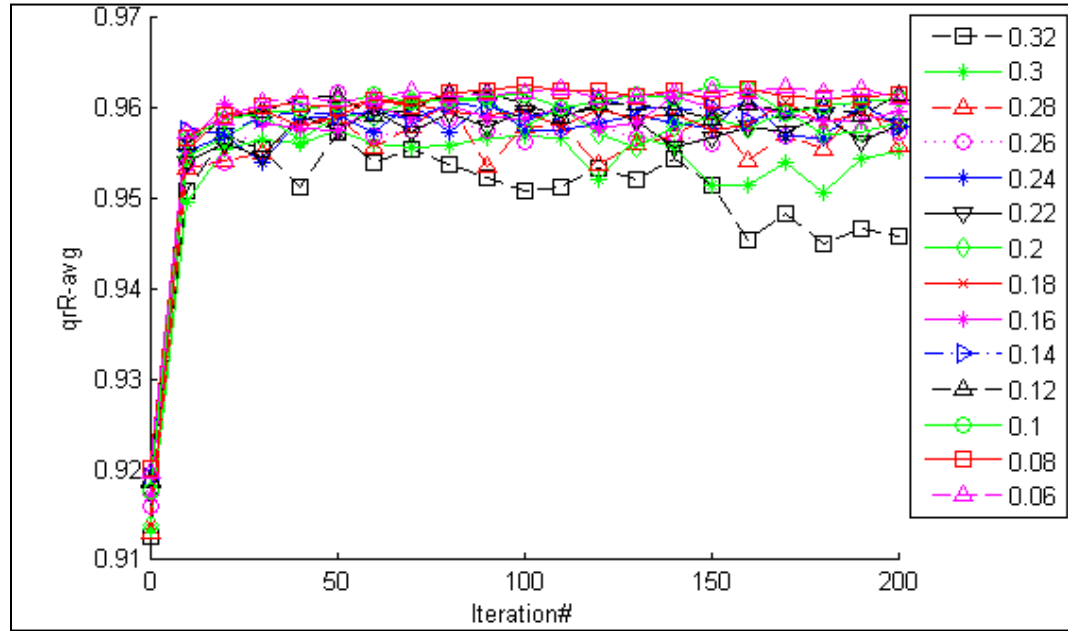


d)

Figure 29: Comparison of Laplace and Taubin smoothing algorithms on geometric accuracy of patient-specific model using relative error in area and volume as a metric. x-axis shows number of smoothing iterations applied and legend denotes different element sizes. a) Laplace smoothing, y-axis: relative area error; b) Taubin smoothing, y-axis: relative area error; c) Laplace smoothing, y-axis: relative volume error; d) Taubin smoothing, y-axis: relative volume error.



a)



b)

Figure 30: Effect of Laplace and Taubin smoothing on surface mesh quality of the patient-specific geometry; x-axis shows number of smoothing iterations applied and legend denotes different element sizes; y-axis: r-R ratio average (ideal value 1); a) Laplace smoothing; b) Taubin smoothing.

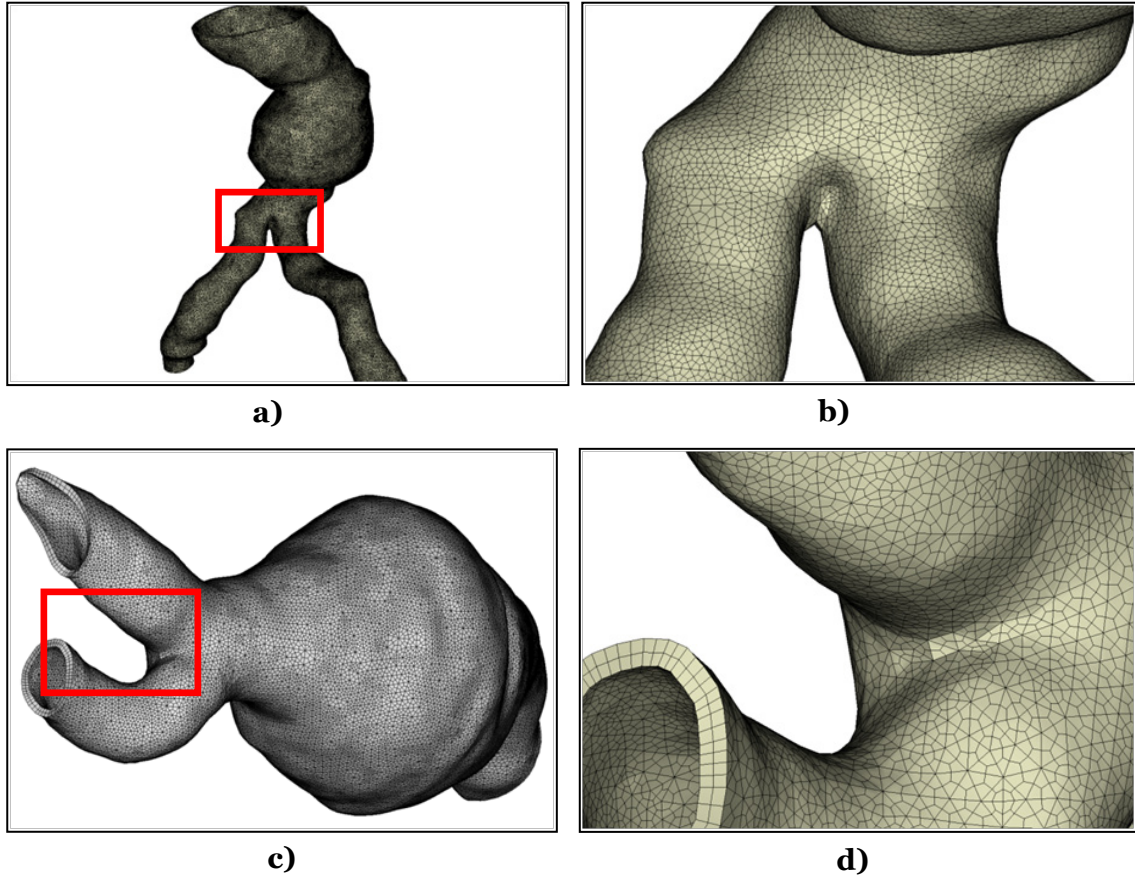


Figure 32: AAAMesh ability to handle acute bifurcations and robustness for handling practical scenarios; (a) case 1, (b) case 1 zoomed at bifurcation, (c) case 2 with free form ends, (d) case 2 zoomed at bifurcation.

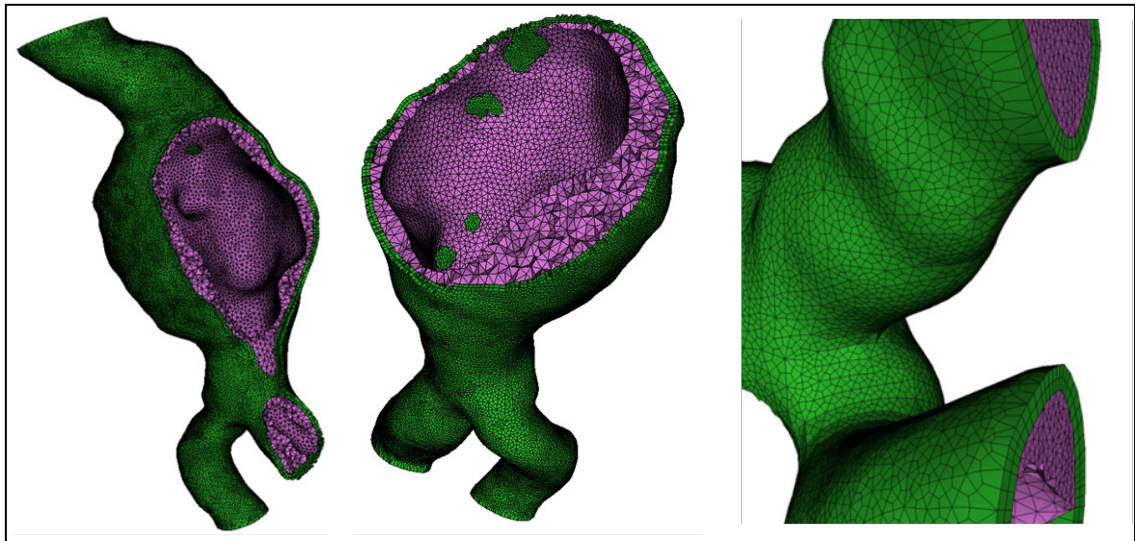


Figure 31: AAAMesh generated multi-domain mesh of aneurysm. Wall is formed by hexahedral elements and ILT by tetrahedral elements. It highlights complex ILT configuration having some part of it exposed at the outlet cross section. Ends are forced to be flat.

2.5 DISCUSSION

2.5.1 Contribution

In this work a novel MATLAB based framework for multi-domain volume mesh creation was presented and smoothing aspects were explored in detail. We also presented a systematic and scientific approach to verify a procedure of surface mesh extraction from volume data and deciding optimal number of smoothing iterations. Different frameworks have been proposed earlier, however, no other work except [172] presented a comprehensive study for evaluating accuracy of results using a known input in order to assess influence of image data and smoothing. One of the important capabilities of presented technique is the ability to incorporate thickness with node-to-node control. Also, surface extraction process as applied to biomodeling is studied in detail here. Overall we observe that error is not exactly deterministic but behavior shows trend albeit with some sporadic fluctuations. However, at the same time, framework is robust to handle challenging cases. Interesting behavior of geometry distortion with two distinct slopes of standard deviation change with smoothing iterations as seen in Figure 24 c) and d), Figure 25 a) and b), Figure 26 a) and b), were noticed and used for deciding optimal smoothing iterations.

We provided extensive verification and characterization work for the proposed framework. Recently the need for standards and benchmarking procedure has been felt in bio-modeling industry [147] and our work may pave way for standardization and benchmarking processes in biomodeling, especially with respect to smoothing iterations based on the interesting observations noted previously. Image generation code is first step in verification. It should be noted that the purpose is to check accuracy of the computational framework. Since, computational meshing process starts from masks it

appears to be more natural choice as a starting point. This aspect is different compared to previous extensive approach used by Antiga et al [172]. We consider that as an important work towards implementation of code, however, for performance evaluation and characterization of a code itself, it is more appropriate to use phantom model of known curvature and surface especially since smoothing effects are very small but cumulative over iterations. This way errors creeping in due to manufacture of physical phantom and measurement are avoided. As seen in Table 5, Table 6, and Table 7 volume is used as an indirect metric to verify that the generated masks for phantoms are correct over often observed range of dimensions in AAA.

2.5.2 Salient features

2.5.2.1 *Node-to-node variable wall thickness and thinner walls*

AAAMesh has ability to incorporate node-to-node variation in wall thickness. It should be noted that the thickness values are incorporated during node creation and can be sourced from any other input and are not necessarily from image data used for surface extraction. Due to such flexible approach, it is possible to couple input from any advanced resolution technique such as black-blood MR that specifically provide accurate spatial distribution of thickness information. It is also immune from any deviation due to mesh smoothing approach, hence, specified thickness is 100% ensured in final FE mesh. Such precision is valuable since a typical anatomical geometry consists of relatively larger bulk enclosed by relatively thinner wall that contributes most of the strength and has different material properties e.g. vasculature, bones with thinner annular region of cortical bone and bulkier cancellous region at core, biological optical lenses, cells, nucleus, bladder etc.

2.5.2.2 Integrated approach

The proposed framework starts with 2D mask information and leads to 3D volume and surface mesh information for multi-domain objects. It is amenable to quick integration with segmentation codes that would provide input for it and also can facilitate output for Finite Element solvers. Such comprehensive approach is targeted at clinical use since major hurdle in clinical implementation is the fact that all different steps are performed by different proprietary software that create more difficulties e.g. increased costs of licensing, probability of errors during information transfer, and need for additional technical expertise in the field of engineering. User friendly GUI facilitates easy user interaction and meshing is single click process even though process pipeline involves four different codes and complex sequence of operations based on intended output.

2.5.2.3 Robustness imparted by non-parametric framework

Except for splines used to define edge, no part of our proposed approach of image-based mesh generation uses mathematical representation of any part of geometry directly for mesh generation and mostly this framework is based on tessellations. Hence, it is more robust to handle practical cases observed in clinical practice. Most of the biological objects have a configuration that is characterized by varying shapes and non-mathematical geometry. Robustness of framework is essential to handle multiple and unknown number bifurcation. In this framework, there is no assumption regarding geometrical topology except that we assume all inlet and outlets are located at top and bottom slice. Also, due to the complicated shapes, it is very important that such framework be robust to handle random, non-parametric shapes.

2.5.2.4 Grid independent mesh pattern

Grid independent mesh pattern which is very important feature since the vasculatures are circular geometries where as typical medical image consists of rectangular coordinate

system. As seen earlier in Figure 11, most commercial softwares based on variants of marching cube algorithms result in rectangular pattern in final mesh. The grid independent mesh characteristics offered by AAAMesh enhances robustness of the framework to handle geometries in any orientations regardless of machine coordinate frame e.g. highly tortuous aneurysm or horizontal branch can be modeled.

2.5.2.5 Multi-domain meshing complexities

2.5.2.5.1 Spatially separate, unpredictable number of ILT

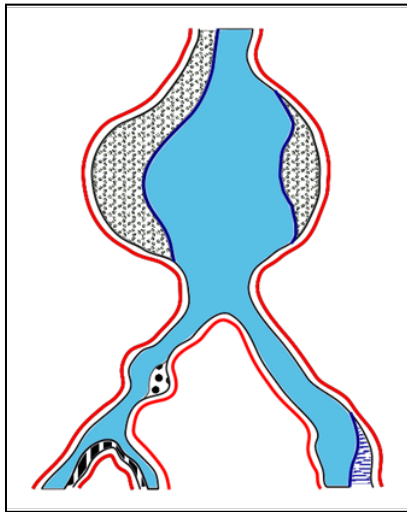


Figure 33: Multi-domain meshing challenges.

AAAMesh can handle a number of complexities especially due to multiple ILT domains and multiple bifurcations. To elaborate this, few possible configurations of ILT lump are depicted in Figure 33. Writing robust software is necessary because of the very fact that number of ILT lumps, their shapes and locations are very random. One can observe few configuration given in schematic where the ILT can be completely inside as it appears in iliac aneurysm or it may be exposed to inlet plane or outlet plane, or it may

have multiple faces open to different planes, it may be present all around the circumference or may pad only part of it.

In the proposed framework, the lumen mesh and inner wall mesh are created at different instants of time and by different approaches. Hence, it is not necessary that they will exactly overlap at the lumen-to-wall interface throughout. This may result in some thin isolated ILT regions resulting from volume trapped in between those surfaces. We provide an option to eliminate such small regions by specifying the maximum

number of them as well as the lower limit of volume of an individual region. All spurious regions are reassigned to the lumen or thrombus domain depending on the user's choice.

2.5.2.5.2 Domain interfaces - identification and management

In addition to multi-domain meshing complexity, it is tedious to keep track of different interfaces e.g. as shown in Figure 33 we may have multiple ILT lumps say ILT1, ILT2, ILT3, and ILT4. Now considering Wall, Lumen and free surface we can list a large number of facesets e.g. Wall-to-ILT1, Wall-to-Top, Wall-to-Bottom-Inlet1, Wall-to-Bottom-Inlet2, ILT2-to-bottom and so on. Even though not depicted in Figure 33 it is possible to have single ILT having free surface at top and bottom. The domain interface information is needed later on for applying boundary conditions. Also, it should be noted that the Wall-to-lumen interface need not be always spatially continuous. Even though it is easy to separately identify each single continuous patch, in case of different discontinuous Wall-to-Lumen patches, we preferred to retain them under same faceset tag keeping in mind that it would simplify application of boundary conditions from clinical implementation point of view. Spatially discontinuous patches such as different outlets and inlets were identified, even though those come under same category as lumen free surface since it would be needed to facilitate individual boundary conditions. Thus, we need a systematic approach which should be consistent all across different modules and techniques used and also under different scenarios targeted e.g. Wall-only, wall-only-surface-mesh, lumen-only etc. We have developed internal data organization scheme that facilitates this as well as helps to track and locate facesets.

2.5.2.5.3 Triple junction

Another complication is modeling the region where more than two domains are joining e.g. consider three different scenarios for ILT adhesion to wall from inside as shown in Figure 34. In this case it is necessary to decide smoothness priority for each domain

based on which we may have different resulting geometry. These nuances are likely to have a significant influence on the wall stress distribution e.g. study of calcification done previously has highlighted this aspect [189]. In presented work, Case C has been targeted. However, sometimes it may be combination of case A and case C in case local tunneling occurs

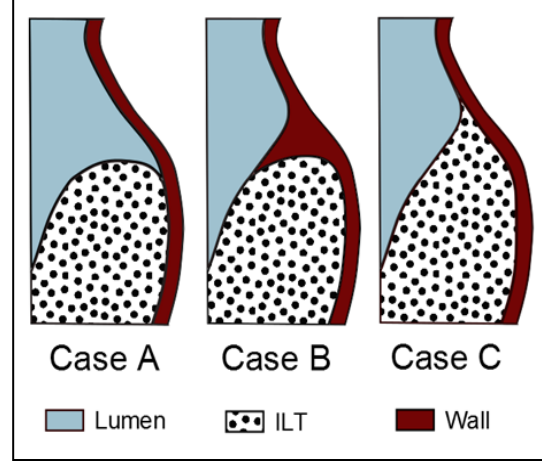


Figure 34: Different approaches to model ILT adhesion to wall.

and we are forced to reallocate few volume elements to lumen. GUI also facilitates an option for assigning forced reallocation to ILT. Ultimately, mesh will have non-sacrificed wall surface continuity in any case and it is important since wall is main stress bearing component and current image does not have resolution to capture three domain interface with confidence anyway.

2.5.2.6 Other distinct advantages

Proposed framework provides following distinct advantages:

- Hexahedral or wedge elements without degenerated elements that are with two or more coinciding nodes. Especially in case of hexahedral element not a single degenerated element needed.
- Robust to handle randomly placed ILT and random number of them.
- Node-to-node contact ensured for wedge-tet configuration. This will reduce errors involved in interpolations during load transfer in fluid-structure-interaction simulation.

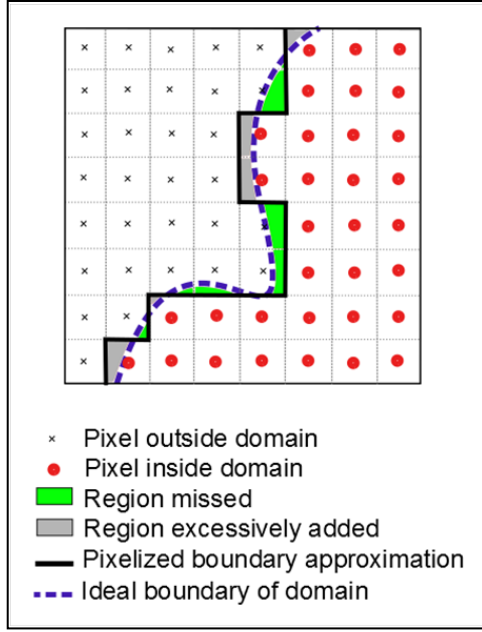


Figure 35: Schematic explaining why voxel based volume estimation closely approximates actual volume

- No requirement of consistency in concavity/convexity of object exterior surface. In case of simple geometries where this assumption of no concavity or convexity is valid, one can use coordinate transformation operations to generate more topologically similar boundaries for outward normal direction or surface offset.

- Internal point selection for volume meshing of thin-walled domain as per approach proposed in [176, 177] is completely done away with and so difficulty in locating internal point as well as non-uniformity in surface points

spacing obtained by ray tracing are avoided.

- Parallelized code for computationally intensive sections of code in MATLAB. Especially, for image operations multiple parallel executions of code are implemented. Steps defined in matrix operations (vectorized coding) ensure better resource utilization.
- Multi-layered material model is possible since wall mesh topology is amenable for assigning different material properties for each layer.
- With few modifications, this wall-E module of framework can offer to implement modeling of support through tendons by representing them in form of a spring using information about local normal vectors. This approach is expected to be computationally less cumbersome than modeling support through contact conditions.

- This framework builds up geometry using ground up approach. Once domain or component mesh is generated it is not dimensionally altered by subsequent meshing process. Every next step is built on top of previous one systematically. These aspects auger well for further improvements and modifications in the framework by offering select interface nodes along the operation sequence.

2.5.3 Distance field interpolation

2.5.3.1 *A note on slice-thickness vs. slice-spacing*

It should also be noted that as per the DICOM format convention, DICOM header field under tag description 'Slice Thickness' i.e. field 0018-0050 is often confused with spatial spacing between neighboring slices. It is actually a finite value of the thickness of a slab that is considered from the object under scanner while creating image which represents it in a plane of infinitely small thickness. Actual spatial distance between neighboring slices is in fact difference between their values under 'Slice Location' tag in DICOM header i.e. values under DICOM header field 0020-1041. In following discussion, this difference is referred to as slice spacing on the similar lines to that of pixel spacing. Even though often 'Slice Thickness' is set to be equal to the difference of 'Slice Location', it should be noted that they are not equivalent.

2.5.3.2 *Rationale for correct volume estimation without surface reconstruction*

Based on the consistent results in Table 5, Table 6, Table 7, and Table 9 we can conclude that image generation code is accurate and volume of object can be accurately estimated, even in case of patient-specific geometry, by simply considering voxel volume provided that the pixel resolution is sufficient compared to average local feature size of geometry. Schematic in 2D given in Figure 35 explains why voxel volume approximates actual

volume. As the number of voxels increases, the probability of excess volume (grey) addition becomes equivalent to that of the missing volume (green).

2.5.3.3 Need for exclusive routine for anisotropic grid 3D interpolation

In practical scenario where often slice spacing is larger than the pixel spacing, resulting

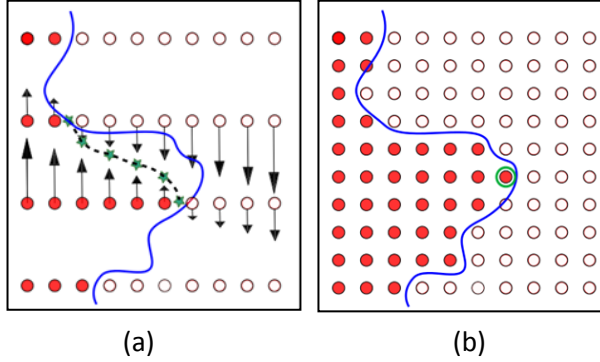


Figure 36: Schematic illustrating 2D distance field creation strategy and anisotropy in grid spacing. Filled circle is inside while unfilled is outside object and arrow length represents distance field magnitude using 2D interpolation with sign change near boundary. Green stars approximately locate zero and dashed black line shows corresponding reconstructed erroneous surface. Green circle locates one location where error would be more if 2D interpolation is used instead of 3D - a) depiction of 2D approach with actual anisotropic grid spacing b) depiction of ideal uniform grid spacing.

in an anisotropic voxel grid that needs special attention during distance field creation. Schematic in Figure 36a shows a vertical slice in stacked image voxel grid with larger spacing in vertical direction (Slice Spacing) compared to that in horizontal direction (Pixel Spacing). In-built routine 'bwdist' in MATLAB (version R2011a) is based on difference in voxel indices and not on Euclidean distance obtained after accounting for grid spacing anisotropy which is often the

case in medical image data.

Prior work [176, 177] circumvented this by working in voxel space entirely and reverting back in Euclidean space by scaling after surface extraction, however, such approach would degrade surface mesh element quality which was actually optimized for voxel space and not for Euclidean space. Alternative of creating and inserting additional dummy slices to obtain isotropic grid has additional complexity that adds more computational load as well as errors due to ambiguity about interpolation of discrete

data as in case of segmented schematics shown in Figure 36b would call for more sophisticated algorithms.

2.5.3.4 Comparison of 0D, 2D, and 3D interpolation

If one considers the horizontal part of boundary, it could be seen that 2D interpolation errors would be more apparent especially with larger difference in slice spacing and pixel resolution (see difference in dotted black line and blue line Figure 36a). Figure 22, Figure 23, Table 8, and Table 11 show effect of distance field creation approach. It is seen that 3D approach is better amongst all. However, it comes with added computational load. We also observe that volume can be approximated with pretty much accuracy for the curvature and pixel resolutions used in case of phantom whereas area is found to be larger.

Roughness in the surface is seen in 0D case. It results in overestimation of surface area (Table 8 and Table 11). Section 2.5.4.1 elaborates rationale behind it. It is being somewhat dampened in case of phantom case (Figure 23) due to the fact that geometry surface is ideal and smooth even in higher order derivative in space. However, as seen in Figure 28, in complex real life patient-specific case this difference is enhanced. Previously mentioned explanation regarding horizontal surface approximation error with 2D distance field applied to anisotropic voxel grid spacing can also be seen here with larger error in volume for 2D distance field creation approach (Table 8 and Table 11) compared to 3D and 0D methods. Ability to capture horizontal surface will also be limited in case of 2D approach. Figure 36a shows distance field schematically assuming that surface lies at zero value of scalar function. It can be obtained both in 2D as well as in 3D. However, considering the horizontal section in case of anisotropic grid spacing one can imagine that the zero isosurface will drift slowly where as 3D consideration

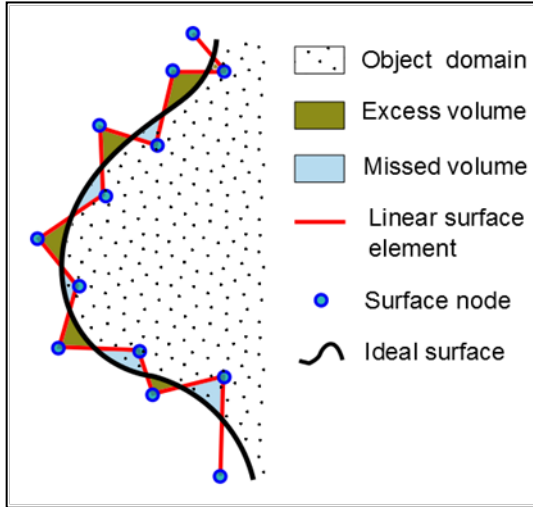


Figure 37: Rationale behind volume accuracy and overestimation of surface area.

would avoid that. This can also be appreciated by observing horizontal surface region in output of 2D and 3D distance field approach shown in Figure 28.

Before moving to a section that describes in detail smoothing due to Laplace and Taubin iterations, it should be noted that as it was seen qualitatively in surface roughness shown in Figure 23 and Figure 28, distance field creation step can

be seen to impart smoothing by itself.

2.5.4 Effect of smoothing iterations

Some very interesting conclusions can be arrived at after noticing results related to the smoothing operation. However, it should be noted that all this discussion pertains to

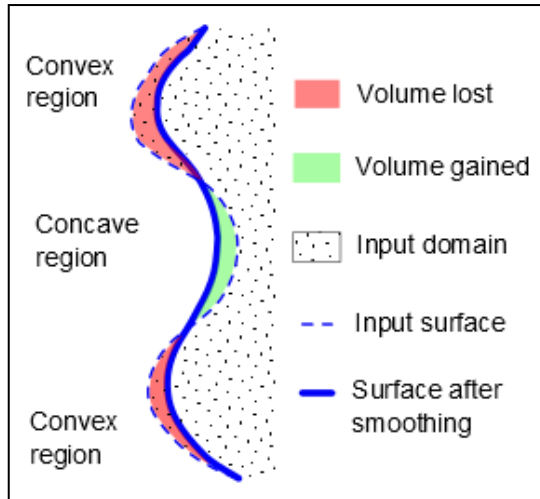


Figure 38: Volume as a shape distortion metric – regional changes may counteract each other.

approximation of a curved surface by a set of linear straight facets. Also, the measured distance error (*distErr*) is cumulative effect of meshing error as well as pixelation error while generating image. The edge nodes (end nodes in 2D schematic) were constrained to move within original plane. This might cause small effect. We expect that it should be negligible and our conclusions would apply even in case of

surface mesh smoothing where there are no edges or where edge nodes are allowed to move out of the plane.

2.5.4.1 Rationale for larger value of mesh derived area

The first observation from Table 8 and Table 11 is that regardless of smoothing algorithm we have larger relative error in surface area calculation than that in volume as well as mesh derived area being always larger than analytical value. Though not ideal, volume can be seen as a better criterion instead of surface area, to evaluate efficacy of code since it agrees well with expected analytical values. We suggest that this observation is applicable irrespective of individual shape of the object being reconstructed as well as type of facet (e.g. triangular, quadrilateral, etc.). This can be rationalized as an effect of piecewise-linear approximation of curved surface as shown in Figure 37. It is seen that volume error shown by shaded areas will cancel out where as area which is represented by the total length of red line in this 2D schematic will be higher than its ideal value which will be equal to length of black line.

2.5.4.2 *distErr* – an ideal metric to evaluate shape distortion

For rigorous verification, we need to have more appropriate metric to measure how closely generated surface approximates the targeted ideal surface. Area and volume metric are easy to evaluate, however, those are not specific to shape. Hence, we focused on *distErr* as the metric. Following sections describe more on this.

2.5.4.2.1 Unreliability of volume and area as a shape distortion metric

Volume and area should be considered only as surrogate markers due to the unreliability involved in using those as shape distortion metrics to evaluate smoothing effect. Section 2.5.4.1 explained about difficulty in correctly evaluating area from surface mesh using PLC. Additionally, it is possible to have two different geometries having the same area, e.g. consider the exterior surface of a pear in 3D. It is possible to have a cylinder of the

same height and volume of the original pear, or the same height and surface area as that of the pear.

In addition, volume as a shape distortion metric will be appropriate only in case of geometries that are dominated by either convexities or concavities. To make it clear one may consider shape of an hourglass as shown in Figure 38. Since, regional volume changes in locally concave and convex regions may counteract, smoothing iteration influence on overall volume change does not precisely quantify shape distortion or discrepancy in given two surfaces.

2.5.4.2.2 *distErr* metric

Smallest possible distance of a surface mesh node, measured in 3D, from the target surface is addressed here as *distErr*. Details about its evaluation were described earlier in Figure 20 and Section 2.3.9. Elaborate framework for testing was created which included creation of test mask image data for known analytical shape and procedure for evaluation of normal distance of reconstructed surface from analytical virtual surface in 3D.

2.5.4.3 *Sensitivity of distErr metric to smoothing*

Smoothing is needed to eliminate roughness in reconstructed surface which is not desired given that most biological organs have continuous smooth surface. However, excessive smoothing may distort the geometry itself. The *distErr* standard deviation plotted in Figure 24 c) and d) can serve as a better metric that collectively represents both surface geometrical accuracy and surface roughness. Hence, the minima of this plot could be used as an indication to answer the question - 'how smooth is smooth enough'.

Sensitivity of mesh to smoothing is dependent on mesh density also. It can also be noted that the average *distErr* in Figure 24 a), b) had a constant slope i.e. linear

behavior with respect to number of iterations. Hence, it can be represented by a family of curves represented by $y = m_{sz}x + C_0$ where slope m_{sz} is a function of size of element and the geometry shape. From plot it is clear that as the mesh becomes finer the slope is closer to zero. Thus, coarse mesh is more sensitive to smoothing iterations. Also, in case of Laplace smoothing, the sign of this slope will be positive for concave geometries and negative for convex geometries. On the other side, for Taubin smoothing with same parameters as used here it will be the opposite. This observation could pave way to the concept of a constant that can be assigned as a characteristic for every mathematical shape that can indicate proportion of convexity relative to concavity when seen globally e.g. such a constant would be zero for equally convex and concave shape.

Comparative exploration of Laplace and Taubin iterations is interesting as shown in Figure 27. For parameter k_{PB} and λ set to 0.1 and 0.5 respectively, it is observed that Taubin iterations are effectively dilating the phantom. It is evident from the positive slope of average distance error plotted against iteration in Figure 24b and for relative volume error plotted against number of iterations in Figure 25b. Laplace smoothing is effectively shrinking the surface (Figure 24a, Figure 25a). However, volume is a global metric and does not indicate regional details about the changes caused by smoothing in addition to previously elaborated argument that there is possibility that compounding effects at convex and concave region may be misleading. Hence, the smoothing effect needs to be visualized as shown Figure 27 where color coded regional distribution of *distErr* in three view of phantom is provided. It can be seen that the left column, that represents Laplace smoothing effect, shows that the nodes in the highly convex zone are displaced more compared to rest of the geometry. Thus, Laplace smoothing action is concentrated at high curvature region as expected. Also, most of the region shows

negative value indicating that surface has shrunk. On the other side, the Taubin smoothing effect, shown in right column shows *distErr* inclined towards positive side i.e. outwards and also it is occurring strongly at multiple distributed locations. Even though it should be noted that there are multiple regionally distributed negative *distErr* locations as well, however, with relatively lower magnitude.

2.5.4.4 Sensitivity of area/volume metric to smoothing

The discussion so far was primarily based on *distErr* metric. However, it is possible only in case of surfaces for which exact mathematical equations are available or true geometry as imaged is known. Frequently, in case of arbitrary shapes such as in clinical in vivo imaging, this gold standard reference is not possible. Hence, it is necessary to explore other surrogate markers for deciding smoothing iterations. Area and volume are such quantities that can be readily evaluated for most of the tessellations irrespective of complexity involved in shapes. However, use of volume as metric needs that the shape should be either predominantly concave or convex.

Figure 25 and Figure 29 show behavior of error in these quantities normalized with some reference values. Relative volume error changes monotonically with smoothing iterations. In case of relative area error however, it is observed that during few initial iterations area decreases at high rate (primary slope) and then it changes with some secondary slope. The secondary slope is found to be negative in case of Laplace smoothing (Figure 25a, Figure 29a) and positive in case of Taubin smoothing (Figure 25b, Figure 29b). Overall we can say that first few iterations yield the most significant changes to the initial surface and thereafter there is a definite trend, i.e. results from separate multiple mesh generation are in agreement.

2.5.4.5 Surface meshing quality

Quality metric plots in Figure 26 and Figure 30 typically show saturation behavior. Although in case of coarse mesh for patient-specific case (Figure 30) quality appears to start degrading after large number of iterations. Considering the numbers, very good quality surface meshes are obtained. It should be noted that minimum quality threshold is as also important as most likely events of miscalculation of stresses is due to minimum quality. Of course, being a local quantity, minimum quality is expected to have many fluctuations, however, it is found to cross minimum threshold. In all generated meshes minimum r-R ratio for surface mesh was above 0.6.

2.5.4.6 Surface meshing comments

2.5.4.6.1 Optimal smoothing iterations and mesh density

Optimal smoothing is different for different mesh densities. In case of patient-specific geometry with a bifurcation, limitation on number of iterations was seen due to the presence of iliac since it has high local curvature implying more sensitivity to smoothing action and smaller dimensions meaning that less ability to tolerate distortion. This is seen in Figure 39c. Fifteen Laplace iterations starting from 0 to 14 were analyzed for element sizes ('radius bound' as per CGAL terminology) ranging from 0.06 to 0.32 cm.

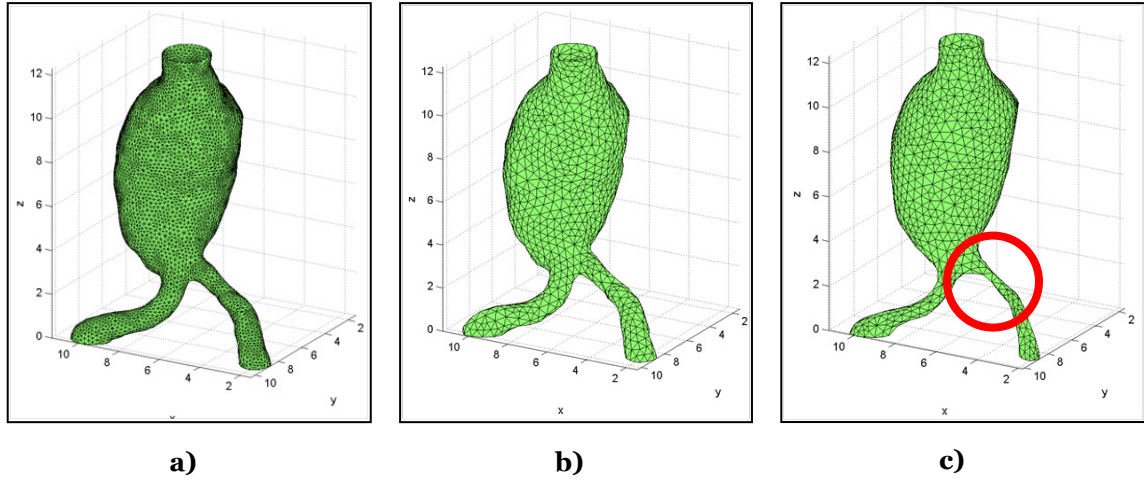


Figure 39: Optimal smoothing iterations different for different mesh density (size); iliac distortion with number of Laplace smoothing iterations (nLaplace) (a) size 14, nLaplace=14, (b) size 32, nLaplace = 1, (c) size 32, nLaplace 14.

2.5.4.6.2 Slope of relative errors in area and volume with increasing iterations

Important fact to be noted from discussion regarding volume and area variation is that two slope observations from distance error discussion do apply in patient-specific case also. Linear monotonous change in volume was observed. And more importantly optimum number of iterations in case Laplace smoothing (~6 iterations) and in case of Taubin smoothing (~20 iterations) are same in both phantom and patient-specific case

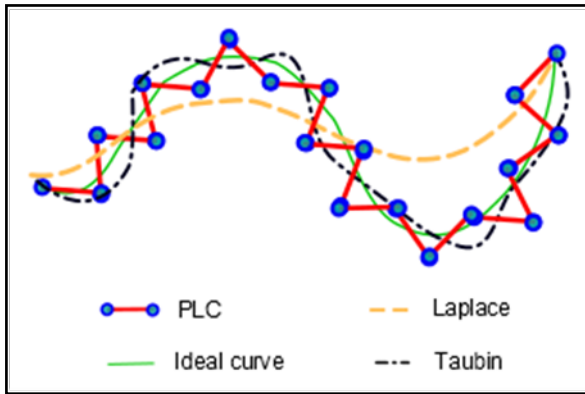


Figure 40: Schematic comparing Laplace and Taubin smoothing action.

for specified mesh density. This observation indicates that discussion based on results for phantom with respect to distance error could be extended to patient-specific case. The conclusions and elaboration regarding two-sloped behavior in average distErr, relAreaErr could be used to identify the

smooth. By treating surface shapes with smoothing we may obtain constants that quantify the convexity of shape.

2.5.4.6.3 Taubin smoothing as a low pass filter

Aforementioned aspects can be explained with the help of the 2D schematic in Figure 40, which illustrates the mechanism for the observed area variation with each iteration type. Continuous line shows ideal surface and the straight line segments represent input unsmooth piece-wise linear surface. As seen by undulations in unsmooth surface, it is having high frequency component. Laplace smoothing acts strongly especially in curved region and moves node to reduce curvature where as Taubin smoothing eliminates high frequency and only retains low frequency. This explains its description as 'low pass filter' in original article [182].

2.5.4.6.4 Smoothing need not to plateau with smoothing

Previous discussion elaborates why perceived notion that smoothing should 'plateau' to ideal surface and stay constant after a while is wrong. It is only true if target surface is flat i.e. without any curvature.

2.5.4.6.5 Surface mesh extraction as a trade-off

Surface mesh extraction process is based on trade-off. Depending on application one may be in a better position to decide various parameters. e.g. if volume estimation of bulkier object is important concern like in growth rate of tumor or fetus where smooth surface is of less importance one may use minimum possible smoothing iterations or even surface reconstruction can be skipped and voxel volumes may be used to approximate total volume pretty closely, where as if computational simulations are of concern as in case of CFD for flow and CSS for stress estimation, the surface roughness will have pronounced effect on the flow pattern or stress distribution and in that case it could be probably more wise to sacrifice 3-4% accuracy in volume estimation. Similarly if

surface is being extracted for biomolecule, then if the reactivity is function of surface area then the approach would be different than that if the reactivity is function of volume. Modeling objective and physics may guide better. e.g. If physics is driven by surface dependent quantities like forces such as electrostatic force or chemical reactivity or diffusion process such as at capillary level then the area calculation gains importance. In that direction also our work can be extended since it highlights the basic fact that the approximation of area using linear PLC would predict higher estimate than actual.

Targeting zero error in area could also be misleading and hence it should not be targeted as we see that even though area may approach to zero but the *distErr* average is moving away from zero along with it.

2.5.4.6.6 Sweeping better than volume filling to mesh thin objects

Given the uncertainty in surface extraction for coarser image, we underline the fact that extrusion based approach is necessary for wall to be able to incorporate wall thickness with confidence as the volume fill approach will be subject to serious discrepancies because uncertainty in surface extraction is of comparable magnitude with the thickness.

2.5.5 Comparisons with other relevant frameworks

Mesh quality and geometrical accuracy are important aspects of modeling outcome; still these aspects often don't receive due attention in computational biomechanics community. Aneurysm biomechanics community has conflicting opinion regarding stress as rupture indicator [13, 105], effect of calcification [128, 129], etc. It is possible that the differences in meshing strategy used by authors are culminating into contradictory results.

The presented framework and approach is novel though some codes implemented in this approach have been inspired from previous literature and

frameworks (Peng [177] and Fang et al [176]). It facilitates modeling of wall by means of surface extrusion, layered wall and also offers multiple types of elements for wall. Volume meshing methods discussed here follow outside-in approach i.e. boundary surface mesh is first obtained followed by filling the empty inner space by elements. It has improved robustness since this approach has eliminated need for internal point selection [176, 177] for thin-walled domain explicitly by taking advantage of the fact annular set of surfaces and noting that same internal point corresponding to lumen can be used for creating all such annular set of surfaces. Wall region as well as sometime ILT region being thin coupled with the fact that surface reconstruction itself might have error may make it likely that internal point, estimated based on voxel information, lies outside the surface mesh from which volume mesh is to be created. Difficulty in locating internal point is taken care of. Non-uniformity in point spacing while generating ϵ -sample is avoided since internal point is away from wall surface making ray-tracing to generate points sufficiently at distance. Another aspect regarding thin wall is that previously reported approach [176, 177] works well with bulk volumes, however, when the domain is skinny the surface mesh of opposite faces are liable to intersect each other forming a non-manifold geometry that not compatible with traditional volume filling mesh methods. [176, 177] are important contributions; however, robustness with respect to thin walled domains demands further improvement. Also, element quality was compromised due to scaling operations since surface extraction from image was done under uniform grid spacing assumption. Although when compared to Fang et al [176], the limitation of this framework is that it is specifically developed for vasculatures. In addition, AAAMesh currently cannot handle vessel entry or exit located on the side walls of voxel data.

Meshing of vasculature has been exclusively targeted by Antiga et al [172]. They proposed entire framework targeting both image segmentation and tetrahedral mesh generation for CFD simulation based on Visualization Toolkit (VTK) and Insight Toolkit (ITK). Implicit deformable models were used for segmentation. Centerlines were obtained from medial axis. Adaptive mesh was possible. Mesh sizing function was defined using distance of surface point from centerline as surrogate for local vessel size. That entire framework was targeted at tetrahedral mesh for studying hemodynamics and in turn used TetGen for volume mesh generation. This framework is targeted only on mesh generation part. However, it has added challenges such as multi-domain meshing, complex shapes presented by ILT and a target of implementation in clinical settings. Antiga et al [172] followed prototype based approach to verify their framework. They extensively report various combinations of settings for evaluation of signed distance error. Here we mention the best results using best quality image. Using CT images (pixel resolution 0.25 mm and slice spacing 1.25 mm) and upwind difference approximation their signed distance error measured at mesh surface node and STL created from prototype ranged between $[-0.25, 0.85]$ with mean of 0.02 and standard deviation of 0.07. Even though more related to practical application, their validation protocol, however, is subject to many sources of error and thus can not be directly compared with results in this work. Considering the goal of that project it appears appropriate, however, we start with image sets for simple mathematical geometry for verification keeping in mind the scope of this framework and targeted precision. We report 0.01 average error with maximum error around 0.04 using image sets with relatively coarser pixel spacing (0.75 mm) and slice thickness (3 mm).

Commercial software A4research has also been reported targeted at AAA biomechanics [123]. Authors used 2D and 3D deformable models. They present meshing strategy for Wall and ILT only. In their framework, template was deformed as per prescribed FEM formulations under the loadings based on image data. In the surface meshing they have targeted quadrilateral elements only. They report the quality of hexahedral mesh by considering average value of determinant of Jacobian evaluated at each of the 8 corner nodes. Worst elements were reported to have this metric in 0.27 and most of the elements above 0.38. Dimensional error in final mesh is not reported in A4research [123]. It can only use Laplace smoothing. Only user based comparison is made which essentially targets segmentation accuracy than mesh generation accuracy. A4research however, is having some commercial interests. Even though hexahedral mesh is targeted, some degenerate elements are possible for ILT.

Young et al [157] reported an approach referred to as extended Volumetric Marching eVoMac. It provides multi-domain capability by being able to handle 3 or more material interfaces. However, this approach is a grid dependent volume mesh generation (see Figure 11). Table 12 shows the results of benchmarking analysis pertinent to volume mesh quality. Clearly, we observe that AAAMesh framework can mesh thinner variable wall thickness whereas Mimics® could not mesh such geometry. Also, depending upon error metric used, we see that Mimics® is sliver-free if we consider the distortion error metric. For all other metrics, we find that the AAAMesh generated mesh quality is superior.

We quantify accuracy of the external surface geometry as well as quality of mesh elements. Also, this code does not have any commercial interest. We have explored wall creation by both outward and inward extrusion. Outward extrusion may be easy to

integrate if previously generated tetrahedral mesh is available for lumen and ILT domains. It is however not robust especially if there are highly curved concave regions. Hence, it is preferred to have inward extrusion direction in application toward bifurcated geometries since the bifurcation is highly concave surface mesh to extrude when looked from outside. This subtle aspect has been leveraged in this approach since, probability of vasculature representing a locally convex bleb of surface curvature stronger than the normally observed curvature of concavity present at bifurcation is less probable especially when applied to aneurysm.

2.5.6 Limitations

Framework proposed here has an inherent limitation. The elements obtained by extrusion of surface along local normal needs that the nodes on the seed surface are sufficiently spaced in comparison with the spatial variation in normal i.e. curvature and extrusion thickness. In case of very sharp changes in surface normal directions and location of the nodes being very close together, there is probability of normals intersecting each other resulting in intersecting volume elements. Moreover, the current code can be executed only on a Windows platform. As mentioned earlier the vessel entrance and exit must be through top and bottom slice only. The strategy for node-to-node contact at interface of wall and other domains would be possible only in case where wall is modeled by wedge elements. The code can be improved in terms of execution time, accuracy, and quality of mesh, making it more efficient by using pointers to transfer data from and into MATLAB while executing binaries. All discussion regarding the smoothing operation pertains to linear approximation. Alternative method that could approximate surface with higher order of curvature may not be amenable to this discussion.

Chapter 3. Evaluation of the Effects of Aneurysm Geometry and Vascular Wall Material Properties on the AAA Wall Mechanics

3.1 INTRODUCTION

Abdominal Aortic Aneurysm (AAA) is a disease characterized by a local permanent expansion occurring in the abdominal region of aorta. It has about 5-9% prevalence in population aged more than 65 years [190]. This disease is a serious health problem with around 150,000 hospital admissions, 40000 repair operations, and 15000 deaths annually in United States [70]. Being asymptomatic, it is a silent killer, and often goes undetected for years. It is four-fold prevalent in smokers than that in non-smokers [191]. Most of the time it is discovered either by chance or due to pain caused by bleeding after its rupture. However, AAA rupture is usually a catastrophic event as mortality rate in case of ruptured aneurysm is reported to be 65% to 80% [191]. Typical guidelines used in clinical management of AAAs use maximum diameter as a criterion for deciding the course of treatment e.g. in clinical practice fusiform aneurysms more than 5.4 cm are recommended for surgical intervention and those smaller than 4 cm are considered at low risk of rupture [192]. Few other morphological parameters in addition to maximum

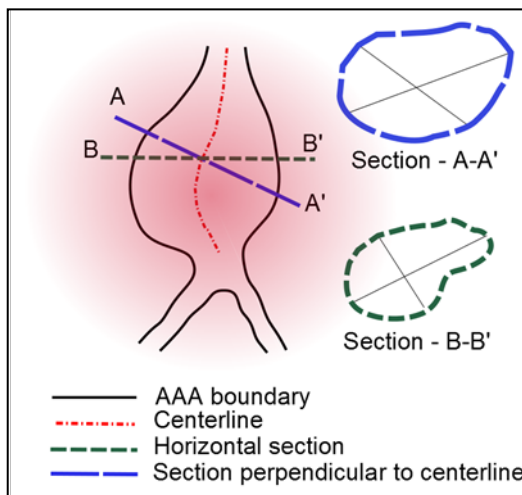


Figure 41: Schematic showing variability in the maximum diameter measurement and its dependence on the orientation of the reference plane.

diameter are also used in clinical practice to assess risk of rupture e.g. volume of AAA [193, 194], rate of expansion of AAA [195, 196], volume of intra-luminal-thrombus (ILT) [118], asymmetry and tortuosity [85].

Morphological parameters are relatively easy to implement in clinical settings, however, they come with certain shortcomings. There is an important drawback in using morphological parameters

that those are purely observation based thumb rules. They lack proper scientific basis for assessing rupture risk with quantities used to assess rupture risk. An autopsy study of 473 AAA cases found that 13% of aneurysms 5 cm in diameter or smaller ruptured whereas 60% of aneurysms of diameter greater than 5 cm did not rupture [78]. Another complication with respect to the widely used criterion involving diameter is that it is hard to uniquely define some length metric as a “diameter” as shown in Figure 41 for an aneurysm like geometries that always have non-circular cross sections and there are multiple slices making it more difficult to select global maximum diameter. Although pseudo-metrics such as hydraulic diameter DH is widely used, defined as $DH = 4 * A/P$ where A is cross-sectional area and P is the perimeter of the cross-section, it does not account for local curvature varying along perimeter or geometry specific to cross-section. A practical complication is that ideally maximum diameter should be measured in a plane perpendicular to the centerline in the region under consideration to draw an analogy with Laplace law; however, it is clear that any cross-section will be too sensitive toward local slope of the centerline that decides plane of cross-section to implement for patient-specific AAA models due to variety of complex geometries. This would get worse in case of expansion rate calculations where base value is smaller as compared to actual diameter. Hence, achieving desired precision in diameter is a formidable task.

Patient-specific biomechanical analysis of AAA is an attractive alternative for rupture risk assessment. This approach is scientific since it is based on proven material failure theories wherein material breaks if a certain quantity such as strain, stress, or strain energy density exceeds threshold limit for that particular material. The beauty of this approach is the fact that it can provide single metric such as mechanical wall stress, wall strain, or strain energy density that represents combined effect of 3D shape, size,

wall thickness, material properties, pressure load, and contact interactions with surrounding tissues. Hence, it could be a clinically feasible metric for rupture risk analysis. Initial work toward patient-specific modeling was reported by Raghavan and Vorp [193] where six patient-specific aneurysm geometries were reconstructed in 3D from medical images and meshed for finite element analysis. One limitation of this work was exclusion of the aortic bifurcation in their models. These finite element models were simulated using shell elements to analyze regional stress distribution. These finite element simulations employed isotropic, hyperelastic, homogeneous material model for the wall. The parameters of the material model were extracted from experimental tensile test data on 69 tissue specimen [3]. It was found that all maximum stress values were located on the posterior side of the AAA. Recently, advanced anisotropic material models [88, 116] and porohyperelastic material models [197] have been incorporated in the study of wall mechanics. Vande Geest et al [90] proposed a statistical model for estimating wall strength using sex, normalized diameter, family history, and local ILT thickness. Subsequently the concept of rupture potential index (RPI) by taking ratio of stress and strength was introduced [106]. Comparative study of wall stress, RPI, and diameter metrics is presented in [198]. Inclusion of ILT is shown to affect computational stresses [199, 200]. Experimental verification of computational assessment reported in [201] adds credibility to computational technique. However, many important questions remain yet unanswered, one of which is quantification of the relative importance of individual shape of aneurysm and individual material property. This kind of comparative sensitivity study is important for addressing uncertainties involved in patient-specific analysis.

The following work is targeted at evaluating the relative importance of inter-patient variation in shape against that in material parameters toward evaluation of biomechanics of AAA. In this controlled study, a diameter-matched cohort of 28 non-ruptured AAA patients is simulated with precisely ensured uniform wall thickness using five sets of material parameters that span 95% confidence interval of previously reported experimental findings [3]. All other parameters except shape and material parameters were maintained the same for these 140 simulations to arrive at conclusion with confidence by eliminating compounding effects of additional uncontrolled factors such as intra-luminal-thrombus (ILT). The objective of this work is not to report estimation of stress under physiological conditions but to evaluate influence of shape vs. that of material that may help to identify priority focus area for further research toward clinical implementation of computation techniques applied to AAA.

3.2 METHODS

3.2.1 The AAA subject population

Our study population consists of total 100 human subjects with non-ruptured AAAs. Patients were recruited as per Institutional Review Board (IRB) approval at Alleghany General Hospital (AGH), Carnegie Mellon University (CMU), and The University of Texas at San Antonio (UTSA). Abdominal DICOM images were acquired using contrast enhanced CT with scan size of 512×512 pixels. The CT images from these 100 patients were segmented and a cohort of 28 patients with the maximum diameter in horizontal plane within range 50 to 55 mm was identified. Important imaging parameters for shortlisted cohort are summarized in Table 13 (for details please refer to Appendix C). Note that these parameters were constant for each image dataset.

Table 13: Summary of DICOM image data for shortlisted cohort (units: millimeter).

Quantity	Minimum	Maximum	Mean	Mode
Pixel spacing	0.6699	0.9511	0.7781	0.7422
Slice spacing	1.5	5.0	3.2	3.0
Max. diameter	50	54.75	52.36	53.78

3.2.1.1 Motivation behind finalized cohort

There were three motivations to shortlist this cohort of 28 patients within 50-55 mm maximum diameter range- 1) Diameter is commonly used norm of risk of rupture in clinical practice and has been related to rupture though it is not the only criterion for rupture risk assessment [2]. Considering pixel-resolution, variability in segmentation, inter-observer differences, and consultation with surgeon regarding keenness on resolution of maximum diameter metric for categorization of patients in terms of assessed risk, span of approximately 5 mm was deemed appropriate for this study. Thus, select cohort more or less at the same risk of rupture as per established norms [192]. 2) From a clinical point of view there is unanimity that AAAs below 40 mm maximum diameter are less likely to rupture and surgical intervention is not justified unless there is any strong reason to do so. On the other side of spectrum, aneurysms more than 60 mm are also unanimously considered for surgical intervention [192]. It is the range between 40 mm and 60 mm that has been matter of debate for several years and hence more focused research is necessary in this range for clinical management of disease. 3) Availability of contrast enhanced CT scans for patients with diameter in this range is better since it is at this point that risk of radiation is offset by the need for better resolution. Availability of larger aneurysms is scarce since surgical intervention is recommended prior to reaching that stage.

3.2.1.2 Image segmentation

The chosen cohort of 28 unruptured patient AAAs has mean diameter was 52.3592 mm with standard deviation 1.4910 mm, average pixel spacing was 0.7781 mm, and mode value of slice spacing was 3 mm. (see Appendix C for details). For each of these AAAs, the CT images between the renal branches and common iliac bifurcation were selected and segmented using our in-house MATLAB based software VESSEG [91] (see Figure 42). Semi-automatic methods in VESSEG define splines for outer wall boundary, inner wall boundary, and lumen boundary for each slice. Reproducibility and inter-observer variability studies for VESSEG have been reported previously [91]. The output of image segmentation is a 4-region binary mask composite, which is further imported into in our in-house code for finite element discretization as follows.

3.2.2 Finite element discretization

The mesh generation framework AAAMesh [202], developed in-house in MATLAB and using CGAL [180] at its core for surface meshing, was employed for high quality mesh generation. A triangular surface mesh for AAA outer wall surface was extracted from segmented CT images and quadrangle surface mesh was derived from it by splitting individual triangles into quadrangles. Local node normals at all nodes of this surface

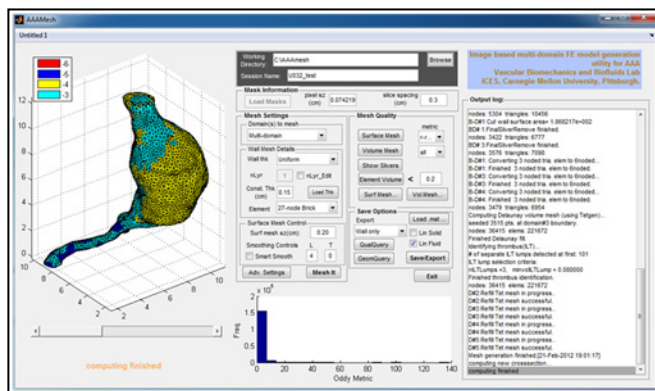


Figure 42: AAAMesh GUI snapshot.

mesh were evaluated. Surface mesh for outer wall was extruded inwards along the local node normal to form 2 layers of extrusion that give volume elements with aspect ratio close to 1 for hexahedrons for the size of

surface mesh element deemed to be sufficiently resolved to capture geometry appropriately. A uniform wall thickness of 1.5 mm was used for extrusion based on median value for the population reported earlier [93]. Finally, wall domain meshed by using hexahedral elements was imported and finite element simulation was performed using commercial code ADINA (ADINA R&D, Watertown, MA, version 8.8.3). Average number of elements per simulations was approximately 66,000.

3.2.3 Constitutive material models

Raghavan and Vorp [3] characterized material model for aneurysmatic abdominal aorta based on 69 tissue specimen. It was observed that strain energy function was dependent only on first invariant of left Cauchy-Green deformation tensor. Hence, material model was proposed as

$$W = c_1(I_1 - 3) + c_2(I_1 - 3)^2 \quad \dots \quad \text{Eqn. 3-1}$$

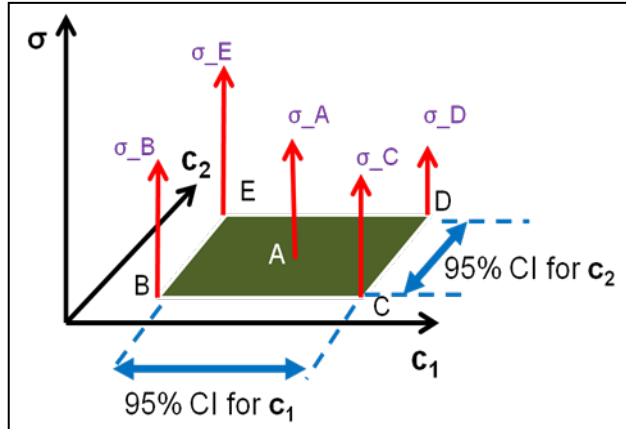


Figure 43: The range of material parameter variation in the c_1 - c_2 space for the hyperelastic isotropic constitutive model.

where, W is strain energy density, I_1 is first invariant of left Cauchy-Green tensor, and c_1 and c_2 are material parameters determined experimentally. Due to its wide use (see Table 2, Table 3, Table 4) this special case of generalized power law neo-Hookean hyperelastic material model was explored in this

computational study with nearly incompressible material properties (Poisson ratio, $\nu = 0.499$).

Table 14: Summary of material models explored.

Model	Location in Figure 43	C_1 (N/cm ²)	C_2 (N/cm ²)
#1	A	17.4 (avg)	188.1 (avg)
#2	B	15.2 (min)	117.6 (min)
#3	C	21.9 (max)	117.6 (min)
#4	D	21.9 (max)	355.7 (max)
#5	E	15.2 (min)	355.7 (max)

We selected five material models – one corresponding to population mean values of c_1 and c_2 and rest 4 corresponding to extreme combinations of c_1 and c_2 using 95% confidence interval reported in [3]. These material models used to probe uncertainty in patient-specific material properties are schematically shown in Figure 43 and corresponding details are listed in Table 14.

3.2.4 Finite element analysis

Wall domain reconstructed from 28 AAA patient medical image data and meshed by 27-noded hexahedral elements was simulated using commercial code ADINA (ADINA R&D, Watertown, MA, version 8.8.3). ADINA solves the force equilibrium, constitutive, and strain compatibility equations of theory of elasticity for the wall domain. Hyperelastic problem is a large displacement and large strain problem for which total Lagrangian (TL) formulation is used [148]. Implicit scheme was used for non-linear static analysis. Mixed interpolation is used to avoid volumetric “locking” since material is hyperelastic and incompressible. 27-noded elements have a node at center of elements which is recommended for mixed interpolation formulations used for hyperelastic materials. Uniform pressure load was applied on inner wall surface and was gradually increased from 0 mmHg to 120 mmHg in 24 steps. All degrees of freedom at top and bottom ends

of AAA model were constrained. Basic equations of static equilibrium are solved using energy criterion with threshold ratio of out-of-balance energy set to 0.001. Stress tensor ($\vec{\sigma}$), strain tensor ($\vec{\epsilon}$), and displacement ($\vec{\delta}$) information was saved at time instants corresponding equilibrium at 40 mmHg (approximation of stress after accounting for the fact that DICOM images were acquired at 80 mmHg pressurized state, neglecting initial stress), 80 mmHg (stress at diastolic phase neglecting initial deformation at diastole), and 120 mmHg (stress at systolic pressure neglecting initial deformation at diastole).

Simulations were performed on a 12-core, 96GB RAM Dell™ Precision T7500 machine and a 6-core, 46GB RAM, Dell™ Precision machine with Intel Xeon processors and running on Linux operating system (CentOS 6.2). Each simulation on average took approximately 90 minutes after adopting an optimized simulation execution strategy (see Appendix D). A generalized bash command script was written to launch simulations back-to-back and to maintain simulation files in an organized manner (see Appendix E). Forming each simulation's descriptive name, selection of file for mesh input, simulation set-up (updating material definition, element property definition, boundary conditions, load definitions, solver settings, time step definition and output options), FE preprocessing in ADINA, and launching of ADINA solver was taken care of by the script, thereby eliminating manual errors and facilitating efficient usage of resource. Total $28 \times 5 = 140$ simulations were performed.

Post-processing of ADINA output was performed in EnSight (Computational Engineering International Inc., Apex, NC, version 10.0.2d). Principal stresses ($\sigma_1, \sigma_2, \sigma_3$) and principal strains ($\epsilon_1, \epsilon_2, \epsilon_3$) were derived from locally averaged stress tensor ($\vec{\sigma}$) and strain tensor ($\vec{\epsilon}$) respectively by evaluating three eigen values of corresponding tensor for

every node. Strain energy densities (ψ) can be calculated from stresses and strains. For i 'th node, Strain energy density (ψ^i) was calculated from principal stresses and strains as given below:

$$\psi^i = \frac{1}{2} (\sigma_1^i \times \varepsilon_1^i + \sigma_2^i \times \varepsilon_2^i + \sigma_3^i \times \varepsilon_3^i) \quad \dots \text{Eqn. 3-2}$$

Spatial maxima for the first principal stress ($\sigma_{max} = \max(\sigma_1)$), first principal strain ($\varepsilon_{max} = \max(\varepsilon_1)$), strain energy density ($\psi_{max} = \max(\psi)$), and displacements ($\delta_{max} = \max(\|\vec{\delta}\|)$) were identified. Their location is qualitatively noted in comparative sense. Both global maximum and sac region maximum values were noted since maximum value may occur in highly curved region near iliac bifurcation. Similarly, volume weighted spatial average values (σ_{avg} , ε_{avg} , ψ_{avg} , and δ_{avg}) were evaluated over sac region using respective nodal values, vertex coordinates, and nodal connectivity information.

3.2.5 Convergence study

Mesh convergence study was performed. One of the AAA model was randomly selected and simulated using population mean values of material model selected by Raghavan and Vorp [3]. Two convergence studies were undertaken:

- A) Seven different mesh densities with 1, 2, and 3 layers each were created for convergence study. Previously mentioned FE analysis settings were used except for uniform pressure load that was applied in 40 steps. Thus, total 21 simulations were executed. Spatial maximum of first principal stress was considered as a metric to reach convergence. Between finest mesh (mesh #7) and second-most fine mesh (mesh #6) mesh 0.6% improvement was noticed in maximum principal stress value. Element size and number of layers were considered to be

the variables to be decided. Reasonably good results were obtained for 2 layer volume mesh and corresponding surface mesh density that gives aspect ratio close to 1 (mesh #6) and still offers feasible computational load. Hence, this combination of surface mesh size and number of layers of extrusion was finalized. Three simulations – mesh#6 with 3 layers, mesh#7 with 2 layers, and mesh #7 with 3 layers could not be completed due to memory limit reported by ADINA. A surface mesh density corresponding to an average edge element length of 0.08 cm was deemed appropriate.

- B) Using identical surface mesh, the wall domain was meshed seven times with different number of layers each time across its thickness. These meshes were used for the execution of simulations as per Section 3.2.4. Two layers across the thickness were adopted considering its impact on spatially averaged quantities and overall computational load.

The final surface mesh density and number of layers obtained from studies A and B also offer the advantage that the aspect ratio is approximately 1 for the specified 1.5 mm wall thickness. For more details please refer to Appendix F.

3.2.6 Statistical analysis

Statistical analysis was performed on the results obtained from the 140 simulations. Mean +/- std. deviation of each of the eight biomechanical parameters – σ_{max} , ε_{max} , ψ_{max} , δ_{max} , σ_{avg} , ε_{avg} , δ_{avg} , and ψ_{avg} was computed in intra-patient (same geometry) and inter-patient (same material model) categories and normalized variation is reported (see Appendix H for details). In addition, to investigate whether material type has an effect on the mechanical variables, we conducted a standard statistical test called analysis of variance (ANOVA). The basic analysis of variance test assumes that all

observations of mechanical quantities are independent and identically distributed random variables, and that the variances of the five "populations" (corresponding to the five material types) are equal. Specifically, for each biomechanical parameter we tested the hypothesis that the means of the biomechanical parameter corresponding to the five material types are all equal.

3.3 RESULTS

3.3.1 Normalized variations

Maximum first principal stress, first principal strain, strain energy density, and displacements were analyzed to explore variability in the results of the 140 simulations in intra-patient and inter-patient approaches. Table 15 summarizes mean and standard deviations for the maximum biomechanical parameters for different patients. Thus, mean values for standard deviation in the maximum biomechanical quantities were 9.53, 0.020, 178897.8, and 0.105 for σ_{max} , ε_{max} , ψ_{max} , and δ_{max} respectively (units as per Table 15).

Table 15: Mean and standard deviations of the four maximum biomechanical parameters for each material model.

Model # (c1, c2)	σ_{max} Mean (std.dev) [N/cm ²]	ε_{max} Mean (std.dev) [non-dim]	ψ_{max} Mean (std.dev) [erg/cm ³]	δ_{max} Mean (std.dev) [cm]
1 (avg, avg)	50.17 (9.44)	0.267 (0.019)	627305.3 (162427.1)	0.469 (0.106)
2 (min, min)	50.72 (9.80)	0.316 (0.022)	751036.8 (199929.8)	0.544 (0.117)
3 (max, min)	48.79 (8.96)	0.288 (0.022)	659559.8 (175977.7)	0.493 (0.104)
4 (max, max)	49.47 (9.46)	0.237 (0.017)	545046.5 (147035.8)	0.411 (0.095)
5 (min, max)	50.98 (9.98)	0.253 (0.017)	624954.1 (209118.7)	0.454 (0.101)

Similarly, Table 16 summarizes the mean and standard deviations for the average biomechanical parameters for different patients. Thus, mean values for standard deviation in average biomechanical quantities were 2.18, 0.008, 24548.6, and 0.035 for σ_{max} , ϵ_{max} , ψ_{max} , and δ_{max} respectively (units as per Table 16).

Table 16: Mean and standard deviations of the four average biomechanical parameters for each material model.

Model #(c1, c2)	σ_{avg} Mean (std.dev) [N/cm²]	ϵ_{avg} Mean (std.dev) [non-dim]	ψ_{avg} Mean (std.dev) [erg/cm³]	δ_{avg} Mean (std.dev) [cm]
1 (avg, avg)	20.70 (2.17)	0.138 (0.008)	179808.1 (23721.9)	0.218 (0.035)
2 (min, min)	22.55 (2.28)	0.167 (0.010)	225691.5 (30024.8)	0.264 (0.041)
3 (max, min)	21.94 (2.23)	0.146 (0.010)	192253.9 (27130.3)	0.230 (0.037)
4 (max, max)	21.22 (2.09)	0.121 (0.007)	153727.9 (20228.3)	0.190 (0.031)
5 (min, max)	21.57 (2.12)	0.133 (0.007)	171066.0 (21637.6)	0.209 (0.034)

To identify the relative importance of the modeling strategies, it is required to quantify and compare the effect of variations in material to that of shape. Because of the nature of this study it is important to inspect normalized variations values rather than absolute variation values. Hence, reference values for normalization were decided as follows. For intra-patient study: motivation for this study is to vary material parameters while maintaining same geometry. Hence, for each patient-specific geometry, simulation results corresponding to population average values of c_1 and c_2 i.e. results of material model #1 of respective geometry were used as reference value. For inter-patient study:

motivation for this study is to vary geometry across cohort while maintaining same material parameters. Hence, for each material model, simulation results corresponding to different patient-specific geometries were averaged and used as reference value.

Percentage variation is calculated by $\Delta = \left(\frac{V-R}{R} \right) \times 100$ where V is the value of a biomechanical parameter for which normalized variation is to be evaluated and R represents corresponding reference value obtained as described above. For additional details please see Appendix H. These results are tabulated in Table 17 and Table 18.

Table 17: Average variation in the normalized absolute maximum biomechanical parameters in intra-patient and inter-patient data analysis.

Approach	σ_{max} Mean (std.dev) [N/cm ²]	ϵ_{max} Mean (std.dev) [non-dim]	ψ_{max} Mean (std.dev) [erg/cm ³]	δ_{max} Mean (std.dev) [cm]
Intra-patient	1.46 (1.89)	7.076 (6.610)	7.996 (11.652)	6.137 (7.492)
Inter-patient	11.08 (12.96)	4.453 (4.729)	15.327 (19.915)	12.939 (15.097)

Table 18: Average variation in the normalized absolute average biomechanical parameters in intra-patient and inter-patient data analysis.

Approach	σ_{avg} Mean (std.dev) [N/cm ²]	ϵ_{avg} Mean (std.dev) [non-dim]	ψ_{avg} Mean (std.dev) [erg/cm ³]	δ_{avg} Mean (std.dev) [cm]
Intra-patient	0.99 (1.34)	5.203 (7.077)	6.442 (8.719)	5.410 (7.362)
Inter-patient	5.10 (5.92)	2.899 (3.553)	6.741 (7.927)	7.373 (10.234)

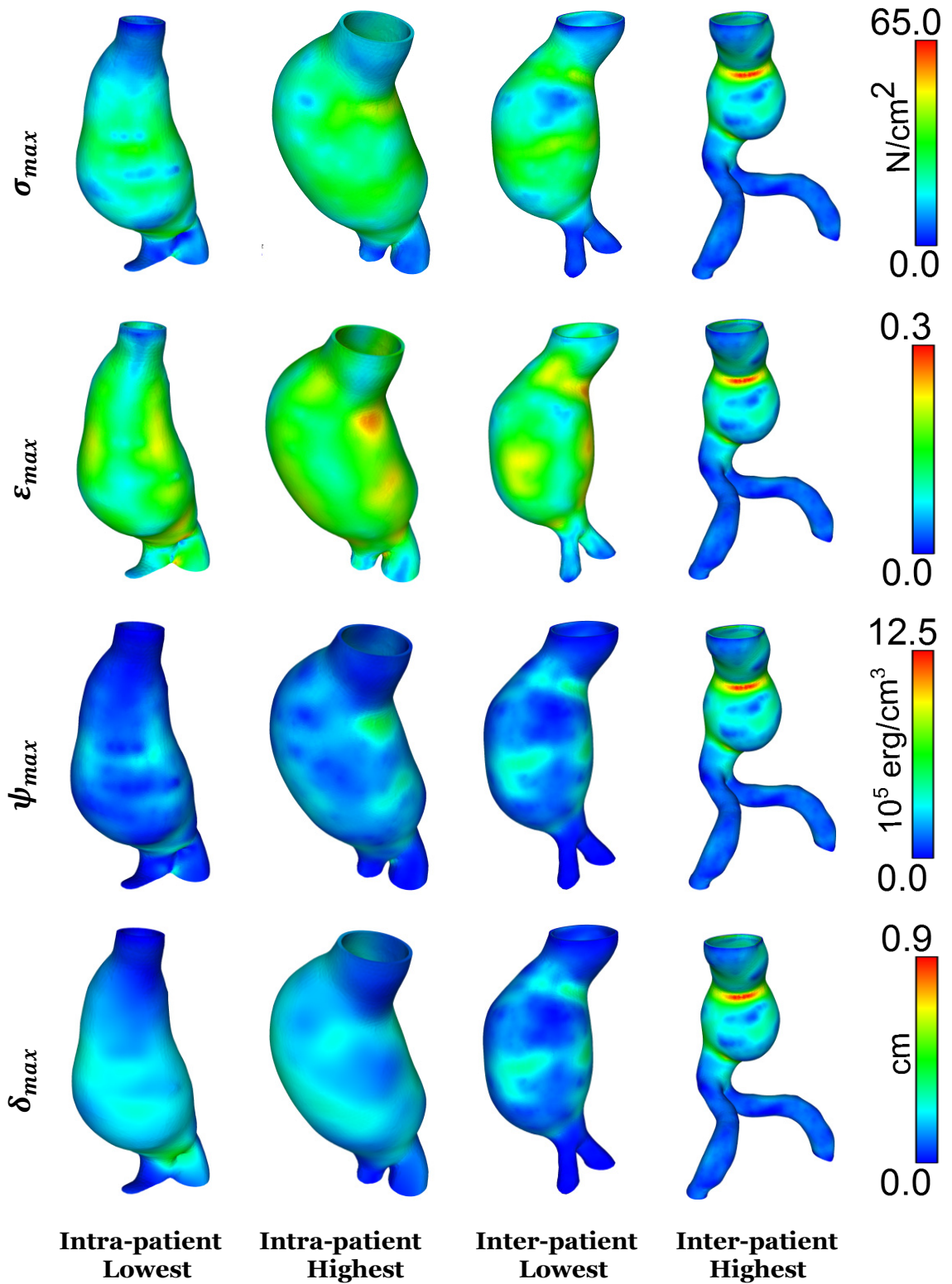


Figure 44: Distribution of the maximum biomechanical parameters in AAA models with the highest and lowest norm of variability in intra-patient and inter-patient data analysis.

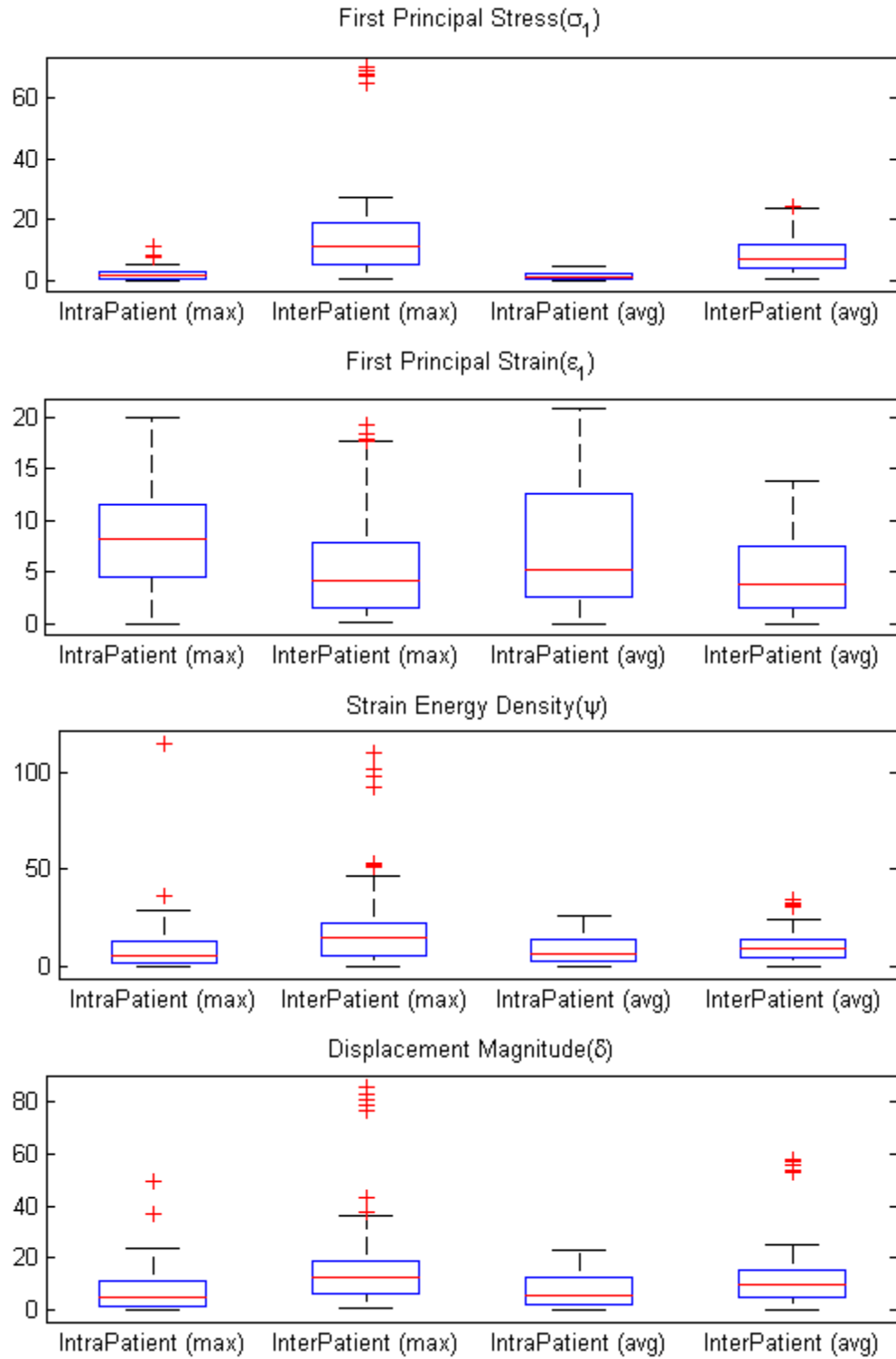


Figure 45: Intra-patient and inter-patient absolute normalized percentage variations in the maximum and average biomechanical parameters.

A qualitative inspection of the distribution patterns in Figure 44 suggested that high stress region, high strain region, and high strain energy density region are almost identical in all cases for same geometry. Higher stresses were observed on inner wall surface where surface is locally saddle shaped. All convex regions were found to have lower stress and saddle surface region having large stresses. Highest displacement mostly occurs in region where diameter is larger. Out of 28 different cases, 23 were modeled with aortic bifurcation. Sixteen (~70%) out of these 23 AAAs resulted in global maxima of biomechanical parameters except displacement located at bifurcation region while remaining 7 had global maximum values located in sac region. No consistency was observed in location high stress regions as well as stress pattern and it was found very much dependent on patient specific geometry. For statistical calculations, spatial maxima and averages in the sac region were considered. Figure 45 illustrates the percentage variations in biomechanical characteristics in inter-patient and intra-patient analyses.

3.3.2 Analysis of variance

For the hypothesis that the means of the % variations in biomechanical parameter corresponding to the five material types are all equal, p-values of ANOVA are shown in Table 19.

Table 19: p-values obtained by ANOVA for maximum and average biomechanical parameters

	σ_1	ϵ_1	ψ	δ
Maximum	0.909	$< 10^{-15}$	0.0013	0.00017
Average	0.222	$< 10^{-15}$	$< 10^{-15}$	$< 10^{-15}$

The main conclusions of the analysis based on the average parameters are exactly the same as those based on the maxima. But the strength of the evidence in support of the conclusions seems to differ from that of the analysis of the maximum parameters. Specifically, the analysis based on the average responses ε_{avg} , ψ_{avg} , and δ_{avg} , seems to support more strongly, when compared to the analysis based on maximum responses, that variations on the material model affect these mechanical responses. In fact, the ANOVA p-values based on ε_{avg} , ψ_{avg} , and δ_{avg} , are less than 10^{-15} , less than 10^{-15} and less than 10^{-10} , respectively, while the ANOVA p-values based on ε_{max} , ψ_{max} , and δ_{max} , are less than 10^{-15} , 0.0013 and 0.00017, respectively.

Both ANOVA analyses suggest that variations in the constitutive material model do not affect spatial maximum of first principal stress.

3.4 DISCUSSION

This work presents a controlled study to analyze behavior of biomechanical quantities in AAA sac region in patient-specific models with aortic bifurcation. Effect of possible variation in material property on biomechanical quantities is compared with the effect of variations in shape of aneurysm. The form of the wall material model [3] employed in this study is a special case of the power law neo-Hookean hyperelastic material model that is dependent on only first invariant of left Cauchy-Green tensor. This wall material model is the most widely accepted in AAA biomechanics as seen in Table 2, Table 3 Table 4. Our mesh generation method ensured exact wall thickness of specified value along local normal direction at every point in the wall, thus eliminating uncontrolled and undesired uncertainty in wall thickness introduced by grid-dependent variation due to popular mask dilation approach as well as those introduced due to surface smoothing operations. Use of shell elements as well as incompressible materials both are recent

field in Finite Elements and relatively less established [148]. Volume elements are correct and are suitable even in case of highly curved region. Hence, use of quadratic 27-noded hexahedral elements adds more credibility to the results of this study. Diameter-matched approach used for selection of cohort of 28 patients in this study focuses only on patients which are at same risk of rupture as per previous observation based studies. It presents a detailed comparative evaluation of biomechanics supported by larger patient-specific data in a diameter-matched cohort. In addition to traditional biomechanical parameters we also explored strain energy density which could be more appropriate for hyperelastic material as a failure criterion [108].

3.4.1 Relevance to prior work

The basis of this work is formed by experimental characterization reported by Raghavan and Vorp [3]. The need for such a study is highlighted due to the fact that p-values were reported to be $p > 0.3$ and $p > 0.1$ for parameters c_1 and c_2 respectively and because reported 95% confidence intervals span about 17.24% and 38.75% of the actual mean values for c_1 and c_2 respectively. A preliminary study of the effect of material variation was also presented in [3]. However, that study had the following shortcomings – i) it investigated only stress distribution, whereas complete biomechanical analysis is described by other variables such as strain, displacement, etc. ii) it was done using a single idealized shape and five combination of material parameters; thus comparison of shape influence vs. material parameter influence was not possible and also clinical fact that AAA shape involves patient-specific local curvature were not included. iii) only one of the material parameters c_1 and c_2 were varied at a time; thus, the extreme combinations that occur at the corners of rectangular region in c_1 - c_2 space (see Figure 43) that lie in 95% confidence interval were not explored. iv) their work uses linear shell

elements with assumption regarding curvature to thickness ratio. Use of such elements is not recommended [148] in patient-specific case where local curvature and thickness could be significantly higher than overall curvature and thickness of enclosure surface respectively.

The effect of model complexity has been studied earlier by Reeps et al [199]. Using 4 geometries, simulations were performed with 7 different levels of complexities. These 7 levels were obtained by combination of five aspects, namely, material law (linear/nonlinear), equilibrium in basic FE formulation (linear/nonlinear), loading (linear/non-linear), pre-stressing (neglected/applied), and ILT (neglected/applied). Their work did show marked difference in results with the difference in modeling approach and it is a valuable knowledge. Displacement in particular was found to be very sensitive as well as stress. However, in our opinion, their conclusion –“Differences of model assumptions are more important for simulation results than differences between patient-specific morphologies” - needs to be interpreted appropriately for couple of reasons. First, they used only 4 different geometries and hence limited variation in geometry to reach statistical significance. Second, it does not present comparative study involving some metrics exclusively to focus on effect of morphology variation vs. variation any particular model assumption. Third, not being a controlled study, it is hard to conclusively comment on anything since effects due to multiple random variable players, e.g. ILT location and volume, diameter and curvature of surface, load variation, and initial stresses affecting the region in stress-strain curve that governs biomechanics under consideration, etc., may compound leaving limited confidence level to associate observations with conclusions. Even if it may appear to contradict results in this work it

is important to note their work had different scope than the scope of this work and it is valuable contribution towards generic preliminary assessment at a broader level.

A study of model complexity has also been reported by Gasser et al [117] with the objective of distinguishing the risk of rupture towards predicting ruptured and unruptured AAA. Geometrical aspects were explored. Four AAA simulation strategies based on wall thickness (uniform/ILT presence based non-uniform) and ILT (neglecting/inclusion) were explored. Authors have nicely used diameter-matched approach similar to that in this work. In addition, they also report cohort formation based on product $diameter \times MAP$ (MAP -Mean Arterial Pressure, DP-match) as a metric to account for rupture risk in crude sense based on basic cylindrical pressure vessel mechanics. They found no apparent correlation in complex stress pattern. Significant differences in peak wall stress were found between ruptured and non-ruptured AAAs when ILT was included. Same results without ILT could not distinguish ruptured and non-ruptured aneurysm. It identifies importance of ILT and non-homogeneous wall thickness. However, it does not explore shape aspect of geometry as done in this study, instead it focuses on wall thickness and ILT aspects.

The correlation of AAA wall stress and shape has been studied rigorously in the past with idealized models and linear material models [86, 87, 89, 104]. Inzoli et al [104] did consider effect of modeling assumptions. Using simple 2D axisymmetric model they looked at variations in stress results due to modeling approach for geometry for i) uniform thickness wall, ii) varying wall thickness along longitudinal direction with reduction in thickness with dilation to maintain constant volume, ii) AAA with ILT, iv) AAA with dissecting ILT, and v) AAA with vertebral contact. However, those are again aspects pertaining to modeling approach and does not corroborate on shape variation.

Subsequent study by Elger et al [86] reported important finding that high stress occurred at inflection point in their axisymmetric fusiform model. They comment that AAA shape variation has small effect on meridional stresses but dramatic effect on circumferential (hoop) stresses. In spite of all extensive result conclusive result is still awaited for comparing material variation with that in shape.

3.4.2 Study outcomes

In this section, we summarize the important outcomes of our study. The goal of our study is to answer the question: is the AAA wall biomechanics more sensitive to shape variation compared to material variations? To objectively answer this question, we have looked at four important biomechanical parameters with respect to rupture prediction, namely, stress, strain, strain energy density, and displacements. With patient-specific variability in shape and controlled variations in material, and under identical simulation settings for loading and FE solver, effects on biomechanical outcomes of simulations were probed in intra-patient and inter-patient aspects. Intra-patient variability in stresses, caused due to possible patient-specific material variation is found to be small compared to inter-patient variability that is caused mainly due to variations in shape of patient-specific AAA (see Table 17 and Figure 45). Hence, it highlights importance of accurate patient-specific AAA geometry reconstruction. This observation is in agreement with recent study by Shum et al [2] that identified 4 geometrical features closely associated with rupture risk prediction, 2 of which are shape-dependent. Image artifacts and segmentation errors introduce artifact in reconstruction, thus those aspects also have implication on AAA biomechanics evaluation.

Another benefit of this work is the fact that use of population average values for material parameters are justified for use in patient-specific simulation as long as stresses

are of concern and isotropic material characterized by Eqn. 3-1 is used in computational analysis. Even though material dependent variability and shape dependent variability is not with stark difference in case of biomechanical quantities discussed here other than stress, it could be extended to those since range of variability in respective results can be predicted from Table 17 to see if that is acceptable. This is important since always there are variations in material parameters due to error and assumptions in characterizations as well as patient-specific heterogeneity in material. It may be possible that this population average material model is sufficient to ignore heterogeneity if stresses are of concern. However, this does not mean that research on material parameters is not needed. Because, except principal stress maximum, all other quantities considered in this work biomechanical factors are having appreciable variation (see Table 17).

Using the values in inter-patient variability some patient-specific AAA geometries were selected that had least norm or variability. These select models can be used in future research as representative cases of patient-specific geometries to represent average behavior of group of 28 cases in this cohort. One such study can be to estimate effect of minor segmentation differences or smoothing differences on biomechanical quantities using same geometry. It is possible to select representative geometry based on criterion of interest e.g. in case where stress is important, geometry corresponding to minimum of root mean square value of stress column can be used or if displacement information is of interest geometry corresponding to minimum of root mean square value in displacement column can be selected.

Qualitatively it is observed that 70% of cases had maximum stress located at iliac bifurcation. Since meshing the aorto-iliac bifurcation is challenging, a low quality mesh was suspected to be a possible reason. However, we found consistently good quality

mesh generated by our framework. We confirmed that it is not a result of deteriorated mesh quality especially at bifurcation. Similar finding has been reported earlier by Speelman et al [203]. Under uniform wall thickness assumption high stresses culminate from diameter and local curvature (see Appendix I for details). Hence, it is natural to find higher stresses in aortic bifurcation that has highly concave surface. Contrasting with this, aneurysm rupture location mostly not being near iliac can be explained by following reasons – i) horizontal surfaces are difficult to segment and reconstruct accurately. Iliac bifurcation is such small region where topology is changing drastically ii) assumption of uniform wall thickness is not valid iii) ignoring complex fiber architecture at bifurcation that is likely to impart higher strength to wall iv) assumption of isotropic material properties, that too derived from sac region. Hence, global maximum if it occurs at bifurcation may be irrelevant while working with simplified models with aortic bifurcation.

3.4.3 Limitations

Even though initial stresses and deformations present in the in vivo acquired geometry are ignored in this analysis, considerations of that aspect will not affect conclusions appreciably due to following reasons. First, hyperelastic behavior of AAA tissue, as seen in Figure 46 reproduced from ex-vivo uniaxial testing by Raghavan and Vorp [3], does not show drastic change in slope in initial loading compared to later part. Thus, sensitivity of deformation to applied load will not be dramatically different. Second, whatever effect this assumption will have, will be applicable to both material variation as well as shape variation. Third, this analysis subjects the model to extreme conditions due to following reasons: i) Figure 46 also approximately depicts the mean values of stresses in Table 15 and Table 16 superimposed on ex-vivo uniaxial testing response curve that

has relatively lower stiffness (slope) for smaller stretch values (λ_1). Thus, for the same loading i.e. pressure increase, higher strains and deformations are expected in beginning when compared to same increase in loading when geometry is already under some higher stress. By ignoring initial stresses our results are likely to result in larger strains and displacements for same pressure increase. ii) While considering prestress in geometry, only 40 mmHg is effective rise in pressure. Here we applied 120 mmHg. In summary, our conclusions will also be applicable in practical scenario, since, it was deduced under extreme conditions from material point of view.

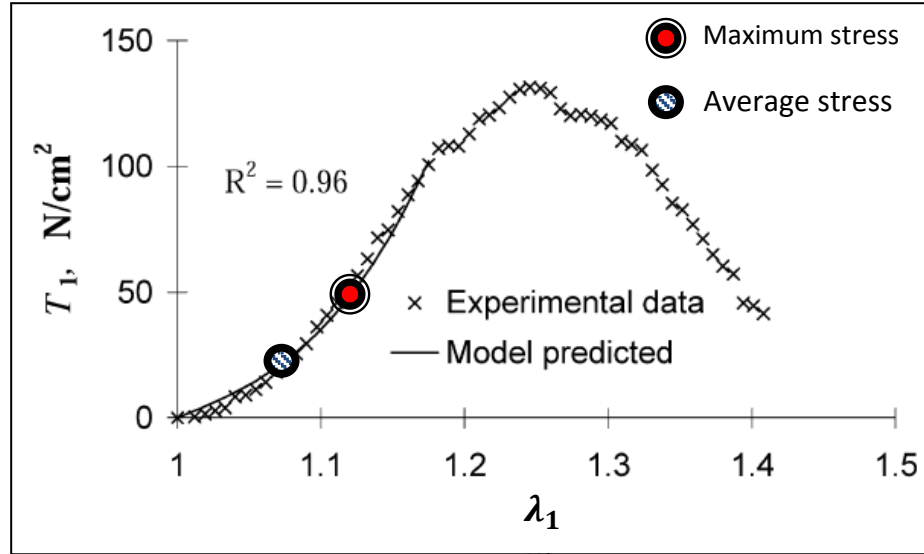


Figure 46: Typical maximum and average stresses obtained in this work superimposed on previously reported uniaxial tensile data reproduced from Raghavan and Vorp [3].

There are other noteworthy limitations of this study. This work assumes isotropic material model though recently it has been reported that AAA wall mechanics differs with anisotropic material model [115, 116]. This study could be extended in the future to include active mechanics models (elastin, collagen, and smooth muscle activation) which have more parameters and hence, instead of simple c_1 - c_2 space explored here, it would

need higher dimensional space to be probed. Shape variability is considered on individual basis as cumulative effects of various factors that govern shape e.g. asymmetry, aspect ratio, and tortuosity; thus, variation of shape is not truly controlled. ILT was neglected as with previous approaches in [3, 13, 87, 137]. Also, AAA wall thickness is not uniform as modeled in this model. Experiments show that it varies from 0.23 mm to 4.26 mm [93]. However, most of our assumptions contribute to make this study a more focused and controlled study by eliminating the complications and possibly counteracting roles of multiple factors and thereby isolating effects of material and shape variations only. Also, it should be noted that this study does not intend to evaluate in-vivo distributions and magnitude of studied biomechanical factors.

3.5 CONCLUSION

This work shows that in case of patient-specific analysis difference due to individual patient-specific shape has large effect on stress distribution compared to the effect of material parameter variation within physiological range. It appears that strain results are more dependent to material model than geometry even though displacement is more dependent on geometry. This work also endorses use of population average material property data for estimation of stresses and use of material property from anterior region of AAA, ignoring heterogeneity, is expected to have relatively small effect on stresses. This work leads to some patient-specific models that can be used for future research for benchmarking since their behavior matches closely with average of all 28 cases. Additional work is needed for repeating similar study with possible variations in anisotropic material model parameters. Detailed controlled study of shape variation in same geometry to represent reconstruction variability will also add more knowledge to the field.

Chapter 4. Assessment of the Effect of Regional Variations in Wall Thickness on the AAA Wall Mechanics

4.1 INTRODUCTION

Wall thickness is an important geometry variable that can potentially increase the accuracy of AAA biomechanical analysis. Rupture is a local phenomenon that should be assessed by modeling spatially varying local geometry, thereby eliminating the role of globally defined criteria such as diameter and sac volume for patient-specific analysis. Vascular wall thickness is hypothesized as the most influential geometric feature for biomechanical stress evaluation. From a mechanics perspective, the shape of an aneurysm and the thickness of the artery dominantly govern the stress distribution compared to the overall size of the aneurysm [204]. Acknowledging that there are limitations inherent to the image acquisition sequences and resolution, deriving accurate segmentation and geometric modeling algorithms have been highlighted as open problems in computational vascular biomechanics [205]. Thickness, nonlinear material behavior, strength of the AAA wall, and the spatial distribution of these variables are said to be essential for achieving accurate AAA Finite Element (FE) simulations and, therefore, also for a realistic prediction of AAA rupture risk [199, 206].

Few studies report experimental measurements of aneurysmatic wall thickness [92, 93, 207], however, with large differences in their findings, as described in Table 20. The autopsy based observation that AAA rupture location mostly is on the posterior wall [78] is in agreement with the finding by Raghavan et al [93] that wall thickness is slightly lower in the posterior region. It should be noted that the severity of posterior rupture is relatively less than that of the anterior rupture. Hence, it is more likely that posterior rupture cases will be documented often in medical literature since patient with anterior rupture may not even reach hospital, thereby compounding above observations. In a healthy aorta, the anterior region of the wall is thicker than the posterior [207] and with

a mean wall thickness of 1.38 mm [208]. The challenge of estimating regional variations of wall thickness and subsequent incorporation in FE analysis is a complex one. Hence, the assumption of a uniform wall thickness in numerical models used in the literature is questionable and there is need for implementing these regional variations on a patient-specific basis.

Table 20: Brief summary of previously reported experimental measurements on wall thickness (eAAA – electively repaired AAA; rAAA – ruptured AAA).

Authors	Year	Reported thickness (mm)	Method	Authors' comments
Di Martino et al [92]	2006	eAAA 2.5 ± 0.1 , rAAA 3.6 ± 0.3 , mean 2.9	Optical method (laser)	Thickness is inversely correlated with local strength; only anterior wall tested; use of laser measurement eliminates compression due to caliper
Raghavan et al [93]	2006	minimum 0.23 maximum 4.26 median 1.48	Caliper measurement	No perceptible difference in thickness for small and large aneurysm; thickness slightly lower in posterior and right walls; thickness quite low in ruptured aneurysm near site of rupture
Thubrikar et al [207]	2001	Posterior 2.73 ± 0.46 Lateral 2.52 ± 0.67 Anterior 2.09 ± 0.51	Customized micrometer with resistivity meter	Thickness decreases from posterior to lateral to anterior walls; accuracy 0.05 mm
Kazi et al [38]	2003	w/ILT ~(0.6 to 1.8) w/o ILT ~(0.9 to 2.3)	Masson trichrome staining with electron microscopy	Wall region covered with ILT thinner than that without ILT

Patient-specific non-invasive estimation of vessel wall thickness can be important for clinical decision making. Martufi et al [101] reported the validation of a set of MATLAB routines for estimating regional vessel wall thickness by comparing it with post-mortem AAA tissue measurements [93]. Comparison of CT image-based wall thickness and caliper measurements on the cadaver tissues validated reproducibility with an average relative difference of 7.8%. A framework for semi-automatic wall detection and quantification of thickness using contrast-enhanced CT images was described by Shum et al [91], resulting in low repeatability and reproducibility errors when compared to the manual segmentations performed by trained vascular surgeons. Quantitative assessment of AAA geometry [100] has shown promising results with wall thickness being one of the morphological indicators for rupture risk stratification. These developments are paving the way for non-invasive, automatic geometric assessment of AAAs yielding population stratification in clinical practice.

The objective of this work is to establish a framework for extracting regionally varying wall thickness information from medical image data and incorporate this information in finite element meshes and to interrogate the importance of individual distributions of wall thickness in the ensuing AAA wall mechanics. Discrete, in-plane, and regionally variable wall thickness of the AAA sac available from segmented images is implemented in a FE mesh with node-to-node control of the thickness and 100% confidence that the prescribed thickness is translated to the FEA solver. The errors involved in assumptions of uniform wall thickness using patient-specific mean wall thickness as well as experimentally measured average wall thickness (approximately 1.5 mm) are estimated. A comparative study of these three wall thickness modeling

strategies is conducted on a diameter-matched cohort of 28 AAA patients with the assumption that the constitutive material properties of the wall are the same for all models. This study focuses exclusively on the wall mechanics to avoid the complex and compounded effects of intraluminal thrombus (ILT) shape, intraluminal pressure, and initial stresses, which also introduce patient-specific variability in the predicted mechanics. Four biomechanical parameters, namely, first principal stress, first principal strain, strain-energy density, and displacement magnitude are analyzed for a total of 84 FEA simulations. To the best of our knowledge this is the first study that incorporates regionally variable patient-specific wall thickness obtained non-invasively in an in vivo assessment of computational AAA biomechanics.

4.2 METHODS

4.2.1 The AAA subject population

For specifics regarding AAA subject population, the reader is referred to Section 3.2.1.

4.2.2 Image segmentation

The image datasets were processed as follows (miscellaneous imaging details can be found in Appendix C). The mean diameter was 52.36 mm with a standard deviation 1.49 mm, average pixel size of 0.7781 mm, and the mode value of slice spacing 3.0 mm. CT images between the renal arteries and the aorto-iliac bifurcation were segmented using our in-house MATLAB code VESSEG [91], schematically shown in Figure 47. Semi-automatic algorithms in VESSEG define splines for the outer wall boundary, inner wall boundary, and lumen boundary for each slice. Wall thickness is estimated at 72 equispaced points along the splines on every slice in the sac by calculating the minimum distance between the inner and outer splines, resulting in a point cloud of wall thickness data as illustrated in Figure 4. Reproducibility and inter-observer variability

assessments, reported in [91], highlight the ability of the code to measure in-plane variable wall thickness. The output of the image segmentation is a 4-region binary mask composite, which is imported into AAAMesh for finite element discretization.

4.2.3 Finite element discretization

The MATLAB based mesh generation code AAAMesh [202] was employed for generating both surface and volume meshes of each image dataset. A triangular surface mesh of the AAA outer wall surface was extracted from the distance field, which was derived from the binary masks; this mesh was then converted to a quadrangle mesh. Local node normals were evaluated at all nodes of the surface mesh. The surface mesh was extruded inwards along the local node normal to form 2 layers of hexahedral elements that provide an aspect ratio of approximately 1. For each of the 28 datasets, 3 FE meshes were generated: i) Uniform thickness model (UT) – with uniform wall thickness of 1.5 mm; ii) Patient-specific uniform thickness model (PSUT) – with uniform thickness equal to the patient-specific mean wall thickness obtained by averaging the in-plane wall thicknesses of the point cloud derived in Section 4.2.2; iii) Patient-specific non-uniform thickness model (PSNUT) - with spatially variable wall thickness. This approach yielded 84 different AAA models that were subjected to FEA simulations.

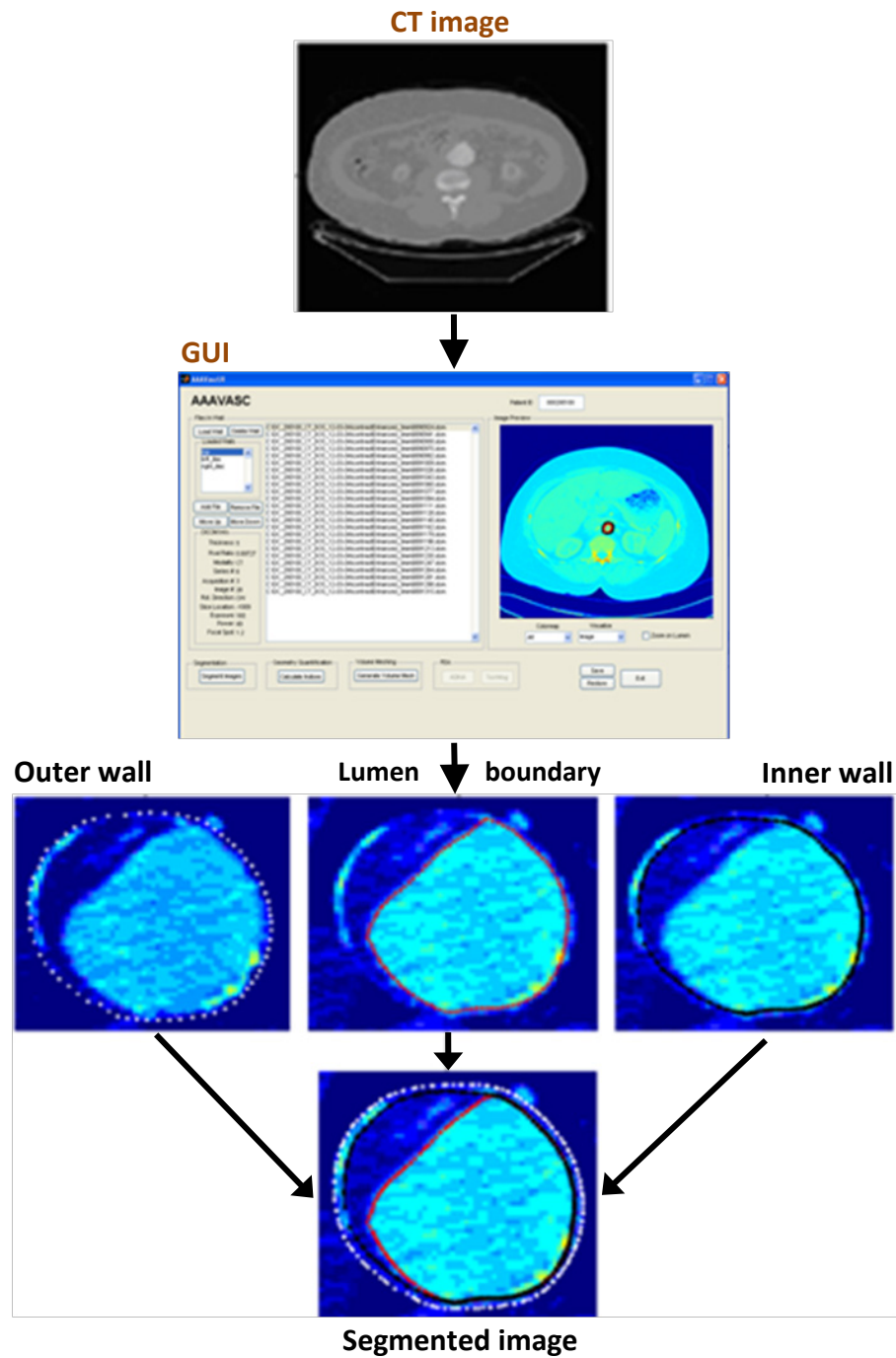


Figure 47: Framework for image segmentation with capability of variable wall thickness estimation [2].

4.2.4 Patient-specific non-uniform wall thickness (PSNUT)

Patient-specific local thickness was sourced from previously estimated in-plane thickness at discrete spatial points [91].

Segmentation based thickness (t_p) was measured in horizontal planes; hence, a correction was applied by multiplying it by the cosine of the angle θ formed by the averaged local normal at each wall thickness data point (based on 4 nearest

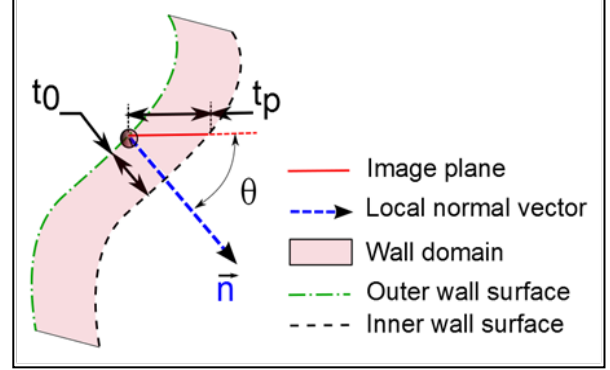


Figure 48: Schematic of cosine correction for mesh extrusion.

neighbor surface mesh nodes and respective normal directions) with the horizontal plane, to obtain the true normal thickness t_0 (see Figure 48), provided $\theta \leq \theta_{threshold}$ to avoid excessive thinning as $\theta \rightarrow 90^\circ$. This work used $\theta_{threshold} = 53^\circ$. If $\theta > \theta_{threshold}$, the cosine of $\theta_{threshold}$ was used for correction. A distance weighted interpolation with 4 nearest neighbor wall thickness data points was used for every surface mesh node in the AAA sac to calculate the individual length for surface extrusion from t_0 defined at data points. If any of the nearest neighbor data points is at a distance greater than threshold distance ($d_{threshold}$, typically set to 3 times the slice spacing), it is replaced by an imaginary data point with a wall thickness value corresponding to iliac wall thickness ($t_{iliac} = 1.05$ mm) [208]. This strategy ensures that wall thickness in iliac region will be consistent with literature derived value if estimated thickness data there is unavailable. Hence, if d^k and t_0^k denote distances of nearest neighbors and corresponding cosine corrected thickness values, the weights are given by,

$$w_k = \frac{P}{d_k \left(\sum_l \frac{P}{d_l} \right)} \quad \begin{cases} \text{if } d_* > d_{threshold}, & d_* = t_{iliac} \\ \text{if } d_* \leq d_{threshold}, & d_* = d_* \end{cases} \quad \dots \text{Eqn. 4-1}$$

where $P = \prod_k d_k$. Symbol Π here denotes product over range of indices i.e. for $k = 4$, $P = d_1 d_2 d_3 d_4$. Distance interpolated thickness (t_1) is given by,

$$t_1 = \sum_k w^k t_0^k \quad \dots \text{Eqn. 4-2}$$

We used 4 nearest neighbors, i.e. $k = l = 1$ to 4. To ensure smooth transition of thickness from sac region to iliac region, distance interpolated thickness value for surface mesh nodes that lie within small transition zone of width z_w below last thickness data slice is tweaked as follows. Another distance weighted interpolation dependent on the distance (δ_z) of surface mesh node under consideration from the last slice with wall thickness data points is performed such that thickness value acquires mean thickness value t_m of last thickness data slice as it approaches it. This thickness value t_2 defined at each surface mesh node is finally incorporated in wall extrusion code.

Only for the surface nodes in the transition region,

$$t_2 = \frac{\delta_z}{z_w} t_1 + \left(1 - \frac{\delta_z}{z_w}\right) t_m \quad \dots \text{Eqn. 4-3}$$

while for the rest of the surface mesh nodes, $t_2 = t_1$.

Twenty-seven noded hexahedral elements were generated by assembling the extruded and original surface nodes. Using an exemplary AAA case, Figure 49 illustrates the intermediate steps followed to generate regionally varying wall thickness, a qualitative comparison of thickness distribution and the final mesh after surface extrusion. Finally, FE mesh was imported to the commercial solver ADINA (ADINA

R&D, Watertown, MA, version 8.8.3) and finite element simulations were performed. The average number of volume elements per dataset was approximately 66,000.

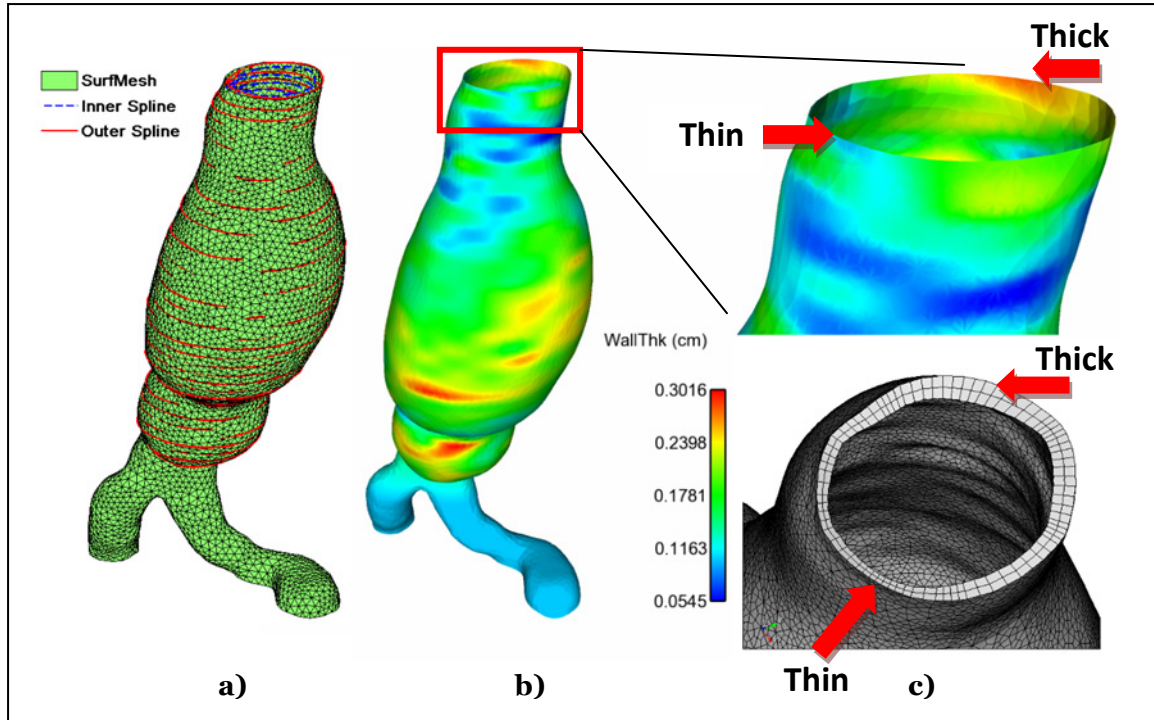


Figure 49: Intermediate steps in wall thickness implementation and qualitative assessment with final mesh, a) superimposition of splines and surface mesh, b) interpolated wall thickness, c) qualitative assessment of thickness modeling by comparing interpolated thickness distribution and final FE volume mesh.

4.2.5 Material model

Model #1 as per Table 14 and Eqn. 3-1 was used. For details please refer Section 3.2.3.

4.2.6 Finite element analysis

For specifics related to Finite Element analysis please refer Section 3.2.4. Results of total $28 \times 3 = 84$ simulations were analyzed.

4.2.7 Convergence study

Based on a previous uniform wall thickness study [209], a representative AAA model that has the smallest deviation from the average biomechanical parameters of the 28

models was used for the mesh convergence study (model with lowest inter-patient norm in Figure 44). Population mean constants were used for the constitutive material model [3] defined by Eqn. 3-1. Seven different mesh densities with 2 wall layers each were created for convergence assessment. Thus, 7 FEA simulations were executed for this analysis and the incremental percentage changes of the biomechanical parameters were calculated. The percentage change at each mesh size decrease was computed using the parameters of the immediately coarser mesh as a reference.

4.2.8 Statistical analysis

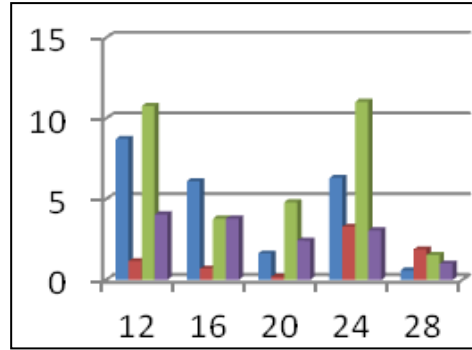
Statistical analysis was performed to assess the significance of the three wall thickness modeling strategies in the ensuing eight biomechanical parameters. Mean \pm std. deviation for each of these – σ_{max} , ε_{max} , ψ_{max} , δ_{max} , σ_{avg} , ε_{avg} , ψ_{avg} , and δ_{avg} were calculated for the UT, PSUT, and PSNUT approaches and the percentage errors is reported for UT and PSUT with PSNUT as the reference standard. In addition, the following 3 hypotheses were tested: (A) There is a significant difference in all eight mechanical parameters when modeling the AAA wall with PSNUT compared to modeling the wall with UT; (B) There is a significant difference in all eight mechanical parameters when modeling the AAA wall with PSNUT compared to modeling the wall with PSUT; (C) There is significant difference in the eight mechanical parameters when modeling the AAA wall with PSUT compared to modeling the wall with UT. A series of two-sample t tests were done at a significance level of $\alpha = 0.05$ to compare the different pairs of wall thickness modeling strategies. Twenty-four two-sample t tests were performed to address the aforementioned hypotheses for each of the biomechanical parameters resulting from the FEA simulations.

4.3 RESULTS

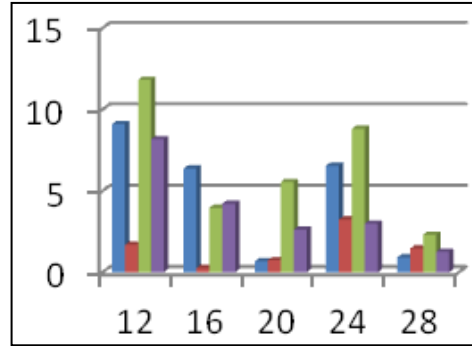
Reasonably good results were obtained for 2 layer volume mesh and corresponding surface mesh density that gives aspect ratio close to 1 (mesh #6) and that was still within feasible computational load. Hence, this combination of surface mesh size and number of layers of extrusion was finalized. Maximum principal stress, maximum principal strain, strain energy density, and displacements were analyzed to explore variability in the outcome of the 84 simulations using UT, PSUT, and PSNUT strategies for modeling the AAA wall. Figure 50 shows the percentage incremental change in these biomechanical parameters for each step of increasing the total number of mesh elements as a part of the mesh convergence study. Table 21 and Table 22 provide details about the mean and standard deviations for biomechanical parameters for different AAA models. As expected, larger variability is found in the maxima of these parameters compared to variability in the respective spatial averages.

For each AAA model, the percentage errors in UT and PSUT were calculated with respect to PSNUT, which is hypothesized to be a more precise estimation of the biomechanical parameters. These errors averaged over 28 cases, with and without accounting for the respective sign, are shown in Table 23 (spatial maximum) and Table 24 (spatial average). Except for displacement, there is a consistent underestimation of the maximum biomechanical parameters by UT and PSUT, as the magnitude of the average percentage error remains the same for both signed and unsigned averages. In case of spatially averaged quantities signed average closer to zero but unsigned average with substantially different magnitude indicate that there is underestimation as well as overestimation relative to PSNUT.

a) 120 mm Hg



b) 80 mm Hg



c) 40 mm Hg

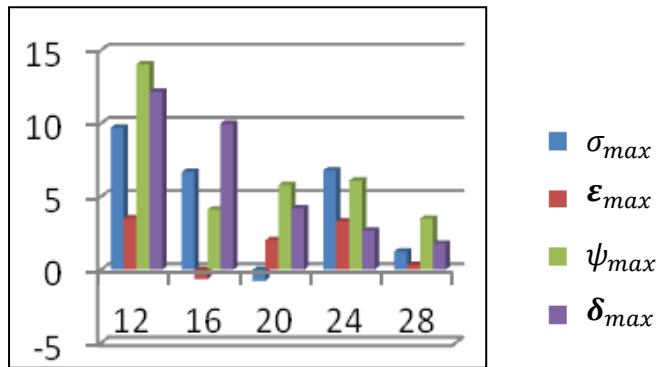


Figure 50: Convergence study showing incremental percentage differences (y-axis) in biomechanical parameters along with an increase in the factor (x-axis) governing average edge length of the surface mesh elements used for wall extrusion (proportional relationship). An increase in the number of elements will have a quadratic relationship with this factor. Convergence study pertaining to: a) systolic blood pressure (120 mmHg); b) diastolic blood pressure (80 mmHg); c) amplitude of pressure wave (40 mmHg)

Table 21: Statistical summary of maximum biomechanical parameters for the wall thickness modeling strategies.

	σ_{max} (N/cm ²)	ϵ_{max}	ψ_{max} (erg/cm ³)	δ_{max} (cm)
UT	50.18 ± 9.45	0.2674 ± 0.0191	627305.3 ± 162427.1	0.4697 ± 0.1067
PSUT	47.36 ± 12.50	0.2594 ± 0.0299	674615.4 ± 209151.9	0.4489 ± 0.1246
PSNUT	63.56 ± 15.51	0.2870 ± 0.0290	864753.8 ± 281824.6	0.4738 ± 0.1256

Table 22: Statistical summary of spatially averaged biomechanical parameters for the wall thickness modeling strategies.

	σ_{avg} (N/cm ²)	ϵ_{avg}	ψ_{avg} (erg/cm ³)	δ_{avg} (cm)
UT	21.70 ± 2.16	0.1383 ± 0.0080	179808.1 ± 23721.9	0.2175 ± 0.0350
PSUT	20.67 ± 5.67	0.1331 ± 0.0188	164540.4 ± 74442.2	0.2089 ± 0.0407
PSNUT	20.99 ± 5.47	0.1336 ± 0.0180	175725.7 ± 65895.4	0.2146 ± 0.0397

Table 23: Signed and unsigned average of percentage errors in 28 datasets considering the maximum biomechanical parameters in the AAA sac. Consistent underestimation is seen as there is little difference in signed and unsigned averages of the %error in biomechanical parameters for UT and PSUT approach (using results from the PSNUT strategy as the reference standard). S – Signed, US – Unsigned.

	σ_{max} %error		ϵ_{max} %error		ψ_{max} %error		δ_{max} %error	
	S	US	S	US	S	US	S	US
UT	-17.70	20.64	-6.16	8.75	-22.02	27.61	1.15	11.23
PSUT	-24.22	24.46	-9.56	9.61	-32.36	32.36	-4.90	6.56

Table 24: Signed and unsigned average of percentage errors in 28 datasets considering average values of the biomechanical parameters in the AAA sac. No consistent underestimation or overestimation is seen as there is appreciable difference in signed and unsigned averages of the %error in biomechanical parameters for UT and PSUT approach (using results from the PSNUT strategy as the reference standard). S – Signed, US – Unsigned.

	σ_{avg} %error		ε_{avg} %error		ψ_{avg} %error		δ_{avg} %error	
	S	US	S	US	S	US	S	US
UT	9.48	22.82	5.17	11.48	15.91	34.95	2.76	11.63
PSUT	-1.79	3.13	-0.38	1.37	-7.38	8.29	-2.75	3.36

Table 25: p-values obtained by ANOVA analysis for maximum biomechanical parameters corresponding to three approaches for wall thickness modeling

	Hypothesis (A) PSNUT and UT	Hypothesis (B) PSNUT and PSUT	Hypothesis (C) PSUT and UT
σ_{max}	0.0003	7. 513e-05	0.3466
ε_{max}	0.0047	0.0010	0.2362
ψ_{max}	0.0004	6. 211e-05	0.2974
δ_{max}	0.8976	0.4601	0.5043

Table 26: p-values obtained by ANOVA analysis for average biological parameters corresponding to three approaches for wall thickness modeling

	Hypothesis (A) PSNUT and UT	Hypothesis (B) PSNUT and PSUT	Hypothesis (C) PSUT and UT
σ_{avg}	0.5263	0.8287	0.3734
ε_{avg}	0.2092	0.9296	0.1857
ψ_{avg}	0.7596	0.5541	0.3088
δ_{avg}	0.7692	0.5972	0.3969

For the maximum biomechanical parameters, with respect to the three hypotheses (A), (B), and (C), postulated for the statistical analysis, the aforementioned results and the Box-and-whisker plots illustrated in Figure 51 support hypothesis (A) for the first three biomechanical parameters (σ_{max} , ε_{max} , ψ_{max}), but this is not so for the

variable δ_{max} ; the p-values were, respectively, 0.0003, 0.0050, 0.0004, and 0.8976. Hypothesis (B) is also found true for parameters (σ_{max} , ϵ_{max} , ψ_{max}), but not for δ_{max} with p-values of 7.513e-05, 0.0010, 6.211e-05, and 0.4601, respectively. In addition, hypothesis (C) is proven for all biomechanical parameters: the p-values were 0.3466, 0.2362, 0.2974, and 0.5043, for σ_{max} , ϵ_{max} , ψ_{max} , and δ_{max} respectively. A comparative regional distribution of the four biomechanical parameters obtained by the UT, PSUT, and PSNUT approaches are shown in Figure 52 and Figure 53 using an exemplary AAA model.

For the spatially averaged biomechanical parameters, none of the hypotheses stated in Section 4.2.8 were found true.

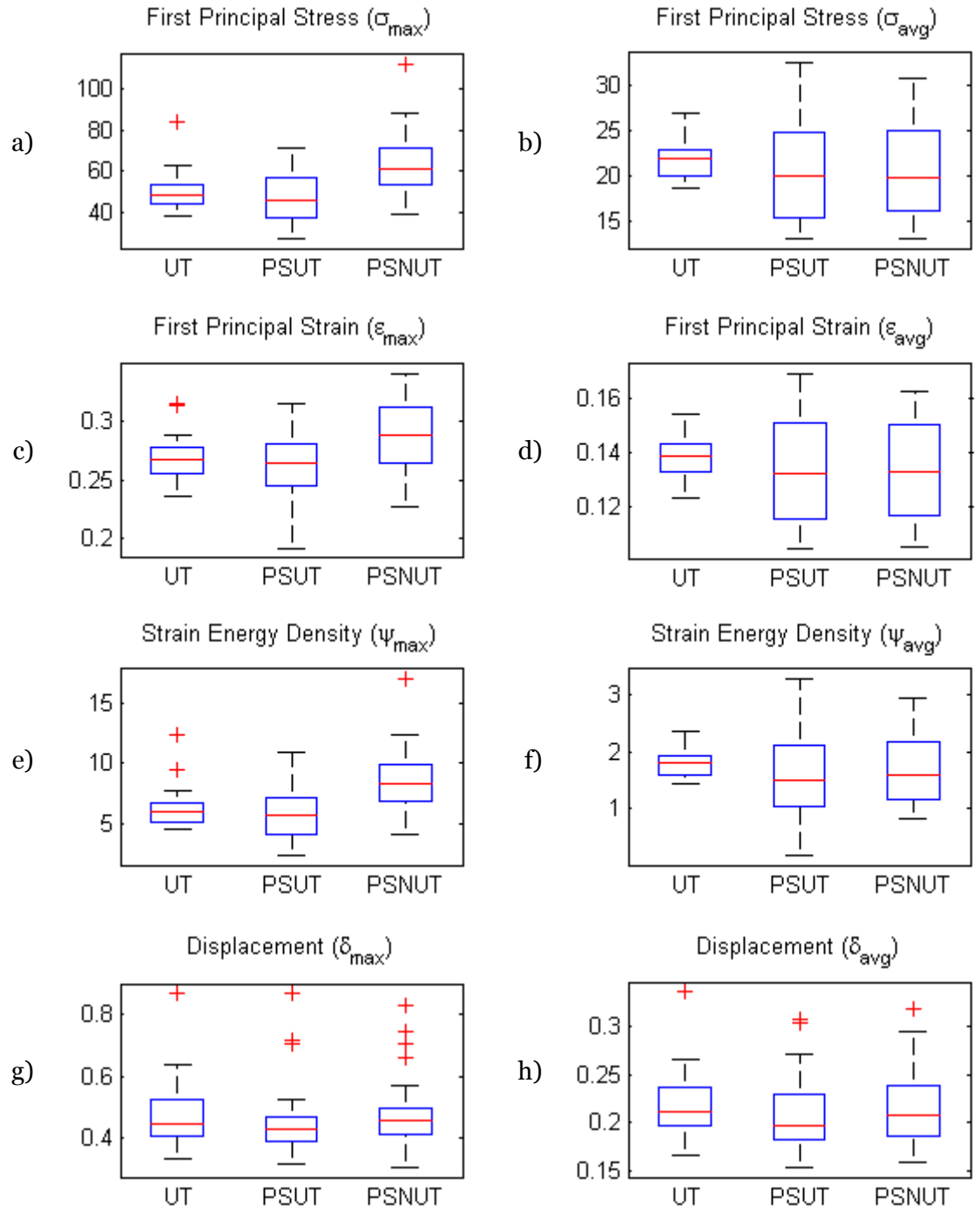


Figure 51: Box-and-whisker plots highlighting differences in results for three wall thickness modeling strategies, a) Maximum first principle stress (N/cm^2); b) Average first principle stress (N/cm^2); c) Maximum first principal strain; d) Average first principal strain; e) Maximum strain energy density ($10^5 \text{ erg}/cm^3$); f) Average strain energy density ($10^5 \text{ erg}/cm^3$); g) Maximum displacement (cm); h) Average displacement (cm).

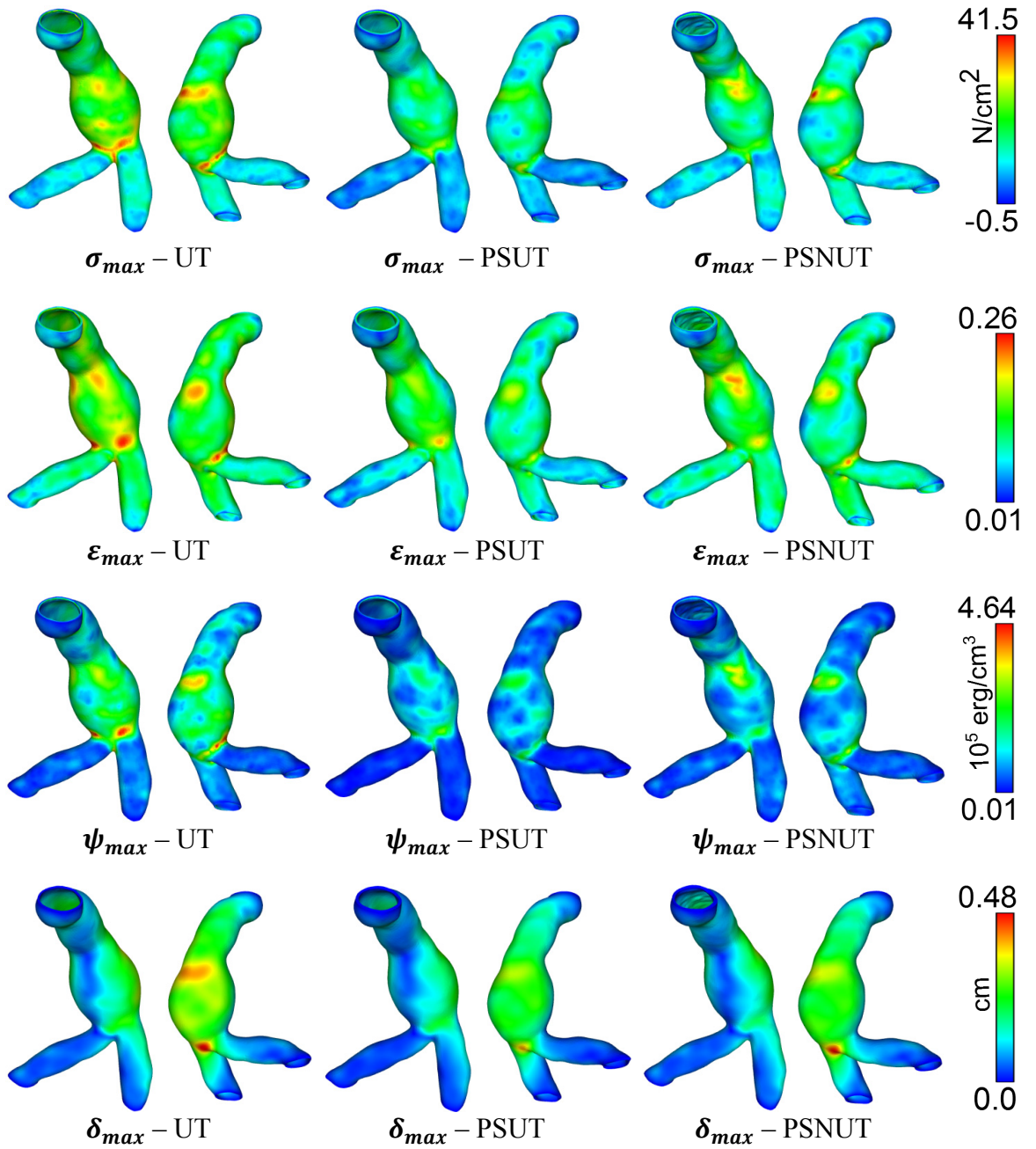


Figure 52: Comparison of regional distribution of the biomechanical parameters for AAA model U037 obtained with UT – uniform thickness (=0.15 cm), PSUT – patient-specific uniform thickness (=0.2044 cm), PSNUT – patient-specific non-uniform thickness (=0.2044 ± 0.0487, minimum 0.07615, max = 0.3991, unit: cm). PS1 – maximum principal stress, PE1 – minimum principal strain, SED – strain energy density, Disp – Displacement magnitude.

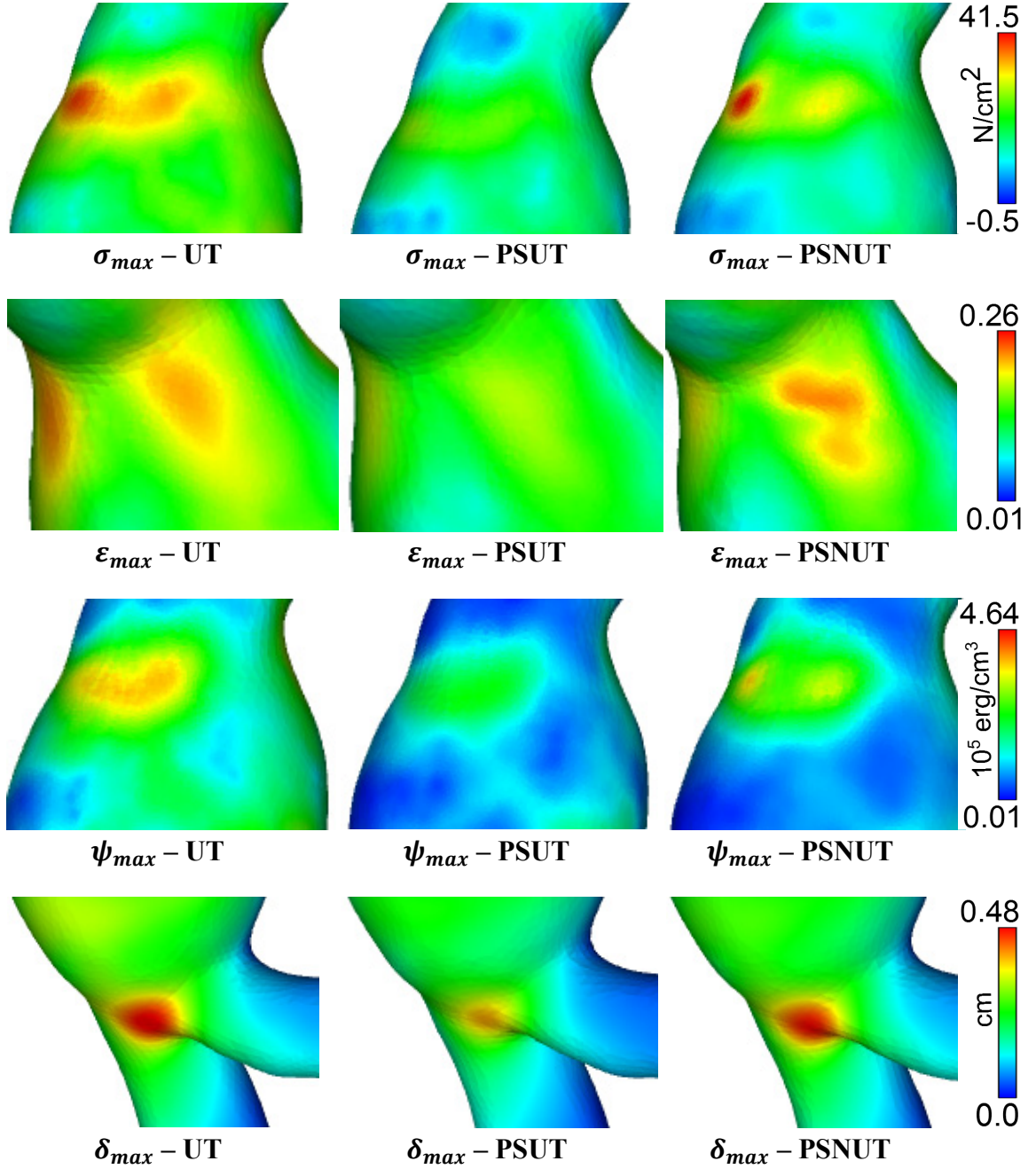


Figure 53: Zoomed view of the comparison of regional distribution of the biomechanical parameters for AAA model U37 obtained with UT – uniform thickness (=0.15 cm), PSUT – patient-specific uniform thickness (=0.2044 cm), PSNUT – patient-specific non-uniform thickness (=0.2044 ± 0.0487, minimum 0.07615, max = 0.3991, unit: cm). PS1 – maximum principal stress, PE1 – minimum principal strain, SED – strain energy density, Disp – Displacement.

4.4 DISCUSSION

This work presents an investigation of in vivo computational analysis of AAA biomechanics with implementation of patient-specific variable wall thickness and the estimation of relative errors when using the traditional assumption of a uniform wall thickness. It advances the vascular biomechanics field toward more realistic modeling for in vivo analysis, as wall thickness is an important aspect of the vessel geometry that affects mechanics [204]. As seen in our analysis of 28 AAA models resulting from the processing of clinical image datasets, modeling regional distributions of individual wall thickness of the AAA sac resulted in statistically significant changes in the outcome of FE analysis assessed by the maxima of the three biomechanical parameters of interest: first principal stress, first principal strain, strain energy density.

4.4.1 The need for modeling non-uniform wall thickness

Recent experimental work reported by Doyle et al [151] is a valuable contribution to the field. They inflated silicon AAA prototypes until rupture and used high speed photography to identify the location of material failure. They note that the average thickness at the site of rupture was significantly lower than the global mean thickness, which agrees with the observation made by Raghavan et al for ruptured AAAs [93]. Although, they further comment that the thinnest wall is not necessarily found at the rupture location and that wall thickness does not correlate with the pressure required for rupture, their observations support the notion that rupture is a local phenomenon and hence keen attention is necessary to model regional geometric variations, especially wall thickness. Doyle and colleagues also note that the location of rupture was generally not at the maximum diameter. Therefore, not only correct implementation of wall thickness is necessary but close attention should be paid to the accuracy of the surface reconstruction to capture surface curvature without losing local feature due to smoothing.

The outcome of the present work strongly advocates for the need to implement patient-specific non-uniform thickness modeling. Since the population sample was selected using a diameter-matched approach, this yields a size-related geometric index as the control variable. In addition, the range of diameters is justified by the fact that all 28 patients would have been eligible for elective repair in the majority of hospitals in the U.S. Based on the analysis of the 84 simulations, the PSNUT modeling strategy results in significantly higher maximum principal stresses, principal strains, and strain energy densities compared to the UT and PSUT strategies. An average difference of about 20% was observed in PSUT and UT with respect to PSNUT for the three aforementioned biomechanical parameters. The difference in displacements, however, was not statistically significant. A qualitative observation of Figure 52 and Figure 53 indicates that even though the magnitudes are different, the regional distribution pattern of these parameters is similar for AAA model U037 irrespective of the wall thickness approach used. Even though calculation of δ_{max} did not appear statistically significant, error calculations as per Table 23 suggest that wall thickness modeling approach affects it too.

The effect of wall thickness modeling approach on spatially averaged values of biomechanical parameters was not significant. Table 24 however implies appreciable error when comparing errors in UT approach vs. PSNUT. In case of PSUT approach, errors were not found as large as errors in the maxima or average parameters using UT approach. As seen in box plots in Figure 51 and Table 22, averaged values for stresses, strains, and strain energy densities had more variability in PSNUT and PSUT approach compared to UT approach amongst 28 patient-specific AAA cases.

Both maximum and spatially averaged displacement values in particular are found to be underestimated as well as overestimated using UT approach when compared

to PSNUT since the signed average of error remains close to zero but appreciable magnitude is observed in unsigned average as per Table 23 and Table 24. The observation that displacement calculation using PSUT is not very different than that of PSNUT together with the difference observed in displacement comparison PSNUT vs. UT implies that displacement is not heavily dependent on regional variation but is a function of overall shape of AAA and average wall thickness value used in modeling wall domain.

These observations are in agreement with recent results published by Shum et al [100], where wall thickness was one of the four important morphological indices that adequately discriminated between ruptured and unruptured AAAs. In that study, the statistical analysis of the morphological metrics showed that maximum diameter alone would have classified ruptured and electively repaired aneurysms with 38.2% accuracy whereas wall thickness was one the four features used in a decision tree model with 86.6% accuracy. The thickness data for this work was previously derived by Shum and colleagues using the method described in [91], which is the only source in the literature with the capability to assess thickness at 72 points on each CT image with low relative errors with respect to reference standards. With the segmentation capabilities of VESSEG, non-invasive quantification of AAA geometry was made possible [99-101], as well as the wall mechanics assessment with regional distributions of wall thickness as described herein.

4.4.2 Wall extrusion vs. mask dilation approach

We have established in our framework that hexahedral mesh generation by means of surface extrusion is a technique inherently suitable for this purpose. A similar approach has been previously reported in the AAA literature, but for a uniform wall thickness assumption [123, 199]. However, outward extrusion from the inner wall surface [198,

199] has the disadvantage that bifurcations exhibit high concavity, which limits the thickness of the extrusion to a smaller value. This *bifurcation challenge* can be solved if we perform extrusion inwards (from the outer wall surface), representing the bifurcation region as a convex surface.

An alternative approach for image based modeling of uniform thickness in vascular wall, widely used in multi-purpose image segmentation and 3D reconstruction software (e.g., Simpleware, Mimics, Amira, etc.), is to use mask dilation. However, as seen Figure 54, there are many shortcomings of this approach in addition to those explained in Figure 11. In-plane errors involve discrepancies introduced due to the rectangular grid of the image and discrete operations (Figure 54a) Additionally, when images are stacked in 3D after dilation, the actual thickness along the local surface normal is dependent on the direction of the normal itself for given constant dilation value 't' (Figure 54b) Finally, effective in-plane dilation is proportionally varying from 1 pixel length (px) along the grid axes to 1.4142 px along a direction 45° to the axes, for every pixel of dilation. These changes are subtle, but important as a 1 px error may yield a significantly different wall geometry given that a typical wall thickness of the abdominal aorta is about 2 mm while the size of 1 px on a CT images is about 0.75 mm. Therefore, a discrete error of one pixel yields a local change of ~40% in wall thickness. These errors may also have implications for the accurate and robust execution of the subsequent mesh generation operations, as it may result in an unrealistic intersection of the inner and outer wall surfaces. Additionally, intermediate surface smoothing actions may distort actual wall thickness that reflects in the final volume mesh. Hence, mask operations are recommended for bulky domains such as ILT and lumen, but not for thin walls for which a surface extrusion operation is inherently suitable.

4.4.3 Comments on convergence study

It should be noted that the mesh convergence study may appear to have unexpected results compared to other widely documented indices of convergence (e.g., the grid convergence index (GCI) used in fluid flow modeling [210]). However, this analysis and the chosen element size are deemed appropriate for the following reasons.

- i) Concerning the ideal requirement of embedded refinement for a mesh convergence study as reported in [148], the present work does not consist of the refinement of a pre-existing mesh where the new dense mesh is generated from an existing coarse mesh. That approach is feasible for ideal shapes and smaller number of elements, but not for patient-specific reconstructions where optimal agreement with the 3D image data is imperative.
- ii) We observe from Figure 50 that with the decrease in surface mesh size, the numerical errors gradually decrease to size 16 and start increasing beyond that size. This can be explained using the aspect ratio of the volume elements. Since the extrusion height per element layer is consistent in all models, a larger size yields elements that tend to be flat (with aspect ratio < 1) whereas with a finer mesh they tend to be elongated (aspect ratio > 1); an element size 16 results in an aspect ratio ~ 1 .
- iii) The surface mesh extrusion method has the inherent limitation that if the base surface mesh is too dense with respect to the length of the extrusion, then the element quality will be poor where the surface curvature is high. Thus, a very refined surface mesh does not ensure accurate results as those could be distorted due to poor mesh quality.

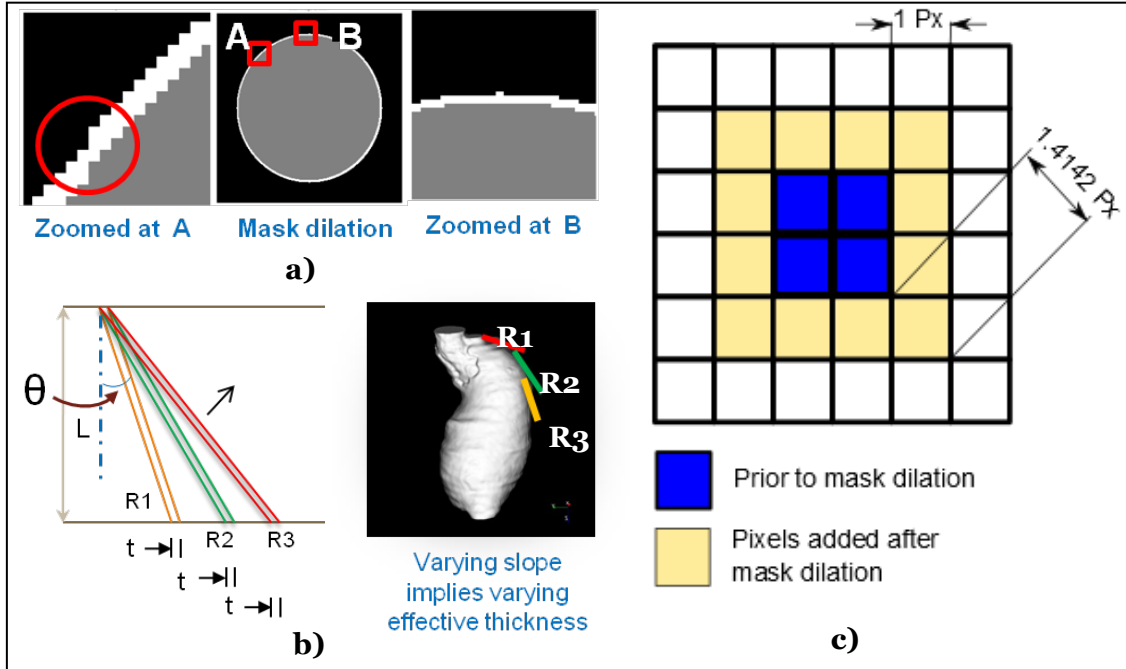


Figure 54: Limitations of mask dilation approach for wall thickness modeling: a) errors due to inherent differences in rectangular image grid and circular shape of the anatomy; b) effective thickness along the local normal direction is a function of the slope in the plane normal to the image for the same dilation 't' in the image plane (L denotes the direction of image stacking); c) Schematic with 1 px dilation showing non-uniform dilation around the periphery (Px – pixel resolution).

4.4.4 Limitations

The present work is subject to limitations that should be taken into account when extending the applicability of its findings for clinical management of AAA disease. The patient-specific data considers only 28 AAA datasets, which is a relatively small sample size. The FEA simulations do not account for the anisotropy of the aortic wall [115, 116] nor is an active mechanics constitutive model considered (elastin, collagen, and smooth muscle activation). Moreover, this work did not consider patient-specific intraluminal blood pressure as a boundary condition and initial stresses were ignored. Nevertheless, as noted earlier [148], AAA wall stress distributions do not change significantly with increasing internal pressure. Hence, it is inferred that the outcome of this work may still be applicable as it is based on the comparison of wall thickness modeling strategies for

the same constitutive material model and intraluminal pressure. A limitation of the wall extrusion approach is that for very thick walls with large local surface curvature, volume elements are likely to intersect with each other, although we expect for the approach to be suitable for modeling most human blood vessels. Finally, when the local surface is more or less tangential to the image acquisition planes, the segmentation becomes complex and even a small error in segmentation yields inaccuracies in the wall thickness estimation. Hence, additional work is necessary to improve image segmentation algorithms suitable for such regions.

4.5 CONCLUSION

Our in-house framework for implementing non-uniform wall thickness has been successfully implemented for AAA biomechanical analysis in a cohort of 28 patient-specific image datasets. Based on the level of significance achieved when testing the statistical hypotheses, we conclude that individual regional variations of wall thickness and their accurate implementation in numerical models should be a required feature for rupture risk analysis of AAA. A uniform wall thickness assumption, typically used in the literature, will yield statistically different stresses, strains and strain energy densities compared to a regionally varying wall thickness model. Conversely, similar wall mechanics results should be expected irrespective of the uniform thickness used in the model. Future work will incorporate a multi-layer structure to the wall geometry and the use anisotropic material properties and active mechanics models.

Chapter 5. Development of a Framework for the Estimation of In Vivo Patient-Specific Strain of the Diseased Abdominal Aorta

5.1 INTRODUCTION

Deformation and strain in an AAA are integral and important part of the arterial biomechanics. It is important to understand local deformation patterns and strains in AAA for better intravascular device design [211, 212] as well as for non-invasive assessment of risk and to improve our knowledge of the disease in general. With recent advances in medical imaging, in vivo assessment of deformation is possible. Knowledge of deformations is also valuable to biomedical engineers for mechanical optimization of balloon angioplasty and stenting, vessel grafts, arterial replacement tissues, and computational simulations[212]. Stiffness of a vessel, and hence changes in the deformation magnitude and pattern, have been related to diagnosis of many diseases. Thus, that is a valuable information for clinicians [212]. Recent literature highlights anisotropic nature of aneurysmatic wall [88, 111].

Artery wall is also reported to be heterogeneous [115]. It is a layered composite material where collagen fiber recruitment offers higher stiffness at higher strains [213]. Even though the ex vivo material characterization [3, 111, 207] aspect has received some attention of research community, the in vivo strain measurement has been neglected to some extent, especially in case of AAA where due to complicated geometry simplified assumptions of cylindrical shape cease to apply.

Different metrics have been used for quantifying deformations and stiffness of blood vessel. Pulsatility [214, 215] measures extent of radial displacement during single cardiac cycle in terms of diameter difference. Longitudinal strain, curvature change, and axial twist have also been reported as metrics to quantify geometry change of normal blood vessels [211]. Similarly, blood vessel stiffness has been expressed in different ways. Distensibility represents fractional change in cross-sectional area or volume per unit

change in intraluminal pressure. Compliance is expressed as volume change per unit intraluminal pressure change [216, 217]. Pressure-strain modulus measures change in pressure per unit change in radial or diametral strain [217]. Stiffness constant is another dimensionless modulus [217]. The Hudetz incremental modulus of elasticity [218-220] characterizes the radial and tangential stiffness complexly.

In vivo strain estimation and characterization of normal healthy arteries has received some attention. Assuming aorta to be a perfectly cylindrical pseudo-elastic orthotropic thick tube under internal pressure, Stalhand et al [221] proposed a material model with parameters that can be calibrated in terms of in vivo measureable data. Work explicitly pertaining to quantification of blood vessel's in vivo deformation has been reported by Muhs et al [214] using AAA patients; however, the diameter changes reported are for the distal thoracic aorta (DTA). Similarly, Van Prehn et al [215] reported diameter changes in the ascending and distal thoracic aorta for AAA patients. To the best of our knowledge, except the work of Tierney et al [220], which identifies four quarters along the circumference for regional distribution of material properties, none of the previous literature toward in vivo characterization of a vessel account for heterogeneity. This aspect is important for AAA material characterization, which has been found to be heterogeneous [93, 207]. With the exception of Choi et al [211], all in-vivo assessments are based on in-plane 2D deformations [214-216, 220, 222, 223]. Out of plane motions are ignored and a circular cross-section is assumed for defining metrics [215].

In this work we present a novel methodology to estimate true 3D surface deformation and strains in AAA. The study involves time resolved black blood MRI (FIESTA) (not a standard of care for AAA patients) as a part of prospective study of 20+ AAA patients. Based on 20-phase ECG gated image data within a single cardiac cycle and

using image based reconstruction of tessellated surface representation for reference (diastolic) and deformed geometry, we identify nodal displacement under the assumption that all nodes move along local normal direction. Using standard continuum mechanics approach strains are evaluated from this displacement field. This novel pipeline makes elegant use of our in-house image-based geometric reconstruction code as well as tools available in standard commercial post-processing software for purely kinematic analysis without involving any Finite Element (FE) simulation. To the best of our knowledge, this is the first work that reports a technique and outcomes for in vivo, 3D, regionally variable strain distribution devoid of FE analysis. It is independent of any assumption regarding local shape approximation (spherical, paraboloid surface patch), as well as global shape approximation (e.g., cylinder, sphere). It also does not need to evaluate the centerline of a blood vessel for anatomical markers.

5.2 METHODS

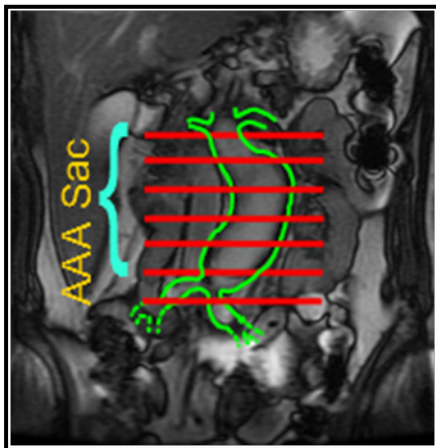


Figure 55: Schematic of the imaged AAA in the coronal plane, from the renal arteries to the aorto-iliac bifurcation; AAA sac slices in a transverse plane were used for this study.

5.2.1 Image acquisition and segmentation

Our study population consists of a human subject with unruptured AAA (73 year-old male, sixty years of smoking history, hypertensive, brachial cuff pressure measurement 144/90 mmHg and heart rate 83 bpm on the day of scanning). Patient was recruited as per IRB approval at Allegheny General Hospital (AGH), Carnegie Mellon University (CMU), and The University of Texas at San Antonio (UTSA). Abdominal DICOM images were

free precession (commercial name - FIESTA) MR pulse sequence. Twenty phases were acquired per cardiac cycle. Slice thickness and slice spacing both were 6 mm with scan size of matrix 256×256 . Pixel resolution was 1.5625×1.5625 mm. Figure 55 shows the imaged region of abdominal cavity and aneurysm sac schematically.

Image segmentation was performed and the contours representing outer surface were generated using the JAVA application based free software MIPAV (version 5.4.3, Center for Information Technology, NIH, Bethesda, MD. <http://mipav.cit.nih.gov/>), which provides image segmentation and visualization capabilities. Segmentation was performed on 10 alternate phases amongst the acquired 20 phases. Binary masks obtained from segmented contours were later used for FE discretization using our in-house MATLAB based software for mesh generation.

5.2.2 3D Surface reconstruction

MATLAB based mesh generation software AAAMesh [202] was employed for generating a high quality surface mesh. Previously generated binary masks corresponding to each phase are stacked along the direction normal to imaging plane (z-axis). Continuous distance field was generated based on discrete values defined at voxels (grid points) in stacked masks. A triangular (3-noded facets) surface mesh for AAA outer wall surface was extracted as an isosurface from distance field derived from the mask data. Finalized size of surface mesh element was deemed to be sufficiently resolved to capture geometry appropriately. Our previous work [202] details quantified errors associated during reconstruction using AAA phantom. Sliver removal procedure ensures very good quality elements (ratio of radii of incircle and circumcircle normalized with ideal value of 0.5 ($r-R$ ratio) > 0.6 , average $r-R$ ratio ≈ 0.96 where, 1 is ideal value). Because of the good quality triangulation of the surface, a set of uniformly distributed discrete points (nodes)

is generated facilitating better capturing of the deformation field. Reconstructed AAA surfaces for phase#1, phase #3, and phase #19 are shown in Figure 56, with superposition of phases #1 and #3, and phases #1 and #19, to illustrate the differences in geometry at each pair of image acquisition phases.

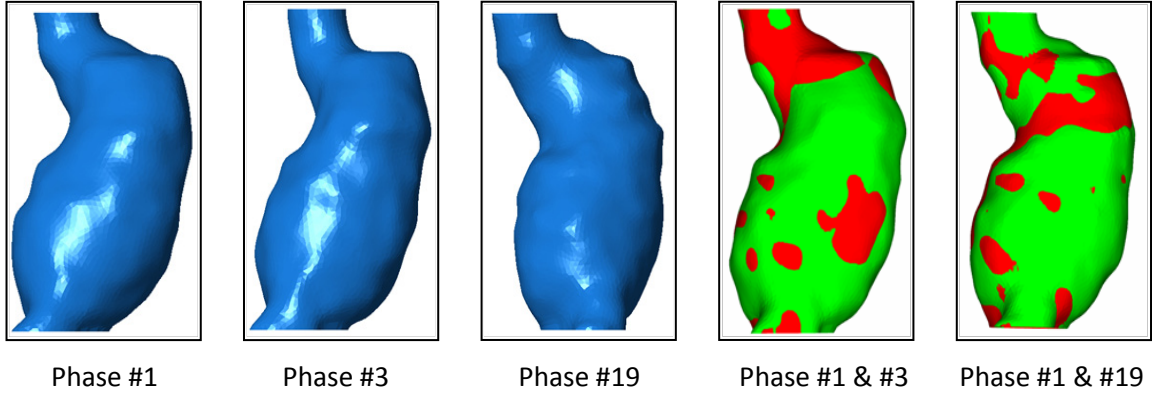


Figure 56: Exemplary reconstructed AAA outer surfaces for phase #1, #3, and #19 and superimposition of phase #3 and phase #19 with phase #1.

5.2.3 Intraluminal pressure estimation

Pressure wave profile is difficult to measure in vivo without invasive means. Hence, we rely on the work by Veer et al [1] who observed that the brachial cuff pressure underestimates systolic pressure inside the AAA by 5% whereas the brachial cuff diastolic pressure was 12% overestimation of AAA diastolic pressure. Thus, we can correlate the systolic brachial cuff pressure (P_{br}^s) and systolic AAA intraluminal pressure (P_{AAA}^s) as well as between diastolic brachial cuff pressure (P_{br}^d) and diastolic AAA intraluminal pressure (P_{AAA}^d):

$$P_{br}^s = 0.95P_{AAA}^s \rightarrow P_{AAA}^s = \frac{P_{br}^s}{0.95} \quad \dots \text{Eqn. 5-1}$$

$$P_{br}^d = 1.12P_{AAA}^d \rightarrow P_{AAA}^d = \frac{P_{br}^d}{1.12} \quad \dots \text{Eqn. 5-2}$$

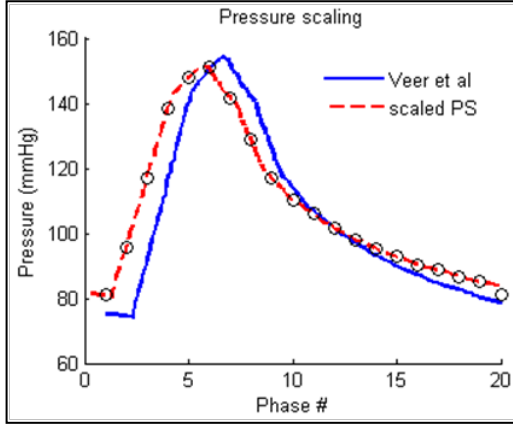


Figure 57: Scaled pressure waveform for patient #1 obtained by combining patient-specific brachial cuff measurements with data reported earlier by Veer et al [1].

Using patient-specific brachial cuff pressure measurements, pressure wave reported by Veer et al [1] can be scaled to satisfy patient-specific aneurysmatic systolic and diastolic pressure obtained by above formulas. Figure 57 shows scaled pressure for patient (scaled PS) where brachial cuff systolic/diastolic pressure 144/90 mmHg was scaled to profile as shown with corrected pressure 151.58/

80.36 mmHg. The advantage of this protocol is that it incorporates patient specificity in prescribed outlet pressures using non-invasive and easily measured cuff pressure. Although more accurate patient specific intraluminal pressure may be obtained by direct measurement using catheter insertion, it is not feasible for obvious reasons.

5.2.4 In vivo strain estimation

5.2.4.1 Continuum theory

Consider a continuum body under deformation as shown in Figure 58. Here, Ω_0 is original reference configuration, Ω' is deformed configuration with $\vec{u} = \vec{x}(\vec{X}) - \vec{X}$ representing Lagrangian description of the displacement field. Note that in this brief derivation \vec{u} is not required to be along the local surface normal as shown, however, in the AAA deformation problem we assumed such normal displacement pattern (both inward and outward) for exploring displacements. This assumption is justified since there is no significant source of shearing (tangential) force in AAA. Figure 64 endorses this assumption.

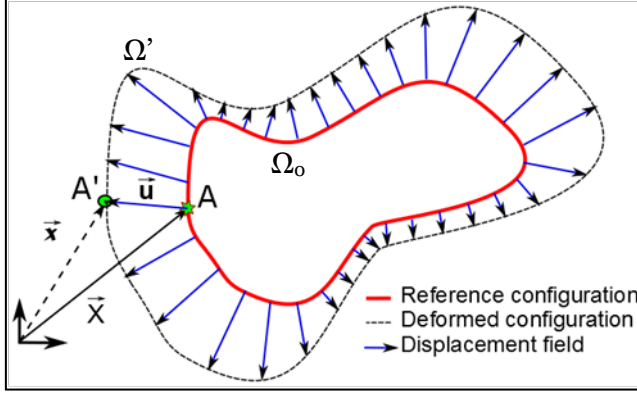


Figure 58: 2D schematic of deformation; reference configuration (Ω_0), deformed configuration (Ω'), displacement vector field (\vec{u}), and position vectors \vec{X} and \vec{x} .

If \vec{X} is position vector for any point A in reference configuration and \vec{x} is position vector of new position vector for the same point after deformation A' , deformation gradient tensor \mathbf{F} is given by,

$$\mathbf{F} = \frac{\partial \vec{x}}{\partial \vec{X}} \quad \dots \text{Eqn. 4-3}$$

However, as seen in Figure 58, $\vec{x} = \vec{X} + \vec{u}$. Hence, we can re-write above equation as,

$$\mathbf{F} = \mathbf{I} + \frac{\partial \vec{u}}{\partial \vec{X}} = \mathbf{I} + \mathbf{Grad}(\vec{u}) \quad \dots \text{Eqn. 4-4}$$

where, \mathbf{I} is identity tensor. Once \mathbf{F} is evaluated, right Cauchy-Green tensor (\mathbf{C}) can be obtained by, $\mathbf{C} = \mathbf{F}^T \cdot \mathbf{F}$. Green-Lagrange strain tensor (\mathbf{E}) is given by,

$$\mathbf{E} = \frac{1}{2} (\mathbf{F}^T \cdot \mathbf{F} - \mathbf{I}) \quad \dots \text{Eqn. 4-5}$$

5.2.4.2 Evaluation of the displacement field

As seen in the aforementioned derivation, the important field to be determined is the displacement vector field \vec{u} . In the present work, reference configuration was configuration at phase #1 which is sufficiently close to diastolic phase. Systolic phase is expected to occur at around phases #6 to #9 based on the voxel volume estimation for a small slab within stacked mask data near the maximum diameter. We used above

approach by collectively using our in-house mesh generation code with commercial post-processing software EnSight (Computational Engineering International, Inc., Apex, NC) to use its capability to calculate distance between two surfaces with prescribed outward local normal direction as the positive direction. We evaluated surface outward normals on reference configuration and provided those as reference directions to dictate positive sign of distance field scalar. It may appear trivial to calculate the minimum distance between two objects by considering node-to-node distance between them. However, it is important to note that unless surface meshes for Ω_0 and Ω' are obtained by mesh generation methodology like deformable bodies that ensure bijective mapping between nodes in reference and deformed configurations, node-to-node distance calculation will not be appropriate as calculated displacement gradient may have serious fluctuations depending on location of nearest neighbor node from other surface mesh. Note that the deformable model approach in turn has its own limitation in terms of how much distortion with respect to template mesh can be sustained without resulting in bad quality mesh. The methodology used in EnSight can calculate distance from elements in addition to that from nodes. Thus, for example, if the closest point on a target surface to a node from source surface mesh lies somewhere mid-way on an edge of an element of target surface, then this approach would give correct minimum distance whereas node-to-node distance might be at huge error as well as there would be spatial fluctuations which would severely distort strain field calculation. Finally, the distance field obtained using above procedure is a scalar field which is then multiplied with local surface normal direction to obtain displacements vector field.

5.3 RESULTS

Using Green-Lagrange strain tensor information, obtained as described earlier, maximum principal strain values are calculated and their distribution shown in Figure 59. However, we noticed that locally intensified unrealistic magnitudes of strains are seen near neck region and near bottom edge. This may be attributed to the failure to capture huge gradients in object surface using current resolution of image and image contrast. Hence, those regions were discarded from analysis. As shown in Figure 60, Zone #1 (cyan) and Zone #2 (green) were identified. Zone #1 covers most of the geometry and can be used as an equivalent of entire aneurysm. Zone #2 is a relatively small zone that was obtained to closely monitor behavior near the maximum diameter as well as due the fact that short axial length would efficiently capture pulsatile behavior avoiding any averaging effects that may occur in larger zone dampening the pulsatile nature.

In Figure 62, variation of first principal strain in zone 1 and zone 2 over entire cardiac cycle is depicted. Note that at phase #9 maximum of zone #1 lies within zone #2 and hence both data point coincide with each other. Outlier point for zone #1 at phase 11 is attributed to located bump in surface probably originating from locally incorrect segmentation contour.

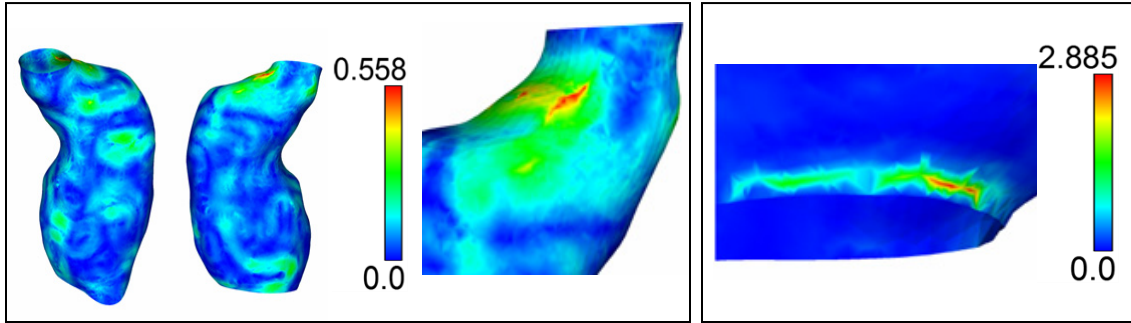


Figure 59: Unrealistic first principal strain near distal end and neck region (likely due to lack of image contrast and resolution related distortions).

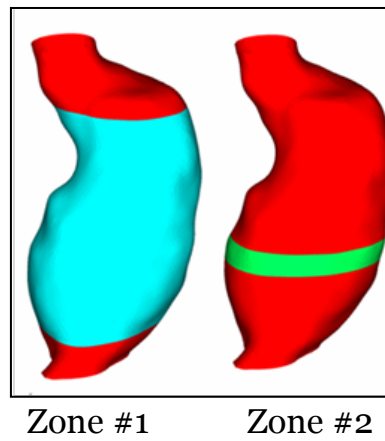


Figure 60: Depiction of zones #1 and #2 considered for analysis.

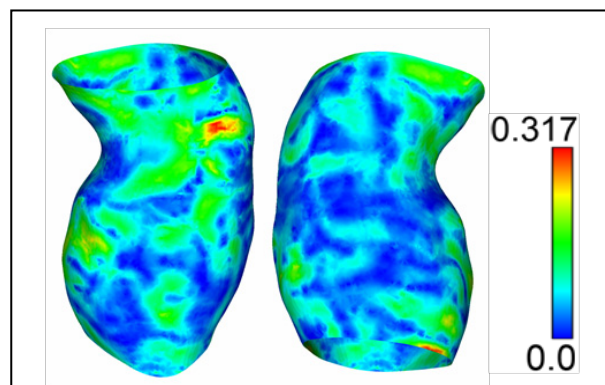


Figure 61: Strain distribution at zone #1 evaluated at near systole.

To make an assessment of the overall mechanical behavior, we explored the area weighted mean of maximum principal strains defined over triangular surface mesh. Figure 63 shows variation of this mean value of maximum principal strain over a full cardiac cycle. It is confirmed that systole occurs near phase #9. Regional variation of the first principal strains in this near-systolic phase is shown in Figure 61. Pressure change, spatially averaged first principal strain values, and corresponding pressure-strain modulus (M) obtained by following equation Eqn. 5.6 is enumerated in Table 27.

$$M = \frac{\text{change in pressure}}{\text{spatially averaged first principal strain}} \quad \dots \text{Eqn. 4-6}$$

Table 27: Pressure-strain modulus calculation.

Phase	AAA Scaled pressure	Spatial Average Strain		Pressure-Strain modulus	
	p (mmHg)	Zone #1	Zone #2	Zone #1	Zone #2
		dE1	dE2	M1=dp/dE1 (mmHg)	M2=dp/dE2 (mmHg)
1	81.049	--	--	--	--
3	116.926	0.0783	0.0681	1493.491	1717.962
5	147.879	0.0705	0.0586	2099.053	2522.348
7	141.804	0.0688	0.0645	2060.811	2200.136
9	117.050	0.0730	0.0718	1603.812	1629.128
11	105.955	0.0707	0.0694	1499.283	1526.132
13	97.879	0.0740	0.0763	1323.278	1282.544
15	92.751	0.0710	0.0609	1306.223	1523.927
17	88.730	0.0693	0.0552	1281.094	1607.421
19	85.078	0.0705	0.0548	1206.537	1551.102

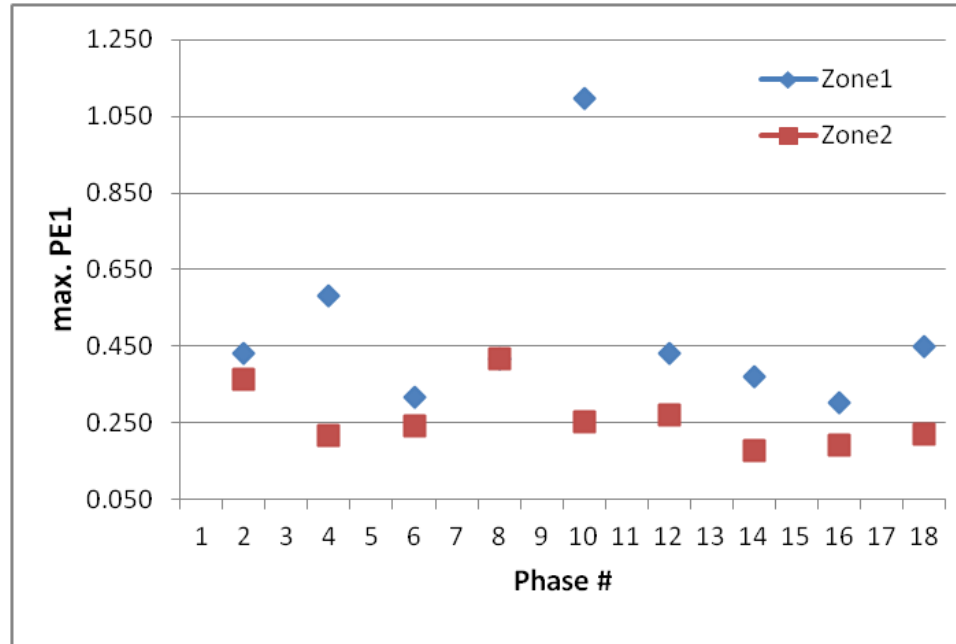


Figure 62: Variation of the maximum first principal strain over one cardiac cycle.

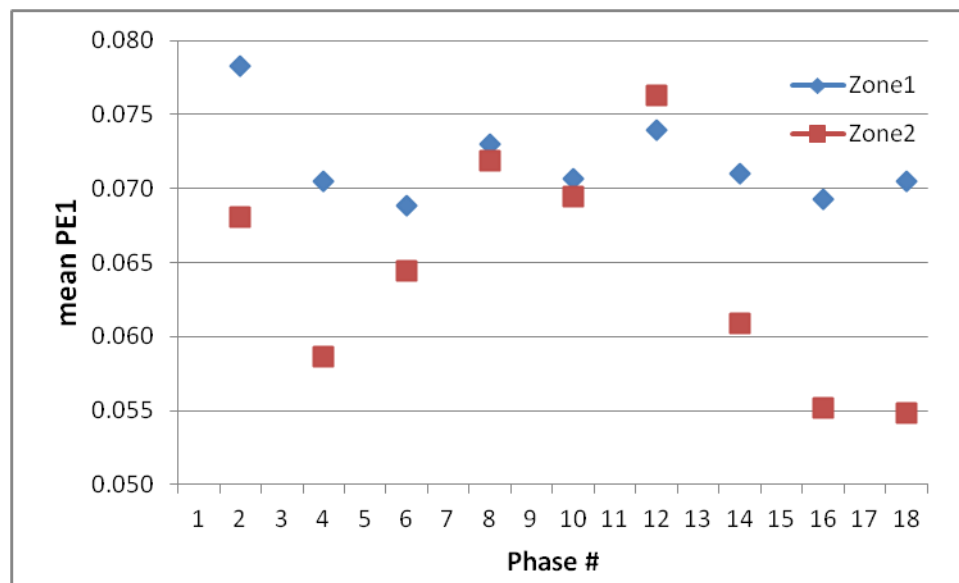


Figure 63: Variation of the area weighted spatial mean of the maximum first principal strain.

5.4 DISCUSSION

Our novel methodology to evaluate strains in vivo has high potential for the future of individual, image-based management of vascular disease. According to Taylor and Humphrey [205]– “*Fundamental to any analysis in continuum biomechanics is a basic knowledge of material behavior under conditions of interest*”. Special attention must be accorded to the phrase “*under conditions of interest*”; it highlights the need for in vivo characterization. We showed that the reconstructed tessellation for an AAA surface, under assumption of node movement being along the local surface normal direction, can be used to estimate strains and effective pressure-strain moduli using the classical continuum mechanics based framework. This methodology, when applied to a patient-specific AAA by making an elegant use of FEA post-processing techniques for a non-FEA study, can estimate patient-specific regional variations in the strain field. Material parameters can be derived from information about mechanical loading and corresponding deformation. Such information of material property and strain fields non-invasively obtained over cardiac cycle is expected to play a significant role in better prognosis of vascular health for a better clinical management. Our method is capable of providing not only strain field but also the strain rate. It is amenable for application in growth and remodeling process of arteries, for better device design, or for in vivo analysis of non-pulsatile forces such as musculoskeletal motions. Due to its non-invasive nature, it could be extended to applications requiring non-invasive access e.g. immigration and security, nuclear applications, cellular biomechanics, etc. We also used patient-specific tailored pressure wave profile that is more appropriate than populations averaged pressure wave for healthy aorta.

The work by Choi et al [211] represents an excellent study for quantification of deformation in arteries in vivo. They have proposed a framework to quantify the dynamic changes of healthy blood vessels from CT images. However, their work is limited by the calculation of a lumen centerline, e.g. a longitudinal strain metric is based on the position of the centerline and does not address regional variation of deformations along the vessel surface. True 3D deformation quantification that should include deformations in the surface of a vessel was not targeted by Choi et al [211]. Moreover, the mathematical approach of Fourier smoothing and Frenet-Serret's formula for 3D curves in [211] renders extension of it to 3D non-mathematical tessellations involved in patient-specific aneurysm models, typically with bifurcations, difficult and computationally costly. In case of AAA, where there is lot of deviation from cylinder-like shape of healthy vessel, centerline cannot truly represent entire geometry and its deformation. Capturing regional variations in any parameter is impossible by using 3D curves.

Previous work in 2D strain estimation is important in that it leveraged imaging techniques for strain estimation. Morrison et al [216] have used Lagrangian method for 2D strain calculations using CT images. They measured in-plane averaged strain along the arterial circumference. True deformation measurement not only should be 3D with out-of-plane motion but also should include rigid body movement and stretch both since deformation gradient tensor \mathbf{F} has both aspects of stretch (\mathbf{U}) rotation (\mathbf{R}) involved in it ($\mathbf{F} = \mathbf{U} \cdot \mathbf{R}$). While their work pertains to thoracic aorta with large pool of patients to explore age related changes, presented work in here is exploratory study to develop a new framework without any need for anatomical markers for tracking motions as was the case earlier [211, 216]. In addition, in our work there is no need any section plane normal to vessel centerline.

Velocity vector imaging (VVI) is another approach for in vivo strain estimation where voxel intensity in an image implies velocity rather than material at that location. Draney et al [222] were the first to apply this technique using cine PC-MR. Velocity information of pixels within wall thickness was used but it demands highly resolved image data especially since approximate blood vessel thickness in aorta is 1.39 mm [208]. Moreover, special velocity encoding and coil is necessary for sensing smaller velocity magnitude of wall [223]. Another approach is to track boundary of vessel as proposed in [223] with subpixel tracking and mag-flow approach. Adding to strain estimations literature, the arterial perimeter was subdivided into four quarters with circumferential length changes being monitored, an attempt to explore heterogeneity of the material properties [220]. However, all these previous studies are limited to 2D stretch-only calculations.

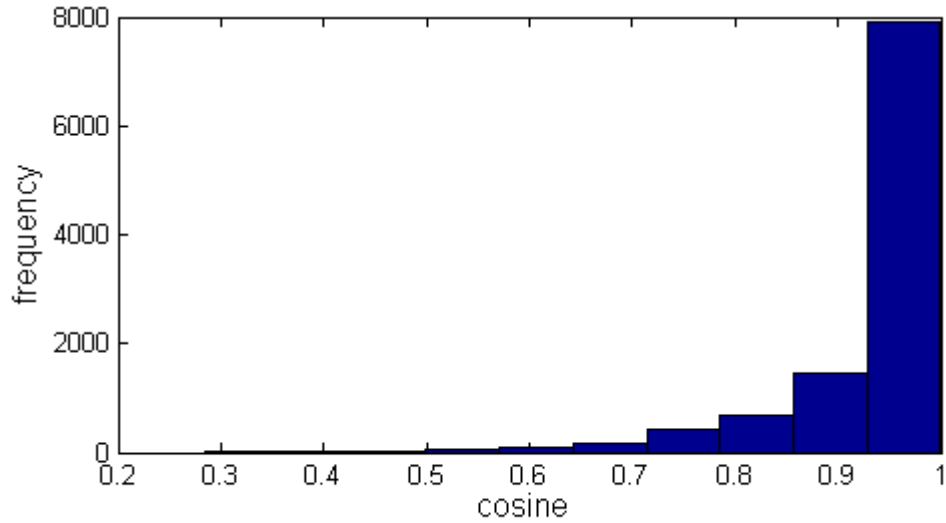


Figure 64: Histogram endorsing the assumption of wall displacement along local normals.

We attempt to validate the assumption regarding movement of surface mesh nodes in AAA sac region being along local node normal. Using the same patient's segmented data, and FE analysis procedure elaborated in Section 3.2.2, Section 3.2.3, and Section 3.2.4, deformation of AAA was simulated. Vectors denoting displacements of the FE mesh nodes on outer surface was interpolated onto each facet of the surface mesh used for creating wall domain volume mesh by extrusion. For each facet, dot product of unit vector along displacement direction was taken with unit vector along local normal direction. This dot product represents value of cosine of the angle between those two. Histogram endorses the assumption we made for nodal displacement and local normal direction.

Some important observations can be inferred from the present work as it relates to the potential application of these outcomes to the clinical management of AAA patients. Displacements without any obvious pattern with magnitude close to zero were observed in posterior side of AAA due to spinal cord support confirming the displacement vector field extraction procedure. Pressure-strain modulus is reported in averaged sense. With further improvements, especially with imaging resolution, regionally variable strain field can be used to estimate regionally variable material property data. We did not find any typical displacement pattern, in contrast to Draney et al [222] who observed larger deformation on the anterior wall, which is a logical outcome. Also we observe that there is larger variability in maximum principal strain than averaged principal strain and hence larger variations in calculated corresponding pressure-strain modulus (M_1). Previously reported strains for FE analysis in Chapter 3 (see Table 15, Table 16, and Figure 44) typically had a value ~ 0.3 for maximum strain and with most of the locations having values around 0.15. The strain estimation in this

work is qualitatively found to be in agreement with those results except for the difference that more heterogeneous behavior is observed in the distribution of strains calculated here. From Table 27, our averaged maximum principal strain for zone #1, which covers most of the aneurysm surface, ranged from 6.88% to 7.93%, whereas for zone#2, which closely replicates the behavior at the maximum diameter, ranged from 5.48% to 7.63% over the cardiac cycle. Previously reported circumferential strains were 10-15% in the thoracic aorta [222]. Overall pressure-strain modulus ranged from 1282 mmHg to 2522 mmHg. Clearly there is larger magnitude and smaller amplitude of strain values when calculated globally (zone #1) than those corresponding to the maximum diameter zone (zone #2). However, at one of the phases (phase #9) it occurred at the maximum diameter region. Since stress and strain increase concurrently, this outcome appears to be in agreement with previous observations that maximum stress does not occur at the maximum diameter but rather at an inflection point on the wall surface. Our study could not confirm previously reported necrotic dip in the pressure profile; likewise, a smooth variation in the strain field from one phase to the next was not observed.

Our study suggests the need for better in-plane resolution and use of a contrast agent. Since these are ECG gated time-resolved images, increased pixel resolution is currently not feasible due to limitation of hardware. We note that smoothing facilitates a better transition in the distance field data prior to surface extraction and reduces effects due to voxelization. In addition, an image plane not perpendicular to the centerline of the vessel is associated with poor contrast resulting in erroneous segmentations in those regions (see Figure 59), especially where local surface normal approaches direction of image plane normal.

There are also important limitations to the present study. First and foremost is the limited pixel resolution and large slice spacing compared to customary CT imaging. Temporal resolution is also a limiting factor in the analysis, as we used only 10 phases out of the 20 phases acquired within the cardiac cycle. This limitation was exacerbated due to most of the pressure variations in the cardiac cycle occur in the first one-third of it. In spite of breatholds, some motion artifacts were observed in the MR images. User bias during segmentation is also likely to affect results. The lack of a zero-pressure geometry to account for the true, unloaded state of the AAA is also a limitation of this work. We used 3-noded triangles for tessellation of the surface; however, the use of higher order discretization is necessary to accurately capture the curved surface topology when predicting distances between deformed and reference frames. Nevertheless, as this is an in vivo analysis, we measure deformation with respect to the diastolic phase as the reference configuration. In addition, the temporal resolution for image acquisition is also a factor when acquiring a phase closest to diastole and to be able to superimpose it with the pressure waveform assuming that there is no phase lag between them as reported earlier [216, 220, 222].

Chapter 6. Conclusions and Future Work

6.1 CONCLUSIONS

With the undertaken PhD research we can state the following general conclusions in addition to the specific conclusions described in Chapters 2-5:

- A robust MATLAB based software was developed for image based reconstruction and meshing of blood vessels with regionally varying wall thickness, tested with many patient-specific geometries, and applied with minimal user intervention while allowing for multiple options for customization of biomechanical analyses.
- Hypothesis #1 given in Section 1.5 was partially valid. Material property variations in the AAA wall were found to have a minimal influence on the distribution and magnitude of stress. However, it was found that strain, strain energy density, and wall displacement are statistically different based on the various hyperelastic isotropic constitutive material models used. Therefore, modeling patient-specific material properties may not be necessary if the objective of a biomechanical analysis is, exclusively, the prediction of wall stress.
- Hypothesis #2 given in Section 1.5 was found to be valid except for displacement. Patient-specific, regional distributions of wall thickness yield statistically different peak stress, strain, and strain energy density when compared to uniformly wall thickness models, when a hyperelastic isotropic constitutive material model is used.
- The feasibility of assessing patient-specific, heterogeneous material properties of the AAA wall was proven with ECG gated dynamic magnetic resonance images of one AAA patient, under the assumption that wall deformation is isotropic during one cardiac cycle.

- It is inferred that the framework developed for the computational assessment of AAAs can be useful in the future for increasing patient-specificity of rupture risk evaluation and potentially aid in clinical management of the disease.

6.2 FUTURE WORK

In the future, AAAMesh can be improved by facilitating mesh gradation. An approach for deciding the outward direction of the node normals for wall extrusion can use any known point outside the surface, e.g. the coordinate system origin or any of the corners of the imaginary enclosure of the surface mesh and then finding the closest facet to it. Once the correct outward normal is confirmed for one facet, the rest of the facets in its neighborhood can be confirmed for a normal direction that is consistent with known results, and this process can be repeated until each facet is confirmed. The quality of the quadrangles, and hence the ensuing hexahedral elements, can be improved by the use of a more elegant approach for converting a triangle surface mesh to a quadrangle mesh. Smoothing for quadrilateral surface elements to remove the pattern arising from splitting triangles into 3 quadrangles may improve the hex quality when modeling only the AAA wall. Additional work pertaining to characterization for optimal mesh settings is possible. The sensitivity of the framework to aspect ratio of the voxel data was not tested. A sensitivity study based on a combination of both Laplace and Taubin smoothing iterations simultaneously, as well as testing with a concave phantom may help build confidence regarding the overall code function. The availability of AAAMesh in binary executables for use without the MATLAB platform may accelerate its implementation in the clinic. Integration with a segmentation code that can facilitate direct conversion of the spline data to a 3D volume scalar field will avoid the data conversion process and errors related to mask creation.

Numerical simulations with anisotropic constitutive material models, calculation of the initial stress or zero pressure geometry, a comparison of different volume element types and a convergence study with embedded mesh for refinement will add more reliability and practical relevance to the present work. The framework for heterogeneous material property extraction in Chapter 5 assumed a simplified linear behavior by considering a pressure-strain modulus defining the vascular material properties. It can be improved upon by leveraging the fact that the complete strain tensor is available from the comparison of the time dependent AAA surface meshes, with the objective of estimating a more complex material property, e.g. anisotropic. The use of membrane theory instead of 3D continuum theory used for extracting the gradient can improve the current directional dependence of the results on the coordinate frame. Further verification of the proposed method is required with a vascular phantom of known material properties. Validation with experimental results may provide additional credibility.

References

- [1] van 't Veer, M., Buth, J., Merks, M., Tonino, P., van den Bosch, H., Pijls, N., and van de Vosse, F., 2008, "Biomechanical properties of abdominal aortic aneurysms assessed by simultaneously measured pressure and volume changes in humans," *J Vasc Surg*, 48(6), pp. 1401-1407.
- [2] Shum, J., 2011, "Risk Assessment of Abdominal Aortic Aneurysms by Geometry Quantification Measures," Carnegie Mellon University, Pittsburgh.
- [3] Raghavan, M. L., and Vorp, D. A., 2000, "Toward a biomechanical tool to evaluate rupture potential of abdominal aortic aneurysm: identification of a finite strain constitutive model and evaluation of its applicability," *J Biomech*, 33(4), pp. 475-482.
- [4] Brady, A. R., Thompson, S. G., Fowkes, F. G., Greenhalgh, R. M., Powell, J. T., and Participants, U. K. S. A. T., 2004, "Abdominal aortic aneurysm expansion: risk factors and time intervals for surveillance," *Circulation*, 110(1), pp. 16-21.
- [5] Ashton, H. A., Buxton, M. J., Day, N. E., Kim, L. G., Marteau, T. M., Scott, R. A. P., Thompson, S. G., Walker, N. M., and Stu, M. A. S., 2002, "The Multicentre Aneurysm Screening Study (MASS) into the effect of abdominal aortic aneurysm screening on mortality in men: a randomised controlled trial," *Lancet*, 360(9345), pp. 1531-1539.
- [6] Holt, P. J., Poloniecki, J. D., Loftus, I. M., Michaels, J. A., and Thompson, M. M., 2007, "Epidemiological study of the relationship between volume and outcome after abdominal aortic aneurysm surgery in the UK from 2000 to 2005," *Br J Surg*, 94(4), pp. 441-448.
- [7] Sakalihasan, N., Limet, R., and Defawe, O. D., 2005, "Abdominal aortic aneurysm," *Lancet*, 365(9470), pp. 1577-1589.
- [8] Brown, L. C., and Powell, J. T., 1999, "Risk factors for aneurysm rupture in patients kept under ultrasound surveillance. UK Small Aneurysm Trial Participants," *Ann Surg*, 230(3), pp. 289-296; discussion 296-287.
- [9] Moll, F. L., Powell, J. T., Fraedrich, G., Verzini, F., Haulon, S., Waltham, M., van Herwaarden, J. A., Holt, P. J., van Keulen, J. W., Rantner, B., Schlosser, F. J., Setacci, F., Ricco, J. B., and European Society for Vascular, S., 2011, "Management of abdominal aortic aneurysms clinical practice guidelines of the European society for vascular surgery," *Eur J Vasc Endovasc Surg*, 41 Suppl 1, pp. S1-S58.
- [10] Vorp, D. A., 2007, "Biomechanics of abdominal aortic aneurysm," *J Biomech*, 40(9), pp. 1887-1902.
- [11] Thompson, S. G., Ashton, H. A., Gao, L., Scott, R. A., and Multicentre Aneurysm Screening Study, G., 2009, "Screening men for abdominal aortic aneurysm: 10 year mortality and cost effectiveness results from the randomised Multicentre Aneurysm Screening Study," *Bmj*, 338, p. b2307.
- [12] Fillinger, M. F., Raghavan, M. L., Marra, S. P., Cronenwett, J. L., and Kennedy, F. E., 2002, "In vivo analysis of mechanical wall stress and abdominal aortic aneurysm rupture risk," *J Vasc Surg*, 36(3), pp. 589-597.

- [13] Fillinger, M. F., Marra, S. P., Raghavan, M. L., and Kennedy, F. E., 2003, "Prediction of rupture risk in abdominal aortic aneurysm during observation: wall stress versus diameter," *J Vasc Surg*, 37(4), pp. 724-732.
- [14] Doyle, B. J., Callanan, A., Burke, P. E., Grace, P. A., Walsh, M. T., Vorp, D. A., and McGloughlin, T. M., 2009, "Vessel asymmetry as an additional diagnostic tool in the assessment of abdominal aortic aneurysms," *J Vasc Surg*, 49(2), pp. 443-454.
- [15] Doyle, B. J., Molony D.S., Walsh M.T., McGloughlin T. M., 2010, *Abdominal Aortic Aneurysms: New Approaches to Rupture Risk Assessment*, Nova Science Publishers, New York.
- [16] Steinwender, G., Zweiker, R., Maier, R., Preidler, K., Tillich, M., Szolar, D., and Watzinger, N., 2010, "Diagnostic accuracy of contrast-enhanced 64-row MSCT-coronary angiography in patients with severe coronary calcification," *European Heart Journal*, 31, pp. 136-136.
- [17] McGloughlin, T. M., and Doyle, B. J., 2010, "New approaches to abdominal aortic aneurysm rupture risk assessment: engineering insights with clinical gain," *Arterioscler Thromb Vasc Biol*, 30(9), pp. 1687-1694.
- [18] International Union of Biochemistry and Molecular Biology. Nomenclature Committee., and Webb, E. C., 1992, *Enzyme nomenclature 1992 : recommendations of the Nomenclature Committee of the International Union of Biochemistry and Molecular Biology on the nomenclature and classification of enzymes*, Published for the International Union of Biochemistry and Molecular Biology by Academic Press, San Diego.
- [19] Walsh, G., 2002, *Proteins: Biochemistry and Biotechnology*, J. Wiley.
- [20] Wassef, M., Upchurch, G. R., Jr., Kuivaniemi, H., Thompson, R. W., and Tilson, M. D., 3rd, 2007, "Challenges and opportunities in abdominal aortic aneurysm research," *J Vasc Surg*, 45(1), pp. 192-198.
- [21] Abisi, S., Burnand, K. G., Waltham, M., Humphries, J., Taylor, P. R., and Smith, A., 2007, "Cysteine protease activity in the wall of abdominal aortic aneurysms," *J Vasc Surg*, 46(6), pp. 1260-1266.
- [22] Higashikata, T., Yamagishi, M., Sasaki, H., Minatoya, K., Ogino, H., Ishibashi-Ueda, H., Hao, H., Nagaya, N., Tomoike, H., and Sakamoto, A., 2004, "Application of real-time RT-PCR to quantifying gene expression of matrix metalloproteinases and tissue inhibitors of metalloproteinases in human abdominal aortic aneurysm," *Atherosclerosis*, 177(2), pp. 353-360.
- [23] Thompson, M., and Cockerill, G., 2006, "Matrix metalloproteinase-2: the forgotten enzyme in aneurysm pathogenesis," *Ann N Y Acad Sci*, 1085, pp. 170-174.
- [24] Freestone, T., Turner, R. J., Coady, A., Higman, D. J., Greenhalgh, R. M., and Powell, J. T., 1995, "Inflammation and matrix metalloproteinases in the enlarging abdominal aortic aneurysm," *Arterioscler Thromb Vasc Biol*, 15(8), pp. 1145-1151.
- [25] Tamarina, N. A., McMillan, W. D., Shively, V. P., and Pearce, W. H., 1997, "Expression of matrix metalloproteinases and their inhibitors in aneurysms and normal aorta," *Surgery*, 122(2), pp. 264-271.
- [26] Longo, G. M., Xiong, W., Greiner, T. C., Zhao, Y., Fiotti, N., and Baxter, B. T., 2002, "Matrix metalloproteinases 2 and 9 work in concert to produce aortic aneurysms," *J Clin Invest*, 110(5), pp. 625-632.
- [27] Wilson, W. R., Anderton, M., Schwalbe, E. C., Jones, J. L., Furness, P. N., Bell, P. R., and Thompson, M. M., 2006, "Matrix metalloproteinase-8 and -9 are increased at the site of abdominal aortic aneurysm rupture," *Circulation*, 113(3), pp. 438-445.

- [28] Nagashima, H., Aoka, Y., Sakomura, Y., Uto, K., Sakuta, A., Aomi, S., Kurosawa, H., Hagiwara, N., Kawana, M., and Kasanuki, H., 2004, "Matrix metalloproteinase 2 is suppressed by trapidil, a CD40-CD40 ligand pathway inhibitor, in human abdominal aortic aneurysm wall," *J Vasc Surg*, 39(2), pp. 447-453.
- [29] Taurino, M., Visco, V., Raffa, S., Ricci, B., Ruggiero, M., Torrisi, M. R., and Fiorani, P., 2004, "Matrix metalloproteinase 9 activity in patients before and after endovascular or surgical repair of abdominal aortic aneurysms," *Vascular*, 12(5), pp. 312-317.
- [30] Petersen, E., Wagberg, F., and Angquist, K. A., 2002, "Proteolysis of the abdominal aortic aneurysm wall and the association with rupture," *Eur J Vasc Endovasc Surg*, 23(2), pp. 153-157.
- [31] Fontaine, V., Jacob, M. P., Houard, X., Rossignol, P., Plissonnier, D., Angles-Cano, E., and Michel, J. B., 2002, "Involvement of the mural thrombus as a site of protease release and activation in human aortic aneurysms," *The American journal of pathology*, 161(5), pp. 1701-1710.
- [32] Swanson, R. J., Littooy, F. N., Hunt, T. K., and Stoney, R. J., 1980, "Laparotomy as a Precipitating Factor in the Rupture of Intra-Abdominal Aneurysms," *Archives of Surgery*, 115(3), pp. 299-304.
- [33] Pyo, R., Lee, J. K., Shipley, J. M., Curci, J. A., Mao, D., Ziporin, S. J., Ennis, T. L., Shapiro, S. D., Senior, R. M., and Thompson, R. W., 2000, "Targeted gene disruption of matrix metalloproteinase-9 (gelatinase B) suppresses development of experimental abdominal aortic aneurysms," *J Clin Invest*, 105(11), pp. 1641-1649.
- [34] Longo, G. M., Buda, S. J., Fiotta, N., Xiong, W., Griener, T., Shapiro, S., and Baxter, B. T., 2005, "MMP-12 has a role in abdominal aortic aneurysms in mice," *Surgery*, 137(4), pp. 457-462.
- [35] Eskandari, M. K., Vijungco, J. D., Flores, A., Borensztajn, J., Shively, V., and Pearce, W. H., 2005, "Enhanced abdominal aortic aneurysm in TIMP-1-deficient mice," *The Journal of surgical research*, 123(2), pp. 289-293.
- [36] Silence, J., Collen, D., and Lijnen, H. R., 2002, "Reduced atherosclerotic plaque but enhanced aneurysm formation in mice with inactivation of the tissue inhibitor of metalloproteinase-1 (TIMP-1) gene," *Circ Res*, 90(8), pp. 897-903.
- [37] Senior, R. M., Griffin, G. L., and Mecham, R. P., 1980, "Chemotactic activity of elastin-derived peptides," *J Clin Invest*, 66(4), pp. 859-862.
- [38] Kazi, M., Thyberg, J., Religa, P., Roy, J., Eriksson, P., Hedin, U., and Swedenborg, J., 2003, "Influence of intraluminal thrombus on structural and cellular composition of abdominal aortic aneurysm wall," *J Vasc Surg*, 38(6), pp. 1283-1292.
- [39] Ailawadi, G., Eliason, J. L., and Upchurch, G. R., Jr., 2003, "Current concepts in the pathogenesis of abdominal aortic aneurysm," *J Vasc Surg*, 38(3), pp. 584-588.
- [40] Reeps, C., Essler, M., Pelisek, J., Seidl, S., Eckstein, H. H., and Krause, B. J., 2008, "Increased 18F-fluorodeoxyglucose uptake in abdominal aortic aneurysms in positron emission/computed tomography is associated with inflammation, aortic wall instability, and acute symptoms," *J Vasc Surg*, 48(2), pp. 417-423; discussion 424.
- [41] Sakalihasan, N., Van Damme, H., Gomez, P., Rigo, P., Lapiere, C. M., Nusgens, B., and Limet, R., 2002, "Positron emission tomography (PET) evaluation of abdominal aortic aneurysm (AAA)," *Eur J Vasc Endovasc Surg*, 23(5), pp. 431-436.
- [42] Xu, X. Y., Borghi, A., Nchimi, A., Leung, J., Gomez, P., Cheng, Z., Defraigne, J. O., and Sakalihasan, N., 2010, "High levels of 18F-FDG uptake in aortic aneurysm wall are associated with high wall stress," *Eur J Vasc Endovasc Surg*, 39(3), pp. 295-301.

- [43] Sun, J., Sukhova, G. K., Yang, M., Wolters, P. J., MacFarlane, L. A., Libby, P., Sun, C., Zhang, Y., Liu, J., Ennis, T. L., Knispel, R., Xiong, W., Thompson, R. W., Baxter, B. T., and Shi, G. P., 2007, "Mast cells modulate the pathogenesis of elastase-induced abdominal aortic aneurysms in mice," *J Clin Invest*, 117(11), pp. 3359-3368.
- [44] Mayranpaa, M. I., Trosien, J. A., Fontaine, V., Folkesson, M., Kazi, M., Eriksson, P., Swedenborg, J., and Hedin, U., 2009, "Mast cells associate with neovessels in the media and adventitia of abdominal aortic aneurysms," *J Vasc Surg*, 50(2), pp. 388-395; discussion 395-386.
- [45] Curci, J. A., and Thompson, R. W., 2004, "Adaptive cellular immunity in aortic aneurysms: cause, consequence, or context?," *J Clin Invest*, 114(2), pp. 168-171.
- [46] Schonbeck, U., Sukhova, G. K., Gerdes, N., and Libby, P., 2002, "T(H)2 predominant immune responses prevail in human abdominal aortic aneurysm," *The American journal of pathology*, 161(2), pp. 499-506.
- [47] Xiong, W., Zhao, Y., Prall, A., Greiner, T. C., and Baxter, B. T., 2004, "Key roles of CD4+ T cells and IFN-gamma in the development of abdominal aortic aneurysms in a murine model," *J Immunol*, 172(4), pp. 2607-2612.
- [48] Saratzis, A., Abbas, A. A., Kiskinis, D., Melas, N., Saratzis, N., and Kitas, G. D., 2011, "Abdominal aortic aneurysm: a review of the genetic basis," *Angiology*, 62(1), pp. 18-32.
- [49] Dawson, J., Cockerill, G. W., Choke, E., Belli, A. M., Loftus, I., and Thompson, M. M., 2007, "Aortic aneurysms secrete interleukin-6 into the circulation," *J Vasc Surg*, 45(2), pp. 350-356.
- [50] Bown, M. J., Lloyd, G. M., Sandford, R. M., Thompson, J. R., London, N. J., Samani, N. J., and Sayers, R. D., 2007, "The interleukin-10-1082 'A' allele and abdominal aortic aneurysms," *J Vasc Surg*, 46(4), pp. 687-693.
- [51] Siwik, D. A., Pagano, P. J., and Colucci, W. S., 2001, "Oxidative stress regulates collagen synthesis and matrix metalloproteinase activity in cardiac fibroblasts," *American journal of physiology. Cell physiology*, 280(1), pp. C53-60.
- [52] Wassef, M., Baxter, B. T., Chisholm, R. L., Dalman, R. L., Fillinger, M. F., Heinecke, J., Humphrey, J. D., Kuivaniemi, H., Parks, W. C., Pearce, W. H., Platsoucas, C. D., Sukhova, G. K., Thompson, R. W., Tilson, M. D., and Zarins, C. K., 2001, "Pathogenesis of abdominal aortic aneurysms: a multidisciplinary research program supported by the National Heart, Lung, and Blood Institute," *J Vasc Surg*, 34(4), pp. 730-738.
- [53] Miller, F. J., Jr., Sharp, W. J., Fang, X., Oberley, L. W., Oberley, T. D., and Weintraub, N. L., 2002, "Oxidative stress in human abdominal aortic aneurysms: a potential mediator of aneurysmal remodeling," *Arterioscler Thromb Vasc Biol*, 22(4), pp. 560-565.
- [54] Zhang, J., Schmidt, J., Ryschich, E., Mueller-Schilling, M., Schumacher, H., and Allenberg, J. R., 2003, "Inducible nitric oxide synthase is present in human abdominal aortic aneurysm and promotes oxidative vascular injury," *J Vasc Surg*, 38(2), pp. 360-367.
- [55] Johanning, J. M., Armstrong, P. J., Franklin, D. P., Han, D. C., Carey, D. J., and Elmore, J. R., 2002, "Nitric oxide in experimental aneurysm formation: early events and consequences of nitric oxide inhibition," *Ann Vasc Surg*, 16(1), pp. 65-72.
- [56] Wanhainen, A., Bergqvist, D., Boman, K., Nilsson, T. K., Rutegard, J., and Bjorck, M., 2005, "Risk factors associated with abdominal aortic aneurysm: a population-based study with historical and current data," *J Vasc Surg*, 41(3), pp. 390-396.

- [57] Wiernicki, I., Safranow, K., Baranowska-Bosiacka, I., Piatek, J., and Gutowski, P., 2010, "Haptoglobin 2-1 phenotype predicts rapid growth of abdominal aortic aneurysms," *J Vasc Surg*, 52(3), pp. 691-696.
- [58] Comley, P. N., 2007, "The ASTM International standard test method for determining the Superplastic Properties of Metallic Materials," *Mater Sci Forum*, 551-552, pp. 105-110.
- [59] Schlosser, F. J., Tangelder, M. J., Verhagen, H. J., van der Heijden, G. J., Muhs, B. E., van der Graaf, Y., Moll, F. L., and group, S. s., 2008, "Growth predictors and prognosis of small abdominal aortic aneurysms," *J Vasc Surg*, 47(6), pp. 1127-1133.
- [60] Higgins, D., 1967, "Anon - Astm Metric Practice Guide," *Spe Journal*, 23(11), pp. 101-&.
- [61] Chen, Y. J., Chen, S. Y., Wang, J. T., and Hsueh, P. R., 2009, "Mycotic aneurysm caused by gas-forming serotype K5 Klebsiella pneumoniae," *Int J Infect Dis*, 13(2), pp. e47-48.
- [62] García, F., Volo, G., and Cabrera, V., 2006, "Aortic Aneurysm Secondary to Streptococcus zooepidemicus," *EJVES Extra*, 11(5), pp. 91-93.
- [63] Morrow, D. R., and Boyle, J. R., 2005, "Ruptured Infected Aneurysm of the Aorta Secondary to Appendicitis," *EJVES Extra*, 9(2), pp. 11-12.
- [64] Bjorck, H. M., Lanne, T., Alehagen, U., Persson, K., Rundkvist, L., Hamsten, A., Dahlstrom, U., and Eriksson, P., 2009, "Association of genetic variation on chromosome 9p21.3 and arterial stiffness," *Journal of internal medicine*, 265(3), pp. 373-381.
- [65] Baumgartner, I., Hirsch, A. T., Abola, M. T., Cacoub, P. P., Poldermans, D., Steg, P. G., Creager, M. A., Bhatt, D. L., and investigators, R. R., 2008, "Cardiovascular risk profile and outcome of patients with abdominal aortic aneurysm in out-patients with atherothrombosis: data from the Reduction of Atherothrombosis for Continued Health (REACH) Registry," *J Vasc Surg*, 48(4), pp. 808-814.
- [66] Ogata, T., MacKean, G. L., Cole, C. W., Arthur, C., Andreou, P., Tromp, G., and Kuivaniemi, H., 2005, "The lifetime prevalence of abdominal aortic aneurysms among siblings of aneurysm patients is eightfold higher than among siblings of spouses: an analysis of 187 aneurysm families in Nova Scotia, Canada," *J Vasc Surg*, 42(5), pp. 891-897.
- [67] Shibamura, H., Olson, J. M., van Vlijmen-Van Keulen, C., Buxbaum, S. G., Dudek, D. M., Tromp, G., Ogata, T., Skunca, M., Sakalihasan, N., Pals, G., Limet, R., MacKean, G. L., Defawe, O., Verloes, A., Arthur, C., Lossing, A. G., Burnett, M., Sueda, T., and Kuivaniemi, H., 2004, "Genome scan for familial abdominal aortic aneurysm using sex and family history as covariates suggests genetic heterogeneity and identifies linkage to chromosome 19q13," *Circulation*, 109(17), pp. 2103-2108.
- [68] Elmore, J. R., Obmann, M. A., Kuivaniemi, H., Tromp, G., Gerhard, G. S., Franklin, D. P., Boddy, A. M., and Carey, D. J., 2009, "Identification of a genetic variant associated with abdominal aortic aneurysms on chromosome 3p12.3 by genome wide association," *J Vasc Surg*, 49(6), pp. 1525-1531.
- [69] Jones, G. T., Phillips, V. L., Harris, E. L., Rossaak, J. I., and van Rij, A. M., 2003, "Functional matrix metalloproteinase-9 polymorphism (C-1562T) associated with abdominal aortic aneurysm," *J Vasc Surg*, 38(6), pp. 1363-1367.
- [70] Gretarsdottir, S., and al, e., 2010, "Genome-wide association study identifies a sequence variant within the DAB2IP gene conferring susceptibility to abdominal aortic aneurysm," *Nature genetics*, 42(8), pp. 692-697.

- [71] Larsson, E., Labruto, F., Gasser, T. C., Swedenborg, J., and Hultgren, R., 2011, "Analysis of aortic wall stress and rupture risk in patients with abdominal aortic aneurysm with a gender perspective," *J Vasc Surg*, 54(2), pp. 295-299.
- [72] Choke, E., Cockerill, G., Wilson, R., Dawson, J., Sayed, S., Loftus, I., and Thompson, M. M., 2005, "Abdominal aortic aneurysm rupture is associated with increased angiogenesis and the overexpression of vascular endothelial growth factor and alpha V-integrin," *Circulation*, 112(17), pp. U290-U290.
- [73] Dai, J., Louedec, L., Philippe, M., Michel, J. B., and Houard, X., 2009, "Effect of blocking platelet activation with AZD6140 on development of abdominal aortic aneurysm in a rat aneurysmal model," *J Vasc Surg*, 49(3), pp. 719-727.
- [74] Wanhainen, A., Nilsson, T. K., Bergqvist, D., Boman, K., and Bjorck, M., 2007, "Elevated tissue plasminogen activator in patients with screening-detected abdominal aortic aneurysm," *J Vasc Surg*, 45(6), pp. 1109-1113.
- [75] Sweeting, M. J., Thompson, S. G., Brown, L. C., Greenhalgh, R. M., and Powell, J. T., 2010, "Use of angiotensin converting enzyme inhibitors is associated with increased growth rate of abdominal aortic aneurysms," *J Vasc Surg*, 52(1), pp. 1-4.
- [76] Hackam, D. G., Thiruchelvam, D., and Redelmeier, D. A., 2006, "ACE inhibitors and aortic rupture," *Lancet*, 368(9547), pp. 1572-1572.
- [77] Hackam, D. G., Thiruchelvam, D., and Redelmeier, D. A., 2006, "Angiotensin-converting enzyme inhibitors and aortic rupture: a population-based case-control study," *Lancet*, 368(9536), pp. 659-665.
- [78] Darling, R. C., Messina, C. R., Brewster, D. C., and Ottinger, L. W., 1977, "Autopsy study of unoperated abdominal aortic aneurysms. The case for early resection," *Circulation*, 56(3 Suppl), pp. II161-164.
- [79] Solberg, S., Forsdahl, S. H., Singh, K., and Jacobsen, B. K., 2010, "Diameter of the infrarenal aorta as a risk factor for abdominal aortic aneurysm: the Tromso Study, 1994-2001," *Eur J Vasc Endovasc Surg*, 39(3), pp. 280-284.
- [80] Mizowaki, T., Sueyoshi, E., Sakamoto, I., and Uetani, M., 2009, "Expansion rate of nonaneurysmatic abdominal aorta: over 10 years of follow-up CT studies," *Comput Med Imaging Graph*, 33(1), pp. 17-22.
- [81] A.D.C., S., 1999, "The folding of the human brain: From shape to function," University of London, London.
- [82] Ma, B., Harbaugh, R. E., and Raghavan, M. L., 2004, "Three-dimensional geometrical characterization of cerebral aneurysms," *Ann Biomed Eng*, 32(2), pp. 264-273.
- [83] Raghavan, M. L., Ma, B., and Harbaugh, R. E., 2005, "Quantified aneurysm shape and rupture risk," *J Neurosurg*, 102(2), pp. 355-362.
- [84] Pappu, S., Dardik, A., Tagare, H., and Gusberg, R. J., 2008, "Beyond fusiform and saccular: a novel quantitative tortuosity index may help classify aneurysm shape and predict aneurysm rupture potential," *Ann Vasc Surg*, 22(1), pp. 88-97.
- [85] Dobrin, P. B., and Mrkvicka, R., 1994, "Failure of elastin or collagen as possible critical connective tissue alterations underlying aneurysmal dilatation," *Cardiovasc Surg*, 2(4), pp. 484-488.
- [86] Elger, D. F., Blackketter, D. M., Budwig, R. S., and Johansen, K. H., 1996, "The influence of shape on the stresses in model abdominal aortic aneurysms," *J Biomech Eng*, 118(3), pp. 326-332.

- [87] Vorp, D. A., Raghavan, M. L., and Webster, M. W., 1998, "Mechanical wall stress in abdominal aortic aneurysm: influence of diameter and asymmetry," *J Vasc Surg*, 27(4), pp. 632-639.
- [88] Rodriguez, J. F., Ruiz, C., Doblare, M., and Holzapfel, G. A., 2008, "Mechanical stresses in abdominal aortic aneurysms: influence of diameter, asymmetry, and material anisotropy," *J Biomech Eng*, 130(2), p. 021023.
- [89] Stringfellow, M. M., Lawrence, P. F., and Stringfellow, R. G., 1987, "The influence of aorta-aneurysm geometry upon stress in the aneurysm wall," *The Journal of surgical research*, 42(4), pp. 425-433.
- [90] Vande Geest, J. P., Wang, D. H., Wisniewski, S. R., Makaroun, M. S., and Vorp, D. A., 2006, "Towards a noninvasive method for determination of patient-specific wall strength distribution in abdominal aortic aneurysms," *Ann Biomed Eng*, 34(7), pp. 1098-1106.
- [91] Shum, J., DiMartino, E. S., Goldhamme, A., Goldman, D. H., Acker, L. C., Patel, G., Ng, J. H., Martufi, G., and Finol, E. A., 2010, "Semiautomatic vessel wall detection and quantification of wall thickness in computed tomography images of human abdominal aortic aneurysms," *Med Phys*, 37(2), pp. 638-648.
- [92] Di Martino, E. S., Bohra, A., Vande Geest, J. P., Gupta, N., Makaroun, M. S., and Vorp, D. A., 2006, "Biomechanical properties of ruptured versus electively repaired abdominal aortic aneurysm wall tissue," *J Vasc Surg*, 43(3), pp. 570-576; discussion 576.
- [93] Raghavan, M. L., Kratzberg, J., Castro de Tolosa, E. M., Hanaoka, M. M., Walker, P., and da Silva, E. S., 2006, "Regional distribution of wall thickness and failure properties of human abdominal aortic aneurysm," *J Biomech*, 39(16), pp. 3010-3016.
- [94] Mower, W. R., Baraff, L. J., and Sneyd, J., 1993, "Stress distributions in vascular aneurysms: factors affecting risk of aneurysm rupture," *The Journal of surgical research*, 55(2), pp. 155-161.
- [95] Venkatasubramaniam, A. K., Fagan, M. J., Mehta, T., Mylankal, K. J., Ray, B., Kuhan, G., Chetter, I. C., and McCollum, P. T., 2004, "A comparative study of aortic wall stress using finite element analysis for ruptured and non-ruptured abdominal aortic aneurysms," *Eur J Vasc Endovasc Surg*, 28(2), pp. 168-176.
- [96] Giannoglou, G., Giannakoulas, G., Soulis, J., Chatzizisis, Y., Perdikides, T., Melas, N., Parcharidis, G., and Louridas, G., 2006, "Predicting the risk of rupture of abdominal aortic aneurysms by utilizing various geometrical parameters: revisiting the diameter criterion," *Angiology*, 57(4), pp. 487-494.
- [97] Fillinger, M. F., Racusin, J., Baker, R. K., Cronenwett, J. L., Teutelink, A., Schermerhorn, M. L., Zwolak, R. M., Powell, R. J., Walsh, D. B., and Rzucidlo, E. M., 2004, "Anatomic characteristics of ruptured abdominal aortic aneurysm on conventional CT scans: Implications for rupture risk," *J Vasc Surg*, 39(6), pp. 1243-1252.
- [98] Georgakarakos, E., Ioannou, C. V., Kamarianakis, Y., Papaharilaou, Y., Kostas, T., Manousaki, E., and Katsamouris, A. N., 2010, "The role of geometric parameters in the prediction of abdominal aortic aneurysm wall stress," *Eur J Vasc Endovasc Surg*, 39(1), pp. 42-48.
- [99] Shum, J., Xu, A., Chatnuntawe, I., and Finol, E. A., 2011, "A framework for the automatic generation of surface topologies for abdominal aortic aneurysm models," *Ann Biomed Eng*, 39(1), pp. 249-259.

- [100] Shum, J., Martufi, G., Di Martino, E., Washington, C. B., Grisafi, J., Muluk, S. C., and Finol, E. A., 2011, "Quantitative assessment of abdominal aortic aneurysm geometry," *Ann Biomed Eng*, 39(1), pp. 277-286.
- [101] Martufi, G., Di Martino, E. S., Amon, C. H., Muluk, S. C., and Finol, E. A., 2009, "Three-dimensional geometrical characterization of abdominal aortic aneurysms: image-based wall thickness distribution," *J Biomech Eng*, 131(6), p. 061015.
- [102] Vilalta G., N. F., Vaquero C., Vilalta J.A., 2010, "Quantitative indicator of abdominal aortic aneurysm rupture risk based on its geometric parameter parameters," *World Academy of Science, Engineering and Technology*(69), pp. 181-185.
- [103] Dobrin, P. B., 1989, "Pathophysiology and pathogenesis of aortic aneurysms. Current concepts," *The Surgical clinics of North America*, 69(4), pp. 687-703.
- [104] Inzoli, F., Boschetti, F., Zappa, M., Longo, T., and Fumero, R., 1993, "Biomechanical factors in abdominal aortic aneurysm rupture," *Eur J Vasc Surg*, 7(6), pp. 667-674.
- [105] Georgakarakos, E., Ioannou, C. V., Papaharilaou, Y., Kostas, T., Tsetis, D., and Katsamouris, A. N., 2010, "Peak wall stress does not necessarily predict the location of rupture in abdominal aortic aneurysms," *Eur J Vasc Endovasc Surg*, 39(3), pp. 302-304.
- [106] Vande Geest, J. P., Di Martino, E. S., Bohra, A., Makaroun, M. S., and Vorp, D. A., 2006, "A biomechanics-based rupture potential index for abdominal aortic aneurysm risk assessment: demonstrative application," *Ann N Y Acad Sci*, 1085, pp. 11-21.
- [107] Speelman, L., Bohra, A., Bosboom, E. M., Schurink, G. W., van de Vosse, F. N., Makaorun, M. S., and Vorp, D. A., 2007, "Effects of wall calcifications in patient-specific wall stress analyses of abdominal aortic aneurysms," *J Biomech Eng*, 129(1), pp. 105-109.
- [108] Volokh, K. Y., 2010, "Comparison of biomechanical failure criteria for abdominal aortic aneurysm," *J Biomech*, 43(10), pp. 2032-2034.
- [109] Thubrikar, M. J., al-Soudi, J., and Robicsek, F., 2001, "Wall stress studies of abdominal aortic aneurysm in a clinical model," *Ann Vasc Surg*, 15(3), pp. 355-366.
- [110] Di Martino, E. S., Guadagni, G., Fumero, A., Ballerini, G., Spirito, R., Biglioli, P., and Redaelli, A., 2001, "Fluid-structure interaction within realistic three-dimensional models of the aneurysmatic aorta as a guidance to assess the risk of rupture of the aneurysm," *Med Eng Phys*, 23(9), pp. 647-655.
- [111] Vande Geest, J. P., Sacks, M. S., and Vorp, D. A., 2006, "The effects of aneurysm on the biaxial mechanical behavior of human abdominal aorta," *J Biomech*, 39(7), pp. 1324-1334.
- [112] Vande Geest, J. P., Sacks, M. S., and Vorp, D. A., 2006, "A planar biaxial constitutive relation for the luminal layer of intra-luminal thrombus in abdominal aortic aneurysms," *J Biomech*, 39(13), pp. 2347-2354.
- [113] Zeinali-Davarani, S., Choi, J., and Baek, S., 2009, "On parameter estimation for biaxial mechanical behavior of arteries," *J Biomech*, 42(4), pp. 524-530.
- [114] Gasser, T. C., Ogden, R. W., and Holzapfel, G. A., 2006, "Hyperelastic modelling of arterial layers with distributed collagen fibre orientations," *Journal of the Royal Society, Interface / the Royal Society*, 3(6), pp. 15-35.
- [115] Rodriguez, J. F., Martufi, G., Doblare, M., and Finol, E. A., 2009, "The effect of material model formulation in the stress analysis of abdominal aortic aneurysms," *Ann Biomed Eng*, 37(11), pp. 2218-2221.

- [116] Vande Geest, J. P., Schmidt, D. E., Sacks, M. S., and Vorp, D. A., 2008, "The effects of anisotropy on the stress analyses of patient-specific abdominal aortic aneurysms," *Ann Biomed Eng*, 36(6), pp. 921-932.
- [117] Gasser, T. C., Auer, M., Labruto, F., Swedenborg, J., and Roy, J., 2010, "Biomechanical rupture risk assessment of abdominal aortic aneurysms: model complexity versus predictability of finite element simulations," *Eur J Vasc Endovasc Surg*, 40(2), pp. 176-185.
- [118] Stenbaek, J., Kalin, B., and Swedenborg, J., 2000, "Growth of thrombus may be a better predictor of rupture than diameter in patients with abdominal aortic aneurysms," *Eur J Vasc Endovasc Surg*, 20(5), pp. 466-469.
- [119] Vorp, D. A., Lee, P. C., Wang, D. H., Makaroun, M. S., Nemoto, E. M., Ogawa, S., and Webster, M. W., 2001, "Association of intraluminal thrombus in abdominal aortic aneurysm with local hypoxia and wall weakening," *J Vasc Surg*, 34(2), pp. 291-299.
- [120] Mower, W. R., Quinones, W. J., and Gambhir, S. S., 1997, "Effect of intraluminal thrombus on abdominal aortic aneurysm wall stress," *J Vasc Surg*, 26(4), pp. 602-608.
- [121] Wang, D. H., Makaroun, M. S., Webster, M. W., and Vorp, D. A., 2002, "Effect of intraluminal thrombus on wall stress in patient-specific models of abdominal aortic aneurysm," *J Vasc Surg*, 36(3), pp. 598-604.
- [122] Georgakarakos, E., Ioannou, C. V., Volanis, S., Papaharilaou, Y., Ekaterinaris, J., and Katsamouris, A. N., 2009, "The influence of intraluminal thrombus on abdominal aortic aneurysm wall stress," *Int Angiol*, 28(4), pp. 325-333.
- [123] Auer, M., and Gasser, T. C., 2010, "Reconstruction and finite element mesh generation of abdominal aortic aneurysms from computerized tomography angiography data with minimal user interactions," *IEEE Trans Med Imaging*, 29(4), pp. 1022-1028.
- [124] Thubrikar, M. J., Robicsek, F., Labrosse, M., Chervenkoff, V., and Fowler, B. L., 2003, "Effect of thrombus on abdominal aortic aneurysm wall dilation and stress," *J Cardiovasc Surg (Torino)*, 44(1), pp. 67-77.
- [125] Polzer, S., Gasser, T. C., Swedenborg, J., and Bursa, J., 2011, "The impact of intraluminal thrombus failure on the mechanical stress in the wall of abdominal aortic aneurysms," *Eur J Vasc Endovasc Surg*, 41(4), pp. 467-473.
- [126] Di Martino, E., Mantero, S., Inzoli, F., Melissano, G., Astore, D., Chiesa, R., and Fumero, R., 1998, "Biomechanics of abdominal aortic aneurysm in the presence of endoluminal thrombus: experimental characterisation and structural static computational analysis," *Eur J Vasc Endovasc Surg*, 15(4), pp. 290-299.
- [127] van Dam, E. A., Dams, S. D., Peters, G. W., Rutten, M. C., Schurink, G. W., Buth, J., and van de Vosse, F. N., 2008, "Non-linear viscoelastic behavior of abdominal aortic aneurysm thrombus," *Biomech Model Mechanobiol*, 7(2), pp. 127-137.
- [128] Li, Z. Y., J. U. K.-I., Tang, T. Y., Soh, E., See, T. C., and Gillard, J. H., 2008, "Impact of calcification and intraluminal thrombus on the computed wall stresses of abdominal aortic aneurysm," *J Vasc Surg*, 47(5), pp. 928-935.
- [129] Maier, A., Gee, M. W., Reeps, C., Eckstein, H. H., and Wall, W. A., 2010, "Impact of calcifications on patient-specific wall stress analysis of abdominal aortic aneurysms," *Biomech Model Mechanobiol*, 9(5), pp. 511-521.
- [130] Raghavan, M. L., Ma, B., and Fillinger, M. F., 2006, "Non-invasive determination of zero-pressure geometry of arterial aneurysms," *Ann Biomed Eng*, 34(9), pp. 1414-1419.

- [131] Gee, M. W., Reeps, C., Eckstein, H. H., and Wall, W. A., 2009, "Prestressing in finite deformation abdominal aortic aneurysm simulation," *J Biomech*, 42(11), pp. 1732-1739.
- [132] de Putter, S., Wolters, B. J., Rutten, M. C., Breeuwer, M., Gerritsen, F. A., and van de Vosse, F. N., 2007, "Patient-specific initial wall stress in abdominal aortic aneurysms with a backward incremental method," *J Biomech*, 40(5), pp. 1081-1090.
- [133] Speelman, L., Bosboom, E. M., Schurink, G. W., Buth, J., Breeuwer, M., Jacobs, M. J., and van de Vosse, F. N., 2009, "Initial stress and nonlinear material behavior in patient-specific AAA wall stress analysis," *J Biomech*, 42(11), pp. 1713-1719.
- [134] Lu, J., Zhou, X., and Raghavan, M. L., 2007, "Inverse elastostatic stress analysis in pre-deformed biological structures: Demonstration using abdominal aortic aneurysms," *J Biomech*, 40(3), pp. 693-696.
- [135] Hsu, M. C., and Bazilevs, Y., 2011, "Blood vessel tissue prestress modeling for vascular fluid-structure interaction simulation," *Finite Elem Anal Des*, 47(6), pp. 593-599.
- [136] Chandra, S., Rodriguez, J., and Finol, E. A., 2011, "Methodology for the derivation of unloaded vascular geometry with hyperelastic isotropic tissue properties," *J Biomech*, (submitted).
- [137] Scotti, C. M., Shkolnik, A. D., Muluk, S. C., and Finol, E. A., 2005, "Fluid-structure interaction in abdominal aortic aneurysms: effects of asymmetry and wall thickness," *Biomedical engineering online*, 4, p. 64.
- [138] Scotti, C. M., and Finol, E. A., 2007, "Compliant biomechanics of abdominal aortic aneurysms: A fluid-structure interaction study," *Computers & Structures*, 85(11-14), pp. 1097-1113.
- [139] Scotti, C. M., Jimenez, J., Muluk, S. C., and Finol, E. A., 2008, "Wall stress and flow dynamics in abdominal aortic aneurysms: finite element analysis vs. fluid-structure interaction," *Comput Methods Biomech Biomed Engin*, 11(3), pp. 301-322.
- [140] Leung, J. H., Wright, A. R., Cheshire, N., Crane, J., Thom, S. A., Hughes, A. D., and Xu, Y., 2006, "Fluid structure interaction of patient specific abdominal aortic aneurysms: a comparison with solid stress models," *Biomedical engineering online*, 5, p. 33.
- [141] Papaharilaou, Y., Ekaterinaris, J. A., Manousaki, E., and Katsamouris, A. N., 2007, "A decoupled fluid structure approach for estimating wall stress in abdominal aortic aneurysms," *J Biomech*, 40(2), pp. 367-377.
- [142] Kim, Y. H., Kim, J. E., Ito, Y., Shih, A. M., Brott, B., and Anayiotos, A., 2008, "Hemodynamic analysis of a compliant femoral artery bifurcation model using a fluid structure interaction framework," *Ann Biomed Eng*, 36(11), pp. 1753-1763.
- [143] Khanafer, K. M., Bull, J. L., and Berguer, R., 2009, "Fluid-structure interaction of turbulent pulsatile flow within a flexible wall axisymmetric aortic aneurysm model," *Eur J Mech B-Fluid*, 28(1), pp. 88-102.
- [144] Chandra, S., Raut, S. S., Jana, A., Beiderman, R., Doyle, M., Muluk, S. C., and Finol, E. A., 2012, "Fluid-structure interaction modeling of abdominal aortic aneurysms: the impact of patient specific inflow conditions and fluid/solid coupling," *J Biomech Eng*, (accepted).
- [145] Rissland, P., Alemu, Y., Einav, S., Ricotta, J., and Bluestein, D., 2009, "Abdominal aortic aneurysm risk of rupture: patient-specific FSI simulations using anisotropic model," *J Biomech Eng*, 131(3), p. 031001.

- [146] Xenos, M., Rambhia, S. H., Alemu, Y., Einav, S., Labropoulos, N., Tassiopoulos, A., Ricotta, J. J., and Bluestein, D., 2010, "Patient-based abdominal aortic aneurysm rupture risk prediction with fluid structure interaction modeling," *Ann Biomed Eng*, 38(11), pp. 3323-3337.
- [147] Erdemir, A., Guess, T. M., Halloran, J., Tadepalli, S. C., and Morrison, T. M., 2012, "Considerations for reporting finite element analysis studies in biomechanics," *J Biomech*, 45(4), pp. 625-633.
- [148] Bathe, K.-J. r., and Bathe, K.-J. r., 1996, *Finite element procedures*, Prentice Hall, Englewood Cliffs, N.J.
- [149] Heng, M. S., Fagan, M. J., Collier, J. W., Desai, G., McCollum, P. T., and Chetter, I. C., 2008, "Peak wall stress measurement in elective and acute abdominal aortic aneurysms," *J Vasc Surg*, 47(1), pp. 17-22; discussion 22.
- [150] Doyle, B. J., Callanan, A., and McGloughlin, T. M., 2007, "A comparison of modelling techniques for computing wall stress in abdominal aortic aneurysms," *Biomedical engineering online*, 6, p. 38.
- [151] Doyle, B. J., Cloonan, A. J., Walsh, M. T., Vorp, D. A., and McGloughlin, T. M., 2010, "Identification of rupture locations in patient-specific abdominal aortic aneurysms using experimental and computational techniques," *J Biomech*, 43(7), pp. 1408-1416.
- [152] S. Flumerfelt, G. H., F. Kahlen, 2012, "Complexity By Design," *Mechanical Engineering*, ASME, pp. 29-33.
- [153] Steven Allender, P. S., Viv Peto, Mike Rayner, 2008, "European Cardiovascular Disease Statistics."
- [154] Kobbelt, L. P., Botsch, M., Schwannecke, U., and Seidel, H. P., 2001, "Feature sensitive surface extraction from volume data," *Comp Graph*, pp. 57-66.
- [155] Cline, H. E., Dumoulin, C. L., Hart, H. R., Jr., Lorensen, W. E., and Ludke, S., 1987, "3D reconstruction of the brain from magnetic resonance images using a connectivity algorithm," *Magn Reson Imaging*, 5(5), pp. 345-352.
- [156] Shephard, M. S., and Georges, M. K., 1991, "Automatic 3-Dimensional Mesh Generation by the Finite Octree Technique," *International Journal for Numerical Methods in Engineering*, 32(4), pp. 709-749.
- [157] Young, P. G., Beresford-West, T. B., Coward, S. R., Notarberardino, B., Walker, B., and Abdul-Aziz, A., 2008, "An efficient approach to converting three-dimensional image data into highly accurate computational models," *Philosophical transactions. Series A, Mathematical, physical, and engineering sciences*, 366(1878), pp. 3155-3173.
- [158] Ju, T., Losasso, F., Schaefer, S., and Warren, J., 2002, "Dual contouring of hermite data," *Acm T Graphic*, 21(3), pp. 339-346.
- [159] Li, Z., Ma, L. Z., Jin, X. G., and Zheng, Z. Y., 2009, "A new feature-preserving mesh-smoothing algorithm," *Visual Comput*, 25(2), pp. 139-148.
- [160] Taubin, G., 1995, "Curve and surface smoothing without shrinkage," *Fifth International Conference on Computer Vision, Proceedings*, pp. 852-857.
- [161] Leif, K., Swen, C., Jens, V., and Hans-Peter, S., 1998, "Interactive multi-resolution modeling on arbitrary meshes," *Proceedings of the 25th annual conference on Computer graphics and interactive techniques*, ACM, pp. 105-114.
- [162] Igor, G., Wim, S., Peter, S., and der, 1999, "Multiresolution signal processing for meshes," *Proceedings of the 26th annual conference on Computer graphics and interactive techniques*, ACM Press/Addison-Wesley Publishing Co., pp. 325-334.

- [163] Mathieu, D., Mark, M., Peter, S., der, and Alan, H. B., 1999, "Implicit fairing of irregular meshes using diffusion and curvature flow," Proceedings of the 26th annual conference on Computer graphics and interactive techniques ACM Press/Addison-Wesley Publishing Co., pp. 317-324.
- [164] Yamada, A., Furuhashi, T., Shimada, K., and Hou, K., 1999, "A Discrete Spring Model for Generating Fair Curves and Surfaces," Proceedings of the 7th Pacific Conference on Computer Graphics and Applications, IEEE Computer Society, p. 270.
- [165] Sacks, M. S., Chuong, C. J., Templeton, G. H., and Peshock, R., 1993, "In vivo 3-D reconstruction and geometric characterization of the right ventricular free wall," Ann Biomed Eng, 21(3), pp. 263-275.
- [166] Sacks, M. S., Vorp, D. A., Raghavan, M. L., Federle, M. P., and Webster, M. W., 1999, "In vivo three-dimensional surface geometry of abdominal aortic aneurysms," Ann Biomed Eng, 27(4), pp. 469-479.
- [167] Shim, M. B., Gunay, M., and Shimada, K., 2009, "Three-dimensional shape reconstruction of abdominal aortic aneurysm," Computer-Aided Design, 41(8), pp. 555-565.
- [168] Johnson, E., 2010, "Improving the accuracy of fluid-structure interaction analyses of patient-specific cerebral aneurysms," Carnegie Mellon University, Pittsburgh.
- [169] Keyak, J. H., Meagher, J. M., Skinner, H. B., and Mote, C. D., Jr., 1990, "Automated three-dimensional finite element modelling of bone: a new method," Journal of biomedical engineering, 12(5), pp. 389-397.
- [170] Muller, R., and Ruegsegger, P., 1995, "Three-dimensional finite element modelling of non-invasively assessed trabecular bone structures," Med Eng Phys, 17(2), pp. 126-133.
- [171] Zhang, Y., Bajaj, C., and Sohn, B. S., 2005, "3D Finite Element Meshing from Imaging Data," Comput Methods Appl Mech Eng, 194(48-49), pp. 5083-5106.
- [172] Antiga, L., Piccinelli, M., Botti, L., Ene-Iordache, B., Remuzzi, A., and Steinman, D. A., 2008, "An image-based modeling framework for patient-specific computational hemodynamics," Med Biol Eng Comput, 46(11), pp. 1097-1112.
- [173] Zhang, Y., Bazilevs, Y., Goswami, S., Bajaj, C. L., and Hughes, T. J., 2007, "Patient-Specific Vascular NURBS Modeling for Isogeometric Analysis of Blood Flow," Comput Methods Appl Mech Eng, 196(29-30), pp. 2943-2959.
- [174] De Santis, G., De Beule, M., Segers, P., Verdonck, P., and Verhegghe, B., 2011, "Patient-specific computational haemodynamics: generation of structured and conformal hexahedral meshes from triangulated surfaces of vascular bifurcations," Comput Methods Biomech Biomed Engin, 14(9), pp. 797-802.
- [175] Zhang, Y., Hughes, T. J. R., and Bajaj, C. L., 2008, "Automatic 3D mesh generation for a domain with multiple materials," Proceedings of the 16th International Meshing Roundtable, pp. 367-386.
- [176] Fang, Q. Q., and Boas, D. A., 2009, "Tetrahedral Mesh Generation from Volumetric Binary and Gray-Scale Images," 2009 IEEE International Symposium on Biomedical Imaging: From Nano to Macro, Vols 1 and 2, pp. 1142-1145.
- [177] Liu, P., 2010, "A Volume Meshing Strategy for Patient Specific Abdominal Aortic Aneurysms," Masters, Carnegie Mellon University, Pittsburgh.
- [178] Boissonnat, J. D., and Oudot, S., 2005, "Provably good sampling and meshing of surfaces," Graphical Models, 67(5), pp. 405-451.

- [179] Amenta, N., and Bern, M., 1999, "Surface reconstruction by Voronoi filtering," *Discrete Comput Geom*, 22(4), pp. 481-504.
- [180] CGAL, "Computational Geometry Algorithms Library."
- [181] Chew, L. P., 1993, "Guaranteed-quality mesh generation for curved surfaces," *Proceedings of the ninth annual symposium on Computational geometry*, ACM, San Diego, California, United States.
- [182] Taubin, G., 1995, "A signal processing approach to fair surface design," *Proceedings of the 22nd annual conference on Computer graphics and interactive techniques*, ACM.
- [183] Taubin, G., 2000, "Geometric Signal Processing on Polygonal Meshes," *Eurographics*, The Eurographics Association.
- [184] Shewchuk, J. R., 2002, "Delaunay refinement algorithms for triangular mesh generation," *Computational Geometry-Theory and Applications*, 22(1-3), pp. 21-74.
- [185] Shewchuk, J. R., 1996, "Triangle: Engineering a 2D Quality Mesh Generator and Delaunay Triangulator," *Applied Computational Geometry: Towards Geometric Engineering*, Springer-Verlag, pp. 203-222.
- [186] Si, H., 2006, "TetGen A Quality Tetrahedral Mesh Generator and Three-Dimensional Delaunay Triangulator," p. 62.
- [187] Knupp, P. M., 2000, "Achieving finite element mesh quality via optimization of the Jacobian matrix norm and associated quantities. Part II - A framework for volume mesh optimization and the condition number of the Jacobian matrix," *International Journal for Numerical Methods in Engineering*, 48(8), pp. 1165-1185.
- [188] Zhang, Y., and Bajaj, C., 2006, "Adaptive and Quality Quadrilateral/Hexahedral Meshing from Volumetric Data," *Comput Methods Appl Mech Eng*, 195(9), pp. 942-960.
- [189] Raut, S. S., Chandra, S., Shum, J., Washington, C., Muluk, S. C., Finol, E. A., and Rodriguez, J., 2012, "Biological, geometric and biomechanical factors influencing abdominal aortic aneurysm rupture risk: a comprehensive review," *Recent Patents In Medical Imaging*, (accepted).
- [190] Thompson, R. W., 2005, "Aneurysm treatments expand," *Nat Med*, 11(12), pp. 1279-1281.
- [191] Limet, R., Sakalihan, N., and Defawe, O. D., 2005, "Abdominal aortic aneurysm," *Lancet*, 365(9470), pp. 1577-1589.
- [192] Chaikof, E. L., Brewster, D. C., Dalman, R. L., Makaroun, M. S., Illig, K. A., Sicard, G. A., Timaran, C. H., Upchurch, G. R., Jr., Veith, F. J., and Society for Vascular, S., 2009, "The care of patients with an abdominal aortic aneurysm: the Society for Vascular Surgery practice guidelines," *J Vasc Surg*, 50(4 Suppl), pp. S2-49.
- [193] Raghavan, M. L., Vorp, D. A., Federle, M. P., Makaroun, M. S., and Webster, M. W., 2000, "Wall stress distribution on three-dimensionally reconstructed models of human abdominal aortic aneurysm," *J Vasc Surg*, 31(4), pp. 760-769.
- [194] Choke, E., Cockerill, G., Wilson, W. R., Sayed, S., Dawson, J., Loftus, I., and Thompson, M. M., 2005, "A review of biological factors implicated in abdominal aortic aneurysm rupture," *Eur J Vasc Endovasc Surg*, 30(3), pp. 227-244.
- [195] Lederle, F. A., Johnson, G. R., Wilson, S. E., Ballard, D. J., Jordan, W. D., Jr., Blebea, J., Littooy, F. N., Freischlag, J. A., Bandyk, D., Rapp, J. H., Salam, A. A., and Veterans Affairs Cooperative Study, I., 2002, "Rupture rate of large abdominal aortic aneurysms in patients

- refusing or unfit for elective repair," JAMA : the journal of the American Medical Association, 287(22), pp. 2968-2972.
- [196] Brown, L. C., Epstein, D., Manca, A., Beard, J. D., Powell, J. T., and Greenhalgh, R. M., 2004, "The UK Endovascular Aneurysm Repair (EVAR) trials: design, methodology and progress," Eur J Vasc Endovasc Surg, 27(4), pp. 372-381.
- [197] Vande Geest, J. P., Simon, B. R., and Mortazavi, A., 2006, "Toward a model for local drug delivery in abdominal aortic aneurysms," Ann N Y Acad Sci, 1085, pp. 396-399.
- [198] Maier, A., Gee, M. W., Reeps, C., Pongratz, J., Eckstein, H. H., and Wall, W. A., 2010, "A comparison of diameter, wall stress, and rupture potential index for abdominal aortic aneurysm rupture risk prediction," Ann Biomed Eng, 38(10), pp. 3124-3134.
- [199] Reeps, C., Gee, M., Maier, A., Gurdan, M., Eckstein, H. H., and Wall, W. A., 2010, "The impact of model assumptions on results of computational mechanics in abdominal aortic aneurysm," J Vasc Surg, 51(3), pp. 679-688.
- [200] Speelman, L., Schurink, G. W., Bosboom, E. M., Buth, J., Breeuwer, M., van de Vosse, F. N., and Jacobs, M. H., 2010, "The mechanical role of thrombus on the growth rate of an abdominal aortic aneurysm," J Vasc Surg, 51(1), pp. 19-26.
- [201] Coyle, P., Doyle, B. J., Grace, P. A., McLoughlin, T., and Kavanagh, E. G., 2010, "Predicting the Locations of Abdominal Aortic Aneurysm Rupture Using Computational Modelling," Irish Journal of Medical Science, 179, pp. S362-S362.
- [202] Raut, S. S., Jana, A., and Finol, E. A., 2012, "A framework for multi-domain volume meshing for FSI analysis of vasculatures: an application to Abdominal Aortic Aneurysm," J Biomech Eng, (submitted).
- [203] Speelman, L., Bosboom, E. M., Schurink, G. W., Hellenthal, F. A., Buth, J., Breeuwer, M., Jacobs, M. J., and van de Vosse, F. N., 2008, "Patient-specific AAA wall stress analysis: 99-percentile versus peak stress," Eur J Vasc Endovasc Surg, 36(6), pp. 668-676.
- [204] Humphrey, J. D., and Taylor, C. A., 2008, "Intracranial and abdominal aortic aneurysms: similarities, differences, and need for a new class of computational models," Annual review of biomedical engineering, 10, pp. 221-246.
- [205] Taylor, C. A., and Humphrey, J. D., 2009, "Open Problems in Computational Vascular Biomechanics: Hemodynamics and Arterial Wall Mechanics," Comput Methods Appl Mech Eng, 198(45-46), pp. 3514-3523.
- [206] Malkawi, A. H., Hinchliffe, R. J., Xu, Y., Holt, P. J., Loftus, I. M., and Thompson, M. M., 2010, "Patient-specific biomechanical profiling in abdominal aortic aneurysm development and rupture," J Vasc Surg, 52(2), pp. 480-488.
- [207] Thubrikar, M. J., Labrosse, M., Robicsek, F., Al-Soudi, J., and Fowler, B., 2001, "Mechanical properties of abdominal aortic aneurysm wall," Journal of medical engineering & technology, 25(4), pp. 133-142.
- [208] Schriefl, A. J., Zeindlinger, G., Pierce, D. M., Regitnig, P., and Holzapfel, G. A., 2012, "Determination of the layer-specific distributed collagen fibre orientations in human thoracic and abdominal aortas and common iliac arteries," Journal of the Royal Society, Interface / the Royal Society, 9(71), pp. 1275-1286.
- [209] Raut, S. S., Jana, A., and Finol, E. A., 2012, "Evaluation of the effects of aneurysm geometry and vascular wall material properties on the AAA wall mechanics," J Biomech Eng, (submitted).

- [210] Hardy, R. J., Lane, S. N., Ferguson, R. I., and Parsons, D. R., 2003, "Assessing the credibility of a series of computational fluid dynamic simulations of open channel flow," *Hydrol Process*, 17(8), pp. 1539-1560.
- [211] Choi, G., Cheng, C. P., Wilson, N. M., and Taylor, C. A., 2009, "Methods for quantifying three-dimensional deformation of arteries due to pulsatile and nonpulsatile forces: implications for the design of stents and stent grafts," *Ann Biomed Eng*, 37(1), pp. 14-33.
- [212] Schulze-Bauer, C. A., Morth, C., and Holzapfel, G. A., 2003, "Passive biaxial mechanical response of aged human iliac arteries," *J Biomech Eng*, 125(3), pp. 395-406.
- [213] Hill, M. R., Duan, X., Gibson, G. A., Watkins, S., and Robertson, A. M., 2012, "A theoretical and non-destructive experimental approach for direct inclusion of measured collagen orientation and recruitment into mechanical models of the artery wall," *J Biomech*, 45(5), pp. 762-771.
- [214] Muhs, B. E., Vincken, K. L., van Prehn, J., Stone, M. K., Bartels, L. W., Prokop, M., Moll, F. L., and Verhagen, H. J., 2006, "Dynamic cine-CT angiography for the evaluation of the thoracic aorta; insight in dynamic changes with implications for thoracic endograft treatment," *Eur J Vasc Endovasc Surg*, 32(5), pp. 532-536.
- [215] van Prehn, J., Vincken, K. L., Muhs, B. E., Barwegen, G. K., Bartels, L. W., Prokop, M., Moll, F. L., and Verhagen, H. J., 2007, "Toward endografting of the ascending aorta: insight into dynamics using dynamic cine-CTA," *J Endovasc Ther*, 14(4), pp. 551-560.
- [216] Morrison, T. M., Choi, G., Zarins, C. K., and Taylor, C. A., 2009, "Circumferential and longitudinal cyclic strain of the human thoracic aorta: age-related changes," *J Vasc Surg*, 49(4), pp. 1029-1036.
- [217] Wang, Z., and Chesler, N. C., 2011, "Pulmonary vascular wall stiffness: An important contributor to the increased right ventricular afterload with pulmonary hypertension," *Pulmonary circulation*, 1(2), pp. 212-223.
- [218] Hudetz, A. G., 1979, "Incremental elastic modulus for orthotropic incompressible arteries," *J Biomech*, 12(9), pp. 651-655.
- [219] Chesler, N. C., Thompson-Figueroa, J., and Millburne, K., 2004, "Measurements of mouse pulmonary artery biomechanics," *J Biomech Eng*, 126(2), pp. 309-314.
- [220] Tierney, A. P., Callanan, A., and McGloughlin, T. M., 2012, "Use of regional mechanical properties of abdominal aortic aneurysms to advance finite element modeling of rupture risk," *J Endovasc Ther*, 19(1), pp. 100-114.
- [221] Stalhand, J., Klarbring, A., and Karlsson, M., 2004, "Towards in vivo aorta material identification and stress estimation," *Biomech Model Mechanobiol*, 2(3), pp. 169-186.
- [222] Draney, M. T., Herfkens, R. J., Hughes, T. J., Pelc, N. J., Wedding, K. L., Zarins, C. K., and Taylor, C. A., 2002, "Quantification of vessel wall cyclic strain using cine phase contrast magnetic resonance imaging," *Ann Biomed Eng*, 30(8), pp. 1033-1045.
- [223] Avril, S., Schneider, F., Boissier, C., and Li, Z. Y., 2011, "In vivo velocity vector imaging and time-resolved strain rate measurements in the wall of blood vessels using MRI," *J Biomech*, 44(5), pp. 979-983.

APPENDICES

APPENDIX A: Analytical calculations of phantom

A) Volume calculation for phantom

Radius variation given by,

$$r(z) = R_{min} + \frac{1}{2}(R_{max} - R_{min}) \left(1 - \cos(2\pi z/L)\right)$$

Rearranging and substituting $R_{avg} = \frac{1}{2}(R_{max} + R_{min})$ and $R_{amp} = \frac{1}{2}(R_{max} - R_{min})$

$$r(z) = R_{avg} - R_{amp}\cos(2\pi z/L)$$

Entire phantom can be considered as a collection of circular disks of cross-sectional area πr^2 and infinitesimal thickness dz . Hence, integrating along Z axis,

$$\begin{aligned} \text{volume } V &= \int_0^L \pi (r(z))^2 dz = \int_0^L \pi \left(R_{avg} - R_{amp}\cos(2\pi z/L) \right)^2 dz \\ &= \pi \int_0^L \left(R_{avg}^2 + R_{amp}^2 \cos^2(2\pi z/L) - 2R_{avg}R_{amp}\cos(2\pi z/L) \right) dz \\ &= \pi \left[\int_0^L R_{avg}^2 dz + \int_0^L R_{amp}^2 \cos^2(2\pi z/L) dz - \int_0^L 2R_{avg}R_{amp}\cos(2\pi z/L) dz \right] \\ &= \pi \left[R_{avg}^2 \int_0^L dz + \frac{1}{2}R_{amp}^2 \int_0^L (1 + \cos(4\pi z/L)) dz - 2R_{avg}R_{amp} \int_0^L \cos(2\pi z/L) dz \right] \\ &= \pi \left[R_{avg}^2 \int_0^L dz + \frac{1}{2}R_{amp}^2 \left(\int_0^L dz + \int_0^L \cos(4\pi z/L) dz \right) - 2R_{avg}R_{amp} \int_0^L \cos(2\pi z/L) dz \right] \end{aligned}$$

Both cosine terms in above equation can be reduced to the form $\int_0^{2n\pi} \cos(\theta) d\theta$ by changing limits with $n=1$ and $n=2$ respectively. Since, total signed area under sinusoidal curve is zero for integration over complete period, both terms become zero. Hence,

$$\begin{aligned} V &= \pi \left[R_{avg}^2 \int_0^L dz + \frac{1}{2}R_{amp}^2 \int_0^L dz \right] \\ V &= \pi \left(R_{avg}^2 + \frac{1}{2}R_{amp}^2 \right) L \end{aligned}$$

Using $R_{min} = 1 \text{ cm}$, $R_{max} = 3 \text{ cm}$ and $L = 9 \text{ cm}$, we get

$$\underline{\text{volume } V = 127.2344 \text{ cm}^3}$$

B) Analytical area calculation for phantom

Using similar approach and terminology as described above

$$\begin{aligned} \text{Area } A &= \int_0^L 2\pi r(z) dz \\ &= 2\pi \int_0^L \left[R_{min} + \frac{1}{2}(R_{max} - R_{min}) \left(1 - \cos(2\pi z/L) \right) \right] dz \\ &= 2\pi R_{min} \int_0^L dz + \pi(R_{max} - R_{min}) \int_0^L dz - \pi(R_{max} - R_{min}) \int_0^L \cos(2\pi z/L) dz \end{aligned}$$

Third integration term can be found to be equal to zero using argument that $\int_0^{2n\pi} \cos(\theta) d\theta = 0$

for $n = 1, 2, 3 \dots$

Hence,

$$\text{Area } A = \pi(R_{max} + R_{min})L$$

Hence, using $R_{min} = 1 \text{ cm}$, $R_{max} = 3 \text{ cm}$ and $L = 9 \text{ cm}$, we get

$$\underline{\text{area } A = 113.097 \text{ cm}^2}$$

C) Wall domain-specific volume

From results derived previously

$$V = \pi \left(R_{avg}^2 + \frac{1}{2} R_{amp}^2 \right) L$$

$$V_w = V - V'$$

where, V' is volume of volume formed by inner wall surface closed at both ends. If t denoted uniform in-plane wall thickness, we can make following approximation ignoring the fact that actual in-plane thickness is not uniform. Ideally thickness measured in local normal direction is uniform and hence in-place thickness will depend on local normal direction.

$$V' = \pi \left((R_{avg} - t)_{avg}^2 + \frac{1}{2} (R_{amp} - t)^2 \right) L$$

$$V_w = \pi \left((2R_{avg}t - t^2) + \frac{1}{2} (2R_{amp}t - t^2) \right) L$$

Using $R_{min} = 1 \text{ cm}$, $R_{max} = 3 \text{ cm}$, $L = 9 \text{ cm}$, $t = 0.15 \text{ cm}$ we get

$$\underline{\text{volume } V_w = 20.2514 \text{ cc}}$$

APPENDIX B: Metric definitions for mesh characterization

In following definitions suffix i implies quantity defined at i 'th node

A) r-R ratio formula

$$r - R \text{ ratio} = 2 \times \frac{\text{radius of incircle of facet}_i}{\text{radius of circumcircle of facet}_i}$$

For triangle with sides of length a, b and c , area A , and semiperimeter $s = \frac{1}{2}(a + b + c)$, circumcircle radius R_c is given by,

$$R_c = \frac{abc}{4\sqrt{s(s-a)(s-b)(s-c)}}$$

Here, denominator is four times area of triangle, since, area A can be calculated using Heron's formula $A = \sqrt{s(s-a)(s-b)(s-c)}$

Radius of incircle, r_I is calculated by,

$$r_I = \frac{2\sqrt{s(s-a)(s-b)(s-c)}}{a + b + c}$$

Hence,

$$rR \text{ ratio} = \frac{2r_I}{R_c} = \frac{16s(s-a)(s-b)(s-c)}{abc(a+b+c)} = \frac{16A^2}{abc(a+b+c)}$$

B) relAreaErr

$$\text{relAreaErr} = \frac{\sum A_i - \text{Reference Area}}{\text{Reference area}}$$

For asymmetric phantom,

$$\text{Reference Area} = \text{Analytical Area}$$

For patient-specific Laplace iterations,

$$\text{Reference Area} = \text{Area at optimum number(6) of iterations}$$

For patient-specific Taubin iterations,

$$\text{Reference Area} = \text{Area at optimum number(20) of iterations}$$

C) *relVolErr*

$$relVolErr = \frac{Volume\ enclosed\ by\ surface\ mesh - Reference\ area}{Reference\ area}$$

For asymmetric phantom,

$$Reference\ Volume = Analytical\ Volume$$

For patient-specific Laplace iterations,

$$Reference\ volume = volume\ at\ optimum\ number(6)\ of\ iterations$$

For patient-specific Taubin iterations,

$$Reference\ volume = volume\ at\ optimum\ number(20)\ of\ iterations$$

D) *distErr*

$distErr_i$:= signed minimum perpendicular distance of mesh node from ideal analytical surface

E) *distErr_max*

$$distErr_max := \max(|distErr_i|)$$

F) *distErr_avg*

$$distErr_avg := \text{mean}(distErr_i)$$

G) *distErr_std*

$$distErr_std := \text{standard deviation}(distErr_i)$$

APPENDIX C: CT image acquisition parameters and AAA maximum diameter for shortlisted cohort

Table 28: AAA maximum diameter and image parameters in the shortlisted population cohort.

Patient	Pixel size (mm)	Slice spacing (mm)	Max. Diameter (mm)
U001	0.935547	2.5	53.78
U009	0.742188	1.5	54.34
U013	0.669922	3.0	52.7
U019	0.742188	3.0	51.78
U020	0.771484	3.0	50.47
U024	0.742188	5.0	54.61
U030	0.796875	3.0	51.15
U031	0.912109	3.0	50.32
U032	0.742188	3.0	52.83
U033	0.742188	3.0	50.59
U037	0.773438	3.0	52.24
U038	0.777344	3.0	52.05
U043	0.792969	5.0	52.13
U044	0.951172	3.0	53.55
U046	0.775391	4.0	54.55
U049	0.742188	3.0	51.78
U051	0.777344	3.0	52.93
U056	0.703125	5.0	50
U058	0.767578	3.0	52.37

U060	0.742188	3.0	50.05
U061	0.794922	3.0	54.22
U075	0.742188	3.0	53.37
U076	0.925781	3.0	52.63
U089	0.796875	3.0	50.51
U101	0.677000	3.0	53.78
U106	0.703125	2.0	51.08
U107	0.804688	5.0	54.75
U132	0.742188	3.0	51.5
Mode	0.742188	3.0	53.78
Mean	0.778086	3.2	52.36
MAX	0.951172	5.0	54.75
MIN	0.669922	1.5	50.00
Std. dev.	0.072364	0.8	1.49

APPENDIX D: Exploration of computational performance of FE solver for optimized settings towards effective computational resource utilization

a) Problem statement

Given a computational resource consisting of N hyper-threading capable cores and M GB RAM, find time efficient configuration with respect to optimal number of simulations running in parallel and respective allotment of cores per simulations for executing hundreds of simulations.

b) Computational Resource:

Hardware

Dell Precisions workstations T7500, 96 GB, 12 cores Intel Xeon X5650, 2.66 GHz processor

Software

ADINA (ADINA R&D, Watertown, MA, version 8.8.3)

c) Methods

Ten different configuration settings were explored.

d) FE Details

All degrees of freedom constrained at proximal and distal ends of vasculature, 3 time steps, pressure ramps from 0 mmHg to 15 mmHg in steps of 5 mmHg, total number of degrees of freedom in sample patient-specific wall-only test case - 1,720,035, element used – 27 noded hexahehral element with two layers across thickness

e) Material Models

Power law neo-Hookean material model dependent on only first invariant of left Cauchy-Green deformation tensor with 3 different combinations of material parameters (Model A, B, and D in Figure 43 and Table 14).

f) Observations and results

Solver time was exactly same for varied material parameter combinations explored. Hence, only one of them (population average material properties) was used for further exploration.

Table 29: Explored configurations for simulation execution and corresponding execution time

Config. #	Hypert-reading	# Parallel simulations	# threads per simulation	Memory per simulation (MB)	Process priority*	Time per simulation (s)
1	Enabled	12	2	7700	-20	59719
2	Disabled	12	1	7700	-20	47045
3	Enabled	11	2	7700	-20	48498
4	Enabled	11	1	7700	-20	36504
5	Disabled	11	1	7700	-20	42391
6	Disabled	6	1	15000	-20	3784
7	Disabled	6	1	15000	-18	3731
8**	Disabled	1	6	15000	-18	891
9**	Disabled	1	12	15000	-18	640
10**	Enabled	1	24	15000	-18	657

* Highest priority: -20; Lowest priority: 20

** Multiple re-executions too avoid possibility incidental load fluctuations since it has only one simulations and random system internal process may perturb measured execution time significantly.

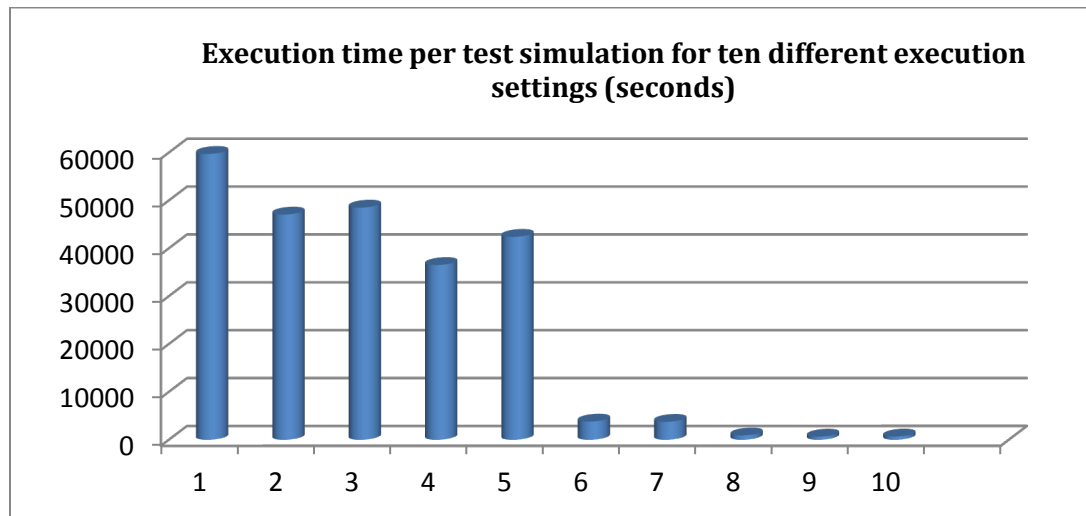


Figure 65: Visual representation of computational performance.

g) Conclusion

Significant variation is observed in performance of solver execution. For optimal execution, a policy of un-hyper-threaded, single simulation at a time with maximum possible number of threads was finalized and used in all simulations reported here.

APPENDIX E: Scripts for pre-processing and automated execution of FEA simulations

a) Bash Script

```
#!/bin/bash
# Author: Samarth Raut < sraut @ andrew Dot cmu. edu>
# Date: 1st June 2012

# Shell script for automated one-by-one launching for Aim01
# Needs mesh file and ADINA scripts for mat 1 2 3 4 5 in the
current working directory
# Needs to be executed as root if nice command is to be used to
launch adina in adinaSolveCmd()
# It is assumed that filenames are not very long so that they can
be contained within single line in
# ADINA journal file script
# Edit following settings as per need especially: Series_Name and
Sim_N_start

Series_Name="Aim02a" # common string in name for all batch of
# simulations launched together
Sim_N_start=873
SimCount=0
Mem_GB=46
Scratch="/home/sraut/Desktop/Aim02"
Mesh_Src_Dir="/home/sraut/Desktop/Aim02"
Adina_In_Src_Dir="/home/sraut/Desktop/Aim02"
Adina_Home_Dir="/opt/adina/8.8.3"
thrdN=6
datTemplateStr="sim" # without extension (.nas is assumed to be
the file extension)
extn=".nas"
matModel_Nstart=1
matModel_Nstop=5
strEndCharNumber=12
FileCount=0

copyCmd_in(){
    # Format: copyCmd_in "$Adina_In_Src_Dir" "$matN"
    "$Work" "$SimName"
```

```

        printf -v Cmd_str 'cp %s/*mat%02d_S.in %s/%s.in' "$1"
        "$2" "$3" "$4"
        $Cmd_str
    }

replaceCmd_sed(){ # $1 -> OldStr, $2 -> NewStr , $3 -> Name of
file to edit
        sed -i "s/$1/$2/g" "$3"
    }

replaceCmd_ed(){ # $1 -> OldStr, $2 -> NewStr , $3 -> Name of
file to edit
        printf '%s\n' "g/$1/ s/$1/$2/g" 'w' | ed -s "$3"
    }

adinaSolveCmd(){
#       nice -n -16 $Adina_Home_Dir/tools/adina8.8 -t ${thrdN} -
mm ${Mem_MB}MB *.dat
        $Adina_Home_Dir/tools/adina8.8 -t ${thrdN} -mm
        ${Mem_GB}GB *.dat
    }

adinaDatCmd(){
        $Adina_Home_Dir/tools/au18.8 -cmd -s ${SimName}.in
    }

runDiffSim(){ # $1 -> file# , $2 -> FileName

        printf 'Starting to work of file #d :%s\n' $1 $2
        date

        for (( matN=matModel_Nstart ; matN<=matModel_Nstop;
matN++ )) # if not in series order then use like: matN
#           in 1 2 4
        do
# Set simulation number
        SIM_N=$(( $Sim_N_start + $SimCount ))
        SimCount=$(( $SimCount + 1 ))
        echo "Simulation number = ${SIM_N}"

# Make directory for simulation
        MeshNameStr=${2:0:$strEndCharNumber}

```

```

printf -v SimName 'sim%04d_%s_%s_mat%02d' "$SIM_N"
"$Series_Name" "$MeshNameStr" "$matN"
#       printf -v SimName 'sim%04d_%s_%s_mat%02d'
"$SIM_N" "$Series_Name" "$Patient_ID" "$matN"
Work="$Scratch/$SimName"
echo "Creating and setting Work directory to : $Work"
mkdir -p $Work

# Copy necessary files in target directory
# No need to copy mesh file since all the simulation can
# look at the same place as
#geometry is same
# copyCmd_mesh="cp $Mesh_Src_Dir/*.nas $Work"
# $copyCmd_mesh

echo "Copying *.in file to $Work"
copyCmd_in "$Adina_In_Src_Dir" "$matN" "$Work"
"$SimName"

# Switch to battle field directory
echo "Switching to directory: $Work"
pushd $Work

# Edit journal file for ADINA data file creation
inFile="$Work/$SimName.in"
replaceCmd_sed "$datTemplateStr.nas" "$2" "$inFile" #
Edit input mesh file name
replaceCmd_sed "$datTemplateStr.dat" "$SimName.dat"
"$inFile" # Edit output .dat file

# Create *.dat file
adinaDatCmd
# Launch simulation
adinaSolveCmd
# Switch back to original launchpad directory
popd
done
}

for FileName in *$extn;
do
((FileCount++))

```

```

runDiffSim "$FileCount" "$FileName"
done
# FileCountFinal=$(( $FileCount - 1 ))
echo "Total number of $extn files used = $FileCount".
printf 'Launched total %#d simulations' $SimCount
printf 'Finished. Exiting shell script now ...\n'
date

```

b) Adina preprocessing commands

*Command file created from session file information stored within AUI database

*--- Author : Samarth Raut < sraut @ andrew. cmu Dot edu>

*---Date : 22nd March, 2012

--- Database created 22 March 2012, 18:43:45 ---

--- by ADINA: AUI version 8.8.3 ---

*

DATABASE NEW SAVE=NO PROMPT=NO

FEPROGRAM ADINA

CONTROL FILEVERSION=V87

*

PARAMETER C1_VAL '1740000.00000000'

*

PARAMETER C3_VAL '1.881000000E+07'

*

PARAMETER NU '0.499'

*

PARAMETER DENSITY_VAL '1.20000000000000'

*Using correlation in Manual BulkMod is as follows

PARAMETER BULKMOD_VAL '2*(\$C1_VAL)/(1-2*\$NU)'

*

NASTRAN-ADIN FILENAME=,

'../sim.nas',

XY-YZ=YES BEAM=THREE SUBCASE=0 RBAR=DEFAULT RBE2=DEFAULT,

NCTOLERA=0.000100000000000000 RBAR-MAT=0,

RBAR-ARE=0.0000000000000000 RBAR-DIA=0.0000000000000000,

RBAR-THI=0.0000000000000000 RBE2-MAT=0 RBE2-ARE=0.0000000000000000,


```

RBE2-DIA=0.0000000000000000 RBE2-THI=0.0000000000000000,
K=0.0000000000000000 M=0.0000000000000000 C=0.0000000000000000,
CONVERT=NONE IN-NODE=4 OUT-NODE=8 SHELL=SHELL-CONDUCTION,
BCELL=REPLACE DUPLICAT=YES DEFAULT=AUI SPLIT=PRO ELFACESE=BCELL,
NODESET=BCELL SOL=106 BCELL-ID=INDEX
*
MASTER ANALYSIS=STATIC MODEX=EXECUTE TSTART=0.0000000000000000 IDOF=111,
OVALIZAT=NONE FLUIDPOT=AUTOMATIC CYCLICPA=1 IPOSIT=STOP,
REACTION=NO INITIALS=NO FSINTERA=NO IPRINT=DEFAULT CMASS=NO,
SHELLNDO=AUTOMATIC AUTOMATI=OFF SOLVER=SPARSE,
CONTACT=CONSTRAINT-FUNCTION TRELEASE=0.0000000000000000,
RESTART=NO FRACTURE=NO LOAD-CAS=NO LOAD-PEN=NO SINGULAR=YES,
STIFFNES=0.000100000000000000 MAP-OUTP=NONE MAP-FORM=NO,
NODAL-DE=" POROUS-C=NO ADAPTIVE=0 ZOOM-LAB=1 AXIS-CYC=0,
PERIODIC=NO VECTOR-S=GEOMETRY EPSI-FIR=NO STABILIZ=NO,
STABFACT=1.0000000000000000E-10 RESULTS=PORTHOLE FEF CORR=NO,
BOLTSTEP=1 EXTEND-S=YES CONVERT=NO DEGEN=YES TMC-MODE=NO,
ENSIGHT=NO IRSTEPS=1 INITIALT=NO
*
TIMEFUNCTION NAME=1 IFLIB=1 FPAR1=0.0000000000000000,
FPAR2=0.0000000000000000 FPAR3=0.0000000000000000,
FPAR4=0.0000000000000000 FPAR5=0.0000000000000000,
FPAR6=0.0000000000000000
@CLEAR
0.0000000000000000
120.00000000000000 120.00000000000000
@
*
TIMESTEP NAME=DEFAULT
@CLEAR
24 5.0000000000000000
@
*
MASTER ANALYSIS=STATIC MODEX=EXECUTE TSTART=0.0000000000000000 IDOF=111,
OVALIZAT=NONE FLUIDPOT=AUTOMATIC CYCLICPA=1 IPOSIT=STOP,
REACTION=NO INITIALS=NO FSINTERA=NO IPRINT=DEFAULT CMASS=NO,
SHELLNDO=AUTOMATIC AUTOMATI=OFF SOLVER=SPARSE,
CONTACT=CONSTRAINT-FUNCTION TRELEASE=0.0000000000000000,
RESTART=NO FRACTURE=NO LOAD-CAS=NO LOAD-PEN=NO SINGULAR=YES,

```

```

STIFFNES=0.0001000000000000000 MAP-OUTP=NONE MAP-FORM=NO,
NODAL-DE=" POROUS-C=NO ADAPTIVE=0 ZOOM-LAB=1 AXIS-CYC=0,
PERIODIC=NO VECTOR-S=GEOMETRY EPSI-FIR=NO STABILIZ=AUTOMATIC,
STABFACT=1.000000000000000E-10 RESULTS=PORTHOLE FEFCORR=NO,
BOLTSTEP=1 EXTEND-S=YES CONVERT=-NO DEGEN=YES TMC-MODE=NO,
ENSIGHT=-UNFORMATTED IRSTEPS=1 INITIALT=NO
*
NODESAVE-STE ELEMSAVE=OVERWRITE
@CLEAR
1 8 24 8
@
*
EGROUP THREEDSOLID NAME=111 DISPLACE=DEFAULT STRAINS=DEFAULT,
MATERIAL=1 RSINT=DEFAULT TINT=DEFAULT RESULTS=STRESSES DEGEN=YES,
FORMULAT=0 STRESSRE=GLOBAL INITIALS=NONE FRACTUR=NO,
CMASS=DEFAULT STRAIN-F=0 UL-FORMU=DEFAULT LVUS1=0 LVUS2=0,
SED=YES RUPTURE=ADINA INCOMPAT=NO TIME-OFF=0.000000000000000,
POROUS=NO WTCM=1.000000000000000 OPTION=NONE DESCRIPT='NONE',
PRINT=DEFAULT SAVE=DEFAULT TBIRTH=0.000000000000000,
TDEATH=0.000000000000000 TMC-MATE=1 RUPTURE=-0
*
LOAD PRESSURE NAME=1 MAGNITUD=1333.220000000000 BETA=0.000000000000000,
LINE=0
*
APPLY-LOAD BODY=0
@CLEAR
'PRESSURE' 1 'ELEMENT-FACE' 1132 0 1 0.000000000000000 0 -1 0 0 0,
'NO' 0.000000000000000 0.000000000000000 1 0 'MID'
@
*
FIXBOUNDARY ELFACESE FIXITY=ALL
@CLEAR
114 'ALL'
115 'ALL'
116 'ALL'
@
*
PPROCESS NPROC=1 MINEL=0 MAXEL=999999999
*

```

EGCONTROL MAXELG=999999999

*

MASTER ANALYSIS=STATIC MODEX=EXECUTE TSTART=0.000000000000 IDOF=111,
OVALIZAT=NONE FLUIDPOT=AUTOMATIC CYCLICPA=1 IPOSIT=STOP,
REACTION=NO INITIALS=NO FSINTERA=NO IPRINT=DEFAULT CMASS=NO,
SHELLNDO=AUTOMATIC AUTOMATI=OFF SOLVER=SPARSE,
CONTACT=CONSTRAINT-FUNCTION TRELEASE=0.000000000000000,
RESTART=NO FRACTURE=NO LOAD-CAS=NO LOAD-PEN=NO SINGULAR=YES,
STIFFNES=0.000100000000000000 MAP-OUTP=NONE MAP-FORM=NO,
NODAL-DE=' ' POROUS-C=NO ADAPTIVE=0 ZOOM-LAB=1 AXIS-CYC=0,
PERIODIC=NO VECTOR-S=GEOMETRY EPSI-FIR=NO STABILIZ=AUTOMATIC,
STABFACT=1.000000000000000E-10 RESULTS=PORTHOLE FEFCORR=NO,
BOLTSTEP=1 EXTEND-S=YES CONVERT=NO DEGEN=YES TMC-MODE=NO,
ENSIGHT=UNFORMATTED IRSTEPS=1 INITIALT=NO

*

MATERIAL MOONEY-RIVLIN NAME=1 C1=\$C1_VAL C2=0.000000000000000,
C3=\$C3_VAL C4=0.000000000000000 C5=0.000000000000000,
C6=0.000000000000000 C7=0.000000000000000 C8=0.000000000000000,
C9=0.000000000000000 D1=0.000000000000000 D2=0.000000000000000,
KAPPA=\$BULKMOD_VAL DENSITY=\$DENSITY_VAL FITTING=0,
VISCOELA=0 TEMPERAT=NO TREF=0.000000000000000 RUBBER-T=0,
RUBBER-V=0 RUBBER-M=0 RUBBER-O=0 MDESCRIP='NONE'

*

ADINA OPTIMIZE=SOLVER FILE=,
'sim.dat',
FIXBOUND=YES MIDNODE=NO OVERWRT=YES

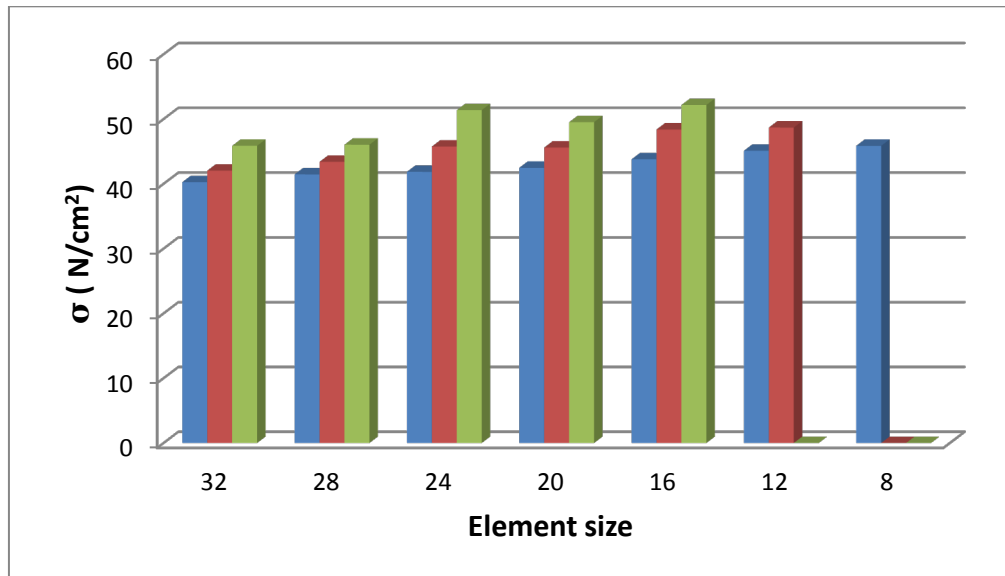
*

*END

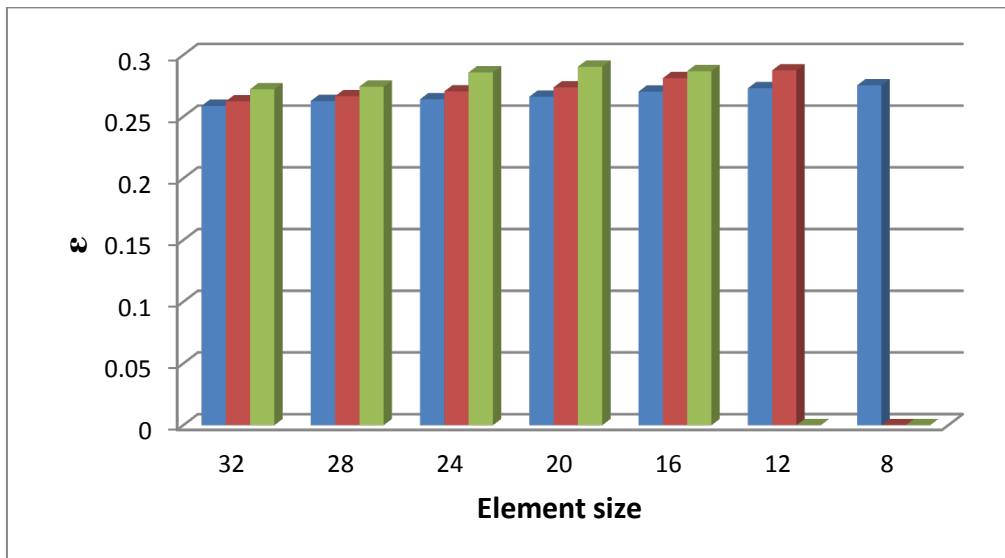
*

quit immediate=yes

APPENDIX F: Results of the mesh sensitivity study for patient-specific model U032



a) Maximum first principal stress

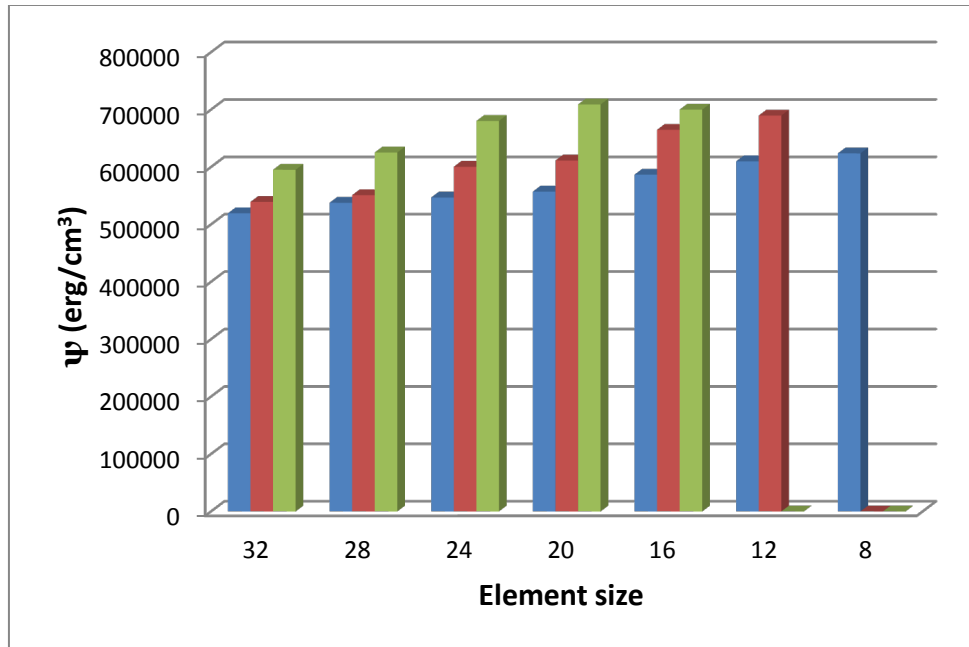


b) Maximum first principal strain

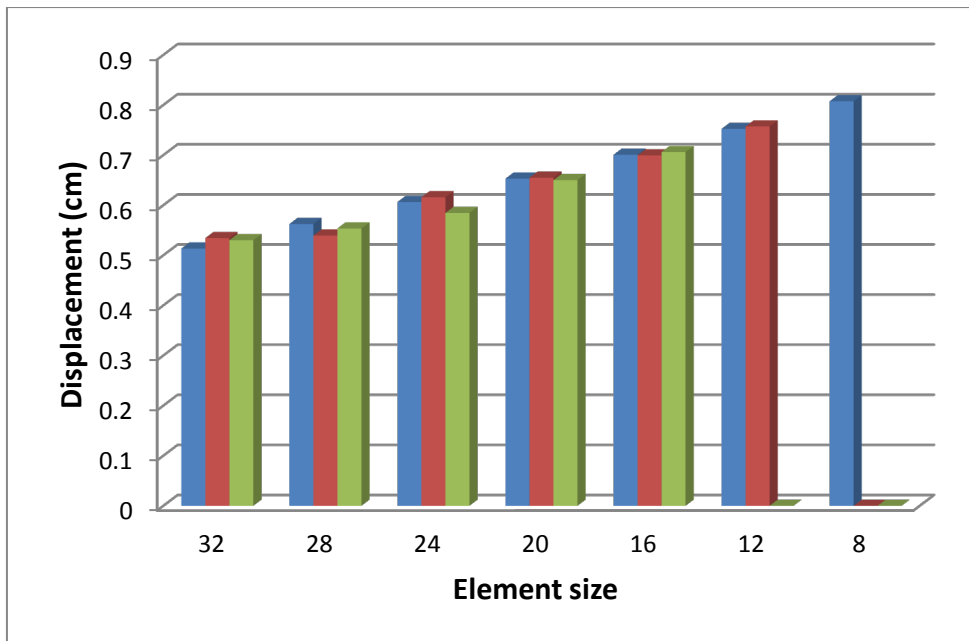
■ Layer 1

■ Layer 2

■ Layer 3



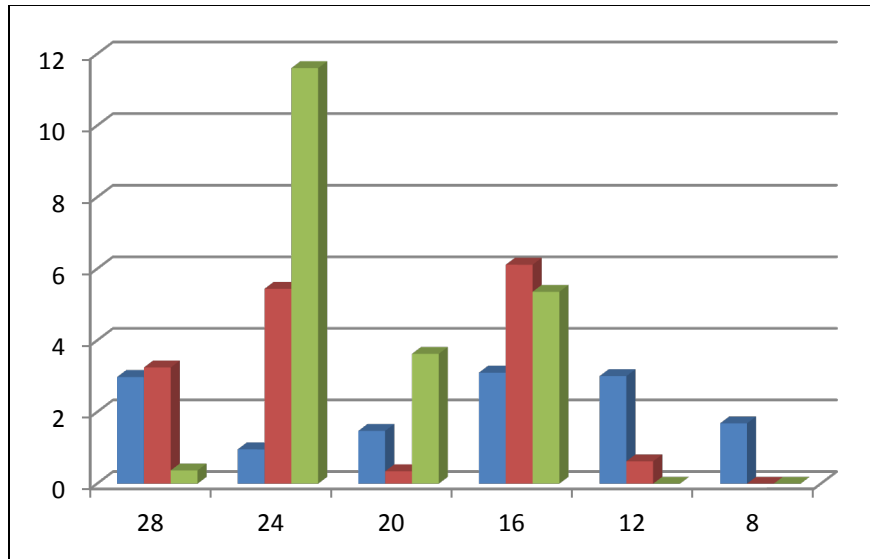
c) Maximum strain energy density



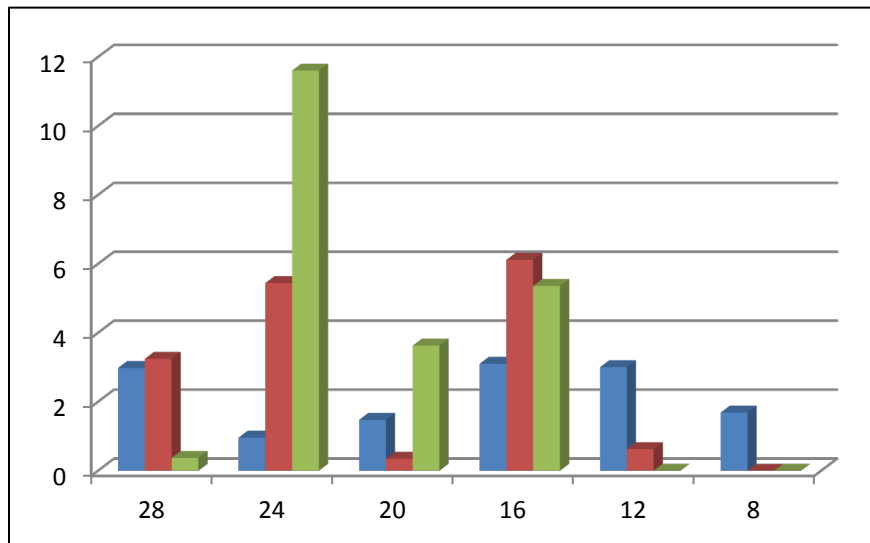
d) Maximum displacement

■ Layer 1
 ■ Layer 2
 ■ Layer 3

Figure 66: Mesh convergence study - biomechanical parameter absolute values

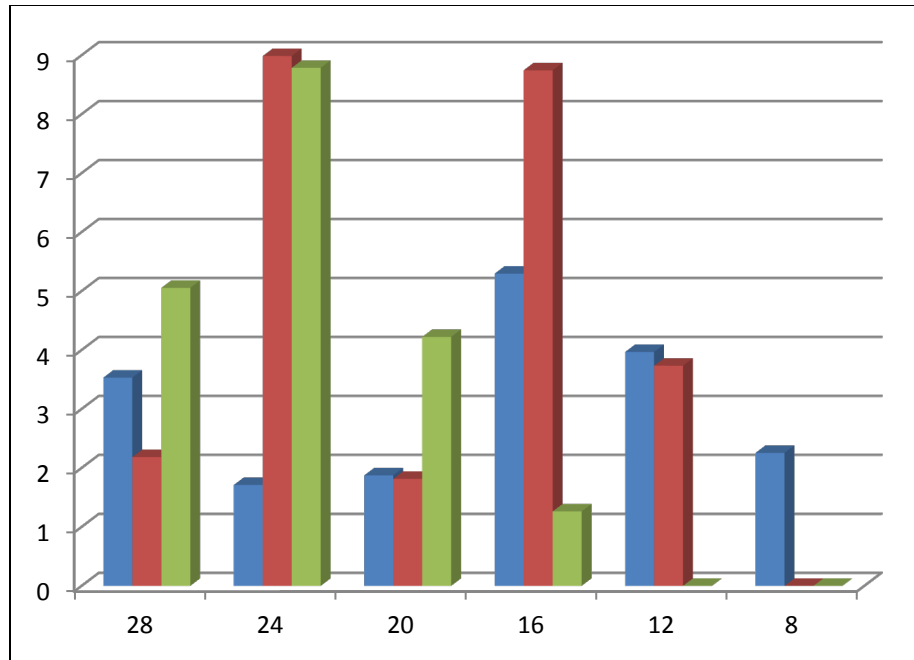


a) Incremental % change in maximum first principal stress (y-axis)

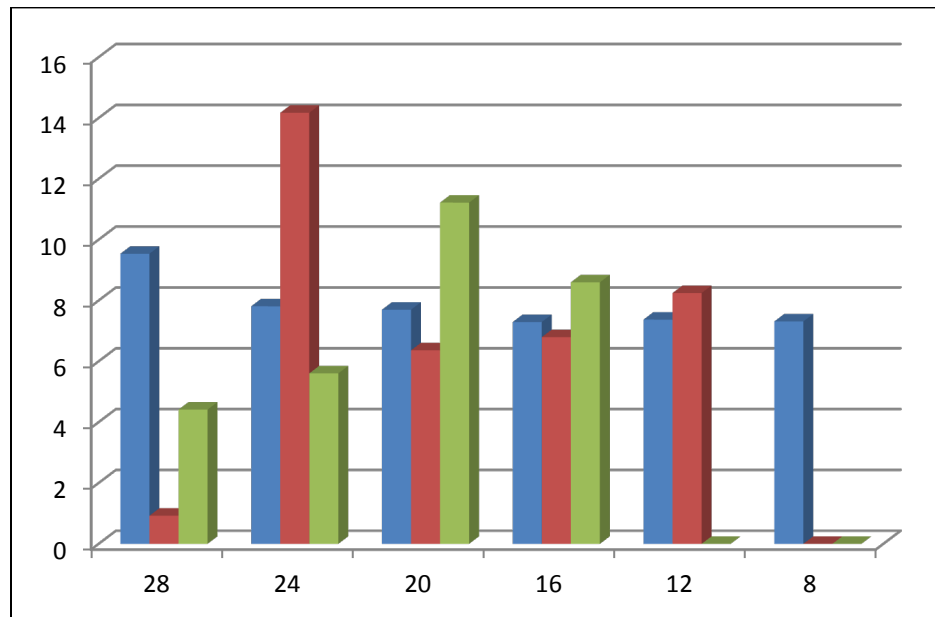


b) Incremental change in maximum first principal strain (y-axis)

■ Layer 1
 ■ Layer 2
 ■ Layer 3



c) Incremental change in maximum strain energy density



d) Incremental change in maximum displacement

■ Layer 1
 ■ Layer 2
 ■ Layer 3

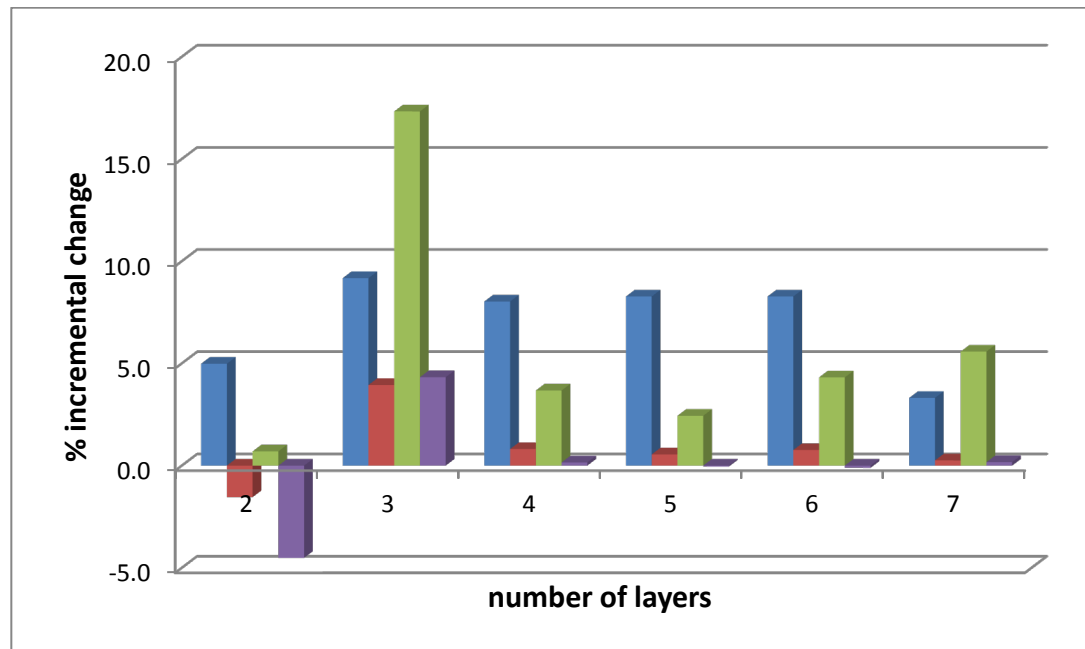
Figure 67: Mesh convergence study - incremental change in biomechanical parameter.

APPENDIX G: Mesh convergence study to assess effect of number of wall layers

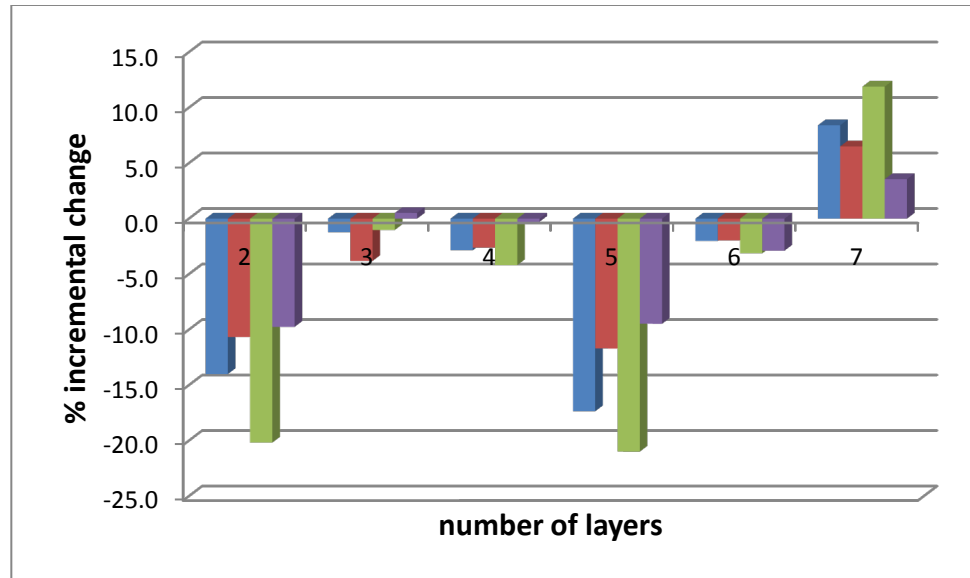
Method: Same patient-specific surface mesh was extruded using wall extrusion code to for volume mesh for the aneurysm wall domain with constant thickness, however, with different number of layers across thickness. Simulations were executed with 24 number of timesteps increasing pressure from 0 mmHg to 120 mmHg. Results were analyzed for maximum and average values of biomechanical parameters and computational load.

Color scheme in plots with multiple legends:

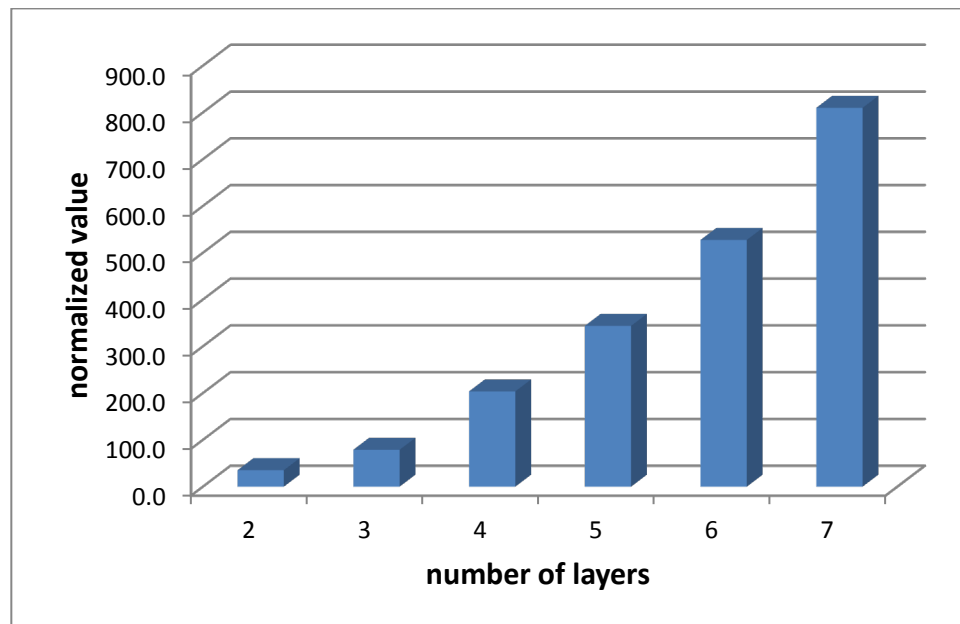
σ_{max} ϵ_{max} ψ_{max} δ_{max}



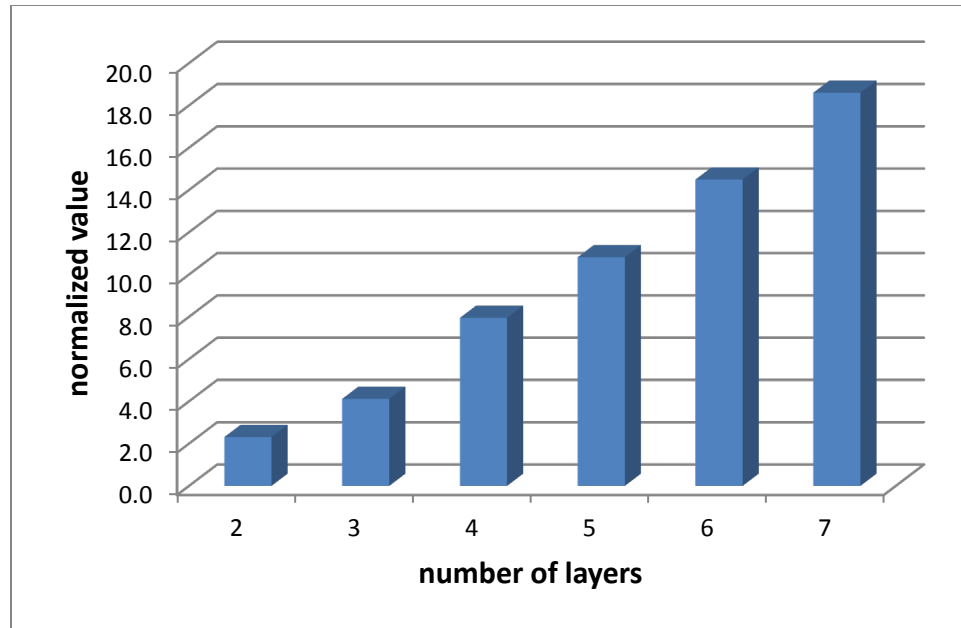
a) Maximum biomechanical parameters



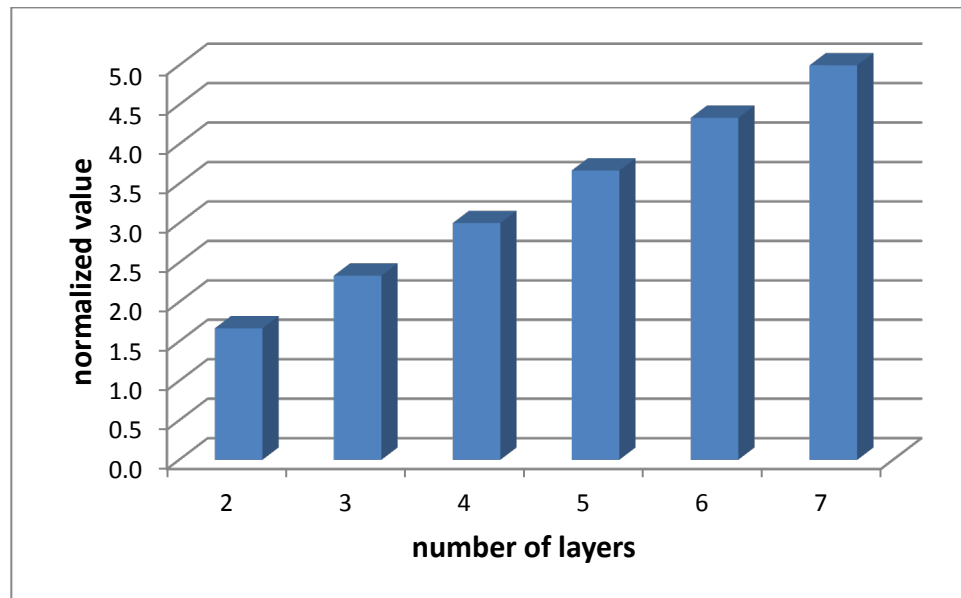
b) Averaged biomechanical parameters



c) Computational time normalized with corresponding value for single layered mesh



d) Computational memory normalized with corresponding value for single layered mesh



e) Number of equations solved normalized with corresponding value for single layered mesh

APPENDIX H: Demonstration of calculation of intra- and inter-patient variability

Let's say outcome of simulations for k 'th patient-specific case are stored in matrix \mathbf{A}^k and let's also follow convention that value in i 'th row and j 'th column is represented by A_{ij}^k . Let's say row number corresponds to material model# and columns 1 to 4 list spatial maximum values for biomechanical quantities, namely, maximum principal stress, maximum principal strain, strain-energy-density, and displacements respectively.

Reference value for intra-patient: For intra-patient category reference values for normalization for k 'th patient-specific case and j 'th biomechanical quantity would be A_{1j}^k . Note that subscript 1 is used since model#1 corresponds to population average material model which is used as reference for material variation.

Reference value for inter-patient: For each inter-patient category, reference values for normalization for i 'th material model and j 'th biomechanical quantity would be R_{ij} such that

$$R_{ij} = \frac{1}{n} \sum_{k=1}^n A_{ij}^k$$

where, n denotes total number of patient-specific cases. In this work $n = 28$.

Intra-patient variability calculation:

If \mathbf{B}^k represent matrix of intra-patient variability values for k 'th patient, then following same conventions as before

$$B_{ij}^k = \frac{A_{ij} - A_{1j}}{A_{1j}} \times 100$$

Inter-patient variability calculation:

If C^k represent matrix of inter-patient variability values for k 'th patient, then following same conventions as before

$$C_{ij}^k = \frac{A_{ij} - R_{ij}}{R_{ij}} \times 100$$

Mean (μ) and standard deviation (σ) of variability:

In intra-patient stud

$$\mu_{intra_j} = mean\{ |B_{ij}^k| \} , \text{ and}$$

$$\sigma_{intra_j} = standard\ deviation\ \{ |B_{ij}^k| \} \quad \text{where } i = 1,2,3,4,5 ; j = 1,2,3,4 ; k = 1,2,3, \dots n$$

In inter-patient study

$$\mu_{intra_j} = mean\{ |C_{ij}^k| \} , \text{ and}$$

$$\sigma_{intra_j} = standard\ deviation\ \{ |C_{ij}^k| \} \quad \text{where } i = 1,2,3,4,5 ; j = 1,2,3,4 ; k = 1,2,3, \dots n$$

Norm calculations:

In intra-patient study

Root mean square norm specific for j 'th biomechanical quantity in case of k 'th patient :

$$L_j = \sqrt{\frac{1}{5} \left(\sum_{i=1}^5 B_{ij}^2 \right)}$$

Overall matrix norm case of k 'th patient:

$$L = \|B\|$$

Maximum absolute column sum norm was used.

In inter-patient study

norm specific for j 'th biomechanical quantity in case of k 'th patient :

$$L_j = \sqrt{\frac{1}{5} \left(\sum_{i=1}^5 C_{ij}^2 \right)}$$

Overall matrix norm case of k 'th patient:

Using maximum absolute column sum norm,

$$L = \|C\|$$

APPENDIX I: Qualitative observations on the location of the AAA maximum first principal stresses

Claim: Instead of inflection point which is related to 2D scenario, stress in AAA in 3D is maximum at a location that features combined effect of larger diameter and local surface saddle point (surface region that has local concavity in one direction and local convexity in relatively perpendicular direction)

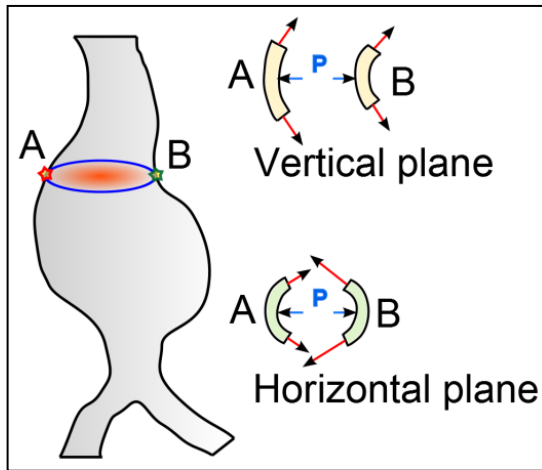


Figure 68: Schematic illustrating rationale behind high stresses in saddle shaped surface region

Rationale: Consider two points A and B in Figure 68 located at all convex and at saddle point (where there is concavity in vertical plane but convexity in horizontal plane) respectively. Consider free body diagram and forces acting as shown in schematic below. The membrane forces augment pressure action from inside in case of B in vertical plane and hence there is increased demand on membrane forces

at B in horizontal plane causing higher stress. On the other side, in-plane membrane stresses in vertical plane ease load on those in horizontal plane. Hence, it is not inflection point, but local saddle point shape of surface that results in higher stresses. These stresses are also dependent on diameter since magnitude of in-plane membrane stress is crudely related to diameter. Hence, it is combination of diameter and local curvature that govern stress pattern under uniform wall thickness assumption.

It is interesting to note how this theory also explains previously reported inflection-stress correlation [86]. In literature it has been frequently mentioned that inflection point has

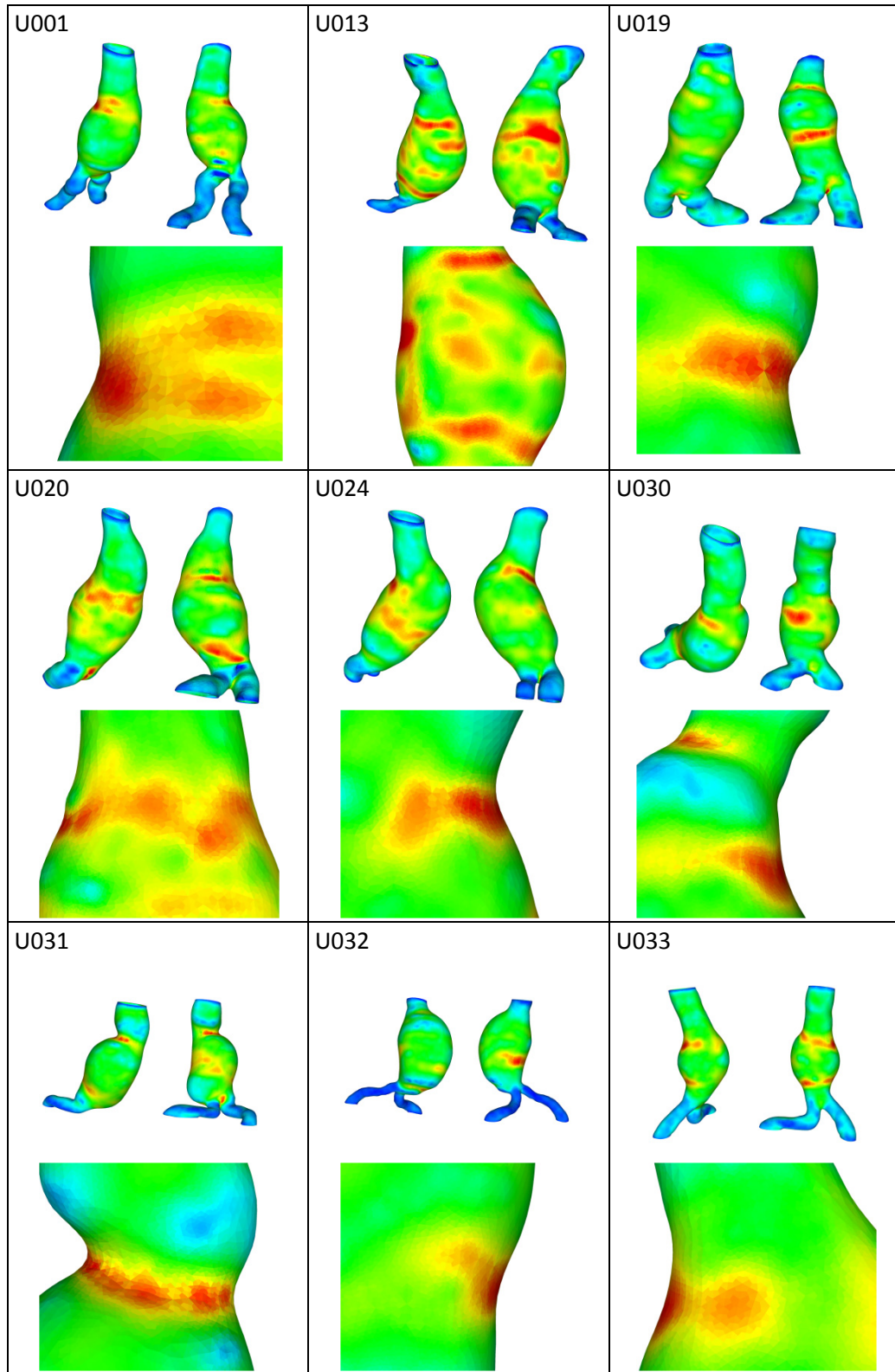
highest stress. However, that concept is more relevant to idealized models where surface is generated by revolution of a curve around an axis. Even in that case, it is actually saddle point like feature that is formed due to reduced curvature in one plane while in perpendicular plane it is convex due to revolution. It is likely to shift towards the direction where diameter is increasing since membrane stresses will increase with diameter. Similar observation has been reported by Vorp et al [87].

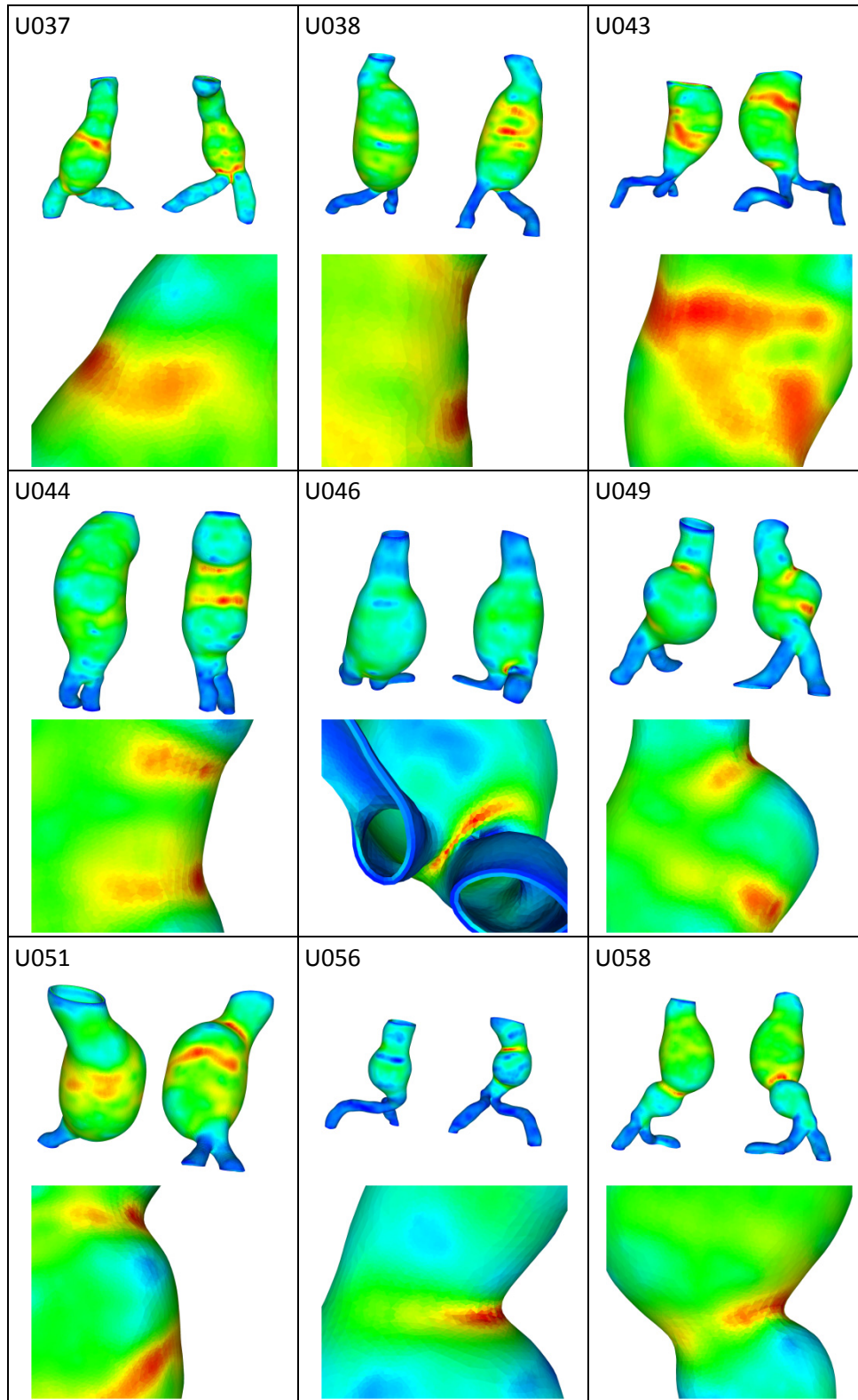
Observations: The following snapshots support above mentioned claim. Note that most of the times it is not inflection point or maximum diameter where high stress occurs. Even though there is no exact formula, extent of local curvature and diameter together influence the maximum stress location. Concavity is seen almost always in zoomed view.

Implications:

It is very likely that stress distribution is function of geometry and to a lesser extent of material. Since it is all about force equilibrium, even anisotropic material would also likely play limited role in governing stresses in displacements/loaded are not excessively high.

Geometric index by combining local curvature (signed) and diameter may be possible to expect location of high stress without FEA.





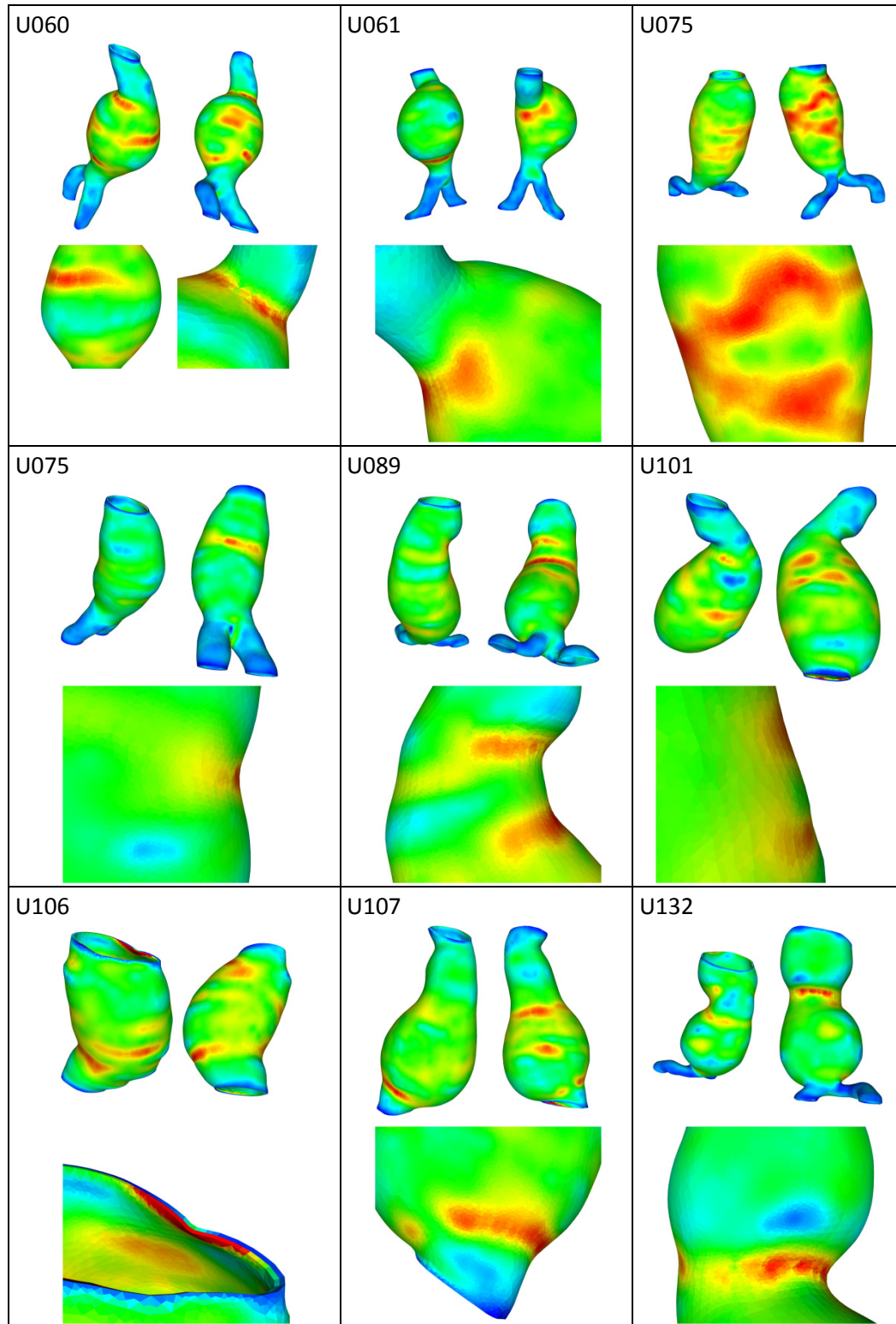


Figure 69: Close correlation in saddle point and high stress region in 28 patient-specific geometries under identical material model parameters and pressure loads.

APPENDIX J: Estimated statistics of wall thickness in AAA sac

In-plane measured wall thickness corrected for local normal direction from 28 patient specific AAA models (unit: cm).

Model	Min.	Mean	Std. Dev.	Max
U001	0.028	0.189	0.060	0.481
U009	0.037	0.140	0.044	0.349
U013	0.051	0.118	0.027	0.251
U019	0.058	0.173	0.026	0.309
U020	0.078	0.191	0.048	0.405
U024	0.061	0.129	0.023	0.229
U030	0.056	0.167	0.050	0.366
U031	0.053	0.200	0.048	0.368
U032	0.055	0.122	0.026	0.265
U033	0.041	0.125	0.020	0.215
U037	0.076	0.204	0.048	0.399
U038	0.064	0.246	0.047	0.361
U043	0.065	0.227	0.057	0.350
U044	0.073	0.174	0.040	0.415
U046	0.075	0.122	0.016	0.182
U049	0.065	0.149	0.036	0.347
U051	0.064	0.166	0.026	0.348
U056	0.041	0.180	0.070	0.480
U058	0.053	0.167	0.044	0.310
U060	0.058	0.129	0.035	0.336
U061	0.059	0.188	0.063	0.390
U075	0.057	0.127	0.023	0.240
U076	0.065	0.152	0.022	0.268
U089	0.063	0.135	0.028	0.252

APPENDIX K: 3D Interactive model (enabled only when using PDF viewer)

Following page shows a 3D patient-specific AAA wall geometry with variable wall thickness reconstructed for one of the patients by extrusion of surface triangular mesh. Please select preset views from dropdown options after clicking on the model as well as use interactive mode facilitating rotate, zoom, section, shading, dimensional measurements (units: cm), and lighting operations. Following features can be appreciated:

- 1) Grid independent mesh generation
- 2) Robust approach for meshing bifurcated region.
- 3) Very good quality mesh
- 4) Uniform distribution of nodes on surface which ensures uniform sampling of points for in vivo strain estimation.

NOTE:

- 1) For the sake of compatibility in order to be able to include this graphics in 3D PDF view, the end facets which are formed by quadrilaterals in actual volume mesh are split into triangles.
- 2) Following page may not appear in print version.

3D model on this page may not appear in print version. Please use PDF viewer (electronic version) for interactive view and click on the model window to start.

